UNIONE EUROPEA
Fondo Sociale Europeo

Ministero dell'Università e della Ricerca

PON RICERCA E INNOVAZIONE

UNIVERSITÀ DELLA CALABRIA

UNIVERSITA' DELLA CALABRIA

Dipartimento di Ingegneria Meccanica Energetica e Gestionale

Dottorato di Ricerca in

Ingegneria Civile e Industriale

Con il contributo di (Ente finanziatore)

PON RI 2014 – 2020

CICLO

XXXII

ANALYSIS OF MECHANICAL PROPERTIES OF COLD SPRAY COATINGS FOR TRIBOLOGICAL AND VACUUM APPLICATIONS

Settore Scientifico Disciplinare ING-IND/14

Coordinatore: **Ch.mo Prof. Franco Furgiuele**

Firma Firma oscurata in base alle linee guida del Garante della privacy

Supervisore/Tutor: **Ch.mo Prof. Carmine Maletta**

Firma Firma oscurata in base alle linee guida del Garante della privacy

Dott. Mario Tului

Firma Firma oscurata in base alle linee guida del Garante della privacy

Dottorando: Dott. Pietro Magarò

Firma Firma oscurata in base alle linee guida del Garante della privacy

Abstract

Cold Gas Dynamic Spray (CGDS) is a process in which solid particle are accelerated in a de Laval nozzle toward a substrate. At the impact, if the particle velocity exceeds a critical value, i.e. the critical velocity, particles undergo plastic deformation and the consequent adiabatic shear instability provides material flow and heat for bonding. This phenomenon is the main driving force for the adhesion of the coating to the substrate. Compared other thermal spray techniques, since it utilizes kinetic rather than thermal energy for deposition, it offers several technological advantages; in fact, residual stresses, oxidation and chemical reactions can be avoided. Materials such as metals, ceramics, composites and polymers can be deposited using cold gas dynamic spray, creating new opportunities in order to obtain particular properties; in fact, good coatings using hard metals can be obtained with the purpose to enhance the tribological properties of such mechanical components. Therefore, the expected qualitative leap in using CGDS is magnified in harsh environments with great benefits predicted in design flexibility gains, precision improvements, production time reductions, cost reduction, integration of additional embedded functionalities.

The purpose of this thesis is to demonstrate the possibility to obtain good deposits of Stellite-6 with the aim to enhance the surface resistance during sliding condition, while mechanical and vacuum properties of pure titanium coatings were analyzed for possible application in ultra high vacuum (UHV) systems at the European Organization for Nuclear Research (CERN).

This thesis, firstly, analyzes the effects of process parameters on mechanical and tribological properties of Stellite-6 coatings. The gas pressure and temperature as well as the traverse speed of the deposition torch were considered as significant process parameters. The aim is to overcome some technical issues arising in the cold spray deposition of hard anti-wear metallic coatings, such as Stellite-6, due to their high strength and melting point. A High-Pressure CGDS equipment was used and systematic studies were carried out for a deeper understanding of the

effects of all investigated process parameters. A particular focus has been put on the substrate temperature, that can be regarded as an indirect process parameter. This latter, in fact, was monitored in-situ during deposition by infrared thermography (IR). The microstructure was analyzed by both optical and scanning electron microscopic observations. Mechanical properties were analyzed by instrumented micro- and nano-indentation measurements. Hardness (H) and Young's modulus (E) were considered as affective parameters to estimate the inter-particle cohesion strength and the work hardening of the coating. Results revealed that the substrate temperature, that is affected by the process parameters, plays a fundamental role in the coating formation process, and, both mechanical and tribological properties, of CGDS Stellite-6 coatings are mainly affected by the impact temperature of the particle-substrate system.

It is also well-known that this alloy undergoes several physical changes at the interface during dry sliding while is sensitive to the loading conditions and environment. Due to these micro-structural alterations, the wear behavior of the alloy is modified, which linear Archard-like wear models could not capture. To better understand the wear performance a Stellite-6 coatings in-situ, a mechanistic model of wear would be desirable, so a systematic experimental study was performed. Tests were done under combinations of sliding speed ($0.1-0.5\ m/s$) and contact pressure ($0{,}5-5\ MPa$). Platelet wear and subsurface cracking was seen in high speed tests, as well as evidence of plastic deformation at the wear surface. These results suggest the platelet wear observed is more likely a consequence of adhesive wear. On the other hand, in low speed conditions detachment and pull-out phenomena mainly affect the worn surface of coatings leading to a type of fatigue wear known as *"nano-grain wear"* that does not allow to use the wear model proposed by Archard. Unique to this study, the cross-sectional nano-indentation study showed the stiffness of material at and below wear interface to drop significantly.

The last section was aimed by the necessity to overcome some technical issues, usually experienced during pure titanium deposition. These latter are mainly related to poor coating compactness and adhesion to the substrates. These technical issues become even more stringent when dealing with vacuum systems as they could affect the leak tightness and gas release in UHV. Preliminary micrographic observations were carried out to select the optimal values of the process parameters, that are pressure (p) and temperature (T) of the propellent gas. Mechanical properties of deposits were subsequently analyzed at the nano/micro and macro scale by instrumented indentations and adhesion tensile tests respectively. Vacuum properties

were analyzed by outgassing rate measurements, thermal desorption spectroscopy (TDS) and helium tightness tests.

Indentation results revealed that compact and homogeneous coatings can be obtained if high energy deposition parameters ($p{\sim}4\,MPa,\ T{\sim}1000°\,C$) are applied. However, a limited adhesion strength on stainless steel substrates is the main technical issue of the coating process. Outgassing and TDS tests revealed an abnormal nitrogen release that is attributed to gas entrapped during deposition or during the production stage of the Ti powders as N_2 is used in the gas atomization process. Finally, helium leak rates were found to be incompatible with UHV requirements applied in modern particle accelerators. Much higher helium leak rates were detected along the interface between the coating and the substrate than through the thickness. These results confirm that the interface represents the weakest point of the bi-material system. Further studies are needed to solve this technical issue.

Sommario

Il Cold Gas Dynamic Spray (CGDS) consiste nell'accelerare delle polveri attraverso un ugello di de Laval verso un substrato. Al momento dell'impatto, se la velocità delle particelle supera un valore di soglia, ovvero la velocità critica, le particelle plasticizzano a causa dell'"adiabatic shear instability" e, per effetto del calore che si genera all'interfaccia, aderiscono alla superficie. Rispetto alle altre tecniche di termo-spruzzatura, utilizzando energia cinetica piuttosto che energia termica durante il processo di deposizione, il cold spray offre numerosi vantaggi; infatti, tensioni residue, ossidazione, e reazioni chimiche possono essere evitate. Diverse tipologie di materiali, come metalli, ceramiche, compositi e polimeri possono essere depositati con il cold gas dynamic spray, creando molteplici opportunità al fine ottenere proprietà specifiche; infatti, usando metalli duri possono essere ottenuti rivestimenti capaci di migliorare le proprietà tribologiche di diversi componenti meccanici. Pertanto, il salto qualitativo atteso nell'uso del CGDS è maggiore se si pensa ambienti particolarmente aggressivi dati i grandi benefici previsti in termini di flessibilità di progettazione, miglioramenti della precisione, riduzione dei tempi di produzione, riduzione dei costi, integrazione di funzionalità aggiuntive.

L'obbiettivo di questa tesi è dimostrare come sia possibile ottenere rivestimenti realizzati in Stellite-6 allo scopo di migliorare la resistenza superficiale in condizioni di contatto strisciante; inoltre, le proprietà meccaniche e da vuoto di rivestimenti in titanio puro sono state analizzate in vista di un possibile utilizzo di tali rivestimenti nei sistemi di ultra alto vuoto (UHV) presso l'Organizzazione europea per la ricerca nucleare (CERN).

La tesi, in primo luogo, analizza l'effetto dei parametri di processo sulle proprietà meccaniche e tribologiche dei rivestimenti in Stellite-6. La pressione e la temperatura del gas, nonché la velocità di scansione della torcia, sono stati presi in esami, essendo questi i parametri di processo che maggiormente influenzano il risultato della deposizione. L'obiettivo, dunque, è quello di superare alcuni problemi tecnici osservati nella deposizione di rivestimenti metallici per applicazioni antiusura, come la Stellite-6, a causa della loro elevata resistenza allo

snervamento e del loro elevato punto di fusione. Per le attività sperimentali è stato utilizzato un impianto ad alta pressione e sono stati condotti studi sistematici dedicati ad una più profonda comprensione degli effetti di tutti i parametri di processo individuati sulla qualità attesa del rivestimento. Particolare attenzione è stata posta sulla temperatura del substrato, che può essere considerata come parametro di processo indiretto. Quest'ultimo, infatti, è stato monitorato *"in situ"* durante il processo di deposizione mediante termografia ad infrarossi (IR). La microstruttura è stata analizzata mediante indagini micrografiche. Le proprietà meccaniche sono state analizzate mediante prove di micro e nano-indentazione strumentata. La durezza (H) e il modulo di Young (E) sono stati scelti per stimare sia la resistenza all'adesione del rivestimento che l'incrudimento subito dalle particelle. I risultati hanno rivelato che la temperatura del substrato, che a sua volta è influenzata dai parametri di processo, svolge un ruolo fondamentale nel processo di deposizione in quanto, sia le proprietà meccaniche che tribologiche, dei rivestimenti in Stellite-6 sono direttamente influenzate dalla temperatura all'impatto del sistema particella-substrato.

È anche noto che, durante il contatto strisciante, all'interfaccia tale lega subisce diverse trasformazioni microstrutturali oltre ad essere sensibile alle diverse condizioni di carico e all'ambiente. A causa di queste alterazioni microstrutturali, il comportamento della lega subisce delle alterazioni che i classici modelli di usura (i.e. Archard) non sono in grado di cogliere. Per comprendere meglio le prestazioni dei rivestimenti in Stellite-6 in termini di resistenza all'usura è stata sviluppata un'apposita campagna sperimentale. I test sono stati condotti in diverse combinazioni di velocità di strisciamento ($0.1 - 0.5\ m/s$) e di pressione di contatto ($0.5 - 5\ MPa$). Crack subsuperficiali e detriti a forma di piastrine sono state osservati nei test ad alta velocità, con zone caratterizzate da evidenti deformazioni plastiche sulla superficie di usura. Questi risultati suggeriscono che i meccanismi di usura coinvolti sono più probabilmente riconducibili ai meccanismi di usura adesiva. D'altra parte, in condizioni di bassa velocità, la superficie d'usura è principalmente caratterizzata da fenomeni di distaccamento del rivestimento e di pull-out, causando un tipo di usura a fatica noto come *"nano-grain wear"* che non consente di utilizzare il modello di usura proposto da Archard. Prove di nano-indentazione lungo la sezione trasversale hanno mostrato che sia la durezza che la rigidezza del materiale al di sotto dell'interfaccia di usura subisce variazioni significative.

L'ultima sezione è stata sviluppata allo scopo di superare alcuni problemi tecnici, di solito riscontrati durante la deposizione di titanio puro. Questi ultimi sono principalmente legati alla

scarsa compattezza del rivestimento e all'adesione al substrato. Tali problemi diventano ancora più stringenti quando si tratta di sistemi da vuoto, in quanto potrebbero influenzarne la tenuta. Sono state eseguite indagini micrografiche preliminari al fine di selezionare i valori ottimali dei parametri di processo, ovvero pressione (p) e temperatura (T) del gas. Le proprietà meccaniche dei rivestimenti sono state successivamente analizzate su scala nano/micro e macro mediante test di indentazioni strumentate e prove di adesione rispettivamente. Le proprietà da vuoto sono state analizzate mediante misurazioni della velocità di degassamento, spettroscopia di desorbimento termico (TDS) e prove di tenuta dell'elio.

I risultati dei test meccanici hanno rivelato che è possibile ottenere rivestimenti compatti e omogenei usando parametri di deposizione ad elevato contenuto energetico ($p{\sim}4\ MPa$, $T{\sim}1000°\ C$). Tuttavia, la limitata resistenza all'adesione su substrati in acciaio inossidabile rappresenta il principale problema riscontrato. I test di degassamento e TDS hanno rivelato un anomalo rilascio di azoto che è stato attribuito al gas intrappolato durante la deposizione o durante la fase di gas atomizzazione delle polveri di titanio. Infine, i "leak rate" ottenuti sono risultati incompatibili con i requisiti di ultra alto vuoto richiesti nei moderni acceleratori di particelle. "Leak rate" più elevati sono stati osservati lungo l'interfaccia tra il rivestimento e il substrato rispetto al solo spessore. Tali risultati confermano come l'interfaccia rappresenti ancora il punto più debole del sistema Titanio-Acciaio. Ulteriori studi sono, dunque, necessari per risolvere tali problematiche.

Acknowledgments

First of all, I would like to acknowledge my Ph.D. supervisor, professor Carmine Maletta, for his endless support, for his motivation, his great knowledge and the encouragement he gave me. His guidance and constant feedback helped me through these years. I cannot imagine a better advisor and mentor for my Ph.D. study.

Besides my supervisor, special thanks have to be given to all professors of my research group, in particular professor Franco Furgiuele, as Ph.D. course coordinator, always helpful and available for any doubt or clarification.

I would like to acknowledge professor Luigi Bruno, Marco Alfano, Leonardo Pagnotta and last but not least, professor Emanuele Sgambitterra for his friendship. I would like also to acknowledge all the other research team members, Giovanna, Fabio, Danilo, Edoardo, Valentina, Carlo and Elio.

I am deeply thankful to Dr. Mario Tului from CSM spa for his generous support, sharing ideas and thoughtful guidance. I first saw the cold spray set up in his lab. Thank you for the hands-on work experience and depositing the coatings to make my work productive and stimulating.

I greatly appreciate the support received during the six months that I spent in the national Center for Advanced Triblogy at Southampton by professor Robert J. Wood who was helpful and provided me with his assistance and his valuable advice.

A special mention is necessary for the MechLab staff, Renato Bentrovato, Diego Pulice and Ernesto Ramundo, for its helpful assistance with experimental set-ups, practical advice, and sample preparation.

I would like to acknowledge my parents, Fiorino and Maria Rosaria, who have never stopped believing in me and encouraging me to follow my dreams allowing me to reach this important milestone, with all the affection and support possible. I would like to thanks my brother, Fabio, my best friend, for his endless support and unconditional love.

As for my girlfriend Chiara, I find it difficult to express my appreciation because it is so boundless. His unconditional love, understanding and sacrifice for me are beyond my words. These past several years have not been an easy ride, both academically and personally. His presence in my life has ensured that I will always cherish my memories of the years away from home. I truly thank Chiara for being not only an amazing girlfriend, but also for his numerous scientific discussions, constructive feedbacks and intellectual input to my work. He has shared this entire amazing journey with me, so it only seems right that I dedicate this thesis to him. I am looking forward to sharing the future with her for many years to come.

Contents

List of Figures

List of Tables

1 The Cold Gas Dynamic Spray technique

Numerous surface treatment techniques nowadays are used within industrial environments to improve the surface properties of various materials without altering their bulk characteristics. From this perspective, coating technologies play a very important role allowing a cost saving through the combination of base material, that satisfy structural requirements (stiffness and strength), and the coating properties, that fulfill surface requirements (corrosion resistance, electrical conductivity, etc.).

The Cold Gas Dynamic Spray (CGDS), or simply Cold Spray, is a material deposition process in which small particles are accelerated toward a substrate via a supersonic jet of compressed gas at temperature lower than the melting point of the powder material. During the impact with a target surface, the solid particles undergoing plastic deformation bond to the surface leading to the formation of a deposited material layer thickness ranging from tens of microns up to several millimeters. This technology consists in a process in which solid powders are accelerated in a de Laval nozzle toward a substrate by a supersonic jet of high-pressure gas. Moreover, the temperature reached by the sprayed particles during the process is below the melting temperature of the material. Due to the adiabatic shear instability, that occur thanks to the high strain rate, the particles are able to undergo large plastic deformation, so that material flow provides the required heat for bonding. This phenomenon, actually, represents the main driving force for the adhesion of the coating to the substrate [1]–[4]. In fact, CGDS technique has been successfully applied in last years for deposition of ductile metals such as copper and aluminum-based alloys, due to their remarkable ductility [5]–[8].

Cold Spray was initially developed in 1980 at the Institute for Theoretical and Applied Mechanics of the Siberian Division of the Russian Academy of Science in Novosibirsk. While they were performing experiments on small particles entraining in a supersonic wind tunnel, they started to study the erosive behavior of this particle-laden flow on an object. It was

discovered by chance that, above a particular particle velocity, an adhesion of the particles occurred leading to the development of a coating on the substrate. In 1994 a U.S. patent regarding this process as a coating technology was issued [9]. This technique has the advantage, over conventional ones, that it produces highly compact deposits and oxide-free structures and prevents tensile residual stresses and chemical contamination.

Some basics principles of the cold spray process together with the basic governing equations and some experimental data regarding the influence of the process variables will be presented in this chapter.

1.1 General features of the Cold Spray process

The term cold spray is used to describe this process since both the gas and the powder temperature are low enough to prevent phase change or high thermal stress in the deposit or substrate. A typical cold spray device is illustrated in Fig. 1.1. A compressed gas with a pressure on the order of $30\ bar$ flows through a converging-diverging (de-Laval) nozzle attaining a supersonic velocity. The feedstock powder (size particles vary from 10 to $50\ \mu m$) is injected into the gas flow upstream of the converging section of the nozzle. The solid powder particles are in this way accelerated (generally in a range between 500 and $1000\ m\ s^{-1}$) by the rapidly expanding gas. To achieve higher gas velocity in the nozzle, the compressed gas is often pre-heated.

The non-exposure of the feedstock material to high temperatures during the process together with the solid state of the particles upon the impact on the substrate differentiate this technique from the numerous thermal spraying ones. Due to these aspects some of the problems related to the thermal spraying-high-temperature process such as compositional changes (macro- and micro-segregations of the alloying elements during solidifications accompany the conventional thermal spray techniques), oxidation and micro-structural changes in the substrate, due to the excessive amount of heat delivered to the coated part, are mitigated.

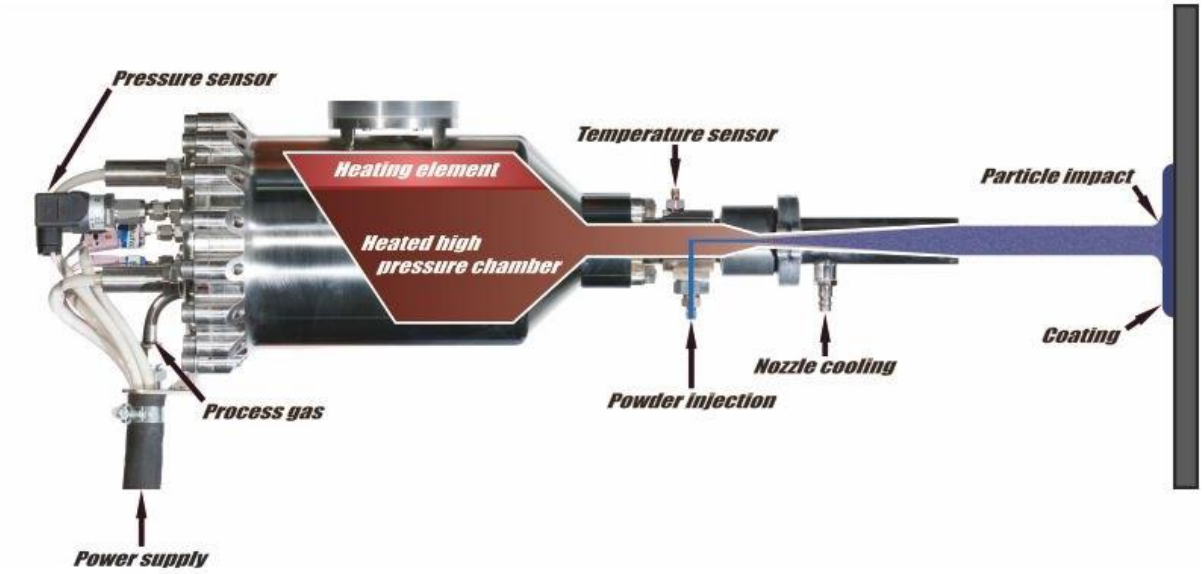

Fig. 1.1: *Schematic of a Cold Spray system [10]*

To build and shape the deposit, the nozzle as well as the substrate can be moved in the work area through a robot arm (see Fig. 1.2).

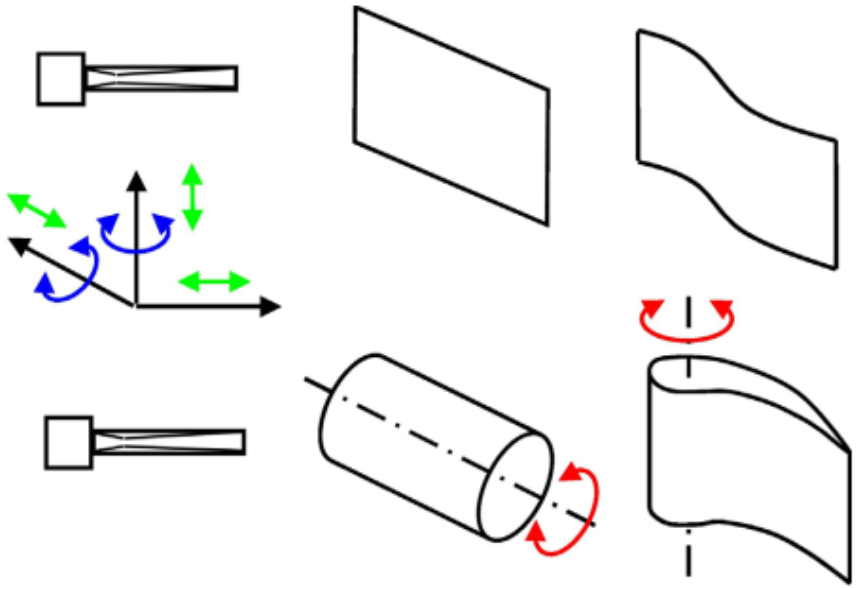

Fig. 1.2: *Typical nozzle and substrate shape and motion in the working area [11]*

According to Alkhimov et al. [9] the most important parameter in the cold spray process is the particle velocity prior to impact on the substrate. The operating pressure and temperature, together with the nature of accelerating gas and the nozzle design play an important role on the

particle velocity [12]. On the other hand, material parameters such as density and particle size influence the acceleration and the deposition behavior of the particles [13].

A dense coating is obtained when particles reached a critical velocity; those that not reached this threshold value contribute to the erosion of the substrate. However, even in the case of deposition efficiencies greater than 80%, Karthikeyan et al. [13] reported that porous coatings may be formed.

1.2 Fluid dynamics model

The cold spray process involves a very large number of parameters (e.g. gas type and temperature, particle size morphology and velocity, substrate and particles material). All these parameters must be optimized on the basis of the type of powder used and the type of application required. For accelerating this process, some empirical relationships have been derived but, considering the extreme effort, computational methods have been developed. These models should allow the users to both customize coating properties, to meet specific requirements without too much experiments, and to improve the design of cold spray systems.

To give an idea about the gas and the particles properties behavior in the nozzle, the gas flow model together with the powder flow model will be introduced in this section. In particular, for basic initial results of gas velocity and temperature in the nozzle it is assumed that the gas flow is isentropic (adiabatic and frictionless) and one dimensional. Moreover, approximating the process gas as a perfect gas with constant specific heats, classical fluid flow equations can be used to obtain the gas flow equations needed and analytical solutions are possible. Thanks to the one dimensional assumption the boundary layers of the nozzle where the gas flow is slower may be ignored. Thus, the gas flow rate found by this approach is slightly higher than the real one. On the other hand, this latter assumption doesn’t allow the use of this model to regions near the jet impingements on the substrate [14].

In accordance with these assumptions, the gas parameters will be functions of the nozzle geometry, the total gas temperature and the stagnation pressure. In particular, an optimization of the flow area with axial distance may accelerated or decelerated the flow; the shape of the nozzle may also be obtained following the analysis presented in this chapter.

Finally, the model that will be considered in this analysis is a typical cold spray converging/diverging nozzle.

1.2.1 Mach number

For the type of model presented in this section the gas conditions are typically written as a function of the total Mach number.

In fluid dynamic, the Mach number is a dimensionless number representing the ratio between the local flow velocity v and the local speed of sound u:

$$M = \frac{v}{u} \tag{1.1}$$

Considering an ideal gas, the speed of sound is given by:

$$c = p\sqrt{\gamma RT} \tag{1.2}$$

where γ is the specific heat ratio and T is the absolute fluid temperature. The Mach number may be used to characterize the different regimes of flow [15]:

- *Incompressible flow* - The Mach number is small compared to unity ($M < 0.3$). The flow is treated as incompressible;
- *Subsonic flow* - The Mach number is large enough so that compressible flow effects are present ($0.3 < M < 1$);
- *Sonic flow* - The Mach number is unity ($M = 1$);
- *Transonic flow* - The Mach number is very close to unity ($0.8 < M < 1.2$);
- *Supersonic flow* - The Mach number is larger than unity ($M > 1$). For this flow, a shock wave is encountered;
- *Hypersonic flow* - The Mach number is larger than five ($M > 5$). At very high Mach numbers the flowfield becomes very hot and dissociation and ionization of gases take place. In these cases, the assumption of an ideal gas is no longer valid, and the flow must be analyzed by the use of kinetic theory of gases rather than continuum mechanics.

1.2.2 Isentropic flow relations

In thermodynamics, an isentropic process is an idealized thermodynamic process that is both adiabatic (no heat transfer) and frictionless (ideal or reversible). Although this process does not occur in nature, compressible flow field are often approximated by it; this is the case of internal flows such as for nozzles [15].

In the analysis presented in this section, the process gas flow is assumed to originate from a large chamber or duct where the temperature is the stagnation temperature T_0, the velocity is

zero and the pressure is equal to the stagnation pressure p_0. The stagnation state is defined as a state that would be reached by a fluid if it were brought to rest isentropically (reversibly and adiabatically) and without work [15]. From now one the stagnation properties will be designed by the subscript 0.

Considering the basic fluid dynamics and thermodynamic relations for compressible flow, the energy equation between two points in the duct where the flow is undisturbed may be written as follow:

$$C_p T_g + \frac{1}{2} v_g^2 = C_p T_0 \tag{1.3}$$

One of the two points that have been considered is the stagnation one where the velocity v_0 has been assumed equal zero and the pressure p_0 as been assumed equal to the total pressure in the flow.

The equation above may be rewritten as follow:

$$\frac{T_0}{T_g} = 1 + \frac{v_g^2}{2 C_p T_g} \tag{1.4}$$

Additionally, considering $R = C_p - C_v$ and $\gamma = C_p / C_v$, the following relation may be obtained:

$$C_p = \frac{\gamma R}{\gamma - 1} \tag{1.5}$$

where γ is the ratio of the constant pressure and the constant volume specific heats which is typically set to 1.66 for monoatomic gases like helium and 1.4 for diatomic gases like nitrogen and oxygen [16].

Combining the two preceding equations and substituting Eq. 1.1 and Eq. 1.2 into Eq. 1.4, the temperature profile may be expressed as function of gas local Mach number:

$$\frac{T_0}{T_g} = 1 + \left(\frac{\gamma - 1}{2} \right) M^2 \tag{1.6}$$

Furthermore, by using the isentropic simplifications of the gas flow from a state 1 to a state 2:

$$\frac{p_2}{p_1} = \left(\frac{\rho_2}{\rho_1} \right)^{\gamma} = \left(\frac{T_2}{T_1} \right)^{\frac{\gamma}{\gamma - 1}} \tag{1.7}$$

the following relations may be deducted:

$$\frac{p_0}{p_g} = \left[1 + \left(\frac{\gamma - 1}{2}\right) M^2\right]^{\frac{\gamma}{\gamma - 1}} \tag{1.8}$$

and:

$$\frac{\rho_0}{\rho_g} = \left[1 + \left(\frac{\gamma - 1}{2}\right) M^2\right]^{\frac{1}{\gamma - 1}} \tag{1.9}$$

Using the equations above, plots for p/p_0 and T/T_0 as a function of position along the nozzle has been produced (see Fig. 1.3). The values at the nozzle throat are denoted by an asterisk. Sonic conditions exist there, so the Mach number is 1.

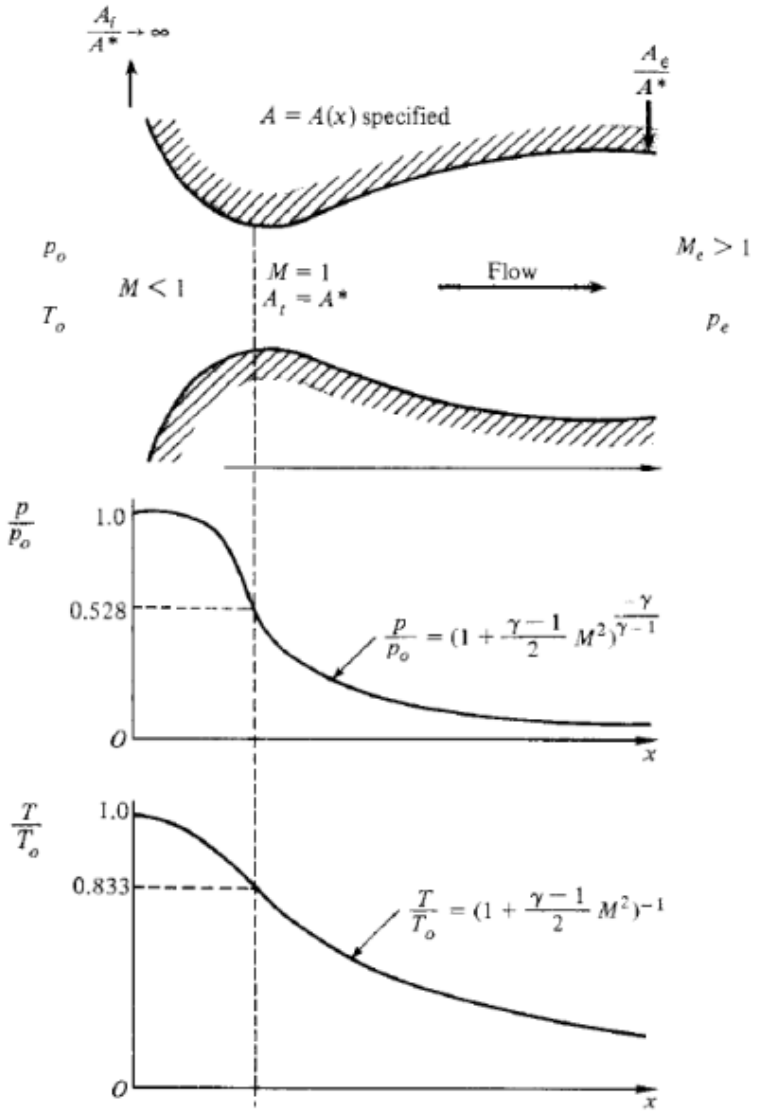

Fig. 1.3: *Isentropic supersonic nozzle flow [17]*

1.2.3 Dykhuizen and Smith model

In this section, a brief overview of the cold spray flow model developed by Dykhuizen and Smith [14] is given. The model assumes that the stagnation temperature T_0 (also known as the total temperature) and the mass flow rate is set by the user. In thermal spray devices the mass flow rate is generally fixed by setting a pressure level upstream of a critical flow orifice in the gas supply line. Should be noted that this pressure is different from the stagnation pressure p_0 of the flow through the nozzle because of the frictional losses associated with the gas passing through the orifice [14]. The gas temperature at the smallest cross-sectional area of the converging/diverging nozzle (T^*), where the Mach number is unity, may be derived using Eq. 1.6:

$$T^* = \frac{T_0}{(1 + \gamma - 1/2)} \tag{1.10}$$

At the nozzle throat, the gas velocity may be obtained from:

$$v = \sqrt{\gamma R T^*} \tag{1.11}$$

The equation above explains why the low molecular weight and monoatomic Helium is a better carrier gas than a higher molecular weight and diatomic gas such as Air (Air is typically modeled as a diatomic gas since it is a mixture of nitrogen and oxygen); for the same total temperature T_0 an higher speed of sound and so a higher particles velocity is obtained with helium. In cold spray the two main gases that are typically used are Helium and Nitrogen. Both these gases are inert. Helium has a high sonic velocity that is approximately three times that of the Nitrogen, but it is more expensive. However, this penalty can be overcome by using a gas recycling system but which also increases the price of the CGDS system. Finally, the sonic velocity of air (a diatomic gas) is slightly less than that of pure Nitrogen, but this option remains the cheapest CGDS process gas available [18].

Known the mass flow rate $\dot{m}$ the sonic gas density may be written as:

$$\rho^* = \frac{\dot{m}}{v^* A^*} \tag{1.12}$$

where A^* is the cross-sectional area of the nozzle throat at it is assumed known. Using the ideal gas law, the gas pressure at the throat is obtained as:

$$p^* = \rho^* R T^* \tag{1.13}$$

At this point the stagnation pressure may be computed as:

$$\frac{p_0}{p^*} = \left[1 + \left(\frac{\gamma - 1}{2}\right) M^2\right]^{\frac{\gamma}{\gamma - 1}} \tag{1.14}$$

Known the conditions at the throat, the gas conditions along the diverging section of the nozzle may be determined.

*1.2.3.1 **Gas conditions along the diverging section***

To determine the gas properties along the diverging section of the nozzle the variation of one of the gas properties (T, p, ρ, v) or the variation of the Mach number or the variation of the nozzle cross sectional area must be specified [16].

Dykhuizen and Smith [14] in their gas flow model considered the variation of the nozzle cross-sectional area known. The conservation of mass leads to the valuation of the Mach number through the following equation:

$$\frac{A}{A^*} = \left(\frac{1}{M}\right)\left[\left(\frac{2}{\gamma + 1}\right)\left(1 + \frac{\gamma - 1}{2} M^2\right)\right]^{\frac{\gamma}{2\gamma - 1}} \tag{1.15}$$

Once the Mach number is known at a given cross sectional area along the diverging section of the nozzle the remaining gas properties (p, v, T and ρ) can be calculated using the previous analyzed isentropic relationships [16]:

$$\frac{p}{p^*} = \left(\frac{\gamma + 1}{2 + (\gamma - 1) M^2}\right)^{\frac{\gamma}{\gamma - 1}} \tag{1.16}$$

$$\frac{T_0}{T} = 1 + \frac{\gamma - 1}{2} M^2 \tag{1.17}$$

$$v = M\sqrt{\gamma R T} \tag{1.18}$$

$$\frac{\rho_0}{\rho} = \left(1 + \frac{\gamma - 1}{2} M^2\right)^{\frac{1}{\gamma - 1}} \tag{1.19}$$

All the previous equations used in this section may be used to determine the gas properties at the nozzle exit only if a normal shock does not take place inside the nozzle [16].

1.2.3.2 Shock waves at nozzle exit

One of the phenomena that may occur in supersonic flow is the shock waves, a discontinuity in the properties of the flow field that happen when the flow velocity exceeds the speed of sound ($M > 1$) [15]. An example of a normal shock wave is shown in Fig. 1.4. To determine if the normal shock will take place inside the nozzle, the ambient pressure should be compared with the following "shock" pressure [16]:

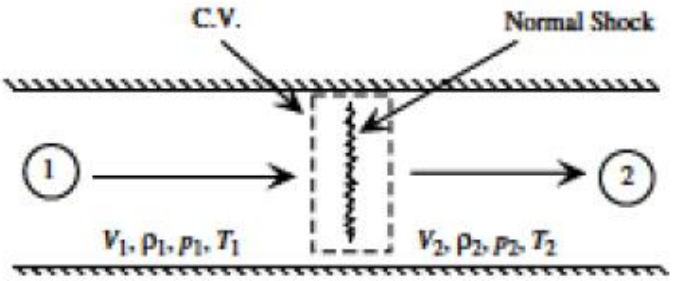

Fig. 1.4: *Stationary normal shock wave [15]*

$$p_s = p_e \left(\frac{2\gamma}{\gamma + 1} M_e^2 - \frac{\gamma - 1}{\gamma + 1} \right) \tag{1.20}$$

The subscript e is used to identify the quantity at the nozzle exit and p_s is the shock pressure. A shock will not occur inside the nozzle if the pressure p_s is higher than the ambient pressure. On the contrary, if a shock occurs the subsequent gas flow is subsonic and the exit pressure is not given by the following isentropic relationship:

$$p = p^* \left(\frac{\gamma + 1}{2 + (\gamma - 1)M^2} \right)^{\frac{\gamma}{\gamma - 1}} \tag{1.21}$$

but it is rather equal to the ambient pressure.

Operating conditions in CGDS entail that the shock pressure is maintained above the ambient pressure and so no shock inside the nozzle occur. Moreover, to maximize the exit velocity of the gas (and thus, the velocity of the powder particles) the exit pressure is generally lower than the ambient pressure [16].

1.2.3.3 Gas velocity at the nozzle exit

The one dimensional gas dynamic model developed by Dykhuizen and Smith [14] entailing the solution of the nonlinear Eq. 1.15 allows to establish the gas velocity at the nozzle exit. To better understand the relationship between the carrier gas and the cold spray process parameters, Grujicic et al. [16] construct an analytical function which can be used to compute the gas exit

velocity for a given set of gas and process parameters. Eq. 1.15 has been solved for the Mach number for different values of the nozzle expansion ratio A/A^* and for several values of the specific heat ratio γ; the results are shown in Fig. 1.5.

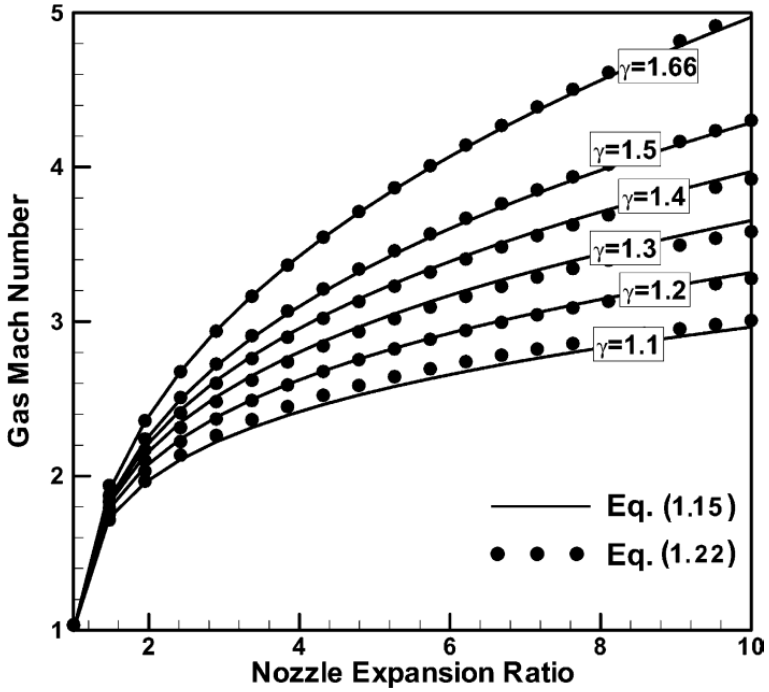

Fig. 1.5: *Variation of the gas Mach number for different nozzle expansion ratio and gas specific heat ratio γ [16]*

To fit the different curves, a nonlinear least squares procedure has been used and the following function has been obtained:

$$M = \left[k_1 \frac{A}{A^*} + (1 - k_1)\right]^{k_2} \tag{1.22}$$

where k_1 and k_{12} are function of the specific heat ratio, γ. This γ-dependence has been used in a nonlinear polynomial regression analysis to obtain:

$$k_1 = 218.0629 - 243.5764 * \gamma + 71.7925 * \gamma^2 \tag{1.23}$$

$$k_2 = -0.122450 - 0.281300 * \gamma \tag{1.24}$$

Fig. 1.5 shows that exists a reasonably good agreement between the M versus A/A^* relation given by the model of Dyhuizen and Smith and the one found by Grujicic, in particular for high γ values.

1.2.4 Particle dynamics model

The success of the cold spray process is not determined by the gas conditions, but rather by the spray particle velocity [14]. Assuming that the two phase flow (gas and solid particles) is enough dilute, the interaction between the gas and the spray particles have been analyzed by Dykhuizen and Smith [14].

Under the above conditions, the particle velocity v_p may be computed by solving the following equation:

$$m_p \frac{dv_p}{dt} = m_p v_p \frac{dv_p}{dx} = \frac{C_D A_p \rho (v - v_p)^2}{2} \tag{1.25}$$

where m_p and A_p are respectively the mass and the cross sectional area of the particles, C_D the drag coefficient, t the time and x the axial position of the particles (measured from the nozzle throat).

From Eq. 1.25 the ultimate particle velocity seems to be equal to the gas velocity [14]. The previous Eqs. 1.15, 1.17 and 1.18 show as the gas velocity within the nozzle is a function of the total gas temperature and the nozzle geometry but it is not affected by the gas pressure. However, Eqs. 1.18, 1.19 and 1.25 indicate that the initial particle acceleration is linearly dependent on the stagnation pressure and independent of the total temperature. Thus, although the stagnation pressure does not affect the maximum particle velocity, to allow the particles to achieve the gas velocity in the short length of the diverging section of the nozzle, it has to be sufficient high [14].

If the gas velocity and density, together with the drag coefficient are assumed constant, Eq. 1.25 may be integrated to yield:

$$ln\left(\frac{v - v_p}{v}\right) + \frac{v}{v - v_p} - 1 = \frac{C_D A_p \rho x}{2 m_p} \tag{1.26}$$

The equation above can be simplified for low values of the spray particle velocity (as compared to the gas velocity):

$$v_p = v \sqrt{\frac{C_D A_p \rho x}{m}} \tag{1.27}$$

This last simplification not only shows the influence of the gas density but also allows to obtain a simple relation in which the spray particle velocity is proportional to the square root of the distance traveled over the particle diameter [19].

1.2.4.1 Effect of Spray Parameters

Starting from the isentropic formulation, Stoltenhoff et al. [20] analyzed the influence of various process parameters on the velocity and temperature of the particles at the nozzle exit. Fig. 1.6(a) shows the trends of particles temperatures T_p and velocities v_p as a function of the gas entrance pressure p_0 for a fixed temperature T_0 and a fixed particle diameter d_p. The particle temperature seems to be independent from a variation in terms of p_0 while the particle velocity shows an increasing for higher value of the gas entrance pressure.

By increasing the gas inlet temperature T_0, the sound velocity increase and the overall gas velocities are higher. This leads to an higher particle velocity when the gas pressure p_0 is maintained constant (see Fig. 1.6(b)). This phenomenon can be observed until the temperature achieve high value. After that, the particle velocity increase less due to the lower gas density on the particle acceleration [20]. Another reason why a further increase in terms of gas temperature should be avoid is the occurrence of nozzle plugging.

Finally, Fig. 1.6(c) shows the variation of the particle exit velocity and temperature as a function of the particle diameter, when the inlet gas temperature and pressure are maintained constant. Although the smallest particles cool down faster, they lead to higher velocity, due to their low inertia and to the fact that the acceleration is inversely proportional to the diameter.

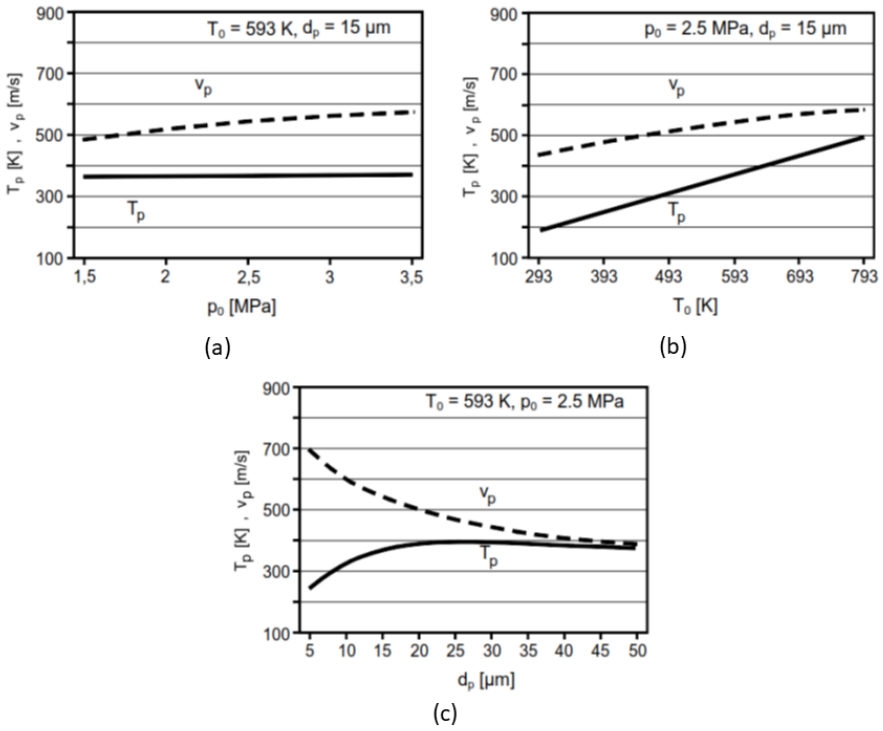

Fig. 1.6: *Variation of temperature and velocity of Cu particles at the nozzle exit as a function of the particle diameter (a), the gas inlet temperature (b), and the gas inlet pressure (c) [20]*

1.3 Bonding mechanism

Micrographs of cold-sprayed materials reveal that the deposition mechanism is primarily, if not entirely, a solid-state process [14]. The actual mechanism by which the solid particles deform and bond during cold spray is still not well understood. However, it is well established that the powder and the substrate undergo an extensive localized deformation during impact. This seems to cause the disruption of the thin oxide surface film that covers every metal surface enabling an intimate conformal contact between the particles and the substrate. This effect together with the high contact pressure given by the supersonic speed of the particles just before the impact are believed to be the necessary conditions for particles/substrate and particles/deposited material bonding [21]. This hypothesis seems to be supported by different experimental findings such as:

- A wide range of ductile materials can be successfully deposited through the cold spray process while non-ductile materials, such as ceramics, do not adhere to the substrate unless a ductile material is used as a matrix where the particles may be trapped.

- To achieve deposition, the particle velocity should exceed a minimum (material dependent) critical velocity. This suggest that to plastically deform the solid material and/or disrupt the oxide layer sufficient kinetic energy must be achieved.

The capability of the particles and the substrate to be joined together may also depend on the interface deformation during the collision. Following the degree of deformation, Raoelison [11] suggested three nature of bonding mechanism. According to him the mechanical bonding can be an interfacial mixing, an embedment in the substrate or an anchoring of particles on the substrate surface. The first phenomenon may occur when the deposit and the substrate are intermixed across the interface within vortices affected zone (see Fig. 1.7(a)). Otherwise, a deep penetration of the particle can lead to a mechanical interlocking which corresponds to an embedment of the particle on the substrate (see Fig. 1.7(b)).

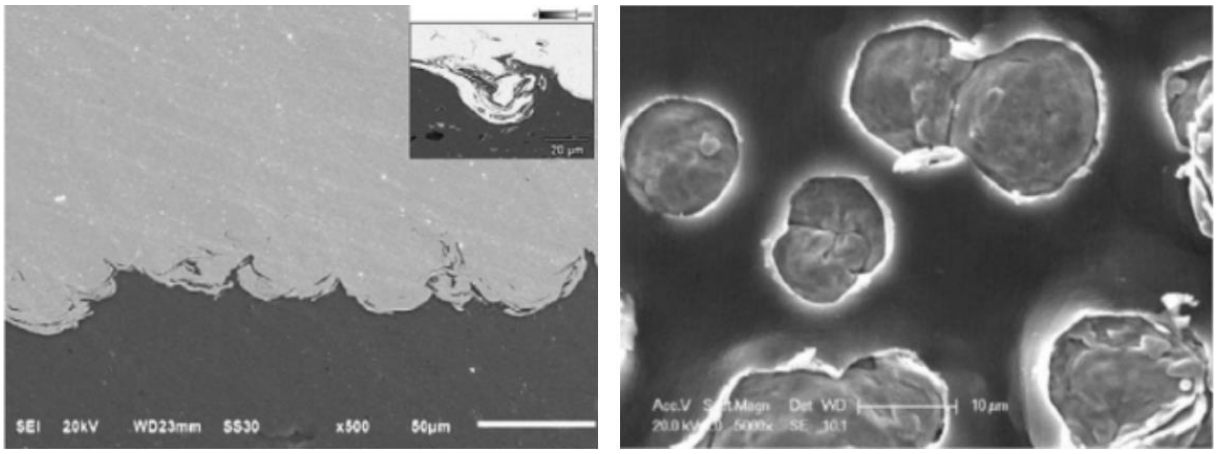

(a) (b)

Fig. 1.7: *Complex material intermixing observed at a Cu/Al interface formed during the cold spraying of copper particle onto an aluminium surface (a) [16], and (b) embedment of copper particles onto the surface of an aluminium substrate (b) [22]*

The substrate can be also indented by the particles without significant penetration as produced during mechanical embedment [11]. However, a weak penetration may cause a mechanical anchoring of the particles. A clear example of this phenomena may be observed in Fig. 1.8.

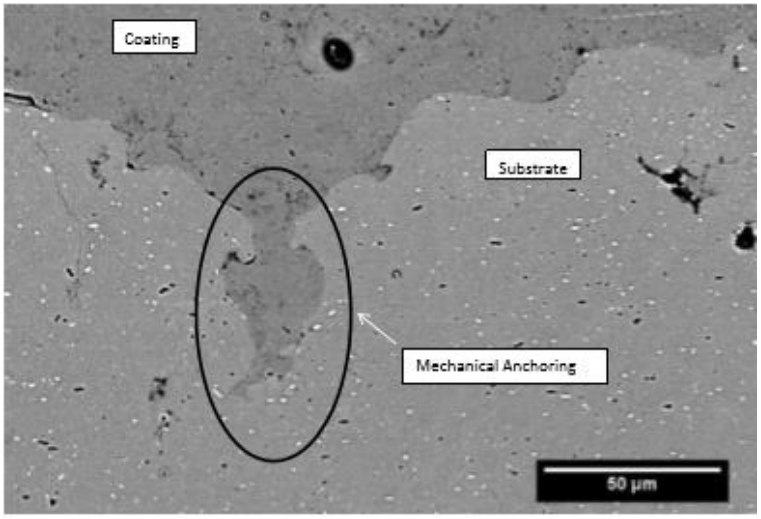

Fig. 1.8: *SEM image (500x) showing cross sectional view of the coating and substrate interface [23]*

1.3.1 Substrate preparation

The conditions of the substrate surface, in terms of topology and temperature, play an important role in the adhesion of the cold sprayed particles. In the cold spray process, a prepared surface, free to contaminations and oxides seems to promote a good bonding [24]. For this reason, prior to the deposition, preparation of the substrate surface is generally recommended. For glass and polymer, degreasing and cleaning steps are normally used. For metals, the typical practice consists of sandblasting or grit blasting or grinding and/or polishing [24]. In particular, sandblasting and grit blasting are used to remove the surface oxide but also to provide an 'activated surface' which is conducive to the particle adhesion instead of facilitate the particles to rebound. It must be pointed out, however, that the surface preparation differs from the various substrate/powders combinations.

Another effect that plays an important role in the adhesion mechanism is the substrate heating. The literature agreed that the thermo-mechanical softening due to this phenomenon promotes the adhesion allowing an embedding of the particles further into the substrate [24].

Finally, a recent technique of surface preparation, that arise from the laser technology, is the surface texturing. A sophisticated equipment with a high energy laser impulse is used to produce a pattern on the surface substrate. The laser treatment generates a textured surface (see Fig. 1.9) with an optimized pattern in terms of shape and size (the diameter and depth of the holes, the inter holes distance and the orientation of the holes may be tailored by the laser

impulse) [25]. Since the deposited particles fills the holes of the pattern this technique seems to improve the mechanical anchoring of the particles on the substrate.

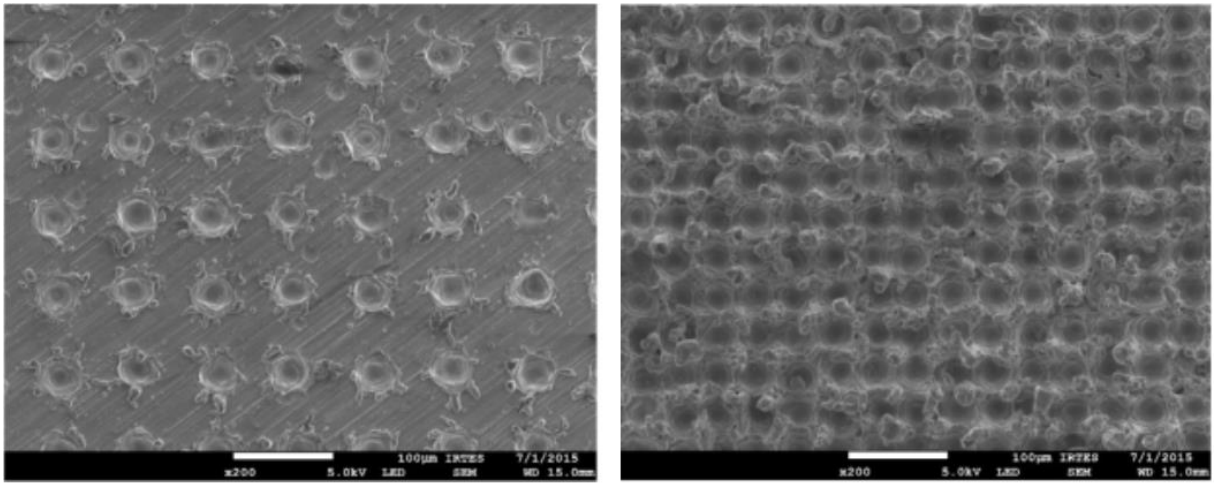

Fig. 1.9: *Typical pattern on the Al surfaces produced using the laser texturing method: (a) a weakly textured surface (Texture 1) and (b) a highly textured surface (Texture 2) [25]*

1.3.2 Adiabatic shear instability

As mentioned in the previous sections, the kinetic energy held by the particles during the impact is lower than the one needed to melt the contact interface between the particle and the substrate. Although the plastic deformation is a dissipation energy mechanism that contributes to a temperature increase, the bond particles/substrate take place through a solid state process. Moreover, due to the very short duration of the impact, not even the interatomic diffusion plays an important role in the bonding particles/substrate [26]

For a typical work hardening material under non adiabatic conditions, the stress strain curve shows a monotonic increase of the flow stress with plastic strain (see in Fig. 1.10 the curve denoted as "Isothermal"). On the other hand, under adiabatic conditions the plastic strain energy dissipated as heat increase the temperature causing material softening. In that conditions, the rate of strain hardening decreases and after reached a maximum value a monotonic decrease in the flow stress with plastic strain takes place (see in Fig. 1.10 the curve denoted as "Adiabatic"). In an ideal material with a uniform distributions of stress, strain, temperature and microstructure, softening may continue indefinitely. In real materials, however, fluctuations in stress, strain, temperature exists. Moreover, real material presents irregular microstructures. All these factors may give rise to plastic flow (shear) localization leading to a highly localized shearing and heating (and consequently softening). The surrounding material regions instead

stops their straining and heating process. In such circumstances, the flow stress quickly drops to zero (curve "Localization" in Fig. 1.10).

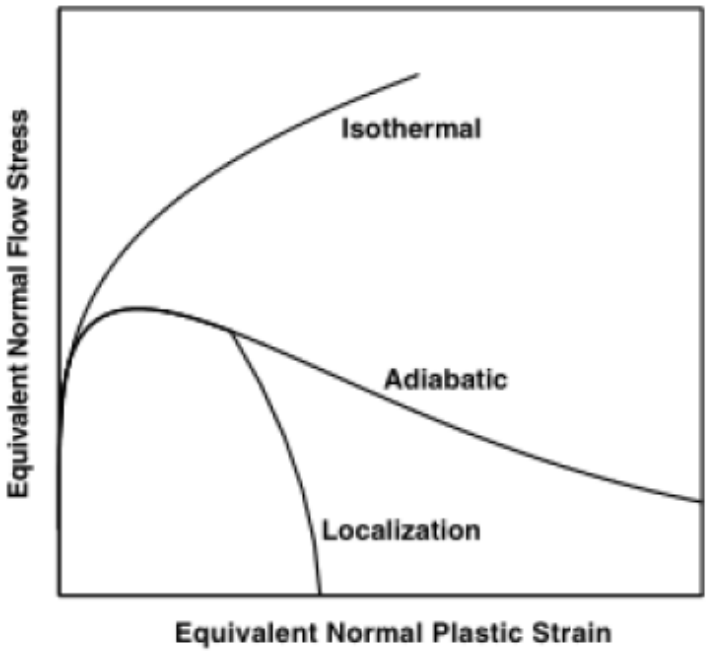

Fig. 1.10: *$\sigma - \varepsilon$ curves in a normal strain hardening material ("Isothermal"), an adiabatically softened material ("Adiabatic") and in a material undergoing an adiabatic shear localization ("Localization") [21]*

The phenomena described above is called adiabatic shear instability and that is what it is supposed to happen at the interface particle/substrate during the cold spray process, since the extreme speed of the impact does not allow a significant heat transfer and therefore, it may be considered similar to an adiabatic phenomenon.

1.3.3 Critical velocity

Material deposition in cold spray takes place from deformation of particles due to a high velocity impact toward the substrate [2]. Bonding occurs only if the particle velocity upon impact v_{pi} exceeds a certain material dependent value; known as the critical velocity v_{cr} [27]. However, the condition to obtain a cold sprayed coating with relative good properties requires that v_{pi} becomes noticeably larger than v_{cr}. On the other hand, exceeding v_{cr} too much may lead to unfavorable effects such as erosion. Therefore, how coating properties are related to the magnitude of v_{pi} become of central importance in the analysis of the cold spraying process [27]. The conditions that lead to particle bonding may be identify in a so called window of

deposition; deposition is observed only for ductile materials in a certain range of velocity and for a given powder size and temperature [2].

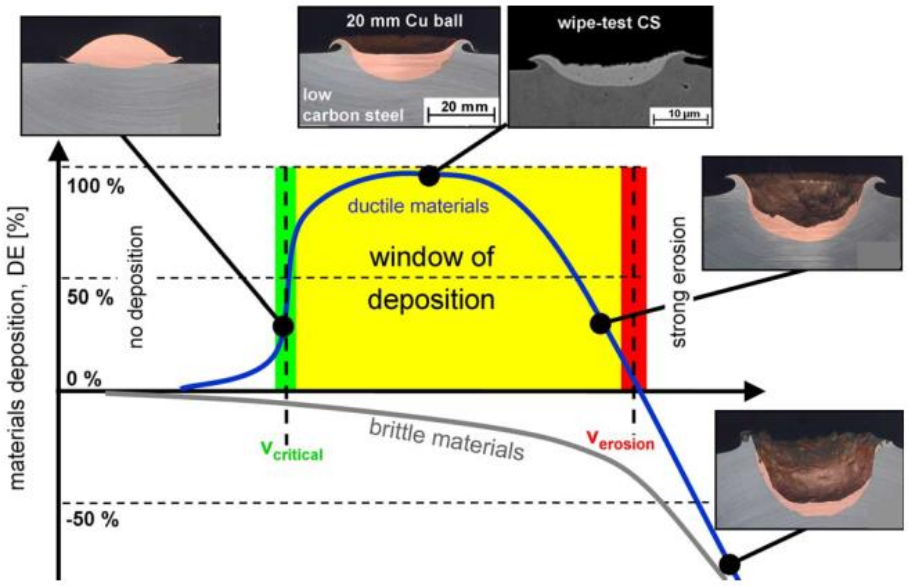

Fig. 1.11: *Scheme of the deposition efficiency (DE) as a function of the particle velocity for a constant impact temperature. Impact effects for different configurations are also shown [2]*

Fig. 1.11 shows a schematic correlation between the material deposition efficiency (DE) and the impact particle velocity for a given temperature. In case of ductile materials, at a given particle velocity, deposition start to occur. A further increase of the velocity leads to a rapid saturation level of the deposition efficiency close to 100%. In this range, where the DE achieve this level of saturation, the optimum coating conditions may be expected [2]. The critical velocity is defined as the one that allows to obtain the 50% of the material deposition (see the vertical green line in Fig. 1.11). In the graph the erosion velocity is also underlined; this is defined as the velocity where the deposition changes to erosion (0% DE). After reaching the level of saturation, for further increase of particle velocity the DE starts to decrease and erosive effect starts to occur. The graph also shown as for brittle materials, such as ceramics, any particle velocity below their melting temperature would cause erosion.

The deposition window is a basic graphical representation aimed at identifying the required spraying parameters in order to obtain a good particle bonding. The critical particle velocity v_{cr} depends on various factors. The effect of the main materials and process parameters on it and also on v_{pi} have been summarized by H. Assadi [27] in Table 1.1. It is easy to understand the continuous challenging in the identification of optimum parameters for each material.

Table 1.1: *Effect of materials and process parameters on v_{pi} and v_{cr} [27]*

Parameter	**Effect on v_{pi}**	**Effect on v_{cr}**
Particle		
Melting temperature	-	↑
Specific heat	-	↑
Hardness	-	↑
Density	↑↓	↓
Size	↑↓	↓
Gas		
Temperature	↑	↓
Pressure	↑	-
Nozzle		
Length	↑	-

The correlation between material properties and the critical velocity is rather an outcome of the interplay between the kinetic energy, the material strength, and the heat generation due to plastic deformation. Based on this analysis, Schmidt et al. [2] expressed the critical velocity as a function of material properties and the materials temperatures just before impact

$$v_{cr} = \sqrt{A\sigma/\rho + BC_p(T_m - T)} \tag{1.28}$$

where σ is the temperature-dependent flow stress, ρ is the density, C_p is the heat capacity, T_m is the melting temperature, T is the mean temperature of particles upon impact, and A and B are fitting constants.

The equation above is valid only for same material and temperature for powder and substrate. The temperature-dependent flow stress can be calculated by the following equation

$$\sigma = \sigma_{ultimate}\left[1 - \frac{T - T_R}{T_m - T_R}\right] \tag{1.29}$$

where T_R is the temperature at which the ultimate strength was determined [2]. Eq. 1.29 assumes a linear softening of the material toward the melting temperature. This together with Eq. 1.28 leads to a temperature dependence of the critical velocity. Must be noticed that Schmidt et al. [2] in their works underline how the kinetic energy needed to obtain the critical velocity is lower than that required for heating and for obtain a complete melting of the particle due to plastic dissipation.

To understand what happens near the interacting surface when the critical velocity is achieved and to analyze the nature of the phenomena that lead to bonding, the impact of particles toward

the substrate has been modeled using a dynamic finite element analysis [2]. Taking into account the effects of strain, strain rate and temperature on the flow stress of the material, Schmidt et al. used an axisymmetric model to simulate the perpendicular impact of a single copper particle with a copper substrate (see Fig. 1.12).

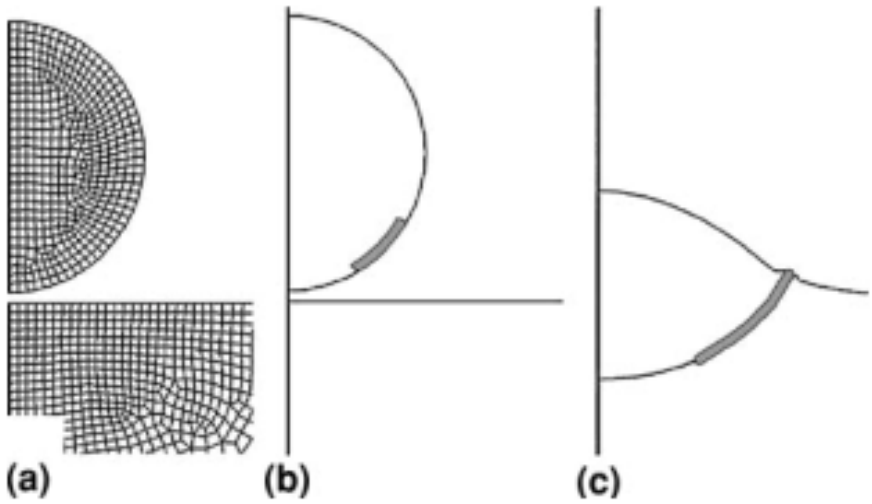

Fig. 1.12: *Axisymmetric model of particle impact, showing (a) the initial mesh, and a monitored element set in two different configurations: (b) un-deformed and (c) deformed [2]*

As a results of the impact, a markedly deformation of particles together with a localized heating has been found. Fig. 1.13 and Fig. 1.14 show how the temperature increase during the impact between the particle and the substrate. In particular, for sufficiently large particles, a suddenly temperature increase in the previous described monitored element can be observed when the impact velocity is beyond $400\ m/s$.

The temperature rise is an indication of the shear instability, which causes extensive flow of material at the corresponding surfaces. The results obtained by Grujicic et al. [21] show the close relation between the minimal impact particle velocity

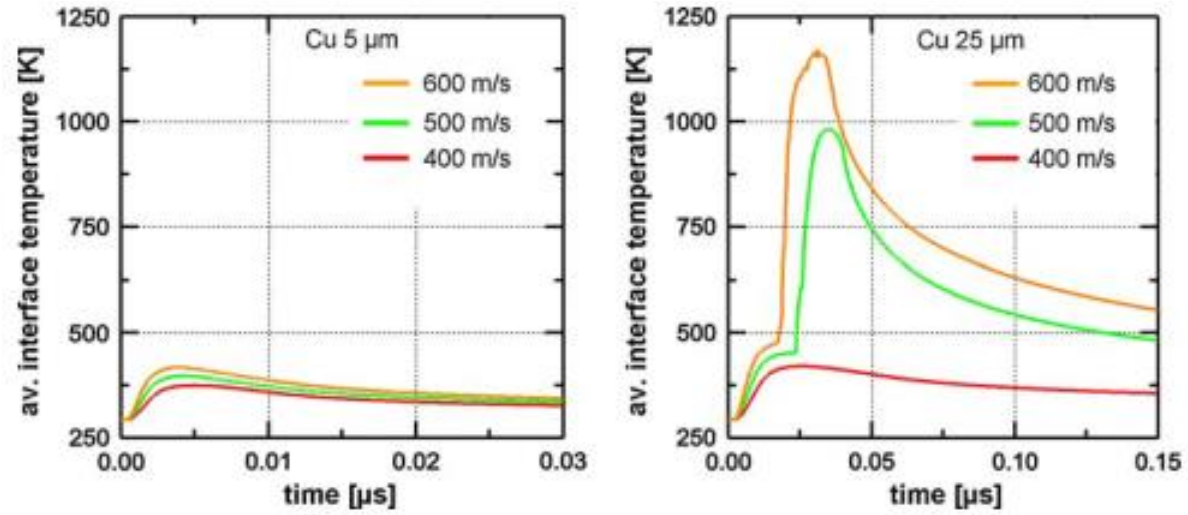

Fig. 1.13: *Temporal evolution of the temperature at the monitored element set shown in Fig. 1.12 for different particle diameters [2]*

needed to produce shear localization at the particle/substrate interface and the critical velocity for particles deposition by the cold gas dynamic spray process, in a number of metallic materials.

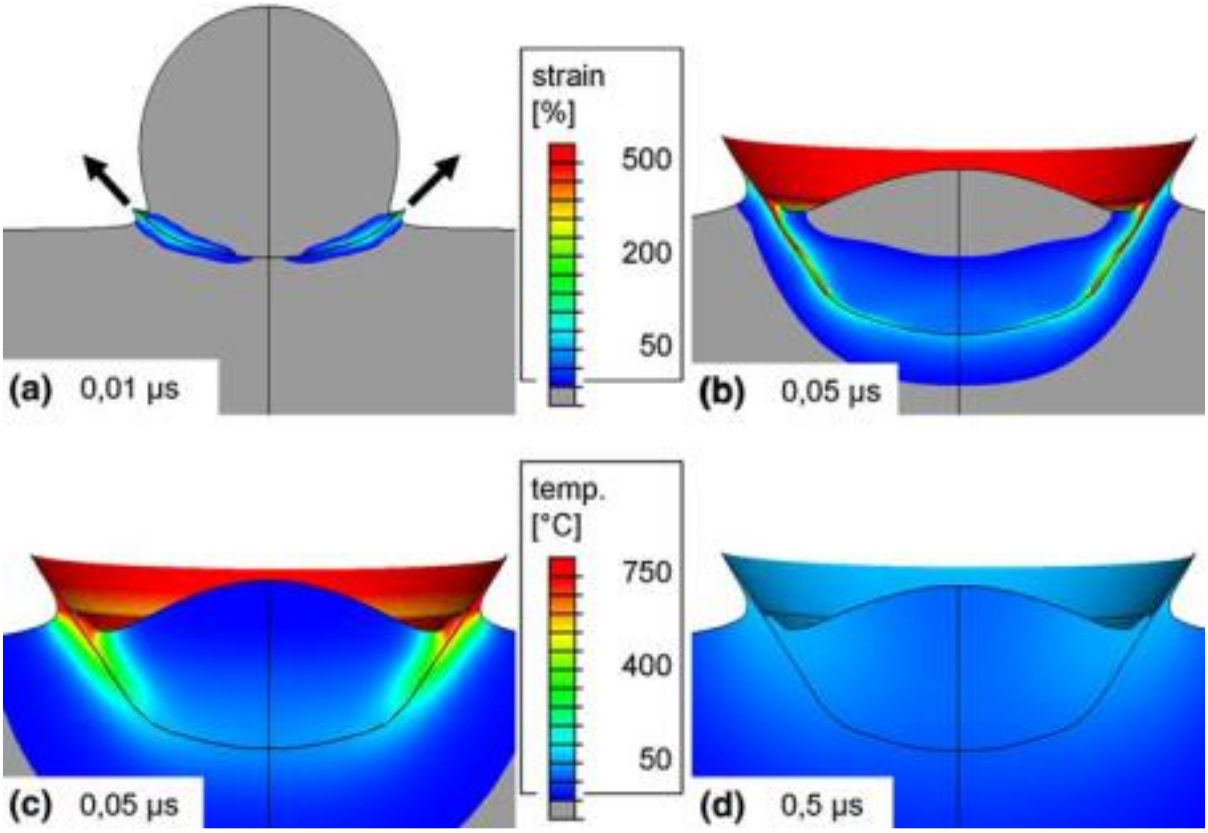

Fig. 1.14: *Strain field (a, b) and temperature field (c, d) during different single sequence of impact [2]*

This finding suggests that the onset of adiabatic shear instability in the particles/substrate interfacial region plays an important role in promoting particle/substrate adhesion and, thus, particle/substrate bonding during the cold gas dynamic spray process [21].

1.3.4 Influence of the impact conditions

Schmidt et al. [2] analyzed the interaction of individual particles with the substrate reproducing single impacts by the so-called wipe-test, in which a polished substrate is moved rapidly through the spray jet. Subsequently, SEM has been used to investigate the morphology of the particle substrate interaction. In their work they also used the wipe test to investigate the shear instability produced for different angular impact. These test are presented in Fig. 1.15 where SEM micrographies are shown for two different spraying angles.

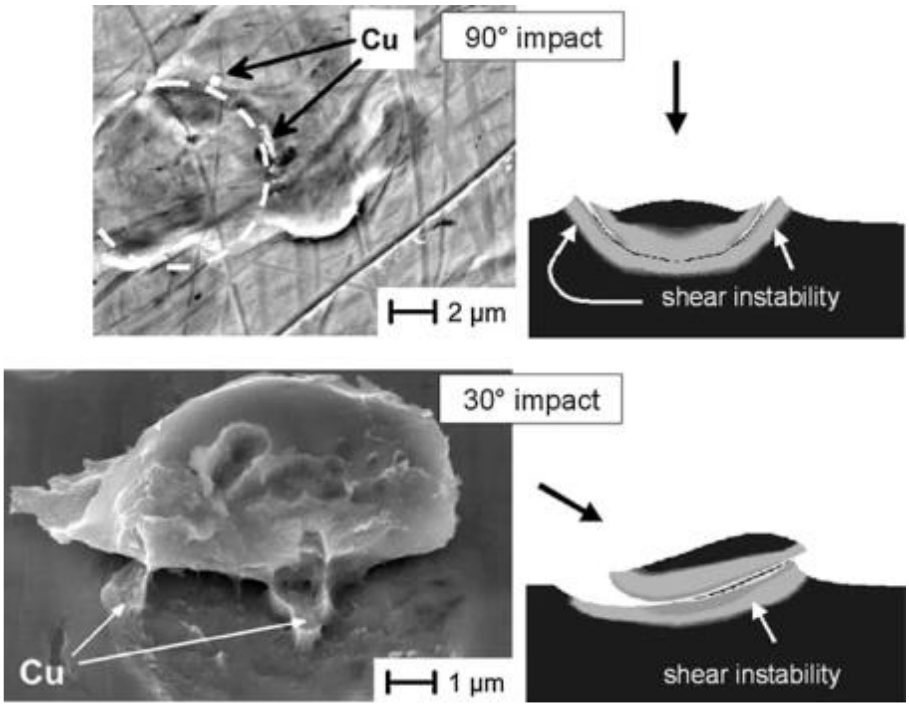

Fig. 1.15: *Location of shear instability in perpendicular and angular impacts [2]*

The top left micrograph is the result of a perpendicular impact of a copper particle. Possibly because of the spring back forces, the particle has bounced back or detached from the substrate after impact. However, partial bonding of the particle occurred during the impact, but presumably the fraction of bonded area was too small to withstand the back spring tensile forces. The top right image instead represents the result of modeling that seems in agreement with the previous result.

The bottom left micrograph shows a case where the impact of the particles has not been perpendicular. In an angular impact, an additional temperature rise can occur at the interface due to frictional dissipation, which could facilitate the occurrence of shear instability. This latter phenomenon can also shift the location of the shear instability in particular when impacts with smaller angles occur (farther away from perpendicular conditions). The tangential component of the momentum of the particle in an angular impact creates a tensile force at the interface, which could be large enough to detach the particle from the substrate [2]. Also for this configuration the model used by Schmidt seems allows to illustrate the location of shear instability in an angular impact.

1.3.4.1 Flattening ratio

The severity of particle deformation as a result of impact could be defined as $1 - h_p/d_p$ as shown in Fig. 1.16. This flattening ratio can be used as a measure of the quality of cold spray coating and so an indicator for its microstructural properties due to the fact that a minimal porosity, a high values of cohesive strength and a large amounts of bonded area are obtained when there is a high deformation of the impacts particles during the deposition process [27].

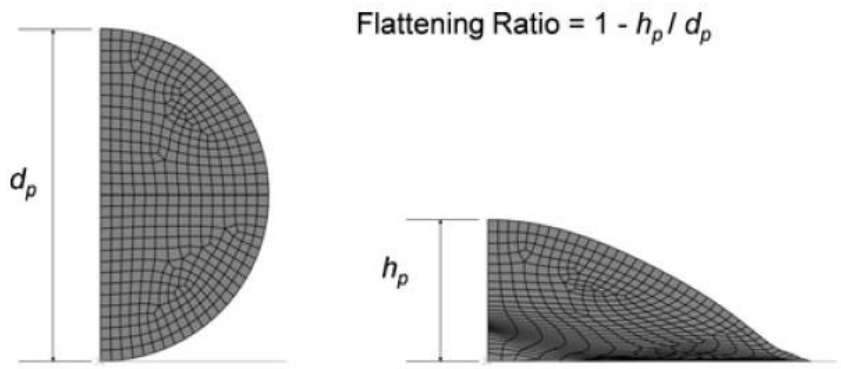

Fig. 1.16: *Example of flattening of a particle due to impact on a substrate [27]*

Assadi et al. [27] have investigated through the software ABAQUS the effect of particle impact velocity on the flattering ratio. They have performed different finite element modeling of plastic deformation during impact for differential initial conditions for the feedstock materials. In their work they show how the increasing of the particle impact velocity leads to an increasing of the flattening ratio, though the rate of this increase depends on material properties (see Fig. 1.17(a)). However, they also found how the flattening ratio when it is plotted against the ratio of the particle impact velocity to the critical particle impact velocity appears regardless of material properties and process parameters (Fig. 1.17(b)).

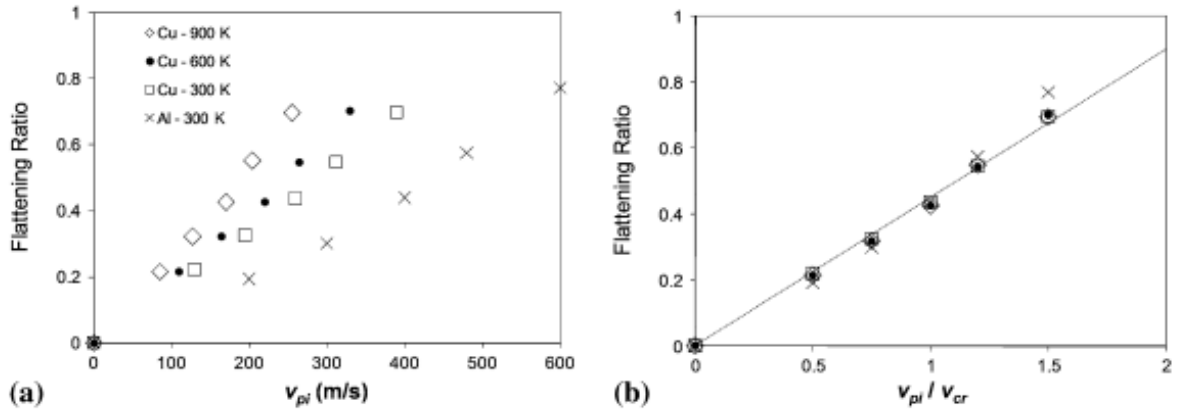

Fig. 1.17: *Flattering ratio as a function of (a) particle impact velocity, and (b) the ratio of particle impact velocity to critical velocity [27]*

The impact conditions seem influence drastically the coating properties. In this optics, computational process analysis is an important tool to attain the best coating qualities and it can be used to analyze the microstructure of the coating (see Fig. 1.18). Depending on the process parameters and material properties, different degrees of deformation and resulting porosities may be predicted.

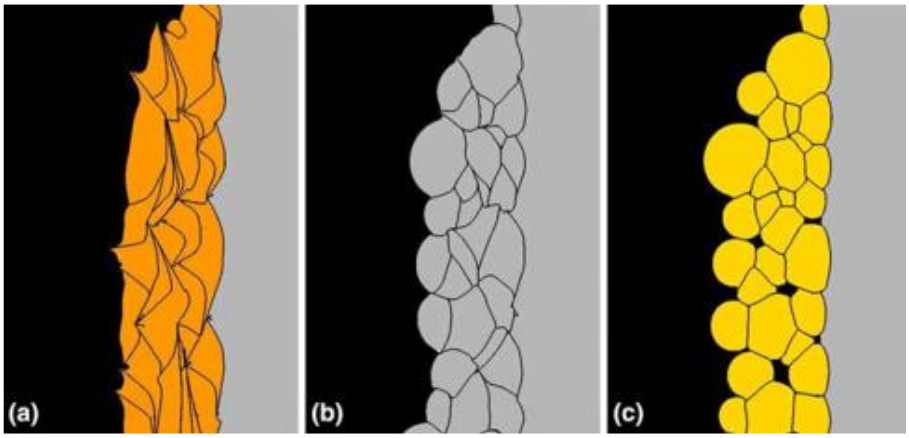

Fig. 1.18: *2D simulation of a multi impact scenario calculated for different material combinations under identical impact conditions [2]. (a) Cu on steel 316L, (b) steel 316L on steel 316L, (c) Ti-6Al-4V on steel 316L*

1.3.4.2 Coating development

According to R.N. Raoelison [11], the deposit formation involves first an adhesion process onto the substrate and then a second phase where the coating can be "built-up". Once the adhesion of the first layer is achieved, the deposit development and so the cohesion of the coating depends on the capability of the deposited particles to be joined together. To explain the deposit

consolidation three main stages have been identified [11]. The deposit growth begins with the deformation of the particles while they impact on the substrate. Then, during the second stage, the plastic deformation of the particles further decreases the porosity and inter-particles bonding starts to occur. Finally, the last stage of the coating build-up is given by a further hardening of the particles. These mechanisms are shown in Fig. 1.19 and they have been considered to explain the deposit formation during the cold spray process of ductile particles.

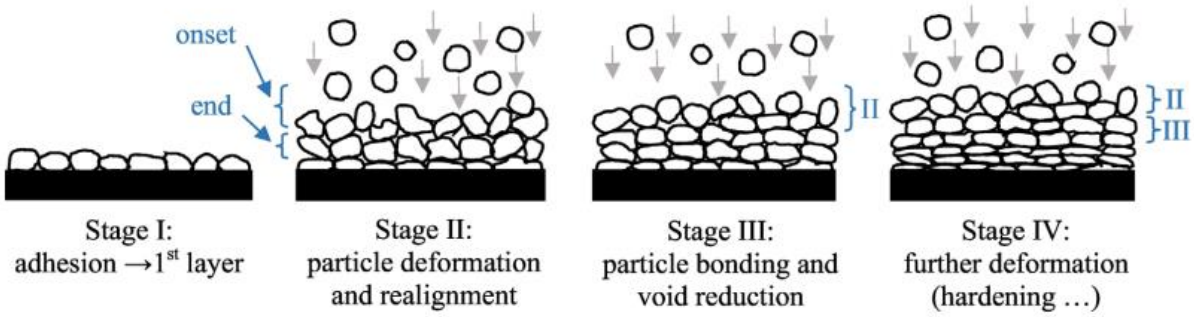

Fig. 1.19: *Phenomenological deposit formation in CGDS for metallic particles [11]*

1.4 Applications

Today, the CGDS deposition covers a wide variety of materials such as metals, polymers, composites and nanomaterials. Globally, four different potential uses of this technique may be defined: surface functionalization, restoration, bulk production to provide particular material properties and art/decoration [11].

Fig. 1.20: *Corrosion protection of deep water riser (a) or welded seams of large metal structures (b) produced by cold spraying [28]*

For metallic structures, thanks to this process, useful improvements were achieved in terms of resistance performance (corrosion resistance, oxidation resistance, erosion resistance and wear

resistance), durability performance (high specific strength and anti-friction capability) and other features such as intermediate joining functions, heat dissipation and abrasive properties.
One example of large scale applications are components subjected to aggressive environments. In this optics, CGDS deposition of corrosion resistant coating is a good solution that contributes to materials saving. Typical cases of this application may be found in aqueous environment (Fig. 1.20(a)), in atmospheric aggressive media (Fig. 1.20(b)) and in the nuclear industry where large containers are used for the sustainable disposal of radioactive waste (see Fig. 1.21).

Fig. 1.21: *Illustration of nuclear fuel container and copper cold sprayed prototype for a sustainable corrosion resistance [29]*

Cold spray has brought engineering solutions for metal structures in different industrial applications, including mechanical (see Fig. 1.22) and thermal fields (see Fig. 1.23). Furthermore, the CGDS technique is receiving nowadays a growing interest in medical field, and in particularly for the elaboration of biocompatible coatings [11].

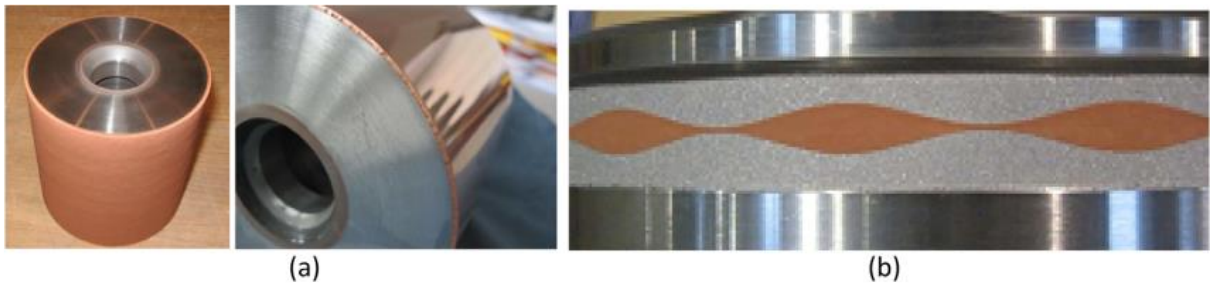

Fig. 1.22: *Copper cold sprayed coating for automotive applications. Coating for printing rolls (a) and specifically shaped coating (b) [30]*

Fig. 1.23: *Copper cold sprayed coating for power electronic heat sinks (a) and for refrigeration units (b) and mass production [30]*

Recently, a huge expansion of this process may be identified in the restoration and repair applications. This solution not only enables saving raw materials but, in addition, may be useful to reduce the lead-time for the replacement of a product. In aerospace industry, efficient repair of several modules have been demonstrated and restorations were performed in accordance with a certified protocol including a series of specific tests. A typical repair is illustrated in Fig. 1.24.

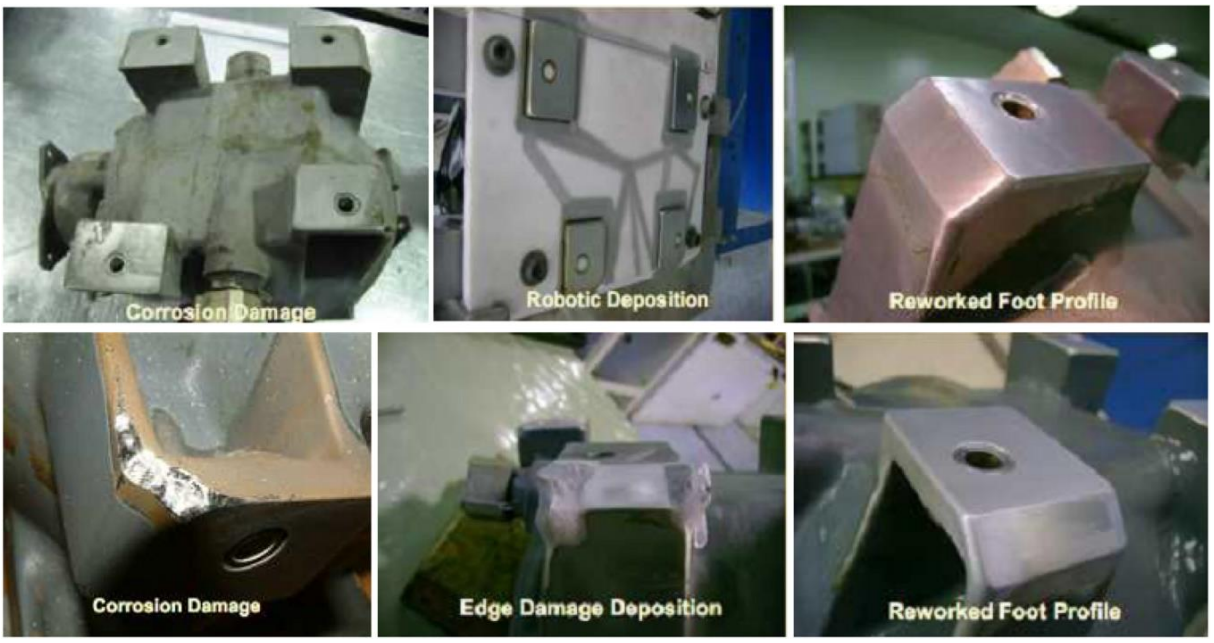

Fig. 1.24: *Cold spraying restoration of corroded surfaces of an helicopter Seahawk gearbox unit [31]*

Another example where the CGDS gave a life extension is the repair of simple wear of keyhole of high speed airplane such as the B1-bomber engine. In such airplanes aluminium panels are

fixed by steel fasteners and repeated maintenance deteriorates the fasteners holes by wear and enlargement [11]. The cold spray deposition provides an innovative solution for a complete restoration of the fasteners holes and then the panel (see Fig. 1.25).

Fig. 1.25: *Cold spray repair of fastener holes that enables a full restoration of a panel structure [32]*

The particular advantage of this technique is to be very flexible; restoration of architectural structure (Fig. 1.26) is another example of the different area that may be covered by this process.

Fig. 1.26: *Restoration of metals sculptures using a portable cold spray equipment [33]*

Besides surface functionalization and repair, the CGDS can be also used to produced bulk components using usual materials. As previously mentioned, by the use of manufacturing robot systems, this method can provide approximately the real shape of the workpiece requiring simple final shaping machining (see Fig. 1.27).

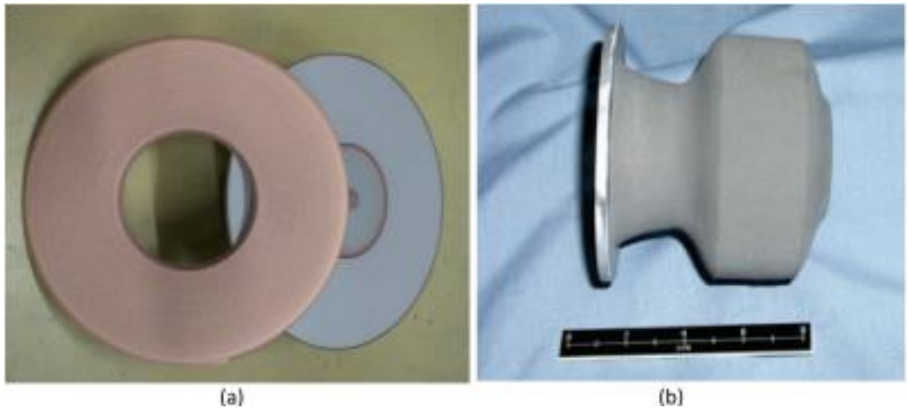

Fig. 1.27: *(a) Cold spray forming of coil components for high magnetic field magnets (inhouse product) and (b) rapid prototyping of Ti6Al4V axisymmetric bulk part [34]*

Finally, in addition to the various industrial applications, artistic and pure aesthetic creation using new combinations of material can be obtained. An example of such application is given by a new nature of painted pictures that have been painted on different supports (glass, copper plate, etc.) by the cold spray deposition of metals powders such as copper, zinc and aluminium (Fig. 1.28).

Fig. 1.28: *Metallic pictures painted by CGDS [35]*

2 Stellite-6 coatings for anti-wear application

2.1 The science of tribology and its economical impact

Originating from the Greek word *tribos*, which means *to rub*, the science of *tribology* involves the physical, chemical and mechanical processes triggered in the interface between two surfaces in mechanical contact. Further, it includes the understanding and optimization of the mechanisms behind friction and wear between surfaces in sliding contact.

From an industrial point of view, the economic impact of understanding tribology is significant. About 15 years ago, it was estimated that 1.5 % of the gross national product would be saved by paying proper attention to tribology in education and research, and then applying the knowledge in industrial applications [36].

Looking into a more everyday example: If the friction losses in a combustion engine would be reduced by 10 %, the fuel consumption would correspondingly decrease with 1.5 % [37]. For a vehicle driving a distance of 20 000 km in one year and consuming an average of 0.1 l/km this would consequently save 30 l of petrol per year. A further consequence is less consumption of natural resources and reduced emissions. The economical and environmental gains of applying tribology knowledge on a worldwide scale are evident.

2.2 Metallic materials suitable for sliding contact

Almost all metallic materials find use in tribological applications. However, through industrial development and research, different categories of materials have been optimized for various applications [38].

2.2.1 Sliding contact

Bearing alloys based on Cu are examples of metallic materials with the potential to give low friction in sliding contact. They also have a reasonably high loading capacity combined with necessary compliance. Cu-based alloys make use of their high thermal conductivity. They are typically alloyed with small quantities of "solid lubricants" in the form of Sn, Pb or Sb. Grey cast irons are another type of metallic materials with similar properties. They are the most commonly used materials in cylinders of automotive engines. Flake like graphite inclusions serve to give low friction.

Any type of steel can also be a candidate for sliding contact. If high contact pressures are expected the surface should be nitrided to reduce the friction and increase the resistance against adhesive wear.

Another class of materials often used in severely loaded sliding contacts are Stellites. Their advantage is a potential for low friction and a high resistance to adhesive and abrasive wear in combination with high thermal resistance.

2.2.2 Abrasive contact

In situations where the sliding contact involves hard particles, or when sliding against a harder material with a rough surface, a material with high abrasive resistance is desired. The abrasive wear resistance typically increases with increasing hardness. Consequently, hardened steel is a very common choice in applications such as excavator and road construction equipment. Severe abrasive attack may require a material strengthened with hard particles (e.g. carbides). Examples of metallic materials that make use of large volume contents of carbides are tool steels and white cast irons. If the latter are alloyed with Cr to give a network of Cr-carbides, their abrasion resistance is further improved. High carbon Stellites have a similar Cr-carbide network, but in a Co-based matrix. They are often used when a combination of heat resistance and abrasive resistance is needed.

Manganese-alloyed steels (Mn steel or Hadfield steel) are another example of abrasion resistant materials. Thanks to their potential to transform from a relatively ductile austenitic to a hard martensitic structure during surface deformation, they are used in heavy abrasive situations such as jaws of rock crushers. Thus, the ideal compound of a ductile bulk with a hard surface layer is self-generated.

2.2.3 "Trouble makers"

Finally, it should be mentioned that some metallic materials are almost always giving trouble in the form of high irregular friction and severe wear in sliding contacts. Common examples are austenitic stainless steels, $Al-$, $Ti-$, and $Ni-$based alloys. For the stainless steels, $Ti-$ and $Ni-$alloys the problem arises due to a relatively thin oxide layer (friction is almost always reduced by the presence of oxides in the interface [39]) in combination with a strong work hardening ability, high fracture elongation, and low thermal conductivity.

The problem of $Al-$alloys is that the oxide (Al_2O_3) is much harder than the $Al-$alloy itself. The oxide layer fractures easily and spalls off. Oxide fragments entrapped in the counter surface will severely abrade the soft $Al-$alloy during sliding.

2.2.4 Surface damage by galling

Common examples of materials showing gross surface damage when exposed to high loads in sliding contact are the austenitic stainless steels. For instance, during sheet metal forming they have a tendency to adhere to the tool surface in the form of deformation hardened patches. These will act as abrasives in consecutive forming operations, generating indents and scratches in the metal sheet. This sequence is usually named galling.

Which are the mechanisms behind this process? When the lubricant fails to separate the surfaces, the sheet metal will adhere to the tool surface [40]. As sliding continues, an increase in shear stress will affect both materials. Shear will deformation harden the surface layer of the austenitic stainless steel, primarily by mechanical twinning and dislocation interactions. Finally, the level of shear stress will be so high that shear fracture will be initiated between the work hardened surface layer and the softer bulk material. The hard patches generated may adhere to the tool surface. However, the shear stress will not be high enough to induce any significant plastic deformation of the harder tool surface.

2.3 How to avoid surface damage

To avoid surface damage in sliding contact shear must be restricted to the interface between the mating materials, i.e. the shear resistance in the interface must be lower than that of the adjacent material in the mating surfaces.

The most commonly used solution is to add a lubricant to the system. This will restrict the shear to the lubricant, since it has the lowest shear resistance in the system. As a consequence, the

shear stress affecting the materials will be significantly reduced, and thus, the friction is reduced and surface damage is avoided.

However, for many reasons, lubrication may partially fail, or it may not even be allowed for the system. Therefore, in an optimum system the materials should have intrinsic properties that spontaneously create a contact that restricts the shearing to the interface, even without lubricants.

2.4 The optimum low friction system

A system that minimizes the shear stresses that affect the surface will also exhibit low-friction properties. The beneficial tribological properties of Stellite follow the classical low friction theories proposed more than 50 years ago by Bowden and Tabor [41]. They concluded that an optimum low friction system has two basic properties: a hard bulk, providing a small area of real contact, and a thin and easily sheared surface layer.

With this combination, the real contact area will be both small and easily sheared, and consequently the system will give low friction. A common way to design such a system is to apply a soft coating or a solid lubricant on a hard bulk material.

2.5 Properties of Stellites

The original Stellite was developed in the beginning of the 20th century by Elwood Haynes and consisted of Co with Cr as the single alloying element [42]. Later, additions of W, Mo and C improved the wear characteristics, and further modifications by adding Ni, Fe, C, Si and B developed other Stellites for use in high temperature and high-impact wear situations. The nominal compositions of two commonly used Stellites are given in Table 2.1 and their mechanical and physical properties compared to those of pure Co in Table 2.2.

Table 2.1: *Nominal alloying content (wt %) of Stellite-6 and Stellite-21*

	Co	Cr	C	W	Mo	Si	Mn	Ni	Fe
Stellite-6	Bal.	28	1.2	4.5		1.1	1	<3	<3
Stellite-21	Bal.	27	0,25		5.5	1.5	1	2.5	<5

(1) Stellite 6 was chosen as primary test materials in this thesis

Table 2.2: Typical values of mechanical and physical properties of Stellite-6 and Stellite-21

	Co	Stellite-6	Stellite-21
Hardness[(1)] [HV]	125	400[(2)] 550[(3)]	320[(2)] 450[(3)]
Modulus of elasticity [GPa]	210	210	210
Yield strength [MPa]		550	500
Ultimate tensile strength [MPa]	250	900	700
Fracture elongation [%]	-	1	9
Thermal conductivity [W/m·K]	69	14.8	14.5
Density [kg/m3]	89000	8460	8340
Melting point [°C]	1495	1350	1280

(1) As a rule of thumb an increasing level of C in Stellites will form more carbides, and consequently increase the hardness. The hardening of Stellites involves both solid-solution hardening and carbide precipitation [15]
(2) Conventionally welded
(3) Laser cladded

2.5.1 Phase composition and crystallographic orientation

A dendritic structure is obtained when Stellites are cast or deposited by conventional welding. Stellite-6 mainly consists of Cr −rich M_7C_3 carbides in a solid solution dominated by Co (M represents W as well as residual elements). The intermetallic phases Co_7W_6 and Co_3W and $M_{23}C_6$ carbides have also been detected [42]–[45].

Stellite-21 has a significantly lower C content than Stellite-6 and consequently forms less carbides, cp. Table 2.1. Further, it contains Mo instead of W, and therefore consists of a Co −rich solid solution mainly containing the intermetallic phases Co_3Mo and Co_7Mo_6 and smaller amounts of the carbide $M_{23}C_6$ [46].

2.5.2 Stress induced phase transformations

In contrast to pure Co, which is transformed from a face-centered cubic (fcc) to a hexagonal closed-packed (hcp) structure when cooled below $417\ °C$ [47], the Co −rich solid solution of the Stellites retains its fcc phase even at room temperature (RT), due to its alloying elements. However, if subjected to sufficiently high stresses, the metastable fcc phase transforms to hcp [48], [49]. The transformation is considered as martensitic and occurs by shear [42]. The stacking fault energy should be minimized if the fcc to hcp phase transformation is to be facilitated. Additions of Mo, W and Cr stabilize the hcp phase, while Ni, Fe, Mg and C increase the stacking fault energy in Stellites [42], [50]. As will be discussed later, the formation of hcp

is essential for the beneficial tribological behavior of Stellites. Therefore, substrate intermixing should be kept to a minimum if the substrate contains Fe, Ni or any other element [43], [51].

2.5.3 Wear resistance

When comparing different Stellites, it was found that an increase in hardness and carbide content is beneficial for the abrasive wear resistance [52], [53].

Attempts to lower the Co content in Stellite-6 have been performed. The properties of the modified materials have been satisfactory in all but one area, namely galling resistance [48]. This implies that Co plays an important role in the tribological behavior of Stellites in sliding contact.

2.5.4 Oxides

Cr and Co, which are the main elements of Stellites, can form a number of oxides of which Cr_2O_3 and CoO dominates. The oxides are very tough and strongly bonded to the matrix [54], [55].

2.5.5 Laser processed Stellites

The laser process utilizes gas-atomized powder that, with the assistance of a laser beam, is locally melted onto a substrate material in a controlled atmosphere, see Fig. 2.1. To create a metallically bonded clad layer the substrate was melted to a depth about $50\ \mu m$. The shallow melt depth and the efficient cooling provided by the substrate material combine to create a clad layer with desired composition and a fine microstructure [56]. Multiple clad layers can be deposited. Comprehensive research has been performed in the area of laser cladding of Stellites (mainly Stellite-6) [56]–[60].

Laser cladding is performed on a variety of industrial components, e.g. valves and shafts. Competing processes as thermal spraying and conventional welding are usually outperformed by the laser cladding process with respect to adhesion of the deposited layer, homogeneity of the deposited material and stability of the component geometry. In addition, laser cladding uses a low, well-controlled heat input and hence low level of substrate intermixing compared to conventional welding [43].

Stellites solidify in a fine scaled dendritic structure when laser cladded, see Fig. 2.2, Fig. 2.3 and Fig. 2.4. The fine structure is a result of a rapid solidification process due to the small amount of material to be solidified (about $10\ mm^3$), and the effective thermal conduction of

the substrate. The hardness of laser cladded Stellites is, consequently, higher than for that of conventionally welded [43], see Table 2.2.

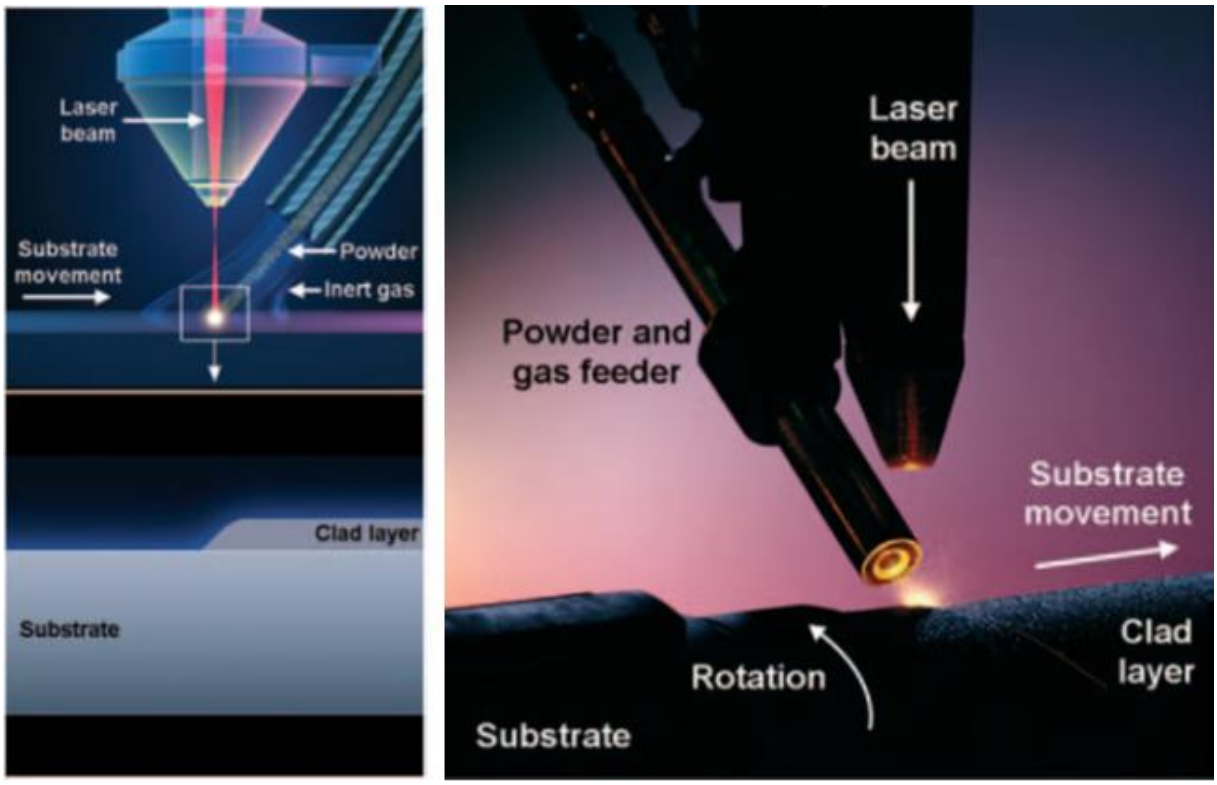

Fig. 2.1: *Principles of the laser cladding process. The laser beam is focused to melt the metal powder added onto the substrate. A flow of inert gas (e.g. Ar or He) carries the metal powder and simultaneously protects the melt pool from detrimental oxidation. A single clad bead is created by moving the substrate relative to the laser beam and by a slight overlap of consecutive parallel beads a clad layer is formed. (a) Schematic illustration; (b) Live image of laser cladding*

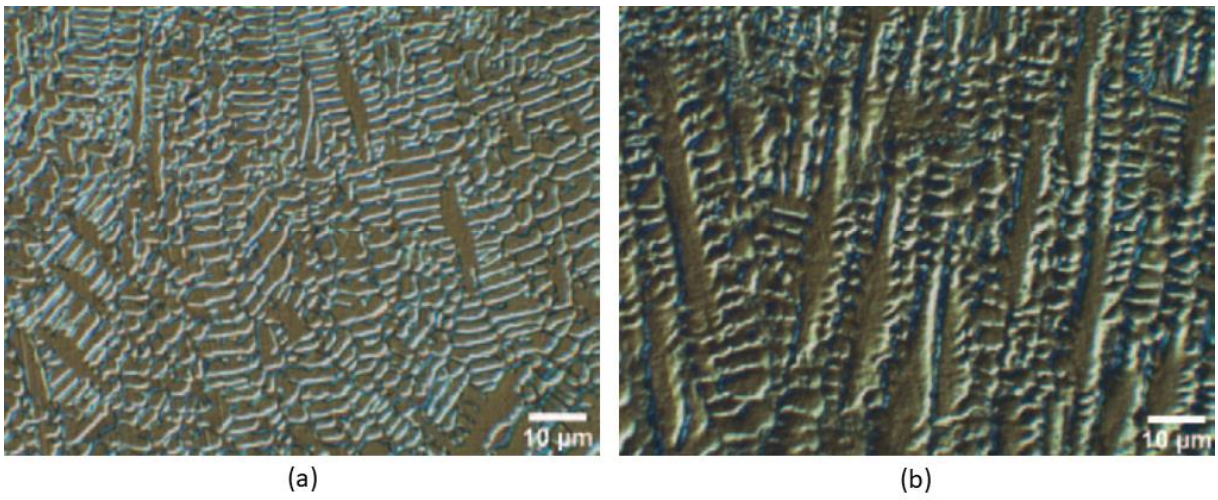

Fig. 2.2: *Light optical micrographs of polished and etched cross-sections of laser cladded Stellite 6 (a) and Stellite 21 (b)*

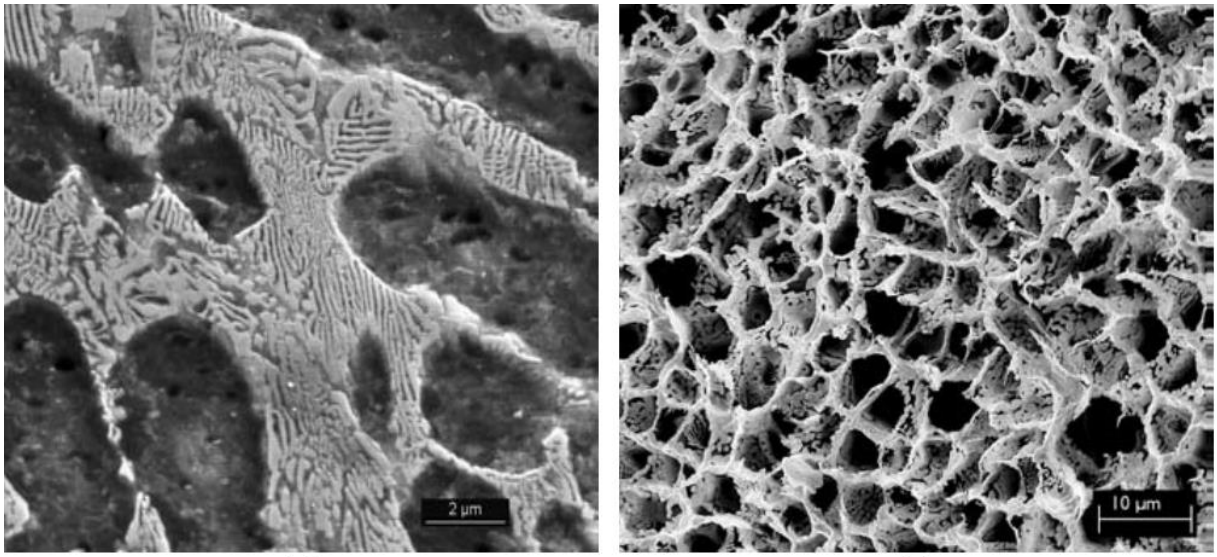

Fig. 2.3: *Carbide network of Stellite 6 as exposed by different degrees of etching. Note the fine structure within the carbide dendrites in (a) and the sponge-like three dimensional structure revealed in (b)*

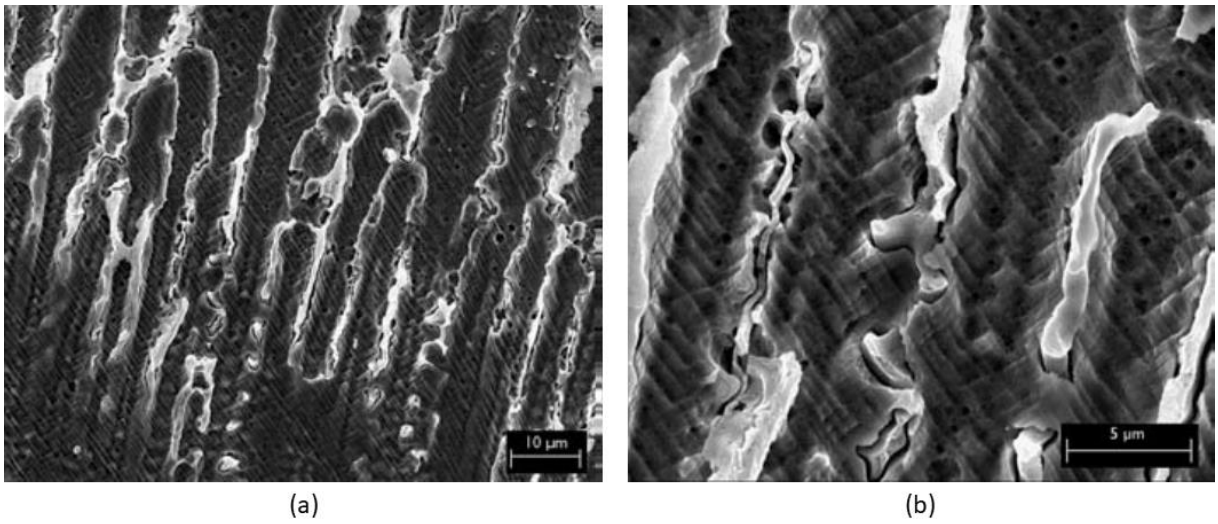

Fig. 2.4: *The structure of Stellite 21. The whiter areas are enriched with Mo (as revealed by EDS), indicating the presence of intermetallic phases. (a) Dendritic structure of the intermetallic phases and carbides. (b) <111> texture of the Cobalt-rich matrix revealed by extensive etching*

X-ray diffraction (XRD) measurements show that the Co −rich matrix of both Stellites solidify in an fcc phase. As also observed by others [61], both materials become strongly textured with the <100> direction perpendicular to the substrate surface. Further, XRD pole figure investigations on a laser cladded low C version of Stellite-21 reveal no preference for the lateral fcc <100> directions.

The toughness of Stellites is primarily determined by the carbide volume fraction and morphology. An increased level of carbides will lower the ductility. Consequently, the hardness and ductility of Stellites have to be optimized to suit the application. However, if only toughness is desired, alloying elements that stabilize the fcc phase should be added [42].

2.6 Mechanisms and tribological performance of Stellites

The selection of Stellites is promoted by properties such as abrasion and corrosion resistance, high-temperature strength, and last but not least, an excellent low-friction performance during unlubricated self-mated sliding under high nominal contact pressures. For instance, Stellite is commonly used as the sealing surface material of gate valves in nuclear power plants. The material exhibits an excellent tribological function under the conditions of high temperature, pressure and humidity prevailing during an emergency situation, thus securing the function of the valve. However, the Stellites have one large drawback in this application. The main part of the background radiation from a boiling water reactor (BWR) primary circuit originates from the Co^{60} isotope. This isotope is a result of activation of Co^{59} in wear and corrosion fragments from Stellite. Consequently, the development of a Co-free alloy replacing the Stellite on critical components in nuclear power plants is desired.

A Co-free material would significantly lower the background radiation in the vicinity of the primary circuit, leading to an improved working environment, e.g. for maintenance.

Numerous investigations of Stellites with respect to their tribological properties in the areas of abrasion [42], [52], [53], adhesion [43], [48], [62] and erosion [42], [49] have previously been conducted. However, though being an established and important group of materials, a satisfactory explanation to why they exhibit low-friction properties under severe sliding conditions was not found in the literature.

In fact, in surface engineering, Stellite alloys are widely used in order to protect various components against wear, corrosion and oxidation. Stellites are, also, widely used as hardfacing materials for components active in severe tribological environments, e.g. turbine blades, bearings, spindles and valves.

These properties are due to the high chromium content, and to the presence of carbides and borides coupled with lattice stress-induced transitions that occurring in the contact region, under high-load sliding conditions. This latter phenomenon provides a remarkably high hardness and good wear properties thanks to the formation of a hexagonal close-packed structure caused by

shear stress during contact in place of the parent face-centered one [63]. In order to obtain good Stellite coatings, different deposition technologies can be used, e.g. plasma transferred arc (PTA) [64] or tungsten inert gas (TIG) welding [65], thermal spraying [43], [66]–[72] or laser cladding [43], [66], [67],[60], [73]–[80], that implies differences in coatings microstructures and consequently in the coating properties.

From the group of thermal spraying technologies, the Cold Gas Dynamic Spray (CGDS) technology represents an interesting option to deposit the Stellite coatings. Furthermore, there is still a limited understanding on how the loading conditions affect the physical response of the alloy and in turn how they influence the wear mechanisms. While the general wear response of such alloys have been investigated experimentally, with a focus of common thermal sprayed stellite coatings, prior to this paper, identifying wear mechanisms such as carbide pull-out and fracture [81], delamination [43] and fatigue of a wear-reducing oxide layer [82], there has not been much focus on the understanding of how these wear mechanisms occur as a result of the loading conditions for cold spray deposits. Use of a mechanistic model of wear which captures the physical response of the system due to the loading conditions and environment, would be useful to understand of how this material behaves in-situ. Typically, the Archard wear equation [83] is used to rank material performance:

$$W_v = \frac{KNs}{H} \tag{2.1}$$

where K is the "wear-rate", H is the hardness of the surface, N is the normal load, and s is the total sliding distance. It is important to note that this equation suggests that the wear behavior is linear for a given system like other typical wear models used to characterize system behavior [83], [84] and do not capture the physics involved during sliding conditions. In fact, any possible changes in the environment and loading conditions have to be considered for the development of a model that can account for these conditions in the case of $Co - Cr$ sliding systems. However, to date, no in-depth study of the effects of load and sliding speed, at room temperature, have been performed for this kind of coatings. Therefore, the aim of this thesis is to understand how loading conditions influence wear mechanisms of Stellite-6 coatings and to identify the relevant physical phenomena at the wear interface that can allow to develop substantial models, able to predict the wear rate of these kind of coatings.

3 Solid-state cold spraying of Ti and its alloys

Coatings of Ti and its alloys by Cold Gas Dynamic Spray (CGDS) have been found limited industrial applications compared to other materials (e.g. Cu and Al), partly due to the special particle deposition behavior of Ti and its alloys and the lack of comprehensive knowledge of its control. In this chapter, therefore, the attention has been focused on the deposition characteristics of Ti and its alloys in an effort to shed light on them and expand their applications.

In fact, cold spray has a proven potential as an additive manufacturing and coating technology for metallic parts exposed to harsh environment, guaranteeing that parts exhibit proper mechanical and physical properties. Nevertheless, no solution exists nowadays to obtain satisfactory coating exposed to harsh environment in the energy production sector.

3.1 Unique deposition features of cold spray Ti and its alloys deposits

Compared to other metals (e.g. Cu, Al and Zn), cold spray Ti and its alloys have unique deposition characteristics [85], because of their distinguishing thermal and mechanical properties as listed in Table 3.1 [1], [86], [87].

An interesting phenomenon that can be noticed during the deposition of Ti-based powders is the flashing jet just next to the nozzle exit as shown in Fig. 3.1(a) [86], and such flashing phenomenon becomes more prominent at elevated gas temperatures as shown in Fig. 3.1(b), which suggests that the surface temperature of the particles in the gas flow jet is extremely high.

Table 3.1: Properties of typical materials discussed in this paper [1], [86], [87]

Property	Unit	Zn	Al	Cu	Ti	Ti6Al4V
Density	kg/m^3	7131	2688	8880	4506	4420
Thermal conductivity	W/m/K	121	237	398	21.9	7.6
Heat capacity	J/kg/K	389	905	386	522	537
Melting point	°C	420	933	660	1680	1660
Latent heat of fusion	J/Kg	102	395	205	440	418,2
Yield strength	MPa	30	44	90	140	880
Ultimate tensile strength	MPa	55	80	210	220	950
Critical velocity	m/s	339	482	451	712	1013

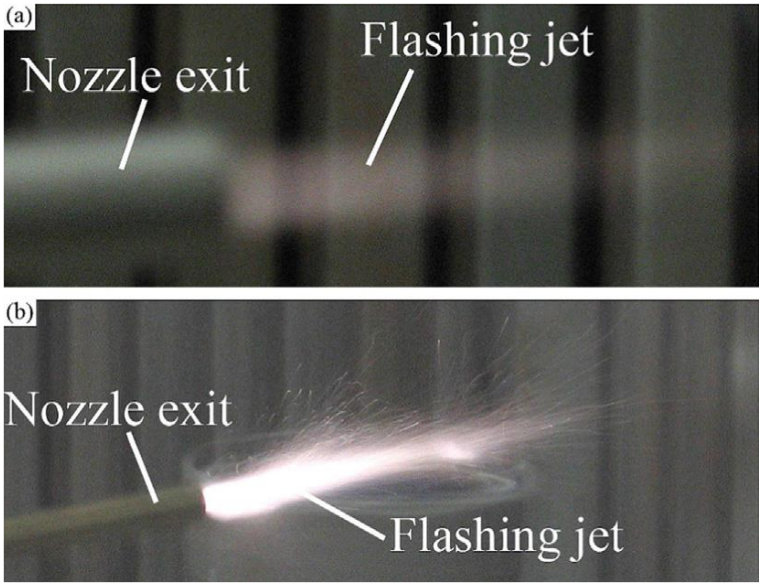

Fig. 3.1: Photos of the flashing jet with Ti powder particles outside nozzle exit sprayed with air at 2.8 MPa: (a) without preheating, jet length from nozzle exit is about 10 cm and (b) with preheating of gas at 520 °C, jet length from nozzle exit is about 40 cm [85], [86]

In addition, it is also difficult for Ti-based particles to generate thermal plastic deformation in the cold spray process due to their high melting point and strength. The critical velocity of particles depends on the density, melting point, ultimate tensile strength and initial temperature of particle materials [4]. Therefore, the critical velocity for successful deposition of Ti and its alloys is normally higher than those of most metals (e.g., over $700\,m/s$ for Ti and over $1000\,m/s$ for Ti6Al4V) [1], [87]. As a consequence, cold spray Ti-based deposits are normally porous as representatively shown in Fig. 3.2 [88]–[90] and 5 [85]. This fact is different from metals, such as Cu, Zn or Al, which can easily undergo large deformation during deposition and form dense deposits [86], [91]–[93].

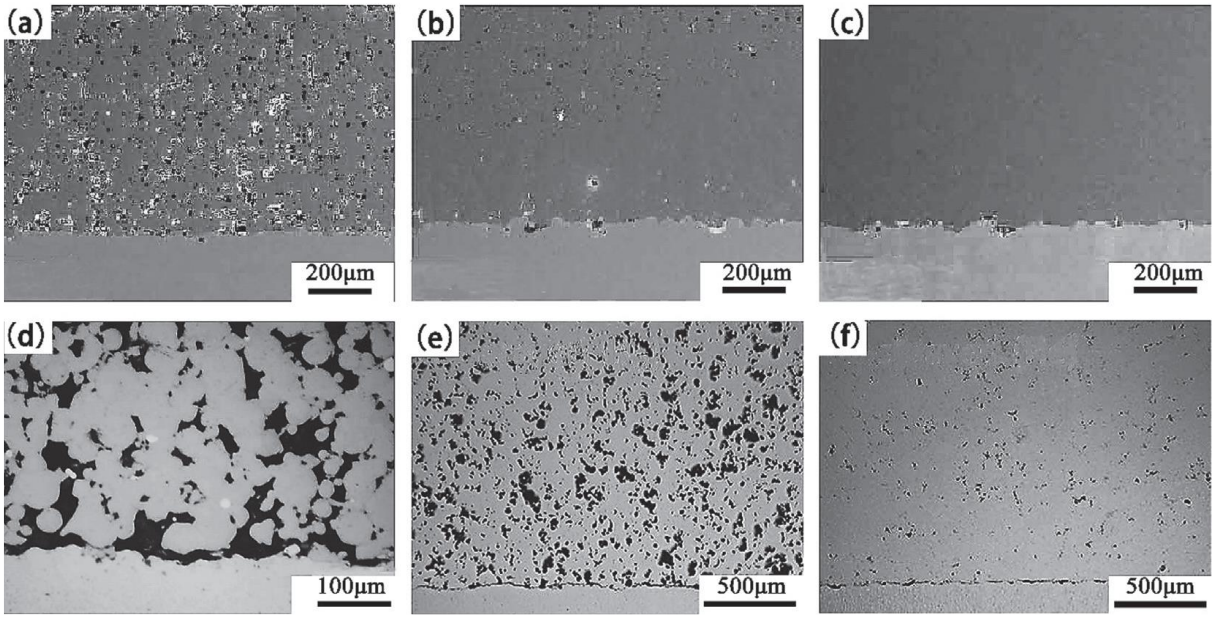

Fig. 3.2: *The microstructure of Ti and Ti6Al4V cold sprayed deposits: (a) Ti on mild steel substrate (nitrogen, 2.5 MPa, 600 °C, without powder preheating), (b) Ti on mild steel substrate (nitrogen, 2.5 MPa, 600 °C, powder preheating 600 °C), (c) Ti on mild steel substrate (He, 1.5 MPa, 600 °C)* [89]*, (d) Ti6Al4V (air, 2.8 MPa, 520 °C)* [90]*, (e) Ti6Al4V on Ti6Al4V substrate (nitrogen, 4 MPa, 800 °C), (f) Ti6Al4V on Ti6Al4V substrate (He, 4 MPa, 350 °C)* [88]*. Note that the feedstock powders are spherical particles*

The porosity of cold spray Ti deposits could reach as high as 20% as shown in Table 3.2 [88]–[90], [94]–[99], and that is even worse for Ti alloys as shown in Fig. 3.3 [85]. However, by increasing gas temperature and pressure, or using helium as the propulsive gas, or applying powder preheating could reduce the porosity to some extends as shown in Fig. 3.2 [88]–[90].

In addition, a *"tamping effect"* was clearly observed in cold spray for fabricating Ti-based deposits. Tamping effect means that the subsequent flying particles impact the deposited particles, tamping them in order to further densify the deposits. Hence, the top of the deposit is still porous though optimized process parameters are used as shown in Fig. 3.4 [100]. The structure becomes denser and denser from the top to the bottom of the deposit [101]. Experiments have also shown that the thickness of the porous region at the top decreases when using helium as the propulsive gas.

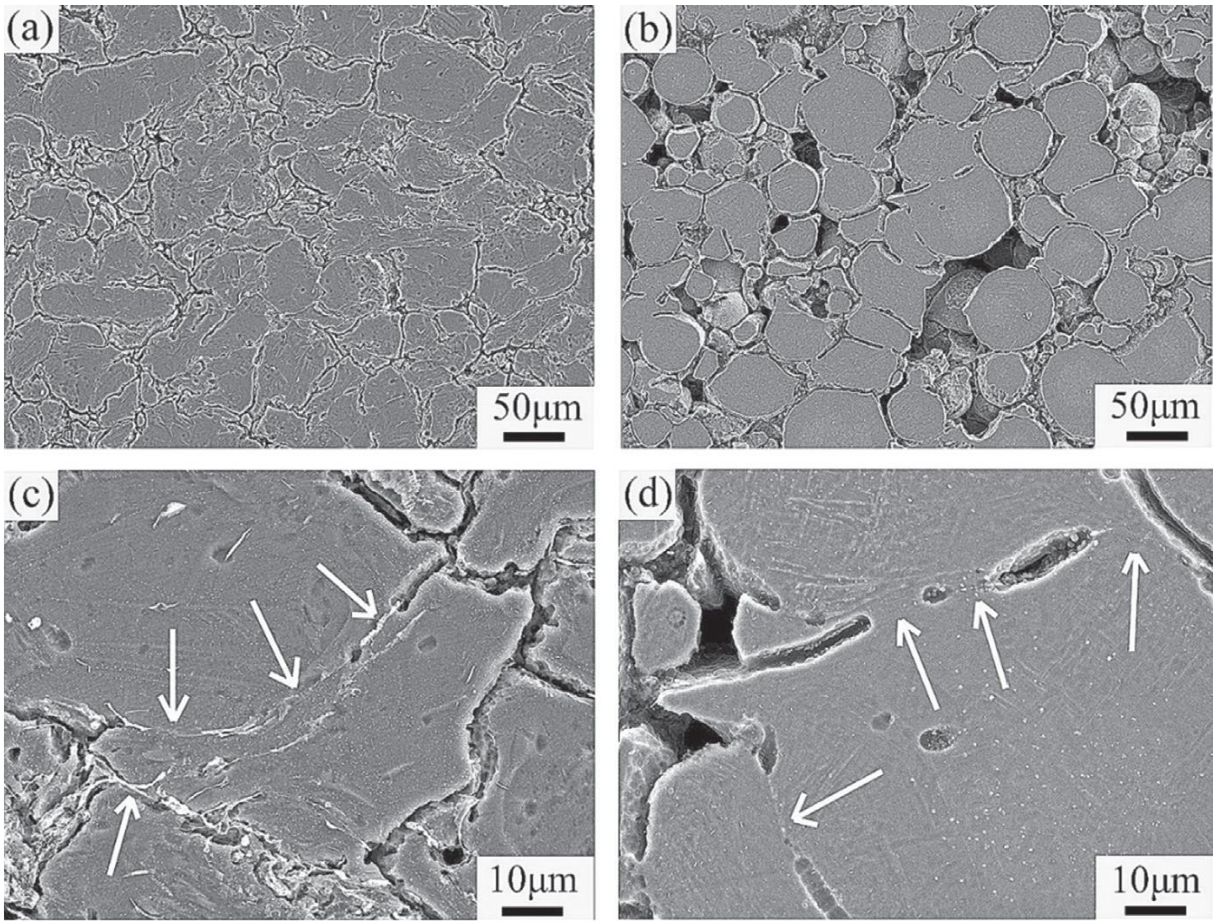

Fig. 3.3: *Typical SEM microstructures of Ti (a, c) and Ti6Al4V (b, d) deposits in the etched state* [85]

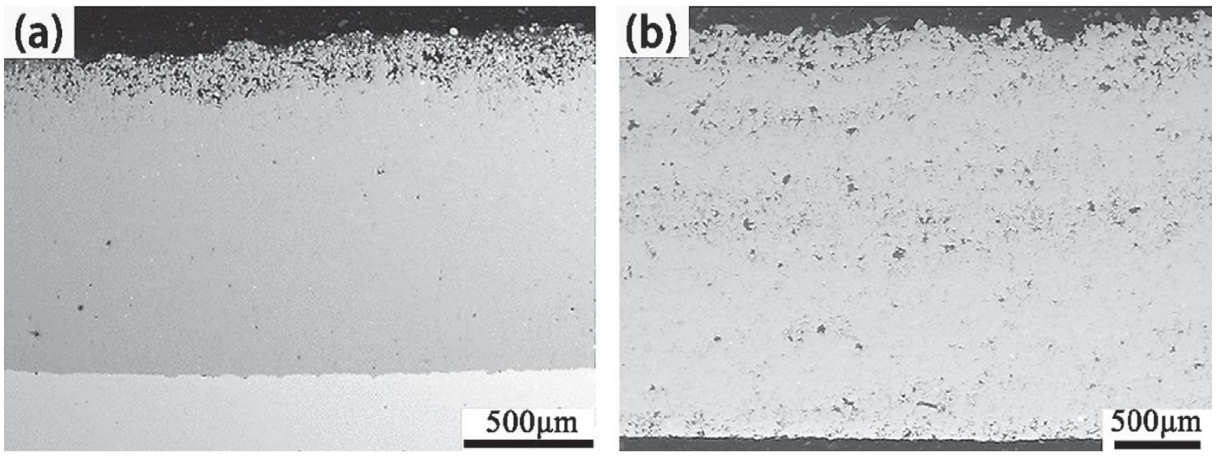

Fig. 3.4: *Cross-sectional micrographs showing top porous layers even for dense inner Ti and Ti6Al4V deposits fabricated with helium gas* [100]

Another difference between cold spray Ti-based materials and other metals is the deposition efficiency (DE). For most of the metal powders, high DE usually suggests that the particles have experienced large plastic deformation upon impact. However, the DE of Ti-based

materials could easily reach 60−95% even though the particles undergo only little or no plastic deformation [85].

The mechanical properties of cold spray Ti and its alloys deposits in the as-sprayed state are typically unfavorable (e.g., low tensile strength, low ductility and low adhesion strength) as shown in Table 3.2. Although the quality of the deposits can be tailored by improving processing parameters, the improvement may be not sufficient for practical applications [102].

Table 3.2: *Typical properties of Ti-based deposits with cold spray reported in the literatures* [88]–[90], [94]–[99]

	Porosity (%)	**Micro-hardness (HV)**	**Adhesion strength (MPa)**	**Cohesion strength (MPa)**
Ti	0.2–20.6	150–368	8–25	49–120
Ti6Al4V	0.5–22.3	357–425	18–70	110–445

3.2 Influential factors for cold spray Ti and its alloys deposits

The quality of cold spray Ti-based deposits mainly depends on the conditions of powder particles. Fig. 3.5 summarizes the dependence of the porosity and micro-hardness of cold spray Ti deposits on the particle impact velocity [89], [94]–[99]. Clearly, the porosity becomes lower and the micro-hardness increases with increasing the particle impact velocity. Fig. 3.5 shows that particle morphology poses an impact on the porosity and micro-hardness.

Actually, apart from gas parameters, a several processing parameters also have significant influence on the deposition such as particle conditions, substrate temperature, spray angle, spray distance and nozzle trajectory. This section will provide a thorough discussion on how these parameters influence the deposition of cold spray Ti-based materials.

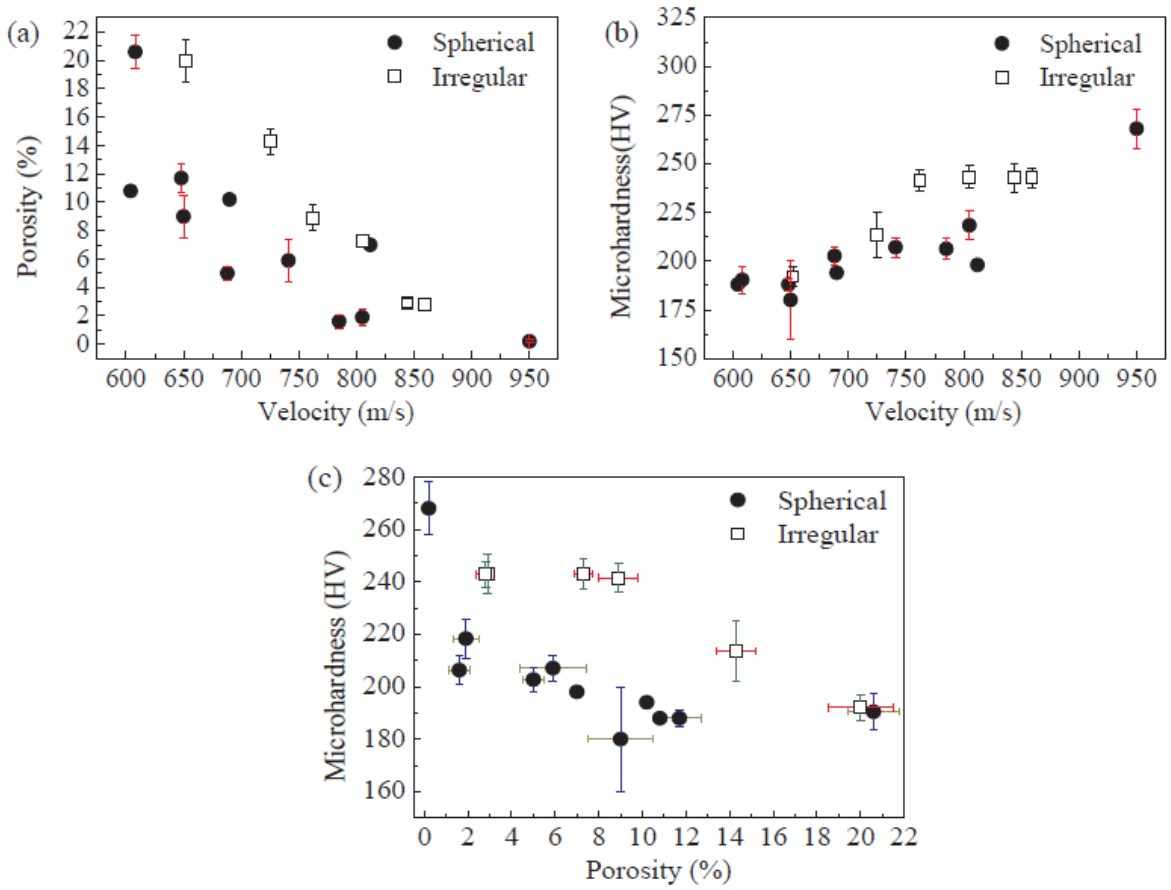

Fig. 3.5: *Relationship between Ti particle impact velocity, porosity and micro-hardness: (a) porosity as a function of impact velocity, (b) micro-hardness as a function of velocity and (c) micro-hardness as a function of porosity*

3.2.1 Nozzle design

Spray nozzle is the key component in a cold spray system as its design directly determines the efficiency of the system, and in particular the deposit microstructure and properties. A cold spray nozzle typically consists of two parts: convergent and divergent sections (Fig. 3.6). Most of the cold spray nozzles have a circular cross-section but some may have a rectangular cross-section. Five geometric parameters are used for nozzle design, including inlet diameter/area, throat diameter/area, exit diameter/area, convergent length, and divergent length.

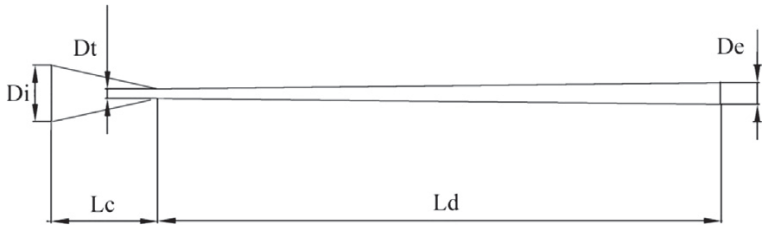

Fig. 3.6: *Schematic dimensions of cold spray nozzle geometry*

Computational fluid dynamics (CFD) software is usually used to study the temperature and velocity of particles in and outside the nozzle [3], [103]. Previous work has demonstrated that the ratio of sectional throat area to exit area (refer to as expansion ratio) and divergent length are two key variables for better acceleration of cold spray particles [104], [105]. In general, the optimal expansion ratio could be $4-10$ depending on the gas parameters and divergent length [104]. The divergent length itself also poses influence on the gas velocity and particle acceleration; most of the existing work used $120-280\ mm$ as the divergent length for the cold spray nozzle [105].

As for the absolute value of throat or exit diameter, they influence gas flow flux (or gas consumption) in the cold spray process. In addition, the nozzle exit diameter determines the spray spot size and therefore the manufacturing accuracy. For large components, the nozzle can be designed with a large throat diameter together with a large exit diameter, in order to improve working efficiency. In this case, a single pass spraying can produce a spot area of over $10\ mm$ in diameter. If a fine deposit structure is required, a small exit diameter is necessary.

3.2.2 Propulsive gas type, temperature and pressure

Gas parameters play a very important role in particle acceleration. The gas type affects particle acceleration behavior more than the temperature and pressure [106]. The existing work shows that the deposits produced with helium have a much lower porosity, and a higher DE and micro hardness because of the higher particle velocities achieved as replotted in Fig. 3.7.

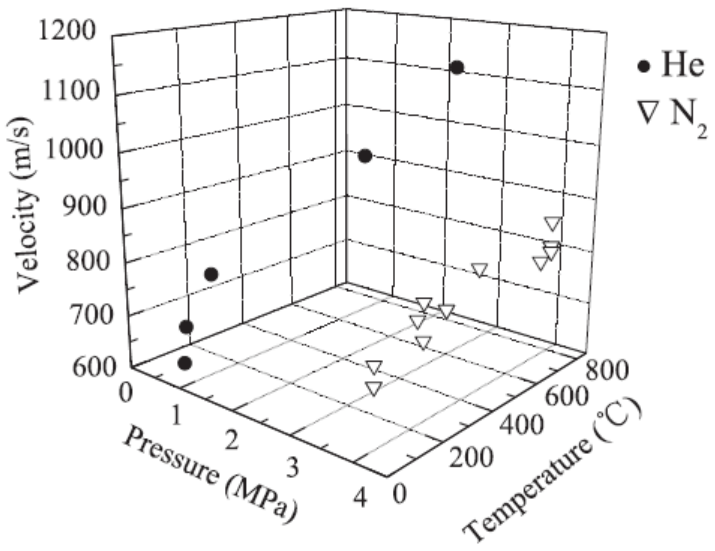

Fig. 3.7: *Plot of velocities of spherical Ti particles as a function of gas pressure and temperature* [106]

The equation that describes the relationship between gas velocity (V_g) and gas parameters is given as follows [104]:

$$V_g = M\sqrt{\gamma R T_g} \tag{3.1}$$

where M, γ, R, and T_g represent the Mach number, specific heat ratio of gas, specific gas constant and gas temperature, respectively. The specific heat ratios (γ) of nitrogen and helium are 1.4 and 1.66; the specific gas constants (R) of nitrogen and helium are 296.8 and 2078.2 ($J/(kg\ K)$). By applying these values into Eq. 3.1, it is derived that the velocity of helium is approximately 2.8 times of that of nitrogen provided all the other parameters are same.

Apart from the gas type, gas temperature and pressure also have effect on gas velocity and thus Ti particle velocity as shown in Fig. 3.8 [107]. The particle velocity increased as both the gas temperature and pressure rose.

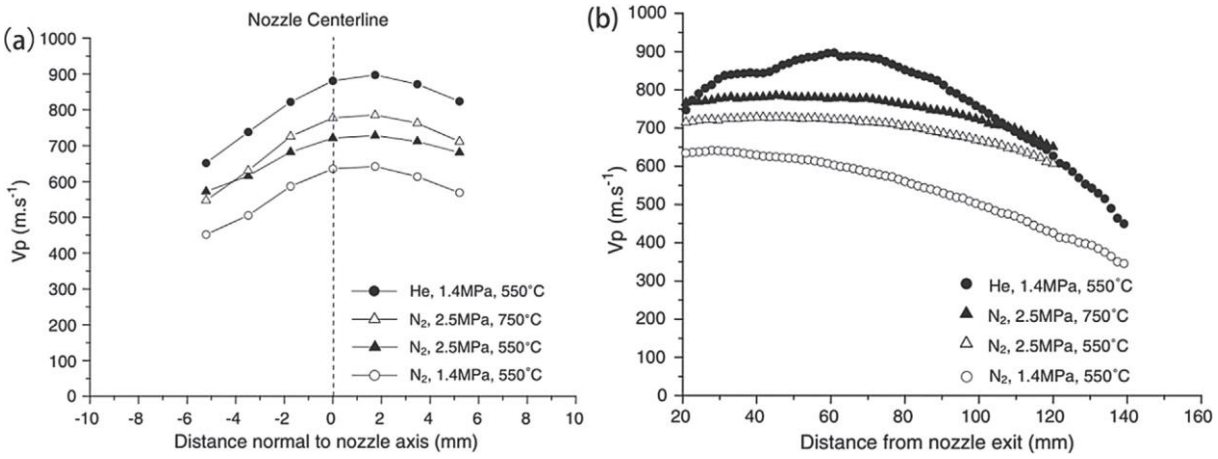

Fig. 3.8: *Comparison of Ti in-flight particle velocity (average size of irregular particles is 27 μm, in-flight velocity measured by PIV): (a) in-flight velocity as a function of distance normal to nozzle axis, (b) in-flight velocity as a function of distance from nozzle exit* [107]

However, as compared to increasing gas pressure, increasing gas temperature would further increase particle temperature, which facilitates the particle deformation and reduce critical velocity [105], [108]. In addition, a higher gas temperature also increases substrate temperature and thus improved adhesion strength.

3.2.3 Particle conditions

Particle size and morphology have significant influence on the acceleration behavior and deposition characteristics of particles. Larger particles are more difficult to be accelerated and thus have lower velocity under the same cold spray conditions than the smaller ones. However,

in contrast, larger particles are more likely to reach higher temperature than smaller ones, which could reduce critical velocity [3]. Fig. 3.9 schematizes the effect of particle size on the particle impact velocity and critical velocity [87]. It is interesting to find that there is an optimum particle size range within which the particle velocity is much higher than its critical velocity. The particles having an optimum size range could result in high-quality deposits.

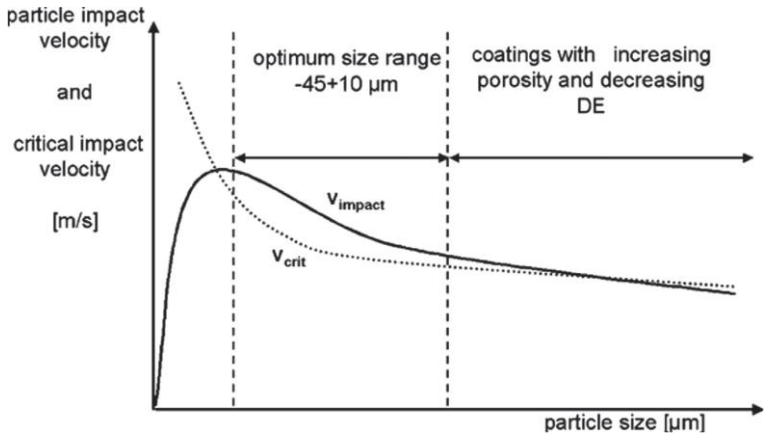

Fig. 3.9: *Relationship between particle impact velocity and critical velocity and particle size distribution in cold spray* [87]

Ti-based particles used for cold spray typically have two different morphologies, spherical and irregular [109], [110]. By plotting the Ti particle velocity against gas pressure and temperature (Fig. 3.10), it is apparent that irregular Ti particles can reach higher velocity than spherical ones under the same processing parameters because of their higher drag coefficients [106].

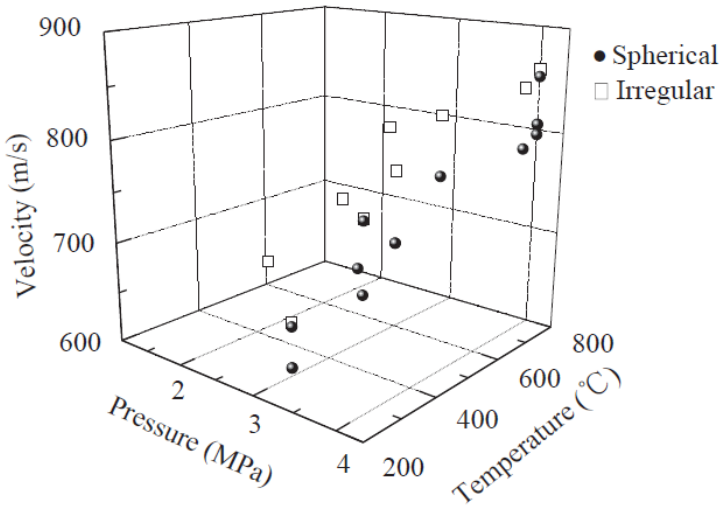

Fig. 3.10: *Effect of Ti particle morphology on its impact velocity under different gas conditions* [106]

Although higher particle velocity facilitates the particle deposition and results in higher DE, the deposits produced with irregular particles are more porous with lower micro-hardness as seen in Fig. 3.5(a).

3.2.4 Substrate temperature and roughness

Substrate preheating is of benefit to particle deposition as it reduces the kinetic energy required for particle deformation, improves adhesion strength and relieves thermal stress of cold spray deposits [111], [112]. For cold spray Ti and its alloys, a single-splat scratching experiment conducted by Goldbaum et al. [113] clearly showed that the adhesion strength of Ti/Ti and Ti6Al4V/Ti6Al4V could be significantly improved from 220 to 284 MPa and from 100 to 250 MPa, respectively, which confirms the positive role of substrate preheating.

Substrate surface preparation was also found to pose effect on particle deposition. Generally, grit-blasted surface would result in the lowest adhesion strength between the deposit and substrate, as shown in Fig. 3.11 [97], due to the surface work hardening effect which lowers the deformation ability of the substrate [97], [114].

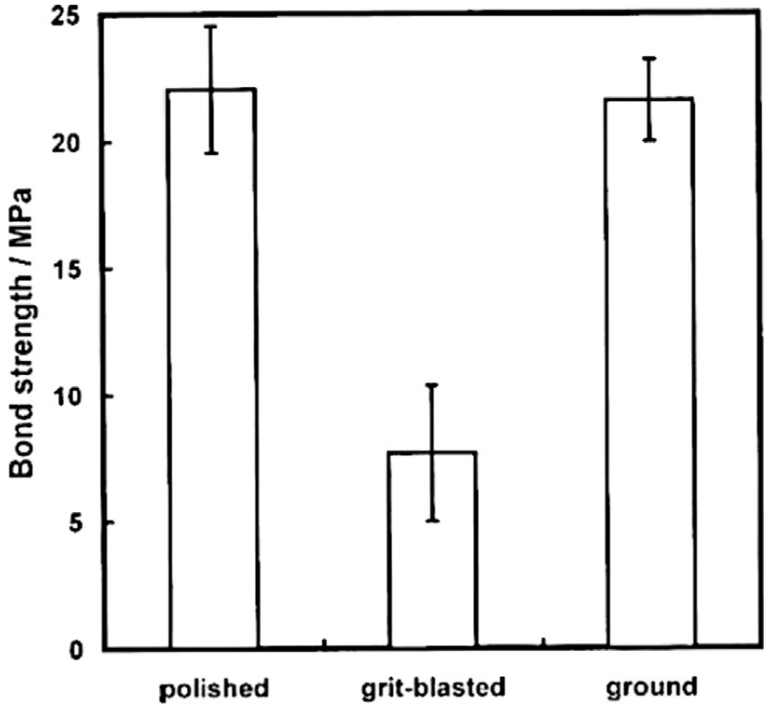

Fig. 3.11: *Effect of substrate preparation on bonding strength of cold sprayed Ti deposits* [97]

3.2.5 Standoff distance, spray angle and nozzle traverse speed

Standoff distance is another parameter that influences particle impact velocity and thus deposit properties [115], [116]. Pattison et al. [117] schematically showed the effect of standoff distance

on DE (Fig. 3.12). The standoff distance was divided into three characteristic regions: (1) small, where DE increases as the standoff distance increases; (2) medium, where DE maintains steady; (3) large, where DE starts to decrease as further increasing standoff distance. In order to achieve high DE, the standoff distance should be set in the medium region [117], [118].

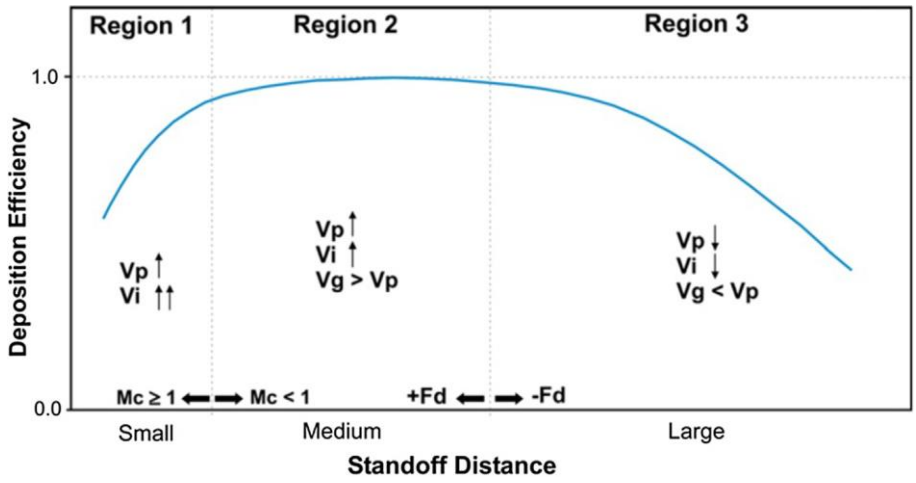

Fig. 3.12: *Non-dimensional chart showing the effect of standoff distance on deposition efficiency. Note that Fd is the drag force, Mc is the centerline Mach number, Vg is the gas velocity, Vi is the particle impact velocity and Vp is the in-flight particle velocity* [117]

Binder et al. [96] studied the influence of spray angle on the properties of cold spray Ti deposits as shown in Fig. 3.13. It was found that when the spray angle deviates from 90°, DE decreases and porosity increases, which was also reported by Yin et al. [119].

When the spray particles are irregular, the effect of spray angle becomes a little complex as shown in Fig. 3.14 [120]. In the 0° case, the contact area is quite large, which produces limited particle deformation and a small metal jet. However, in the 90° case, the metal jet is noticeable with a small contact area. As the top half of the particle does not deform an unstable bridge-like formation may develop, which increases the probability of pore formation. So, the deposit of an irregular particle has a more porous structure than that produced with spherical particles [120].

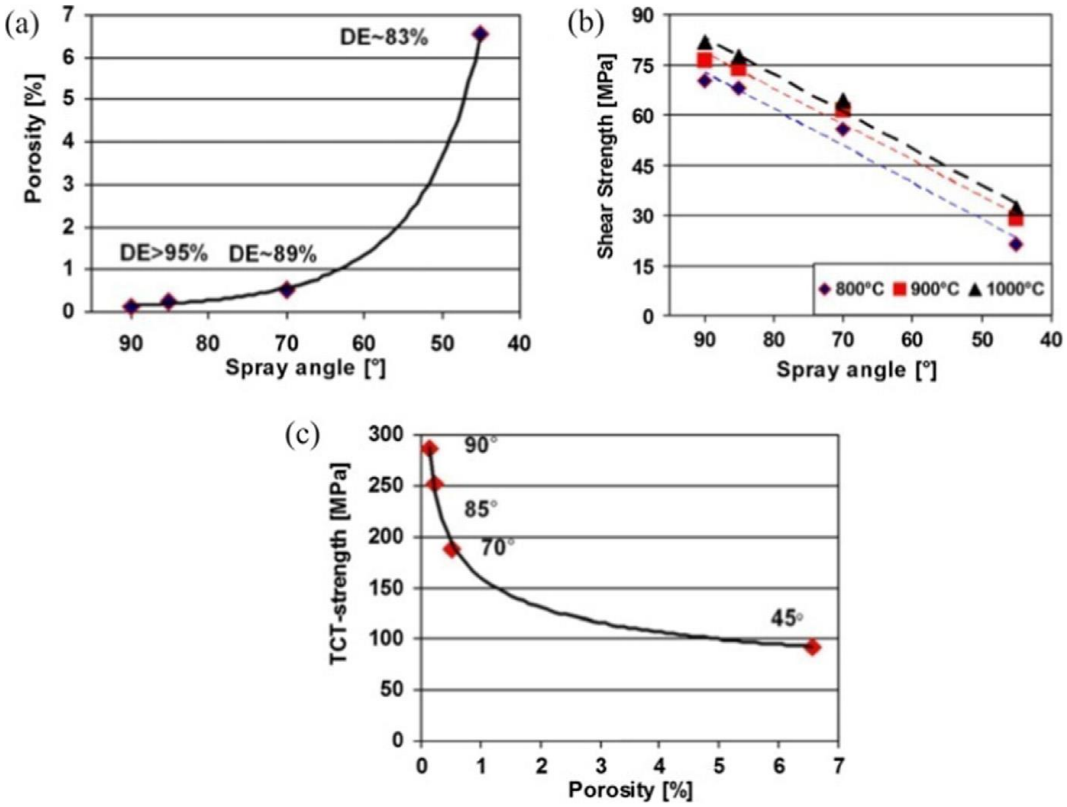

Fig. 3.13: *Correlation between spray angle and Ti deposit porosity as well as deposition efficiency (DE), shear strength and cohesion strength at various gas preheating temperatures: (a) porosity and DE, (b) shear strength and (c) cohesion strength* [96]

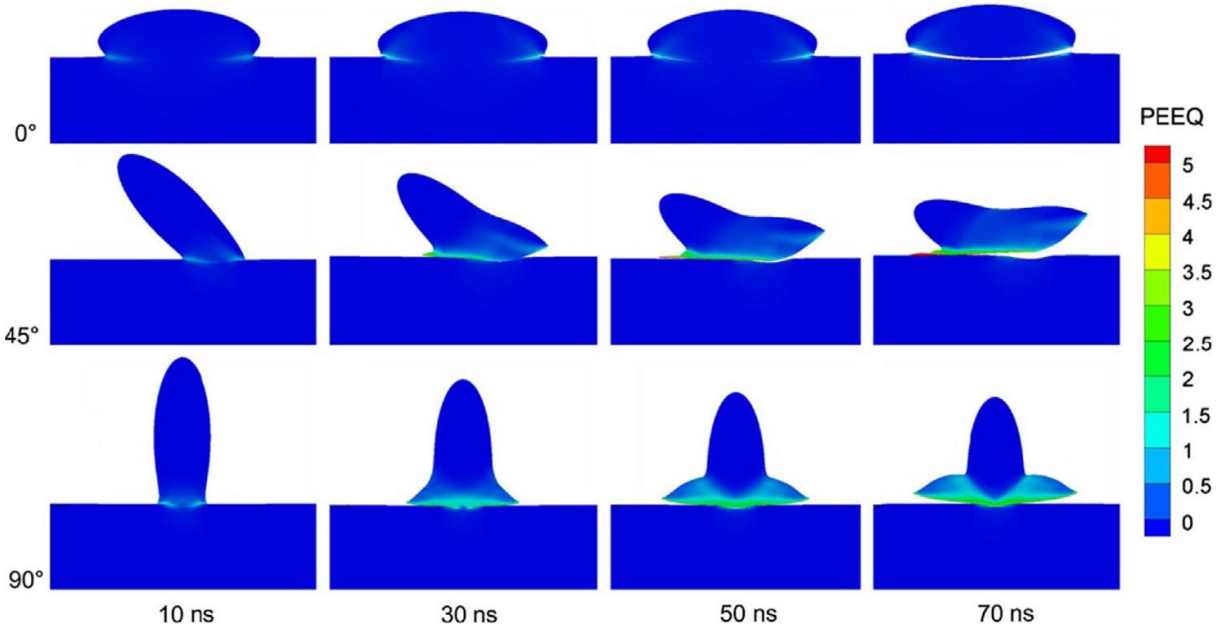

Fig. 3.14: *Equivalent plastic strain (PEEQ) contours during impact of a single Ti particle on a stainless steel substrate at different spray angles* [120]

Another parameter that affects particle deposition is nozzle traverse speed. The major properties that are influenced by nozzle traverse speed include porosity, deposit thickness and substrate temperature. Wong et al. [121] produced Ti deposits with a same thickness at two different traverse speeds: $150\ mm/s$ and $5\ mm/s$. The resultant deposits showed porosities of 0.9% and 0.1%, respectively. The reason for the difference was attributed to the improved particle deformation at higher substrate temperature caused by lower nozzle traverse speed. Tan et al. [115] drawn a same conclusion by using Ti6Al4V powders; the porosity in the Ti6Al4V deposit increased as the traverse speed increased (Fig. 3.15).

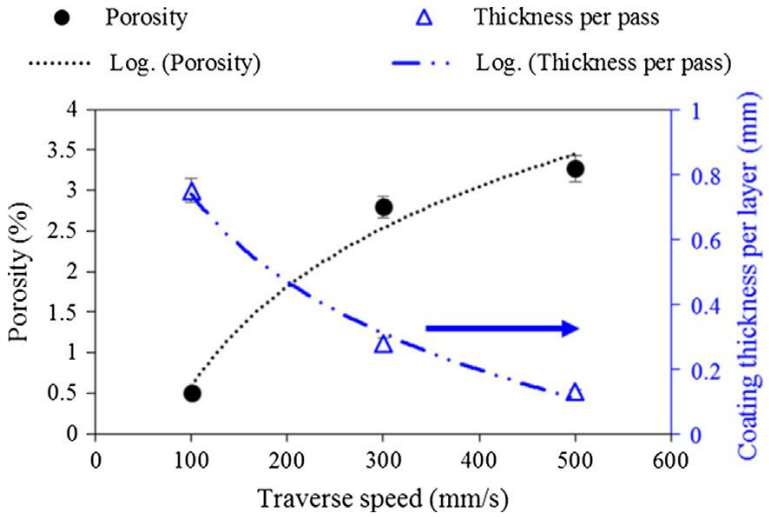

Fig. 3.15: *Porosity and thickness per pass of Ti6Al4V deposit as a function of traverse speed* [115]

3.3 Bonding mechanisms of Ti and its alloys in cold spray

3.3.1 Bonding behaviors of Ti and its alloys particles

It is believed that the above-mentioned general bonding mechanisms are suited to the bonding of Ti and its alloys particles in cold spray. For example, a single Ti particle impacted on steel substrate and showed a typical splat shape as shown in Fig. 3.16 obtained by using FIB + TEM techniques [122]. It is clearly seen that the bonded region is located at the marginal zone and there is a non-bonded region near the impact center zone, which is confirmed by the simulation result [123].

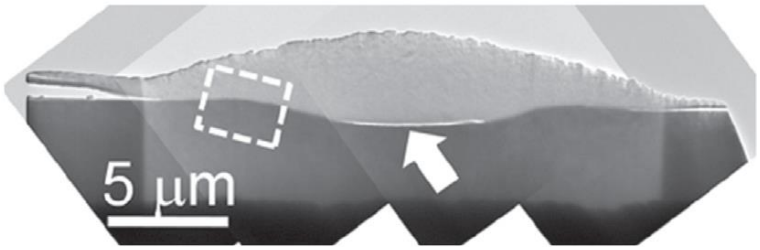

Fig. 3.16: *Cross-sectional TEM image of a Ti splat and steel substrate comprising several low-magnification scans. The boxed area and the arrow indicate the bonded region and the non-bonded region, respectively* [122]

Another example is shown in Fig. 3.17 [1], where a single Ti6Al4V particle impacts on a Ti substrate in cold spray, bonding starts at the edge of the contact zone of the deformed particle and the substrate, and with particle impact velocity increasing, the bond extends inwards to the center of the contact zone. However, there is no bond at the center of the contact zone as shown in Fig. 3.17, where a smooth surface around the particle center is surrounded by a rough and fractured ring structure [1], [124]. Some studies also showed that the degree of single particle plastic deformation depends on the material properties (Ti and Ti6Al4V) and spray parameters in cold spray. Using high-temperature nitrogen or helium as propulsive gas can promote the particle plastic deformation during cold spray, and the plastic deformability of Ti6Al4V particle is much lower than that of Ti under the same spray conditions.

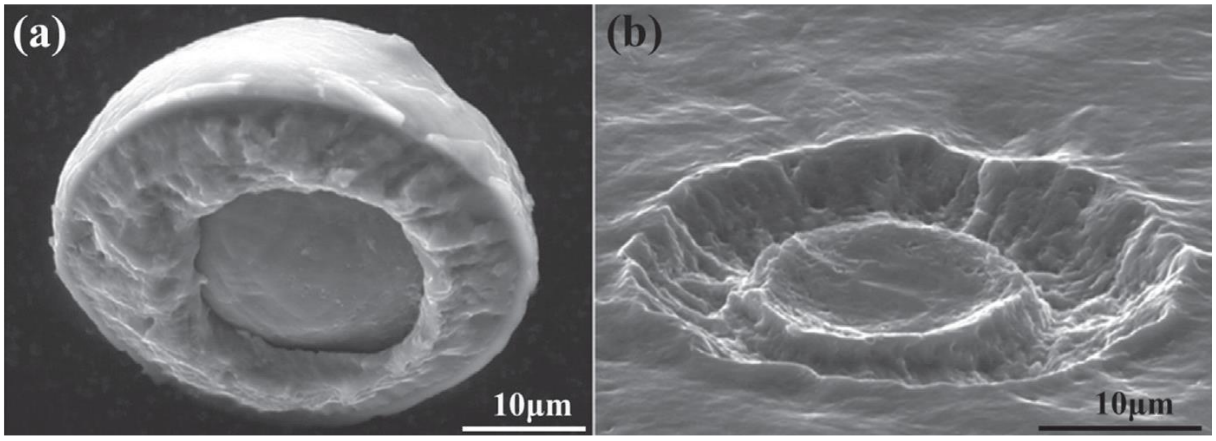

Fig. 3.17: *SEM micrographs of single Ti6Al4V particle impacting on Ti substrate in cold spray: (a) residue of substrate on a detached particle (by ultrasonic cavitation), and (b) imprint on the substrate as a result of impact and detachment of a part of substrate material related to (a)* [1]

However, unlike Cu and Al particles, Ti and its alloys, especially Ti6Al4V, can form deposits usually with pores and low bonding strength due to limited particle plastic deformation upon impact [101].

3.3.1.1 Microstructural evolution at the impact interface

Grain refinement by recrystallization at the local impact regions is another typical feature in cold spray Ti and its alloys deposits. It has been proposed that recrystallization occurs at the interface of cold spray Ti and its alloys deposits. Kim et al. [125], [126] observed the single splats of Ti particles after high velocity impact (realized by the low temperature HVOF process). Fig. 3.18 shows one splat on steel substrate and the formation of fine grains (in nanoscale) because of adiabatic shearing and rotational dynamic recrystallization during the initial stages of impact [125]. Fig. 3.18 shows one splat on steel substrate and the formation of fine grains (in nanoscale) because of adiabatic shearing and rotational dynamic recrystallization during the initial stages of impact [125].

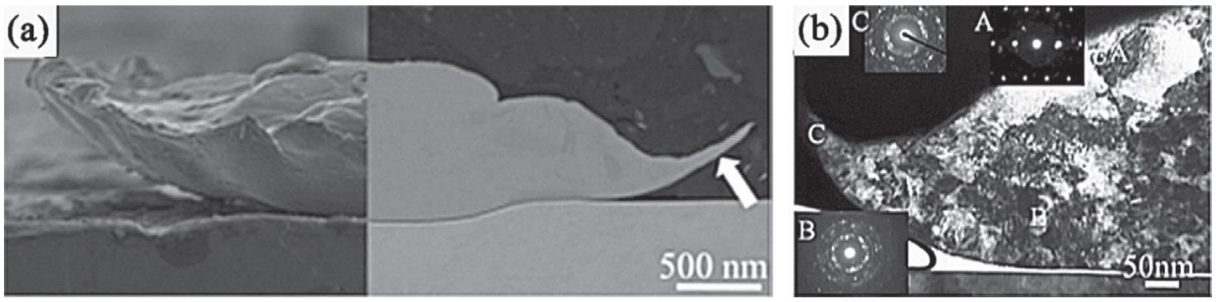

Fig. 3.18: *Cross-sectional view of a single titanium splat on steel substrate after high velocity impact (a), and a magnified TEM image of the splat (b) with inserted selected area diffraction patterns (SADP) from the upper region (marked A), lower region (marked B), and metal jet (marked C)* [125]

Hence they proposed one grain refinement mechanism by dynamic recrystallization as shown in Fig. 3.19 [125]. As one Ti particle impinges the substrate, the high impact pressure generated produces intense shear stress which deforms the particle, and ASI begins. The greatly deformed grains and sub-grains accompany the metal jet.

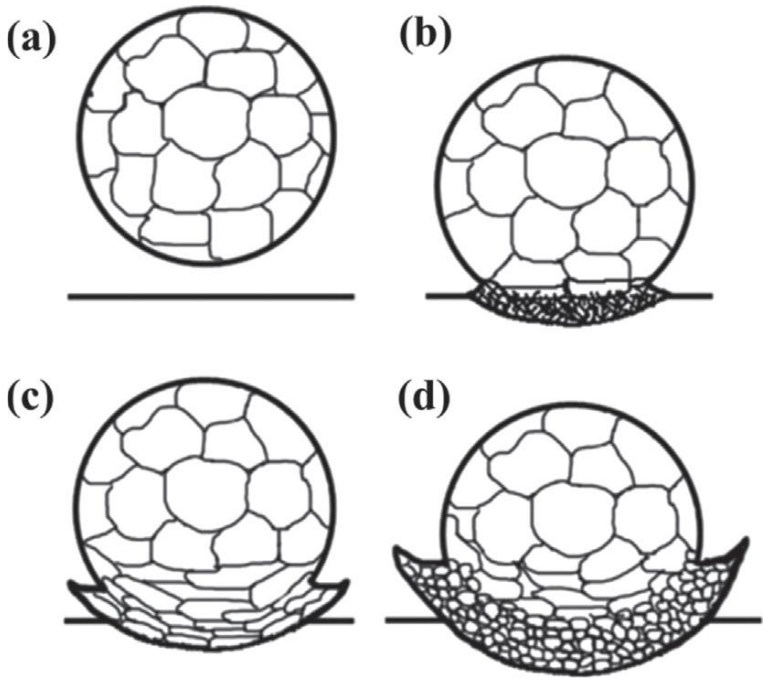

Fig. 3.19: *Schematic of grain refinement by dynamic recrystallization during impact: (a) spraying Ti particle onto the substrate, (b) entanglement of dislocations, (c) formation of dislocation cells (and sub-grains) and re-elongation, and (d) break-up, rotation and recrystallization of sub-grains by thermal softening effects enough to trigger the viscous flow* [125]

When local strains and temperatures exceed a critical value, these sub-grains recrystallize to trigger more viscous flow [125]. Interestingly, they observed two overlapped Ti splats by TEM as shown in Fig. 3.20 [126]. Apart from the grain refinement at the impact interface, the void formed at the impact center by the tamping effect of the succeeding particle was clearly seen. These are expected to affect the particle bonding and improve the mechanical and transport properties of deposits, like thermal and electrical conductivity [126].

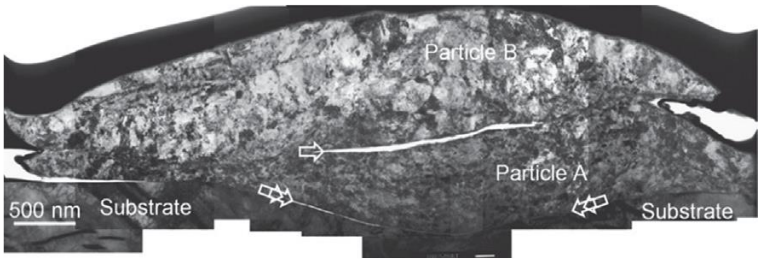

Fig. 3.20: *TEM image of two Ti splats on steel substrate after high velocity impact* [126]*. Single arrow indicates a void formed between particle A and particle B, while two double arrows indicate the boundary of particle A and substrate. Note that compared with the void between particle A and particle B, the void formed between particle A and substrate could be closed by the tamping effect of particle B*

As for Ti6Al4V, the microstructure evolution at the interface region is slightly more complex, not only because of its high strength but also complicated $\alpha + \beta$ phase changes. Usually, the spherical Ti6Al4V particle is predominantly martensitic. The strong thermos-mechanically coupled deformation occurs at the local impact interface. Brit et al. [127] investigated in detail the bonding regions in cold spray Ti6Al4V deposits with both nitrogen and nitrogen-73% helium mixture as propulsive gas using FIB + TEM techniques. As shown in Fig. 3.21 [127], two regions within the deposited particles are identified. The smooth region is argued as transformation near the particle-particle boundary, and the textured region has the broken martensitic lathes and the elongated or distorted grains. There are also nano-grains in the smooth region as that has been reported for cold spray Ti. Surely the strong thermomechanical coupling at the impact interface zone promotes these phenomena and in turn facilitates the bonding.

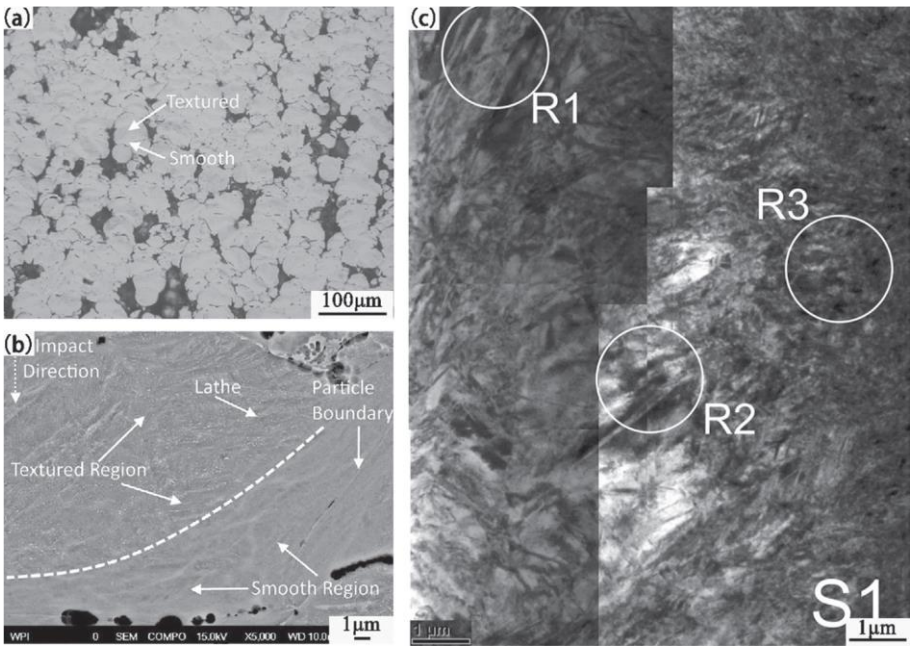

Fig. 3.21: *Microstructure characterization of the cold-sprayed Ti6Al4V deposit with nitrogen at 790 °C and 3.6 MPa: (a) OM image of etched cross section showing small bands of the smooth transformation region, (b) SEM-BEI of cross-section showing in detail the smooth region and the textured region, (c) TEM image of sample S1 taken from the particle interface zone showing reveals a disorganized, broken structure (R1), an organized, stacked lamellar structure (R2) and a fine-grained structure (R3)* [127]

3.3.2 Bonding strength of cold spray Ti and its alloys deposits

When one mentioned the bonding strength of a deposit or coating, it may mean the adhesion strength between the deposit and substrate, or the cohesion strength of the deposit itself. From

the above bonding mechanism discussion, many factors influence the bonding strength of cold spray deposits, e.g. parameters causing higher particle velocity and temperature but within the window of deposition, substrate surface preparation and preheating temperature. Another important factor influencing the bonding strength that is worth mentioning is the residual stress generated concurrently with the bonding process during cold spray Ti and Ti6Al4V particles, which usually decreases the bonding strength in most cases.

3.3.2.1 Adhesion strength

Common macroscopic adhesion strength is tested by the pull-off method which is initially used for adhesion strength testing of thermal sprayed coatings, where epoxy resin is used to glue the cold spray deposits (with substrate) to another couple sample. The macroscopic adhesion strength of Ti- based alloy is relatively low. For example, the adhesion strength between the Ti6Al4V deposit and substrate ranged from 15 to 75 MPa as shown in Fig. 3.22. In addition, the macroscopic adhesion strength of the Ti6Al4V deposit is negatively correlated with the porosity of the deposit.

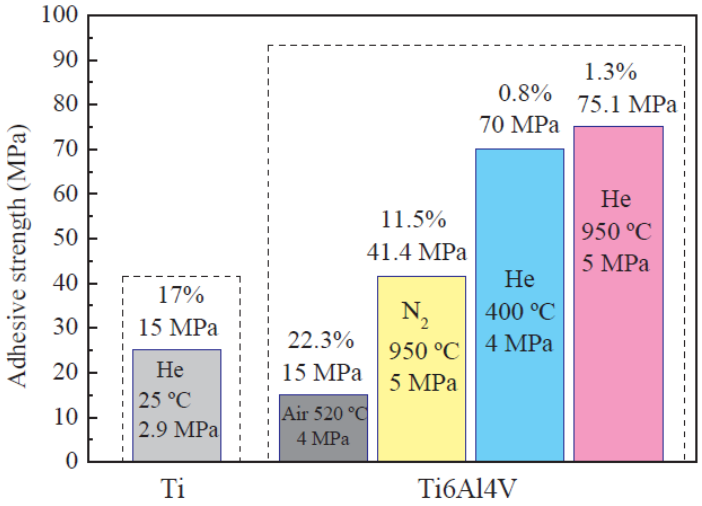

Fig. 3.22: *Macroscopic adhesion strength between Ti or Ti6Al4V deposit and substrate and porosity under different cold spray conditions*

Some researchers also used the micro-scratching method to test the adhesion strength of a splat onto substrate, which could be referred to as the microscopic adhesion strength. After scratching tests, the adhesion value is calculated by a developed equation [113], [128]:

$$Adhesion\ Stregth\ [MPa] = \frac{F_{TPeek}[mN] - F_{TBaseline}[mN]}{\pi(\frac{d[\mu m]}{2})^2} * 1000 \qquad (3.2)$$

where F_{TPeek} and $F_{TBaseline}$ is the peak and baseline tangential force in the recorded force curve, respectively, d is the splat diameter. In the scratching tests, failure through the splat is associated with a good bonding interface, while failure at the interface is typically associated with a general bond (not high enough, sometimes week).

The microscopic adhesion strength of cold spray Ti-based splats on the Ti-based substrates is shown in Fig. 3.23 [113], [129]. It is clear that the microscopic adhesion strength increases with the increase of particle impact velocity (Fig. 3.23(a) and (b)). Generally, the microscopic adhesion strength of Ti6Al4V splats is lower than that of Ti splats. In addition, it is also found that the microscopic adhesion strength of the splats deposited by using helium as propulsive gas is higher than that of the splats made with nitrogen as propulsive gas (Fig. 3.23(a) and (b)) [113], [129].

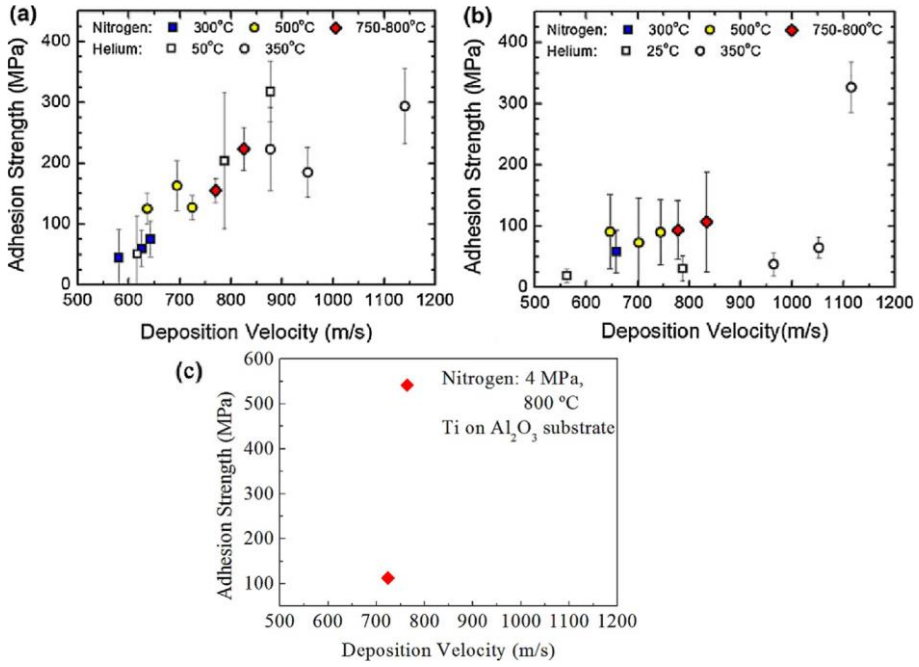

Fig. 3.23: *The microscopic adhesion strength of Ti and Ti6Al4V splats under different cold spray conditions: (a) Ti particles on Ti substrate, (b) Ti6Al4V particles on Ti6Al4V substrates, and (c) Ti particles on Al2O3 substrates* [113], [129]

Furthermore, they also found that the preheating of substrate could significantly improve the microscopic adhesion strength of the splats as shown in Fig. 3.24 [113], [129]. It should be pointed out that the microscopic adhesion strength of the splats is much higher than that of the macroscopic adhesion strength obtained from the pull-off tests, which may suggest that the bonding of the first layer is higher than that among the following layers.

The data were replotted in Fig. 3.23(c) for comparison, suggesting that the deposition of Ti particles on a ceramic substrate may have a better adhesion than on the metal substrate.

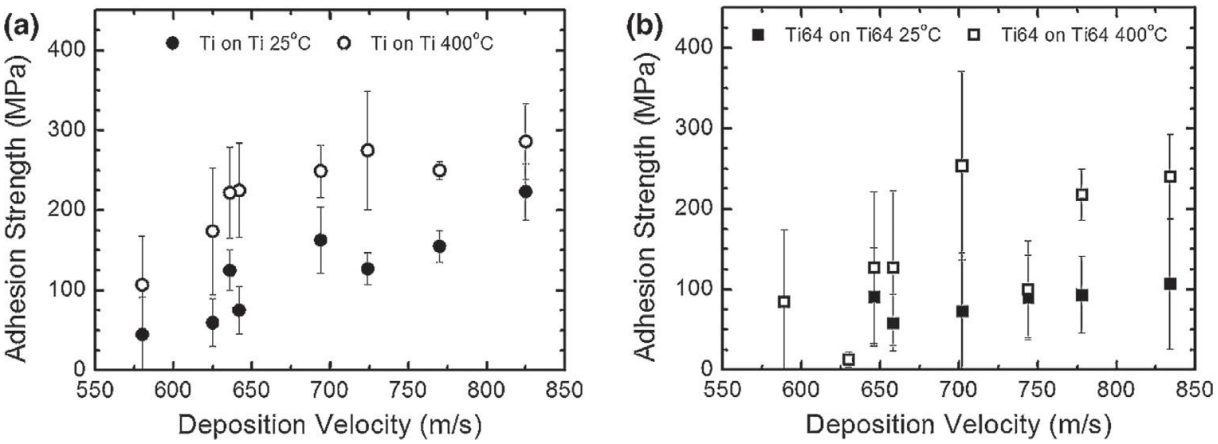

Fig. 3.24: *The microscopic adhesion strength as a function of particle impact velocity for Ti (a) and Ti6Al4V (b) splats by preheating the substrates* [113], [129]

3.3.2.2 Cohesion strength

Cohesion strength refers to the bonding strength of the deposit itself. One can get this value by a tensile test of the free-standing cold spray deposit, where the tensile strength can be regarded as the cohesion strength of the cold spray deposits. According to literature [93], [130], [131], the cohesion strength of a cold spray deposit presents an anisotropic feature. However, very few cohesion strength data were reported for cold spray Ti and its alloys. The cohesion strength of Ti and Ti6Al4V deposits under different cold spray conditions are shown in Fig. 3.25. Generally, the cohesion strength of Ti-based deposits is also relatively low; using helium as the propulsive gas could improve the cohesion strength to some extent but still not too much.

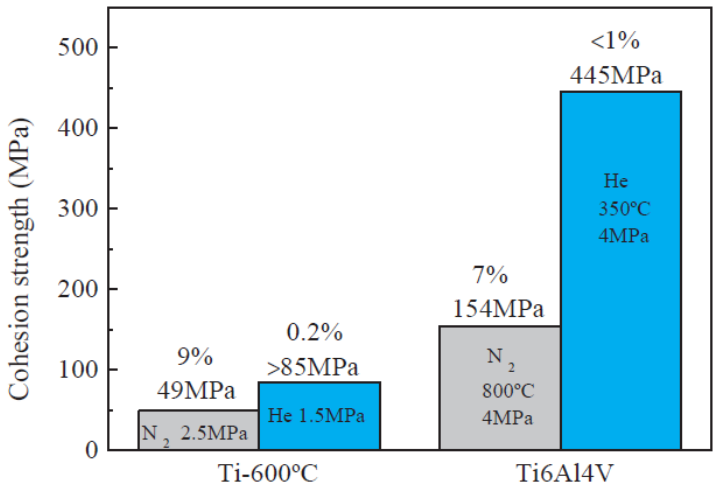

Fig. 3.25: *Cohesion strength of Ti and Ti6Al4V deposits under different cold spray parameters*

4 Materials and Method

The analysis of the literature showed that the gas temperature and pressure strongly affect the quality of the cold sprayed coatings. For this reason, it is important to carefully identify a proper deposition window, where these parameters should be varied, in order to obtain deposits with good mechanical properties in terms of low porosity, high adhesion strength and good tribological performance.

This last consideration has led the author to carried out a first experimental campaign with the purpose to identify, starting from literature data, the best combination of process parameters for Stellite-6 as reported in detail in the first section of this chapter.

After that, a second experimental investigation was carried out by introducing a further process parameter, i.e. traverse speed, together with higher energy deposition parameters, i.e. gas temperature and pressure, as reported in the second section of this chapter.

In the third section is described the strategy adopted to evaluate the tribological behavior of optimized Stellite-6 coating in dry sliding condition.

Finally, the mechanical and vacuum properties of pure titanium coatings have been analyzed, as described in section four, in order to demonstrate the suitability of this technology for ultra-high vacuum application.

4.1 Development of parameter window for deposition of Stellite-6

4.1.1 Coating process

All coatings tested during the activities were made using a high pressure CGDS equipment (Impact Spray System 5/11, Impact Innovation, Germany). A commercial Stellite-6 powder (Diamalloy 4060NS, Oerlikon Metco, Switzerland) obtained by gas-atomization process, with particle size of $-45 + 15\ \mu m$, was employed as feedstock. Coatings were deposited onto stainless steel (*AISI 304*) plates. The sample surfaces were previously degreased in acetone

ultrasonic bath. As preliminary investigation, the values of the main process parameters, i.e. traverse speed (v), temperature (T) and gas pressure (p), were identified based on literature results [132], [133] and preliminary tests, while an experimental campaign was planned, in order to investigate the effect of the gas stagnation temperature and pressure on the quality of the coating. Several deposition runs were carried out, varying such process parameters in the ranges $800 - 970\ °C$ and $3.5 - 4\ MPa$, respectively. All the other process parameters were kept constant. In particular, stand-off distance was set to $20\ mm$ and traverse speed to $300\ mm/s$; all the samples were coated with three subsequent passes. In Table 4.1 are reported the combinations of process parameters used for preliminary investigations.

Table 4.1: Combination of process parameters used for preliminary investigations

Set ID	Temperature (°C)	Pressure (MPa)
1	800	3.8
2	900	3.5
3	900	3.8
4	970	4.0

4.1.2 Micrographic observations and hardness tests

In order to evaluate the quality of the so obtained coatings as a function of the spraying parameters, samples were cut, embedded in resin and polished to observe their cross section by Scanning Electron Microscopy apparatus (JSM 6480L, JEOL, Japan).

Hardness measurements were carried out on coating samples deposited by using a gas temperature of $970\ °C$ and a pressure of $4\ MPa$. A micro-hardness tester (MHT, CSM Instruments, Switzerland) equipped with a Vickers diamond tip was used, while a matrix of 100 micro-indentations was made on the top surface. Samples were previously cold mounted and, with the aim of investigate the non-homogeneous mechanical properties of the coatings at the micro-scale, a low value of the indentation load was chosen, in particular a normal force F_n equal to $1000\ mN$ was selected.

4.1.3 Wear experiments

Wear properties of the coatings were measured by pin-on-disk experiments (Tribometer, CSM, Switzerland) according to ASTM G99-03 [134]. Also in this case, a gas temperature of $970\ °C$ and a pressure of $4\ MPa$ were used to coat the specimens for the tests.

Circular samples with a diameter $d = 50\,mm$ and a thickness $t = 5\,mm$ were used. Before testing, the coated samples were grinded in order to obtain a flat surface characterized by a surface roughness approximately equal to $1\,\mu m$ ($Ra = 1.26 \pm 0.34\,\mu m$), with the purpose to replicate a contact system typically employed in several industrial fields. All tests were carried out at an environment temperature around $25\,°C$ and a humidity around 20%. A $6\,mm$ diameter AlO_3 ball, a sliding speed of $0.06\,m/s$ was used as a counterpart, a track radius of $12\,mm$ and a sliding distance equal to $1000\,m$ were selected. Two different values of the normal load were chosen: $5\,N$ and $10\,N$. The friction coefficient was measured during all tests.
The wear rate W ($mm^3\,N^{-1}\,m^{-1}$) was calculated from the volume loss in the wear track [135] obtained from profilometer measurements.

4.2 Effect of process parameters on the properties of Stellite-6 coatings (influence of the traverse speed)

4.2.1 Modeling

Preliminary studies revealed that high energy parameters are required for obtaining good deposits of Stellite-6 alloy, due to its high yield strength and melting point. Moreover, since the adhesion mechanism are strictly linked to the particle temperature and particle velocity [4], the method proposed by Assadi [27] was employed, with the purpose of defining the deposition window. In particular, an 1D isentropic model that simulate the gas flow through the nozzle was used to calculate the gas temperature and velocity profiles inside the nozzle. The differential equation of drag force exerted by the gas on the particles was used to evaluate the particle velocity at the nozzle exit, where the drag coefficient CD was set at 0.65 since the particle spherical shape. The equations system proposed by Stoltenhoff et al. and Wong et al. [3], [121] was used to calculate the particle temperature at the nozzle exit. All data used in this phase are reported in Table 4.2.

Table 4.2: *Input parameters for the numerical calculations*

Symbol	Description
D* [mm]	Nozzle diameter at the throat
D_e [mm]	Nozzle diameter at the exit
D_i [mm]	Nozzle diameter at the inlet
L_c [mm]	Length of the converging part of the nozzle
L_d [mm]	Length of the diverging part of the nozzle
T_o [K]	Gas stagnation temperature
p_o [MPa]	Gas stagnation pressure
d_p [μm]	Particle diameter
ρ_p [kg/m^3]	Particle density
c_p [J/K*kg]	Specific heat capacity of the particle

Obviously, this model is not able to consider the effect of the traverse speed. Therefore, in this phase only process gas pressure and temperature are taken into account. Two sets of process parameters, in terms of gas temperature and pressure, were investigated as reported below:

- $Set\ 1$: $970\ °C - 4\ MPa$;
- $Set\ 2$: $1050\ °C - 5\ MPa$.

4.2.2 Deposition trials

Also in this case Diamalloy 4060NS was employed as a feedstock, while on the CGDS equipment a pre-chamber with a length of $135\ mm$ was installed. Nitrogen was used as process gas. In the deposition trials, the process gas pressure and temperature, and traverse speed were varied in the following ranges: $4 - 5\ MPa$, $970 - 1050\ °C$, $5 - 300\ mm/s$, respectively. All the other process parameters were kept constant. In particular, stand-off distance was set equal to $20\ mm$. Two deposition campaign were carried out. The first campaign was devoted to the measurements of the substrate temperature as a function of the process parameters. A stainless steel (*AISI 304*) sheet $350 \times 200 \times 3\ mm$ was used as a substrate and two different deposition areas were chosen; the first one characterized by a dimension of $200 \times 10\ mm$ and the second one by a dimension of $30 \times 10\ mm$. These two areas were chosen in order to evaluate also the effect of the path length followed by the torch on the temperature reached by the substrate during the deposition process. An IR (Infra-Red) thermographic camera (FLIR A615, FLIR

Systems Inc, USA) was installed at a distance equal to 300 mm on the back of the sheet. A schematic representation of the experimental set-up employed is shown in Fig. 4.1. The back surface of the sheet was painted in black by using a thermo-resistant paint, in order to achieve an emissivity coefficient of 0.98 (measured by the thermographic camera, comparing the temperature with a point measurement obtained with a thermocouple).

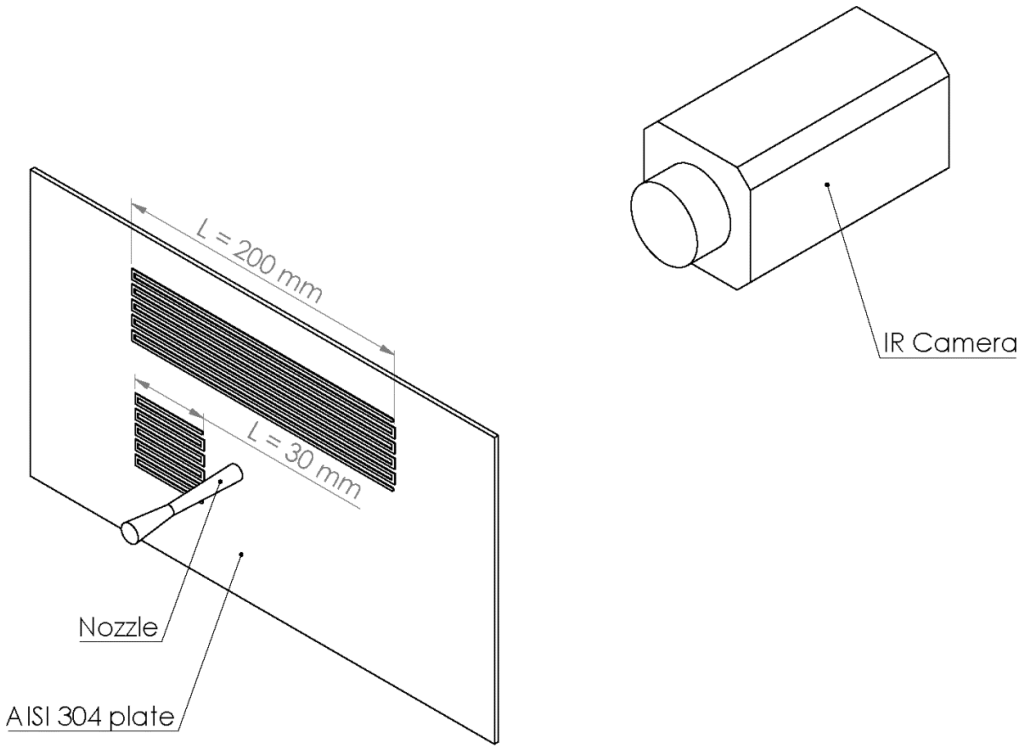

Fig. 4.1: *Schematic diagram of the set-up used in the present study for estimating the substrate temperature during the CGDS process*

Several deposition simulations were performed, in each of these latter the torch scanned a limited region of the plate with 10 parallel passes spaced apart by 1 mm, as in a real deposition. In addition, the effect of the presence of the stellite on the temperature reached by the surface was also evaluated, so same trials were carried out inserting the powder in the gas streaming.
For each trial, the temperature versus time of all the points on the back of the sheet was recorded. The complete experimental plan is reported in Table 4.3. An additional test was carried out to evaluate the maximum temperature that could be reached in the given process conditions, holding the torch in front of the plate, as reported in the last row of Table 4.3.

Table 4.3: Matrix of experimental campaign for substrate temperature estimation

Deposition parameters			Deposition area		
Temperature (°C)	**Pressure (MPa)**	**Traverse speed (mm/s)**	**200x10 mm Without powder**	**30x10 mm Without powder**	**30x10 mm With powder**
970	4	300	✓	✓	✓
970	4	100	✓	✓	×
970	4	30	✓	✓	✓
970	4	5	✓	✓	×
1050	5	300	×	✓	✓
1050	5	30	×	✓	✓
970	4	0	×	✓	×

In the second deposition campaign, six sets of coated samples were produced, spraying on stainless steel (*AISI 304*) flat $50 \times 30 \times 3\ mm$ substrates. Before the deposition, the samples were degreased in acetone ultrasonic bath. The process parameters used to coat the six samples sets are reported in Table 4.4.

Table 4.4: Samples ID and deposition parameters

Sample ID	Temperature (°C)	Pressure (MPa)	Traverse speed (mm/s)
1.1	970	4	300
1.2	970	4	100
1.3	970	4	30
1.4	970	4	5
2.1	1050	5	300
2.3	1050	5	30

It should be specified that each sample has been coated with just one pass with the exception of these samples obtained at $T = 1050\,°C$, $p = 5\,MPa$ and $v = 300\,mm/s$, where three runs were carried out. This approach was necessary because with this set of spraying parameters the coating thickness would be too thin for the following experimental activities.

4.2.3 Coating characterization

A sample for each deposition set was cut, embedded in resin and polished, to observe its cross section by scanning electron microscopy (LEO 1550-ZEISS, McQuairie, UK).

Porosity content was estimated using the image analysis software Image J. However, the limited number of analyzed fields per sample $(2-3)$ is not sufficient to have a statistical estimate that complies with the standard ASTM E2109 [136] ($n > 20$). Therefore, the reported values should be considered as indicative.

Hardness tests were carried out on nano- and micro-scale using in both the cases instrumented indenters. The characterization on micro-scale [137], [138] was carried out using a micro-indenter (MHT, CSM Instruments, Switzerland) equipped with a Vickers diamond tip. A matrix of 100 micro-indentations was made on the top surface using a normal force F_n equal to $1000\ mN$. Mechanical properties, in terms of hardness and reduced Young's modulus, were analyzed because these latter can be considered as reliable indicators of the wear resistance in a coating.

The characterization at the nano-scale [138]–[140] was carried out on the cross section, using a nano-indenter (NHT, CSM Instruments, Switzerland) equipped with a Berkovich diamond tip. An indentation load equal to $50\ mN$ was chosen for the tests because a low value of penetration load on the cross section allows to obtain specific information about work hardening occurring in the strained material, i.e. particles of which coating is made. Moreover, nano-indentations on the cross section are able to identify possible inhomogeneities along the thickness of the coating. With regard the number of indentations, it depends on the thickness. The matrix for each sample was characterized by a spacing of $40 \times 40\ \mu m$ and a number of indentations of $5 \times$ "N", where "N" is between 10 and 25 depending on the thickness of the obtained coating, which depends in turn on the traverse speed.

A typical force-displacement curve obtained from instrumented indentation is illustrated in Fig. 4.2. Indentation data were used to estimate hardness and Young's modulus.

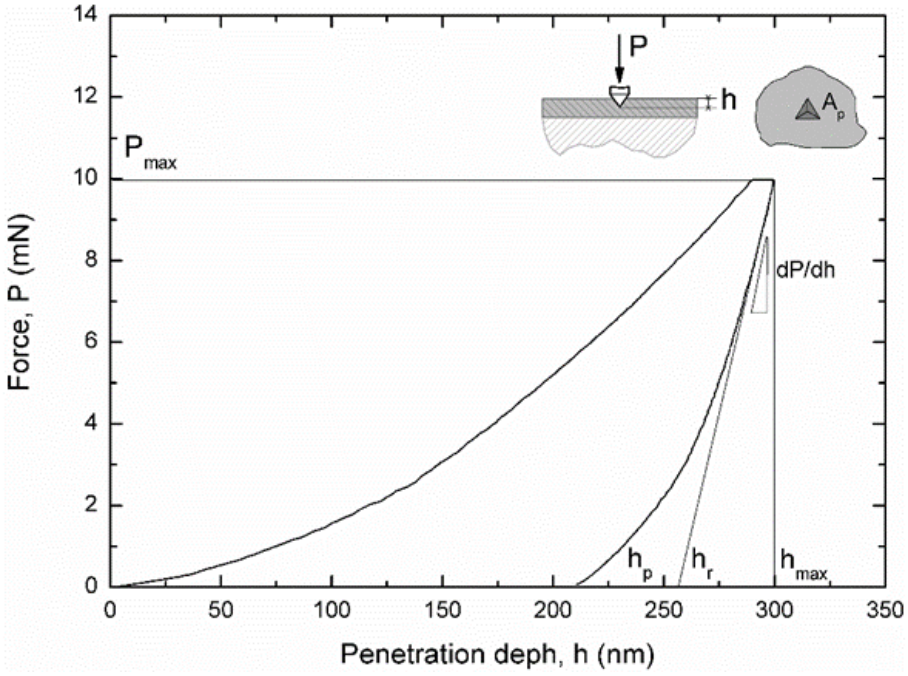

Fig. 4.2: *Instrumented nano-indentation curve: indentation force vs penetration depth*

The reduced Young's modulus (E_r) was calculated from the contact stiffness ($S = dP/dh$), that is the slope of the initial path of the unloading curve (see Fig. 4.2), according to the standard ISO 14577-1 (2002) [141], based on the Oliver and Pharr (1992) method [142]:

$$E_r = \frac{1}{2\beta}\sqrt{\frac{\pi}{A_p(h_p)}}S \tag{4.1}$$

Where A_p is the projected area of the indent after indentation, that is obtained geometrically as a function of the residual depth h_p, dP/dh is calculated in the range $0.7 - 0.95\ P_{max}$ and β is a constant equal to 1.034 for the Berkovich tip. The indentation modulus of the material, E_{IT}, can be obtained from E_r by considering the elastic properties of the indenter tip ($E_i = 1140\ GPa$ and $\nu_i = 0.07$ for diamond):

$$E_{IT} = (1 - \nu^2)\left(\frac{1}{E_r} - \frac{1 - \nu_i^2}{E_i}\right)^{-1} \tag{4.2}$$

Additional parameters can be obtained from the force-displacement curve to estimate the competition between elastic and plastic phenomena, i.e. the elastic work (W_{el}, the area below the unloading path in Fig. 4.2) and the plastic work (W_{pl}, the area between loading and unloading curves).

Tribological properties were evaluated by pin-on-disk experiments, according to ASTM G99-03 [134]; a tribometer from CSM (Switzerland) was used as reported in the previous section. For these experiments the sliding speed was imposed equal to $0.06\ m/s$, the sliding distance was set equal to $2000\ m$ and a normal load of $5\ N$ was imposed. Two values of the radius track were chosen: 8 and $20\ mm$ respectively. The friction coefficient was recorded during the test, while the wear coefficient W ($mm3/Nm$) was calculated from the volume loss in the wear track, measure by a profilometer equipment as proposed by Christian [135].

4.3 Tribological behavior of cold sprayed Stellite-6 during reciprocated dry sliding

With the purpose to better understand the nature of wear mechanisms that affect the cold sprayed Stellite-6 coatings in dry sliding conditions, a specific experimental campaign was carried out. In particular, a reciprocating sliding condition was chosen, whereas the sliding geometry was cylindrical area-on-flat type.

4.3.1 Characterization

Spraying conditions were optimized as reported in the previous section and were as follows: gas temperature and pressure equal to $970\ °C$ and $4\ MPa$ respectively, stand-off distance equal to $20\ mm$, while traverse speed was set equal to $300\ mm/s$. Coating was obtained from three spraying layers and its cross-sections were mounted using epoxy resin, grinded using wet SiC grinding papers, and polished using diamond solution and silica both with polishing cloths. The samples were examined by optical microscope (DM4000 M, Leica, Germany) equipped with a high resolution camera (MC190 HD, Leica, Germany).

Microscopic material properties were characterized using the nano-indentation method. A nano-indenter (NHT, CSM Instruments, Switzerland) equipped with a Berkovich diamond tip was used in all cases controlled up to a load of $50\ mN$ and a 10 by 10 indentation map was taken with a $30\ \mu m$ spacing between indents.

4.3.2 Wear tests

The experimental tests were carried out on a reciprocating sliding test rig, i.e. TE77 (Phoenix Tribology, Berkshire, UK) in dry room condition, i.e. $T = 25\ °C$ and $RH = 40\ \%$. A schematic depiction of the test equipment can be seen in Fig. 4.3.

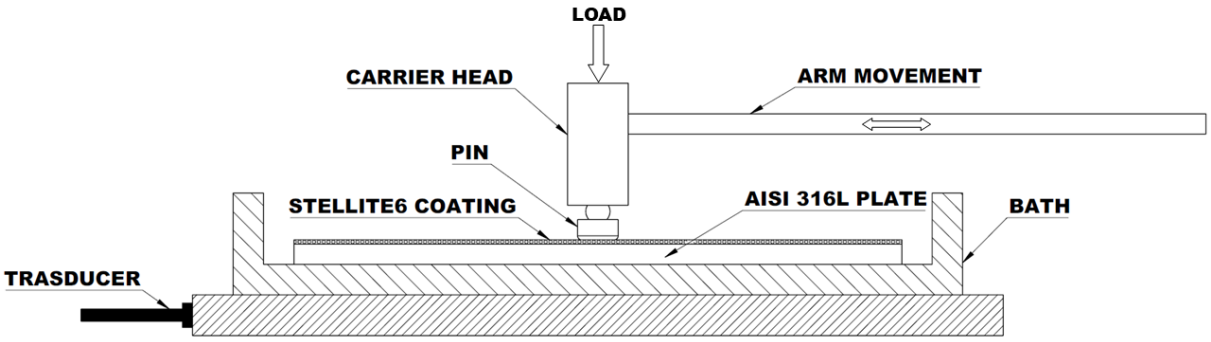

Fig. 4.3: *Schematic depiction of the experimental equipment*

Frictional data, i.e. the evolution of coefficient of friction, were recorded using a transducer connected to the TE77 rig. The wear tests were performed in order to evaluate the influence of the sliding speed and of the applied load on the wear mechanisms. The proposed experimental campaign has been developed in order to in deep investigate the wear performance of stellite-6 coating in all the range of low contact pressure, i.e. $0.5 - 5\ MPa$. The full test matrix is reported in Table 4.5.

Table 4.5: *Range of parameters used in different combinations for wear tests*

Load (N)	Pressure (MPa)	Velocity (m/s)	Distance (m)
100	2	0.1	500
150	3		
200	4		
250	5		
25	0.5	0.5	
100	2		
150	3		
200	4		
250	5		

The sliding geometry chosen was an *"area-on-flat"* with a cylindrical pin of $7.94\ mm$ $(5/16")$ diameter realized in chromium *AISI 52100* steel. This latter material was hardened to $60 - 67$ Rockwell Scale equivalent to $700 - 900\ HV$ (Vickers Scale). These were slid against plates of dimension $20 \times 60 \times 3\ mm$. Each test surface was diamond lapped to obtaining a surface finish of $0.2\ \mu m\ \pm\ 0.05$ average roughness (Ra), in order to replicate a contact system that reflect a specific application within industry. Surface roughness was measured using a profilometer used was a Taylor-Hobson Talysurf. Post-wear characterization consisted of weight change measurements for the plate and pin. Wear scars were characterized using a light

microscope (DM4000 M, Leica, Germany) equipped with a high resolution camera (MC190 HD, Leica, Germany).

4.4 Mechanical and vacuum properties of cold sprayed Ti coatings for ultra-high vacuum applications

Mechanical and vacuum properties of cold sprayed titanium to steel coatings were also analyzed for possible application in ultra high vacuum (UHV) systems at the European Organization for Nuclear Research (CERN). A new generation of high-pressure CGDS equipment was employed with the aim to overcome technical issues usually experienced when dealing with hard material coatings and substrates. These latter are mainly related to poor coating compactness and adhesion to the substrates. These technical issues become even more stringent when dealing with vacuum systems as they could affect the leak tightness and gas release in UHV. They open interesting perspectives for the development of hard and compact coatings in high demanding applications [143], including vacuum systems for equipment used in high-energy physics, providing low outgassing and leak rate are achieved. To this aim, activities have been undertaken at CERN to assess the possible use of CGDS as a viable technology for future accelerator. In fact, CGDS copper coatings is being studied for applications as thermal links to facilitate heat transfer generated by synchrotron radiations in the Future Circular Collider (FCC) beam screens [144]. In parallel, a study concerning the use of titanium coatings as heating elements for bakeout inside or outside vacuum vessels is ongoing.

So, with the aim to assess CGDS as a technique for manufacturing of coated/layered components to be used in the UHV systems of the accelerator, grade-1 titanium coatings on *AISI 316L* stainless-steel substrates were manufactured and analyzed.

4.4.1 Materials and coatings process

A commercially pure titanium powder (TLS-Technik, Germany) was employed as feedstock material. It was obtained by an atomization process and the particle size was about $45\ \mu m$. The Ti coatings were deposited onto *AISI 316L* austenitic stainless steel, which is frequently used as structural material for vacuum components at CERN. The sample surfaces were degreased in acetone ultrasonic bath before coating. The high pressure CGDS equipment (Impact Spray System 5/11, Impact Innovations, Germany) was used and nitrogen was employed as propellant gas.

Preliminary studies were carried out to identify optimal operational gas pressure (p) and temperature (T) as shown in Table 4.6. Other coating parameters were kept constant, such as the stand-off distance ($20\ mm$), the traverse speed ($300\ mm/s$) and the traverse deposition step ($1\ mm$). The samples were coated by three subsequent passes. Table 4.6 reports the total thickness for the analyzed combinations of coating parameters.

Table 4.6: *Combination of coating parameters and total thickness (μm) obtained by three passes*

	Pressure (MPa)		
Gas temperature T (°C)	**3.4**	**4.0**	**5.0**
350	620±31	502±26	-
400	690±39	653±24	-
450	612±37		-
970	-	567±20	-
1050	-	-	547±20

The lower values of the temperature ($350°\ C$, $400°\ C$ and $450°\ C$) and pressure (3.4 MPa and 4.0 MPa) in Table 4.6 were taken from literature studies in which helium was the propellant gas [101], [145]. The combinations of higher temperatures ($970\ °C$ and $1050\ °C$) and pressures (4.0 MPa and 5.0 MPa) are typical for the new generation of high-pressure CGDS systems and were found to provide good depositions results by using nitrogen as carrier gas [107], [146].

4.4.2 Mechanical characterization

4.4.2.1 Microscopic investigations and indentation tests

The samples were cold mounted and polished to analyze the effects of process parameters by microscopic observations and indentation tests. The cross sections were firstly observed by an optical microscope. Only coatings with apparent good adhesion and low porosity were subsequently analyzed by micro- and nano-indentations (MHT and NHT, CSM Instruments, Switzerland). Instrumented micro indentations were carried out on the top surface of the coatings by using a Vickers diamond tip and a load of $500\ mN$. A matrix of 10×10 points with a spacing of $50\ \mu m$ was made to capture possible material inhomogeneities due to the local powder deposition mechanisms. The evolution of the material properties along the coating thickness was also analyzed by nano-indentation, by using a Berkovich tip and a force of $10\ mN$. A matrix of 13×10 indentation points was made on the cross sections of the coatings,

with a spacing of 40 μm. Finally, local nano-indentations were made at higher indentation loads (100 mN) to obtain intents that have a size comparable with the one of the powder grains. These measurements were carried out both within the splat and at the splat boundaries, to assess the inter-particle interfacial strength.

4.4.2.2 Adhesion tests

Adhesion tests were carried according to the ASTM standard C633 [147]. The method allows to measure the degree of adhesion (bonding strength) of a coating to a substrate or the cohesion strength of the coating. Cylindrical sample made of two pins bonded together, as shown in Fig. 4.4, were tested by a tensile testing machine.

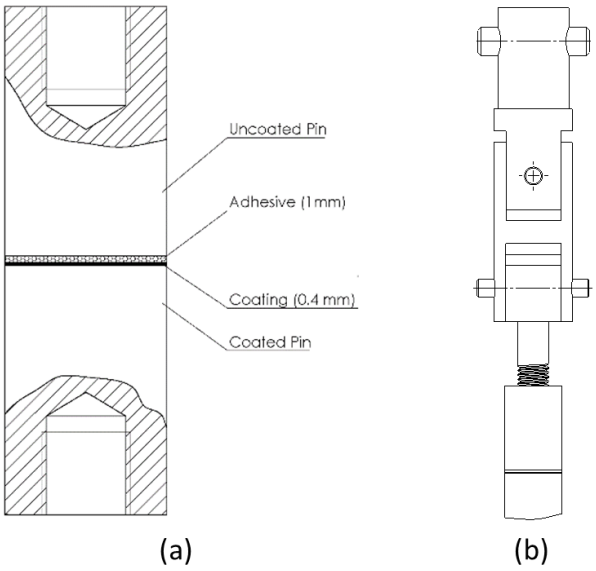

Fig. 4.4: *Sample for adhesion tests: (a) sample geometry and (b) upper part of the self-aligning loading tool (symmetric)*

In particular, one face of the first pin was coated by CGDS and bonded to the uncoated face of the other pin by a structural adhesive with a suitable tensile strength (34 MPa − $DIN\ EN\ ISO\ 527-1$). Care and special fixtures were adopted to allow a precise alignment of the two pins during bonding as well as to control the thickness of the glue ($t = 1\ mm$). The samples were tested by using a self-aligning device to avoid possible eccentric loads or bending moment (see Fig. 4.4). Only optimized coatings were analyzed ($T = 970°\ C$ and $p =$ 4.0 MPa). Six samples, with coating thickness around 500 μm (see Table 4.6), were tested.

4.4.3 Ultra-high vacuum characterization

Vacuum acceptance tests usually consist of outgassing and leak rate measurements [148]. Outgassing rate of different titanium coatings were analyzed using the accumulation-expansion technique. Furthermore, Thermal Programmed Desorption (TPD) tests were carried out on selected samples to better understand results obtained from outgassing tests. An ad-hoc set up was used to assess the leak tightness properties of the coated material, that is to analyze the efficiency of the coating as a gas barrier. A special CERN's standard cleaning procedure was adopted for all samples before testing, to avoid any surface contamination that could influence the material outgassing. Methods and testing conditions are described in the following subsections.

4.4.4 Outgassing tests

The accumulation-expansion method [149] was used to measure the outgassing rate at room temperature for two sets of samples with 300 and 500 μm coating thickness, respectively. The coating parameters are $T = 970\ °C$ and $p = 4.0\ MPa$. The substrates were made of *AISI 316L* steel plates, with size of $200 \times 25 \times 2\ mm^3$. The plates were vacuum fired before coating to reduce the outgassing rate of the substrate. Vacuum firing is usually performed at CERN for austenitic stainless steel components used in UHV. The standard treatment is performed at $950\ °C$ for 2 hours in a vacuum furnace whose ultimate pressure at the temperature of the treatment is of the order of $10^{-6}\ mbar$. Coating was applied on both sides of the plates and accumulation tests were carried out by using a set of four samples simultaneously, to maximize the outgassing rate, resulting in a total surface area of $4 \times 10^2\ cm^2$.

The experimental set-up is schematically depicted in Fig. 4.5. The set of samples is isolated by a variable leak valve (VLV) in a separated vessel where the gas is accumulated for a time Δt. Then the VLV is slowly opened and the quantity of accumulated gas is measured in a test dome by a calibrated residual gas analyzer (RGA). The effective pumping speed acting at the level of the RGA is $22.17\ l \cdot s^{-1}$; it is defined by the conductance of an orifice connecting the test dome and the pumping system. The latter is pumped by a turbomolecular pumping unit and non-evaporable getter (NEG) strip.

The accumulation vessel has an internal surface of approximately $264\ cm^2$; it is made of vacuum-fired $AISI\ 316L$ stainless steel. The VLV is thermally pre-treated to reduce its outgassing rate. The whole system is pumped down and baked for $24\ h$. The bakeout

temperature was 250° C for most of the system, 350° C for RGA and gauges, and 150° C for the accumulation vessel including the samples.

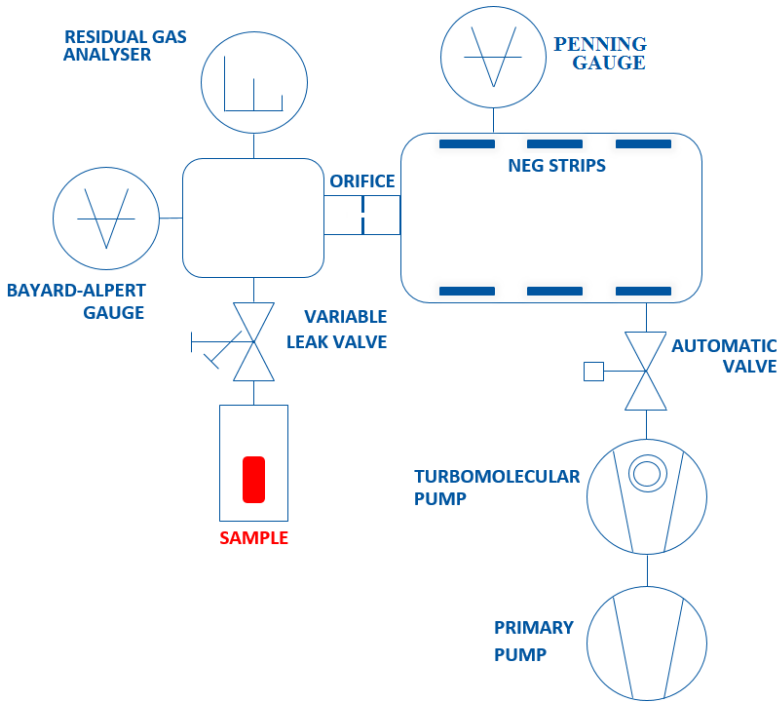

Fig. 4.5: *Schematic drawing of the set up for thermal outgassing measurement by the accumulation-expansion method.*

At least 24 hours after the bakeout, once the system ultimate pressure is achieved, the accumulation starts for different time. For a given Δt, the accumulated gas quantity Q $[mbar \cdot l]$ for the gas of interest is calculated as:

$$Q = C \int_0^{\Delta t} I_{RGA}\ \alpha_{RGA} \tag{4.3}$$

where:

- C is the conductance of the orifice $[l \cdot s^{-1}]$ for the gas of interest
- I_{RGA} is the current recorded for the gas of interest $[A]$
- α_{RGA} is the calibration factor for the gas of interest $[mbar \cdot A^{-1}]$

The quantity Q is plotted as a function of Δt to obtain the outgassing rate q $[mbar \cdot l \cdot s^{-1}]$ from the slope of the linear increase. This method can be applied only if the outgassing rate is constant in the time of accumulation and repumping is negligible. If the outgassing rate of the accumulation vessel and the VLV are negligible, the specific outgassing rate of the samples is obtained dividing Q by the total geometrical surface area of the samples.

4.4.5 Thermal Programmed Desorption tests

TPD was performed using the Hiden TPD Workstation (Hiden Analytical, UK). A ramping rate of $5\ °C/min$ was used to measure gas desorption from $25\ °C$ to $950\ °C$. *AISI 316L* stainless-steel samples ($10 \times 10 \times 2\ mm^3$) coated on one side were used. The plates were vacuum fired before coating; the same coating thicknesses ($300\ \mu m$ and $500\ \mu m$) used for the accumulation-expansion method were tested. Gas concentrations were obtained by integrating the desorption curves.

4.4.6 Leak tightness tests

Leak tightness was measured by a high-sensitivity ($\sim 10 - 11\ mbar \cdot l \cdot s^{-1}$) helium leak detector. As shown in Fig. 4.6, special vacuum chambers were designed and manufactured for the leak tests. One extremity of the chamber is connected to the vacuum pump and to the mass spectrometer by a quick conical connection flange; the coated sample is mounted on the other extremity. An elastomer gasket is used to seal the interface between the vacuum chamber and the sample.

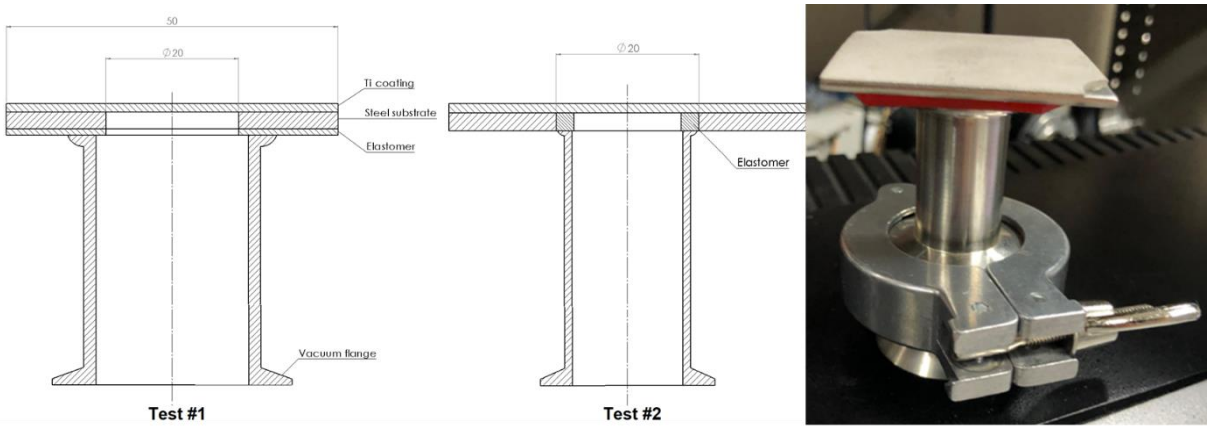

Fig. 4.6: *Setup for leak tightness tests: (a) schematic depiction of two different sample configurations; (b) vacuum chamber assembly*

The size of the *AISI 316L* stainless-steel plates is $50 \times 50 \times 2\ mm^3$. Two coating thicknesses were tested ($500\ \mu m$ and $800\ \mu m$); they were obtained by the optimized parameters $T = 970°\ C$ and $p = 4.0\ MPa$ with different numbers of CGDS passes. To obtain a full trough-thickness titanium layer, a central blind hole ($D = 20\ mm$) on the steel side was obtained by machining the steel substrate up to the coating interface.

Two different tests were performed for each sample, as schematically depicted in Fig. 4.6. In test #1, the samples were mounted onto the vacuum chamber through the steel side. This test configuration allows to detect possible leaks through the coating thickness as well as across the steel/coating interface. In test #2, the interface is not within the vacuum chamber and, therefore, only through-thickness leaks can be detected.

5 Results and discussions

5.1 Development of parameter window for deposition of Stellite-6

Fig. 5.1 shows SEM observations of the cross sections of samples obtained starting from the process parameters reported in Table 4.1. The coatings were carried out by three subsequent deposition layers.

It is noticeable that samples obtained using low values of gas temperature ($800\ °C$), as shown in Fig. 5.1(a), exhibit a remarkable reduction in the thickness of the coating; splats boundaries are clearly visible with their round shape. In fact, total thickness appears to be about $320\ \mu m$ in all conditions except in in the case of gas temperature and pressure were set equal to $800\ °C$ and 3.8 MPa respectively. In this latter case a thickness around $200\ \mu m$.

The presence of pores near the interface is also observable in Fig. 5.1(a), (b) and (c), while a good adhesion to the substrate characterizes the coating obtained at $T = 970\ °C\ and\ p = 4\ MPa$, together with a reduced presence of pores along the thickness.

As shown in Fig. 5.1, process parameters play a very important role on the coating properties [2], [3], [27], [87], [96], [113], [150]. In fact, non-homogeneous mechanical properties of the coatings at the micro-scale are attributed to the extremely complex coating mechanisms and thermo-mechanical loading paths of each particle, starting from the gun nozzle to the impacted surface. In particular, marked plastic flows and material hardening occur during impact of the particles which represent the main driving force for adhesion mechanisms. However, non-homogenous distribution of plastic deformation could occur depending on several factors, including the local morphology and hardness of the impact zone which, in turn, are process parameter sensitive.

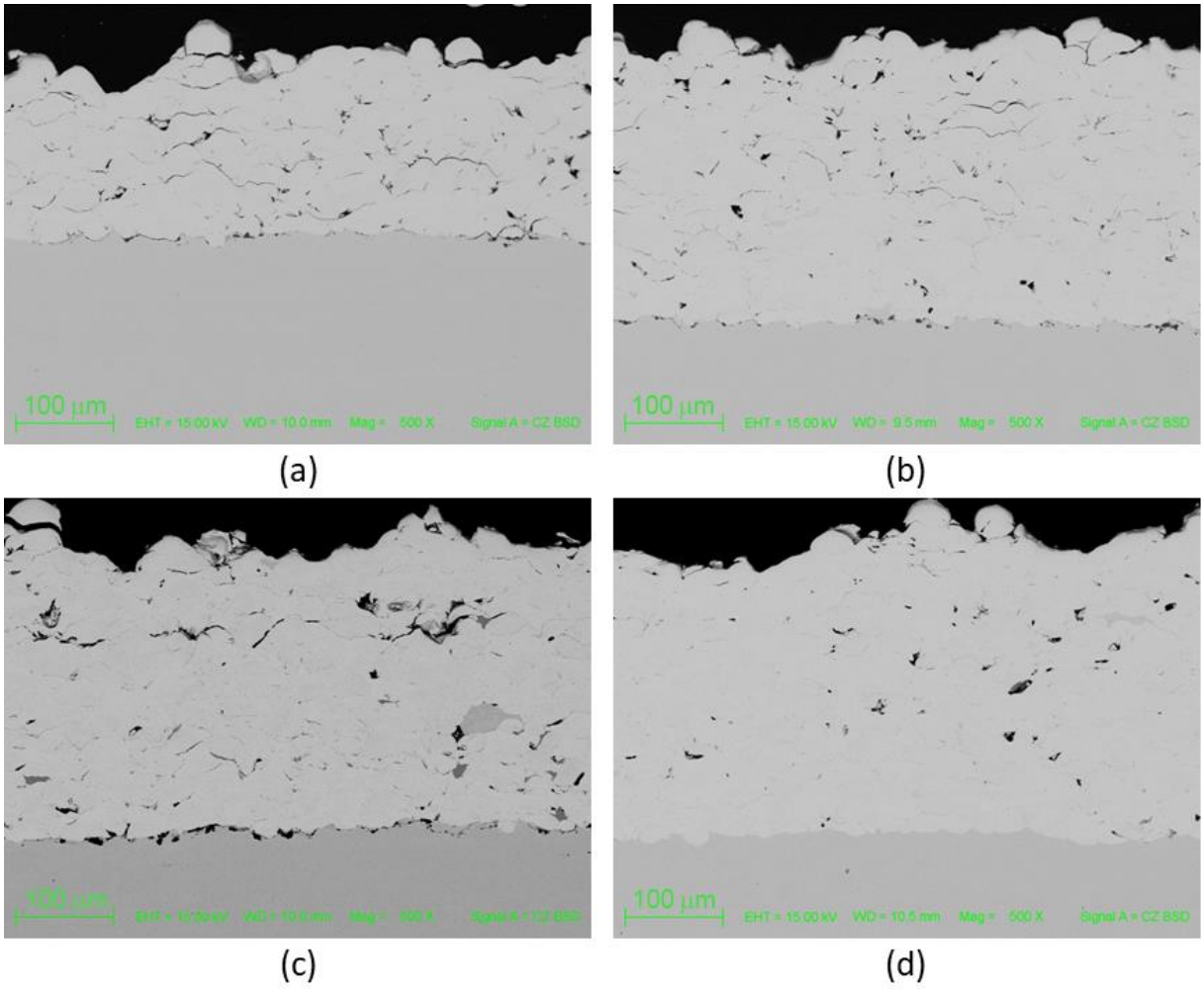

Fig. 5.1: *Cross section of a sample, observed by SEM deposited with: (a) T=800 °C and p=3.8 MPa, (b) T=900 °C and p=3.5 MPa, (c) T=900 °C and p=3.8 MPa, (d) T=970 °C and p=4 MPa*

Local inhomogeneity was also captured from hardness measurements as shown in Fig. 5.2 and Fig. 5.3. In particular, Fig. 5.2 reports the Gauss probability density and cumulative functions of the Vickers micro-hardness ($HV_{0.1}$), obtained from a matrix of 10×10 indentation tests carried out on the top surface of the coated sample, together with the average value and standard deviation ($\mu = 700.3$, $\sigma = 135.0$). The average value is higher than the one of Stellite-6 bulk material (around $400\ HV_{0.1}$ [133]) as a consequence of the large plastic deformation and hardening occurring during particle impact. However, a significantly dispersion was obtained, with a coefficient of variation (σ/μ) around 0.2, even for the optimized samples due to the local mechanisms described above.

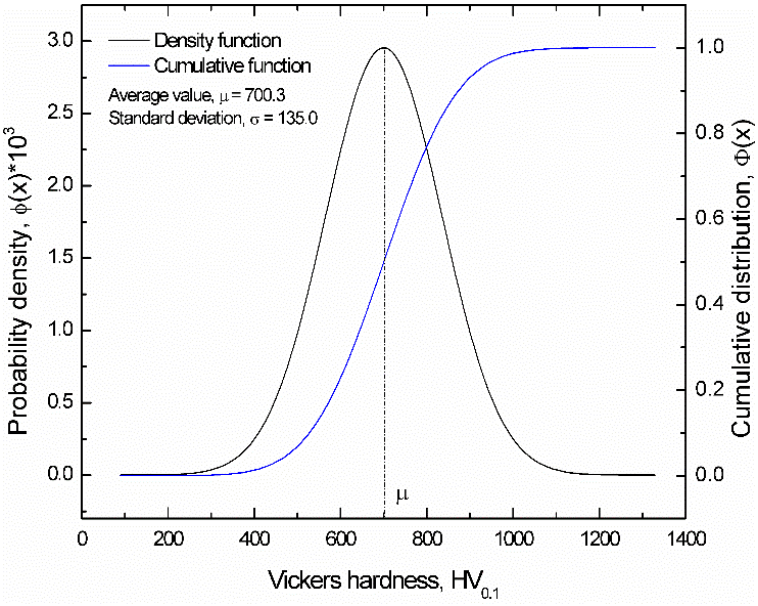

Fig. 5.2: *Gauss probability density ($\Phi(x)$) and cumulative ($\Phi(x)$) functions of the surface Vickers micro-hardness ($HV_{0.1}$) obtained from a matrix of 10×10 indentation points*

These local effects were also analyzed by microscopic observations of the indents as shown in Fig. 5.3. In particular, the figures show three typical indentations in a cracks and porosity free zone (Fig. 5.3(a)), i.e. where one can expect that the coating mechanical properties are good, and near porous zones (Fig. 5.3(b) and (c)). Fig. 5.3(b) shows a possible debonding mechanism, induced by indentation, near the splat boundary. This observation demonstrates that splat boundaries represent a weak point of the coating. Finally, Fig. 5.3(c) represents a typical indentation carried out near a local porosity where, as shown, the indent area is much larger and, consequently, local hardness is significantly reduced.

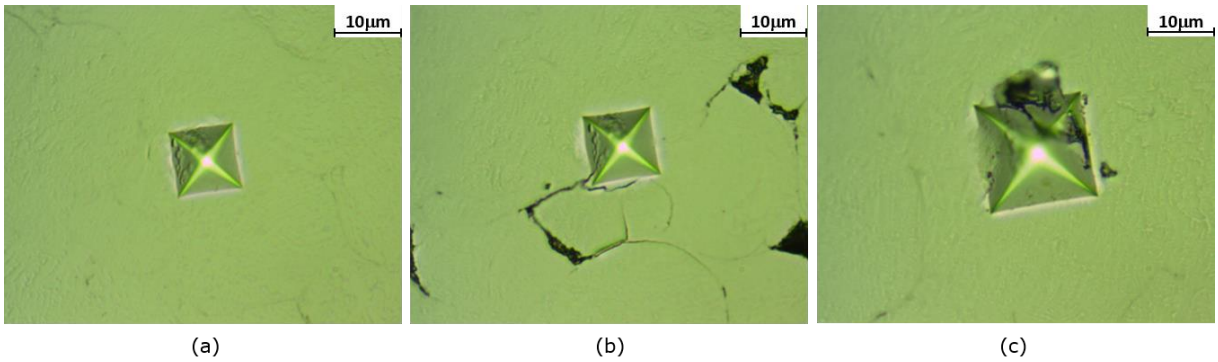

Fig. 5.3: *Microscopic observations of the indents*

Fig. 5.4 reports the evolution of the friction coefficient measured during the wear tests; in particular, Fig. 5.4(a) shows the COF evolution for a test carried out under a normal load equal to 5 N whereas in Fig. 5.4(b) is reported the COF for a test carried out at 10 N.

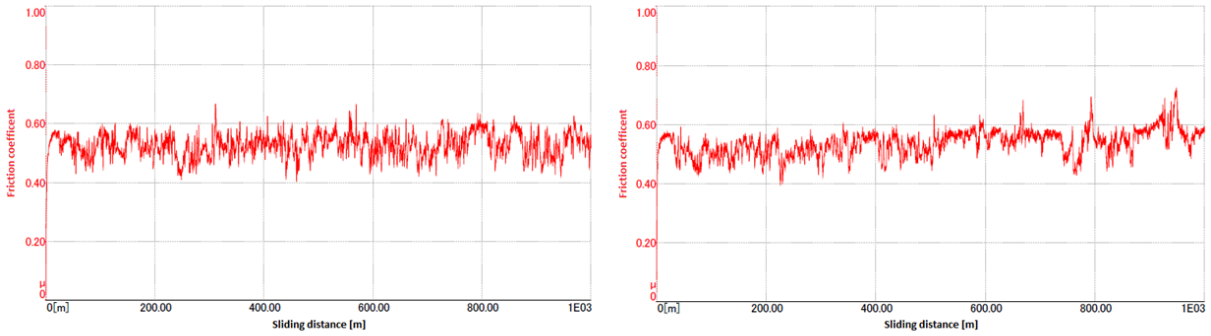

Fig. 5.4: *Friction coefficient of two wear tests carried at 5 N and 10 N respectively*

The same behavior can be observed, as shown further in Fig. 5.5, in which a comparison between the mean value of the friction coefficient for tests carried out under 5 and 10 N is reported. This latter does not show significant difference between the two value of the applied load, and it could indicate that oxidation phenomena do not occur during the tests.

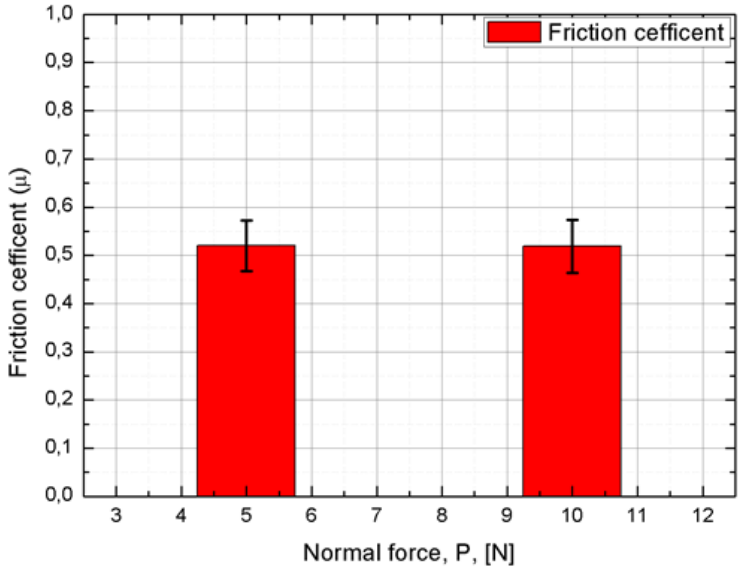

Fig. 5.5: *Mean values of friction coefficient measured during the tests*

In Fig. 5.6 the results of the wear tests are reported, where it is clearly shown that the sample wear rate is higher when the applied load is equal to 5 N. This behavior could be attributed to the local damage phenomena observed also during indentation tests, as shown in Fig. 5.7.

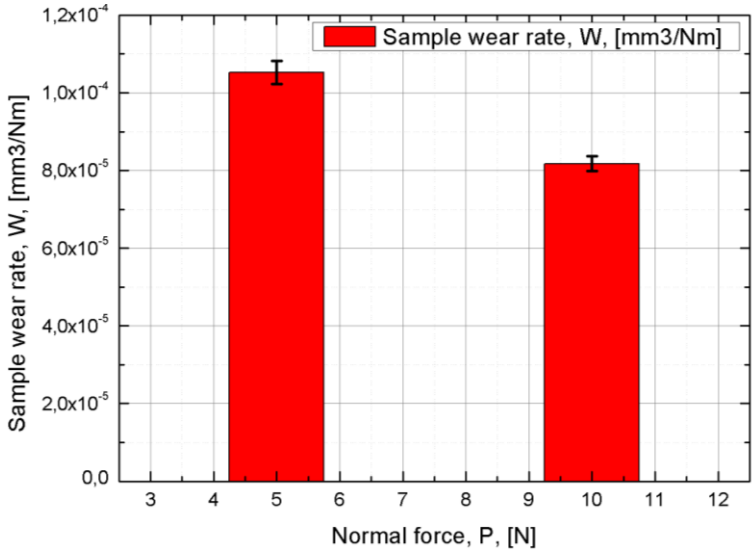

Fig. 5.6: *Mean values of wear rate obtained from tests carried out at 5 N and 10 N*

In particular, pull-out phenomena can be observed in Fig. 5.7(a), where a light micrograph of the wear track under 5 N is shown. Due to these phenomena a third-body abrasive effect can occur, which increase the surface damage. On the contrary, when the applied load is equal to 10 N, the surface of the wear track seems to be less affected by these phenomena, as shown in Fig. 5.7(b).

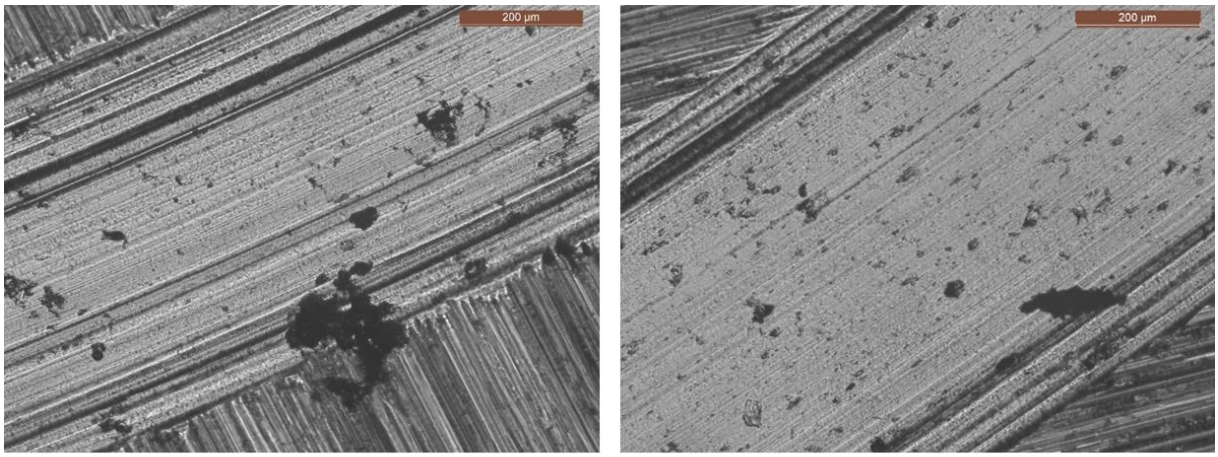

Fig. 5.7: *Light micrograph images of the wear track for the test carried at 5 N and 10 N*

5.2 Effect of process parameters on the properties of Stellite-6 coatings (influence of the traverse speed)

5.2.1 Modeling

Fig. 5.8(a) and (b) report the particle velocity and temperature as a function of particle size in the size range of the powder ($15 - 45\ \mu m$), according to the unidimensional model.

It can be observed that both particle velocity and temperature at the nozzle exit are higher when the second set of spraying parameter is selected. Particle velocity, in the entire size range, as shown in Fig. 5.8(a), is around $60\ m/s$ greater if $set\ \#2$ was chosen compared to the velocity reached when $set\ \#1$ was adopted. Regarding particle temperature at the nozzle exit, its values as a function of the particle size for both sets of spraying parameters are reported in Fig. 5.8(b): the influence of process parameters on the temperature is more significant for the largest particles; in fact, comparing the results for $set\ \#1$ and $set\ \#2$, it can be observed an increment equal to $50\ °C$ for the particles with a diameter of $15\ \mu m$ and equal to $90\ °C$ for the particles with a diameter of $45\ \mu m$. This effect is well known in literature, and has been observed by other authors on different materials [151]. It depends on the greater thermal and kinetic inertia of the largest particles, which are less affected by heat exchange with the colder gas downstream of the nozzle throat.

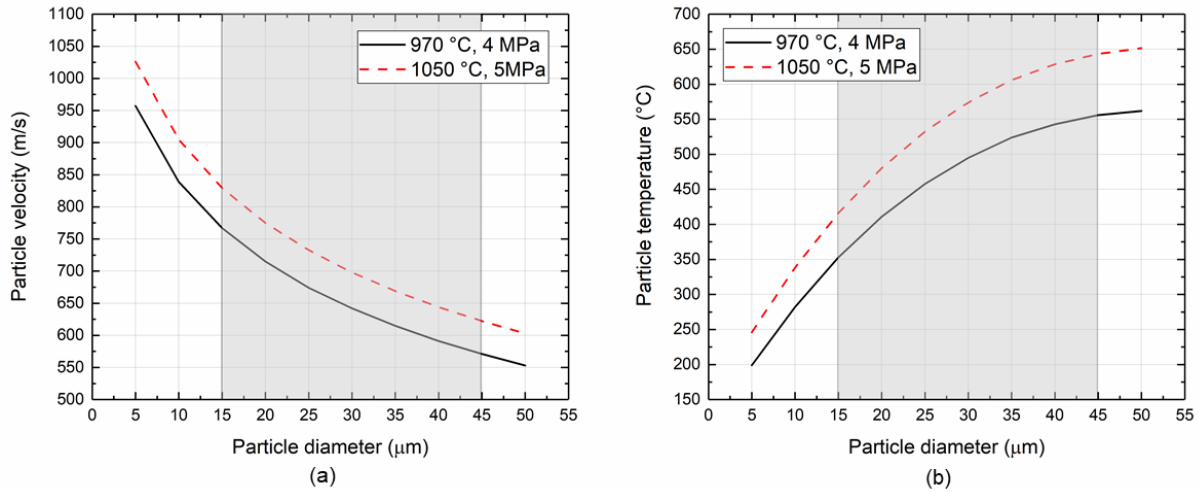

Fig. 5.8: *Estimated variation of particle velocity (a) and particle temperature (b) as a function of particle size in the size range of the powder (15 – 45 μm) according to the unidimensional model*

5.2.2 Deposition trials

The first campaign was devoted to measure the temperature of the substrate as a function of spraying parameters as reported in the previous section, due to the possibility of reach a different temperature depending on the length of the coating surface. In Fig. 5.9(a), it is reported the measured surface temperature, on the back side of the plate, as a function of the time when the torch was kept fixed in front of the steel plate; due to the relatively high conductivity of the steel and the small thickness of the sheet, it is possible to conclude that measured temperature can be approximated with the substrate temperature. An upper bound equal to $670\ °C$ was found reached after 15 seconds for the $set\ \#1$ of the investigated spraying parameters. This allow to estimate the maximum value of the substrate temperature that can be achieved when the temperature and pressure of the process gas were set equal to $970\ °C$ and $4\ MPa$ respectively.

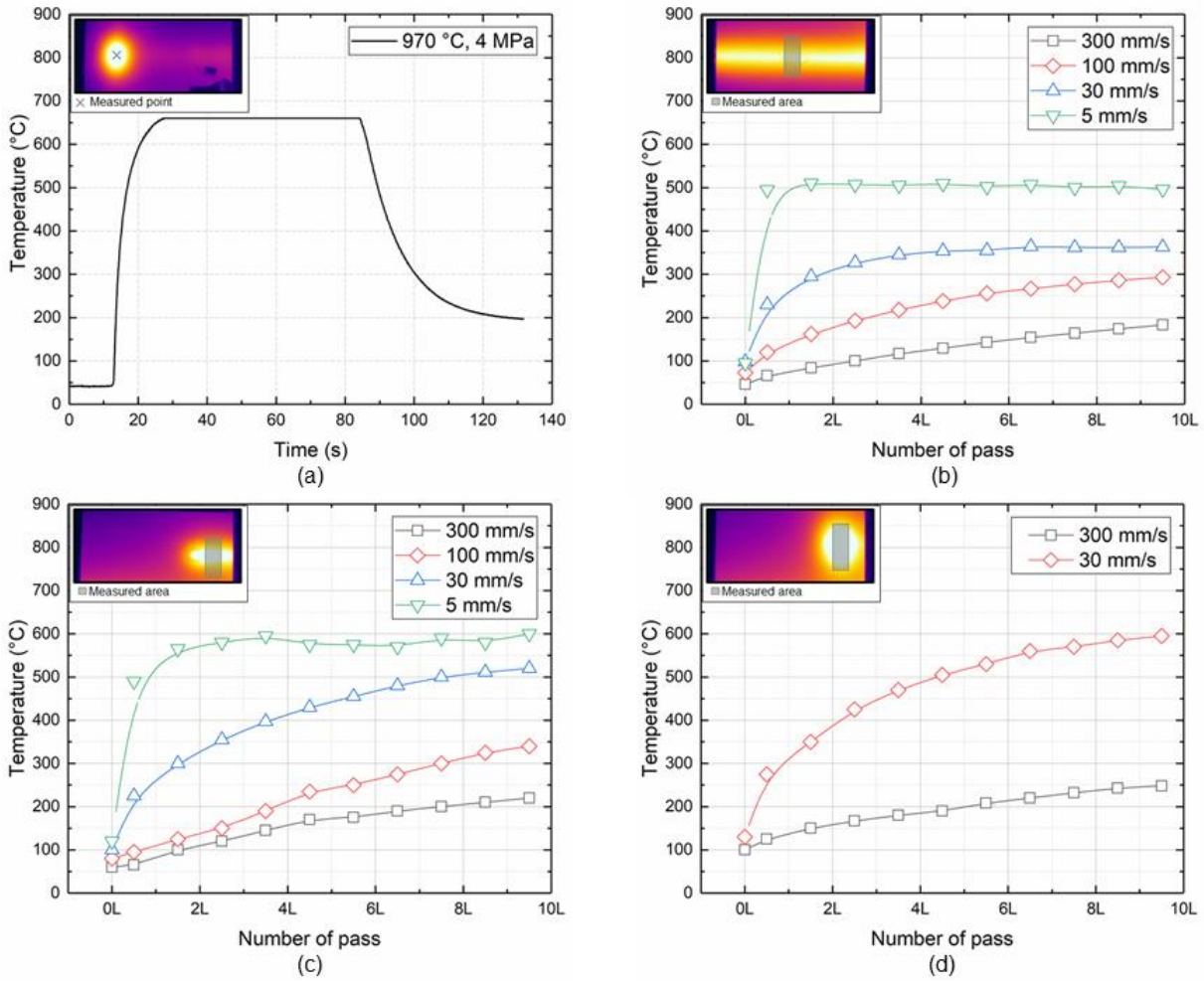

Fig. 5.9: Evolution of the substrate temperature as a function of the number of passes for each set of gas temperature and pressure for different dimension of the scanned area: (a) 970 °C – 4 MPa – stationary, (b) 970 °C – 4 MPa – 200×10 mm, (c) 970 °C – 4 MPa – 30×10 mm and (d) 1050 °C – 5 MPa – 30×10 mm

To obtain a representative value of the substrate temperature reached during a deposition process, or rather when the torch scans the surface of the sample at different traverse speed, the IR images were analyzed considering a region in the middle of the scanned area with a height equal to the height of the entire deposition path ($10\ mm$) and a width equal to $3\ mm$, and measuring the maximum value of the temperature within the area of concern. This approach allows to exclude the boundary effects due to the stop and inversion at the ends of the scanned area.

In Fig. 5.9(b) and (c) the values of the substrate temperature as a function of the number of pass of the torch are reported for each value of the investigated traverse speed; gas temperature and pressure were set equal to $970\ °C$ and $4\ MPa$ respectively. A size effect was observed comparing the results obtained in the long and short deposition, due to the different time lapse between two subsequent scanned point.

An increasing trend of the maximum temperature achieved in the region of interest can be observed for both deposition areas. It is interesting to note that, while during the deposition trial carried out setting the traverse speed equal to $5\ mm/s$, the measured temperature reaches an equilibrium value after just a cycle, this value is never reached using the other traverse speed investigated. In particular, the substrate temperature is as much lower as the traverse speed is greater. In Fig. 5.9(d), is reported the substrate temperature for the trails carried out at $1050\ °C$ and $5\ MPa$, when an area of $30 \times 10\ mm$ is scanned, in order to simulate the spraying condition of the deposition campaign developed for the mechanical characterization.

The effect of the presence of hot powder in the gas streaming is also evaluated. Fig. 5.10 shows the evolution of the substrate temperature, in which are compared the reached values in various process conditions, when powder was or was not inserted into the gas stream.

It can be observed that the temperature reached by the substrate increases of some tens of degrees when the powder is inserted in the gas stream, for all process parameters sets.

The temperature rise is due to the heat capacity of the particles. The pure gas jet can only transfers heat to the substrate by forced convection but, when hot particles that reach temperature up to $650\ °C$, as shown in Fig. 5.8(b), are deposited onto the substrate, an even more effective energy transfer occurs. Hot particles carry a considerable amount of heat, which becomes directly "embedded" in the system as soon as they are deposited, and is transferred to the colder substrate by conduction [142]. Moreover, the high kinetic energy of the powder must be taken into account; in fact, during the impact, deformation and material flow, resulting in

friction, provides to increase the temperature of the substrate [4]. The temperature rise is higher at lower values of traverse speed; this phenomenon could be explained considering the higher amount of hot particles impinging on the surface per time unit, e.g. the temperature rise observed spraying the coating at $T = 970\,°C$ and $p = 4\,MPa$ was approximately $65\,°C$ at $300\,mm/s$, whereas at $30\,mm/s$ was almost $90\,°C$.

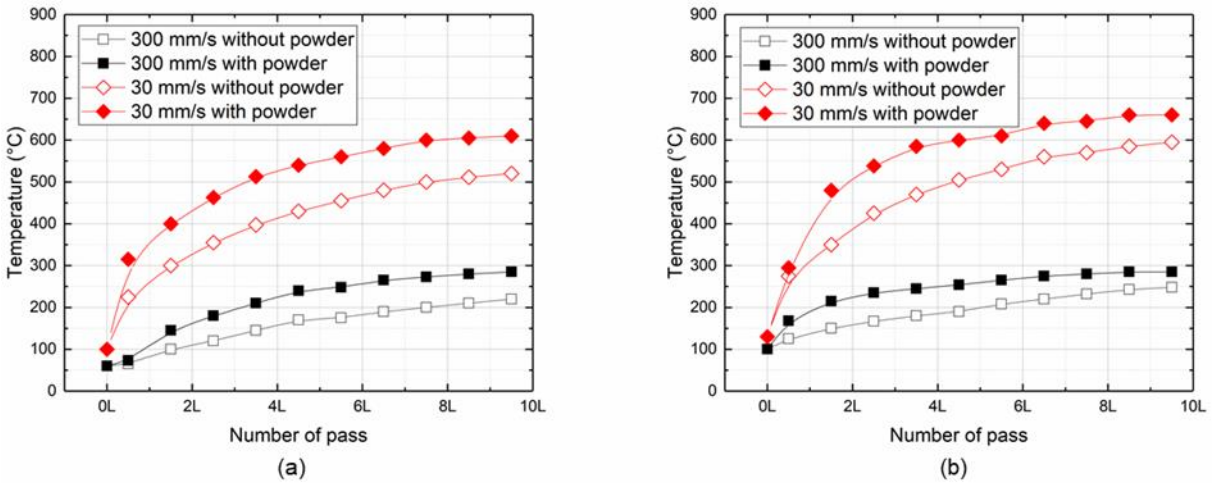

Fig. 5.10: *Comparison of the temperature reached by the substrate when only gas was used and when the powder in the gas streaming was inserted: (a) 970 °C – 4 MPa, (b) 1050 °C – 5 MPa*

5.2.3 Coating characterization

Fig. 5.11 shows the SEM micrographs of the coatings. It can be observed that for samples sprayed using the first set of parameters ($970\,°C$ and $4\,MPa$), decreasing the traverse speed the thickness increases and the porosity content tends to decrease. In particular, the estimated porosity varies from a value of 1.9 % at $300\,mm/s$ to a value of 0.4 % at $5\,mm/s$.

Samples sprayed using the second set of parameters ($1050\,°C$ and $5\,MPa$) show high compactness (splats boundary can be hardly identified) and low porosity ($< 0{,}3$ %), regardless the traverse speed.

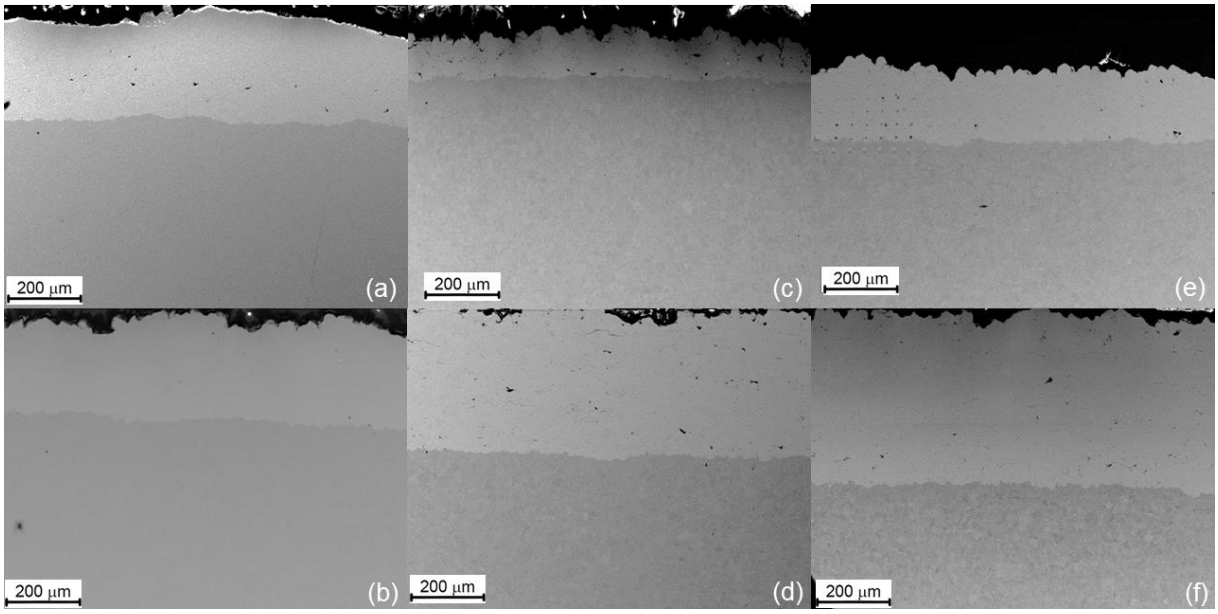

Fig. 5.11: *Scanning electron micrographs of the coatings cross-section at different temperatures, pressures and traverse speeds: (a) 1050 °C – 5 MPa – 300 mm/s, (b) 1050 °C – 5 MPa – 30 mm/s, (c) 970 °C – 4 MPa – 300 mm/s, (d) 970 °C – 4 MPa – 100 mm/s, (e) 970 °C – 4 MPa – 30 mm/s and (f) 970 °C – 4 MPa – 5 mm/s*

In Fig. 5.12 SEM micrographs at high magnification are reported; they allow to deeper analyze the deformation mechanism to which the particles are subjected for different combination of spraying parameters. It is confirmed that, using the spraying parameters $T = 970\ °C$ and $p = 4\ MPa$, the coatings appear more coherent and the splats boundaries tend to become less visible as the traverse speed decreases. This phenomenon can be attributed to the higher temperature reached by the substrate in different cases, as shown in the previous section. On the other hand, when deposition parameters $T = 1050\ °C$ and $p = 5\ MPa$ are used, the quality of the coating does not appear to be affected by the traverse speed; SEM micrographs show a very similar microstructure with similar the same porosity content. This can be explained considering that the highest gas temperature and pressure values allow the particles to enter the deposition window independently of the temperature reached by the substrate, as a consequence of the highest values of particle velocity and temperature at the nozzle exit.

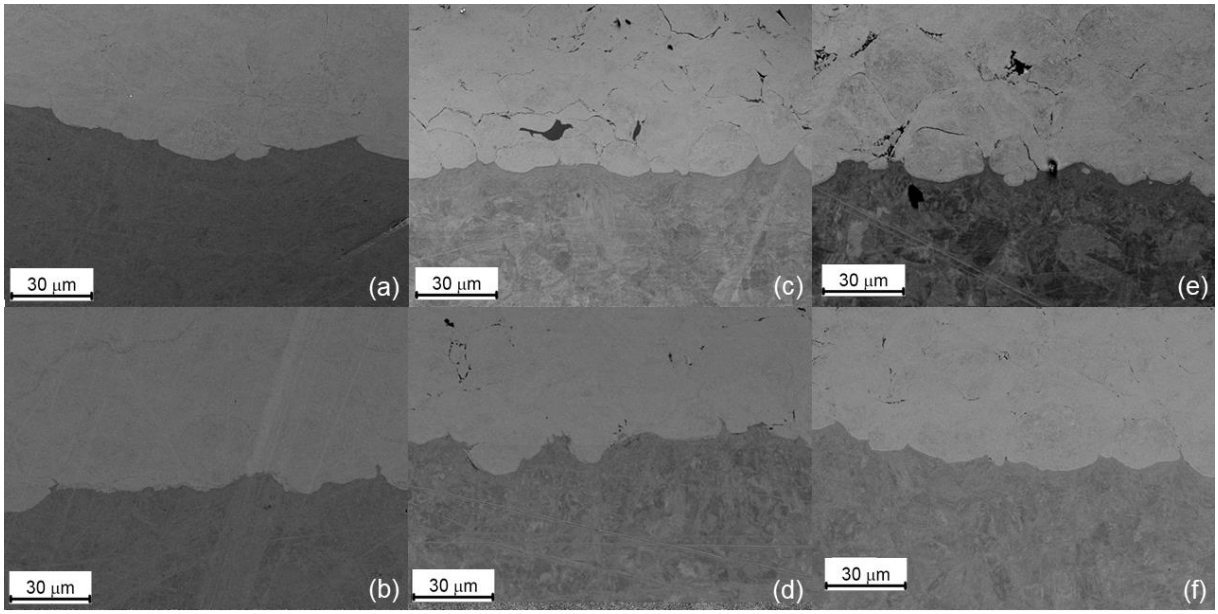

Fig. 5.12: *Scanning electron micrographs of the coatings cross-section at different temperatures, pressures and traverse speeds: (a) 1050 °C – 5 MPa – 300 mm/s, (b) 1050 °C – 5 MPa – 30 mm/s, (c) 970 °C – 4 MPa – 300 mm/s, (d) 970 °C – 4 MPa – 100 mm/s, (e) 970 °C – 4 MPa – 30 mm/s and (f) 970 °C – 4 MPa – 5 mm/s*

Similar results were obtained from the experimental tests carried out on the nano and micro-scale. In Fig. 5.13(a) and (b) the trends of the micro-hardness and of the reduced Young's modulus, calculated on the top surface, are reported as a function of the traverse speed. In both sets of deposition parameters investigated it is possible to observe how both the micro-hardness and the reduced Young's modulus tend to increase by decreasing the value of traverse speed.

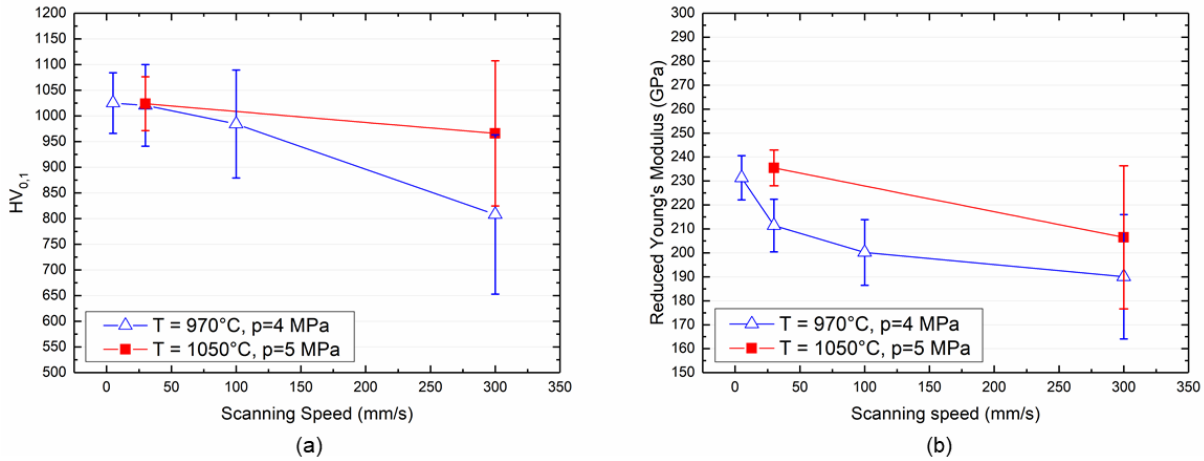

Fig. 5.13: *(a) Micro-hardness and (b) Reduced Young's Modulus of the top surface of Stellite-6 coating as a function of the traverse speed for different values of gas temperature and pressure*

Nevertheless, the value of both analyzed parameters is greater when the coating is obtained using $T = 1050\,°C$ and $p = 5\,MPa$ compared to those obtained at $T = 970\,°C$ and $p =$

$4\ MPa$. The same considerations can be made in relation to the tests conducted on nano-scale if the indentation response for the different values of the spraying parameters were selected. Fig. 5.14(a) and (b) show the indentation response of the coating cross section obtained at $T = 970\ °C$ and $p = 4\ MPa$ and $T = 1050\ °C$ and $p = 5\ MPa$ respectively when traverse speed changes. In the first, case a systematic reduction for both maximum penetration depth (h_{max}) and residual depth (h_{res}) were observed, whereas when gas temperature and pressure were set equal to $1050\ °C$ and $5\ MPa$ the curves seem to be unaffected by traverse speed.

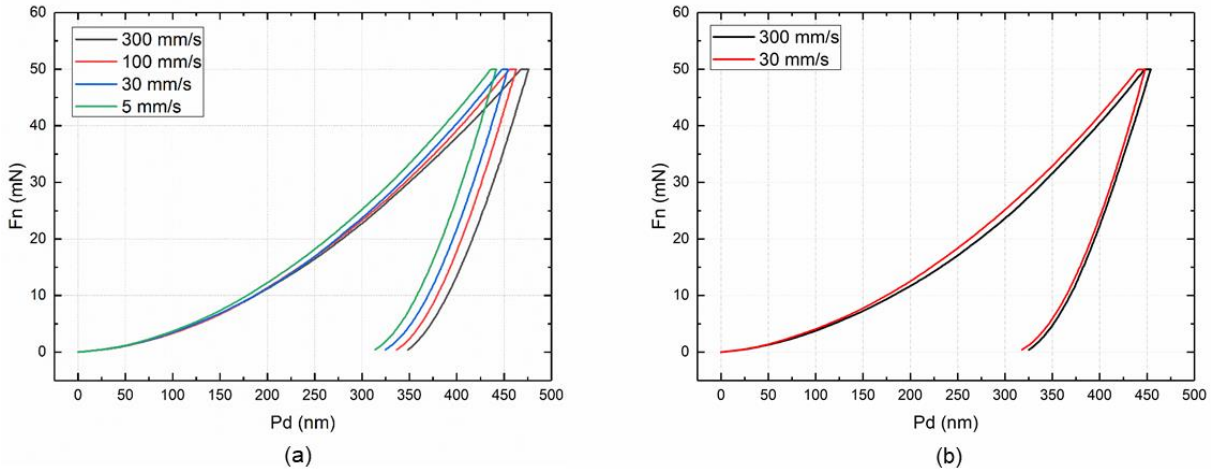

Fig. 5.14: *Nano-indentation response on the cross section of cold sprayed Stellite-6 coating for different values of gas temperature and pressure: (a) 970 °C – 4 MPa and (b) 1050 °C – 5 MPa*

Fig. 5.15(a) and (b) show the measured values of nano-hardness and reduced Young's modulus, calculated on the cross section, for each combination of process parameters chosen. The latter are calculated starting from the theory of Oliver and Pharr [142]. It can be observed that nano-hardness increases by decreasing the traverse speed for the coatings obtained imposing $T = 970\ °C$ and $p = 4\ MPa$ as spraying parameters, while the coatings obtained imposing $T = 1050\ °C$ and $p = 5\ MPa$ show a flat trend in the nano-hardness response. It should be taken into account that an increase in the nano-hardness value strongly depends on the plastic deformation which the particles are subjected. It should be assumed that similar results in the measured nano-hardness values are a consequence of similar level the plastic deformation due to the impact with the scanned surface. Thanks to this consideration it is possible to conclude that the coatings obtained at $T = 970\ °C$ and $p = 4\ MPa$ are characterized by a different amount of plastic deformation and therefore of dissipated energy. This latter, in fact, decreases when the traverse speed is increased, while it is more or less the same for the coatings obtained at $T = 1050\ °C$ and $p = 5\ MPa$. This consideration does not mean that the work hardening

introduced during deposition process is the same when the measured nano-hardness does not show significant differences, as will be better explained in the following section. In fact, the hardening occurring during the impact strongly depends by the elastic properties of the particles at the time of impacting with the surface, because these latter are affected, firstly, by their temperature at the time of the impact.

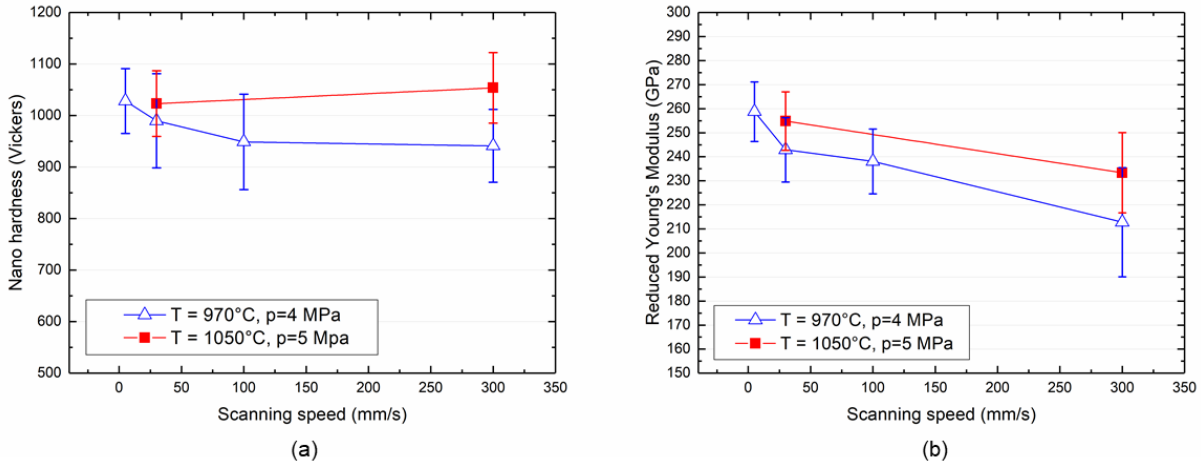

Fig. 5.15: *(a) Nano-hardness and (b) Reduced Young's Modulus of the cross section of Stellite-6 coating as a function of the traverse speed for different values of gas temperature and pressure*

For the reduced Young's modulus, even though the residual depth seems to be not affected by the traverse speed, an increasing trend can be observed reducing the traverse speed for both sets of spraying parameters, as reported in Fig. 5.15(b). This result can be explained taking into account that while hardness response depends only on the plastically deformed volume, the elastic response affects all of the coating so that reduced Young's modulus comes from a bigger volume of material. This shows how inter-particle cohesion is improved when traverse speed is reduced independently from the gas temperature and pressure conditions. Moreover, also the porosity content plays a very important role in the elastic response of the coating; a reduced amount of pores and defects inside the coatings decreases any possible rigid motions of particles not perfectly adhered to the coatings. In fact, even though the $1050\ °C$ and $5\ MPa$ conditions produce high hardness irrespective of the traverse speed, the modulus changes because it is even more sensitive to coating cohesion, which improves when using lower traverse speed.

Regarding the work hardening to which the coating is subjected, it can be analyzed in terms of the ratio between W_{pl} and W_{tot}, where W_{pl} represents the energy spent in plastic deformation and W_{tot} represents the total energy made available during the indentation, i.e. the sum of W_{el} (energy spent in elastic deformation) and W_{pl}. In particular, to calculate the values of W_{el} and

W_{pl} the data obtained from nano-indentation tests were used. An increase in this ratio, in fact, can be seen as an indicator that the material was more able to undergo plastic deformation during the indentation, which implies a decrease in the work hardening [152]. In Fig. 5.16 can be observed how the value of the W_{pl}/W_{tot} ratio decreases increasing the traverse speed, showing as, for both sets of spraying parameters chosen, work hardening, introduced during deposition process, grows increasing the traverse speed.

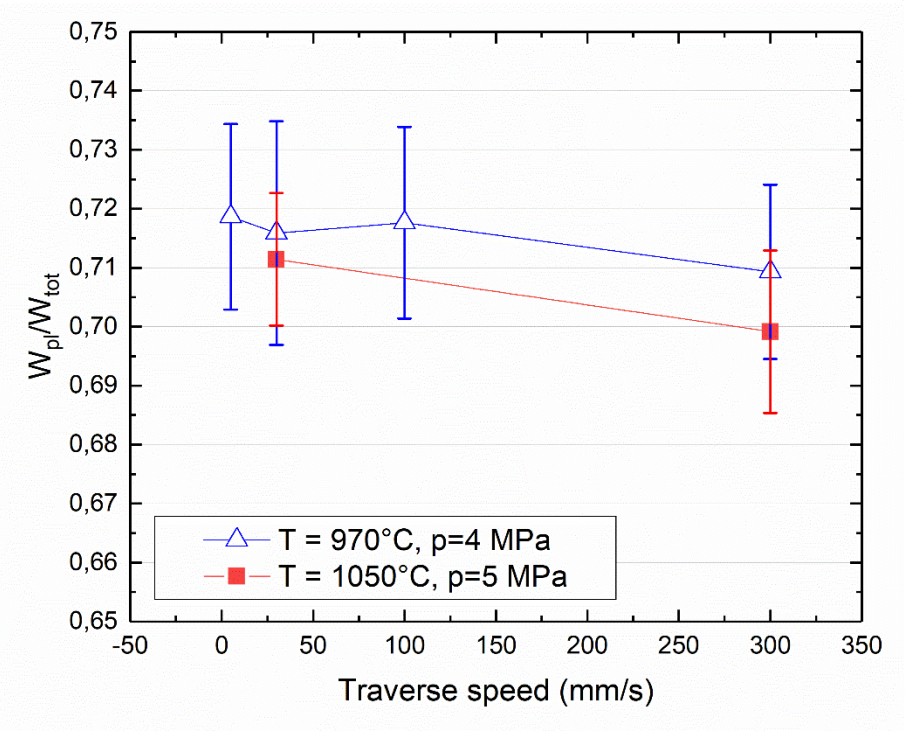

Fig. 5.16: *W_{pl}/W_{tot} ratio of Stellite-6 coating calculated on the cross section as a function of the traverse speed for different values of gas temperature and pressure*

This phenomenon is principally due to the higher temperature of the impacted region. The thermal softening that occur could be recognized as the main reason for the reduction in the work hardening which the coating is subjected. It is interesting to note that when the traverse speed is fixed at $30\ mm/s$, very similar values of the W_{pl}/W_{tot} ratio can be observed, vice versa when traverse speed is set at 300 mm/s. It should be acknowledged that, for the depositions carried out at $v = 30\ mm/s$, the thermal effect on the properties of the coating and on the work hardening is very similar, so that very slight differences are noticeable. On the contrary, significant differences can be observed in the W_{pl}/W_{tot} ratio when the deposition is carried out imposing a traverse speed equal to $300\ mm/s$. In this latter case increasing gas temperature and pressure i.e. $T = 1050\ °C$ and $p = 5\ MPa$, work hardening that occurs

during deposition process increases because of the reduced substrate temperature. The higher particle velocity implies a further amount of energy that was spent in work hardening during the impact with a colder substrate, where its reduced temperature is not enough to induce the thermal softening needed to reduce the consequent hardening due to the high deformation of the particle.

Regarding tribological coating performance, the values of the measured wear coefficient is reported in Fig. 5.17. The results do not seem to show differences that are sensitive to changes in the process parameters; the mean value of the wear coefficient obtained for both values of the track radius are $W = 7{,}91 \times 10^{-5} \pm 4{,}31 \times 10^{-06}\ mm^3/Nm$ and $W = 8{,}66 \times 10^{05} \pm 9{,}05 \times 10^{-06}\ mm^3/Nm$ respectively. The obtained results do not seem to be sensitive to the radius track if the dispersion of the data is considered. Nevertheless, some differences can be observed comparing wear coefficient obtained for samples sprayed using the highest value of the traverse speed, as it is evident in Fig. 5.17.

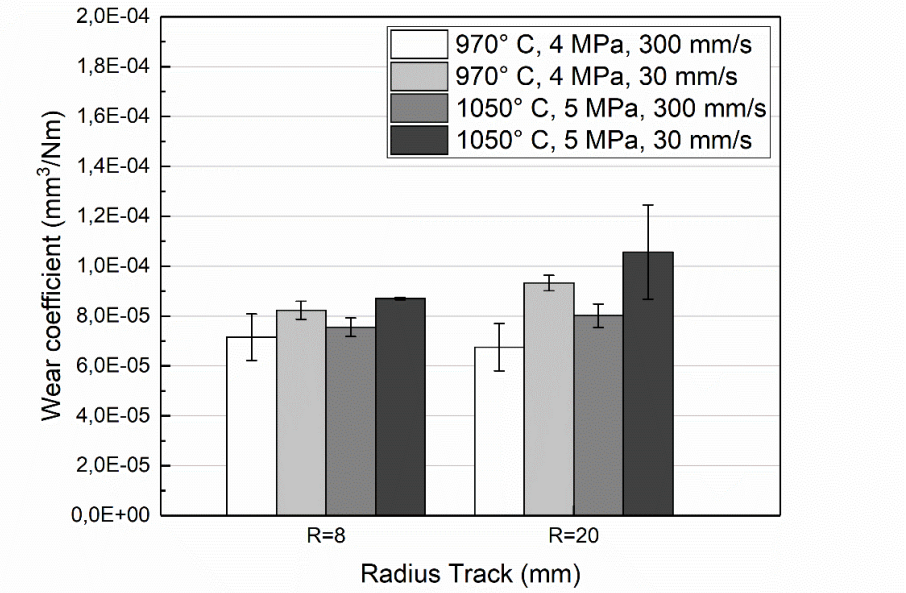

Fig. 5.17: *Wear coefficient of Stellite-6 coatings*

This phenomenon can be described taking into account that wear behavior is strongly related to elastic strain-to-failure ratio, reported in Fig. 5.18, which can be expressed in terms of the ratio between the hardness (H) and the elastic modulus (E). It was recognized by several authors that the H/E ratio can be seen as an important parameter needed to discuss about the quality of a material in terms of wear [153]. It is also significant that the ratio between H and E appears widely quoted as a valuable measure in determining the limit of elastic behavior in a surface contact, which is clearly important for the avoidance of wear [154], [155]. According with this

statement, it can be observed how for both sets of spraying parameters selected (gas temperature and pressure), this ratio tends to increase when the highest value of traverse speed is selected. Moreover, different wear mechanisms can be observed analyzing the morphology of wear surface.

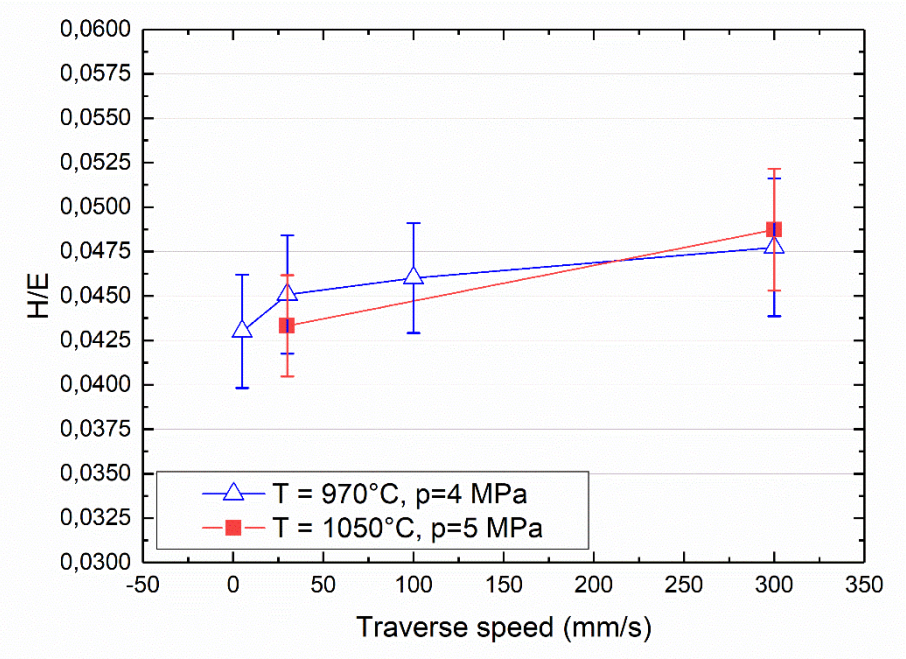

Fig. 5.18: *Strain-to-failure ratio (H/E) as a function of the traverse speed for different values of gas temperature and pressure*

Wear tracks of the coating produced using $T = 970\,°C$, $p = 4\,MPa$ and $v = 300\,mm/s$ are characterized principally by the presence of worn material especially in central region of the track. This latter appears to have been pressed, adhered and displaced across the surface as can be observed in Fig. 5.19. Moreover, plastic flow and delamination of the metal itself are not visible; this consideration allowed the authors to exclude that adhesive mechanism is the main reason for the wear of the coating.

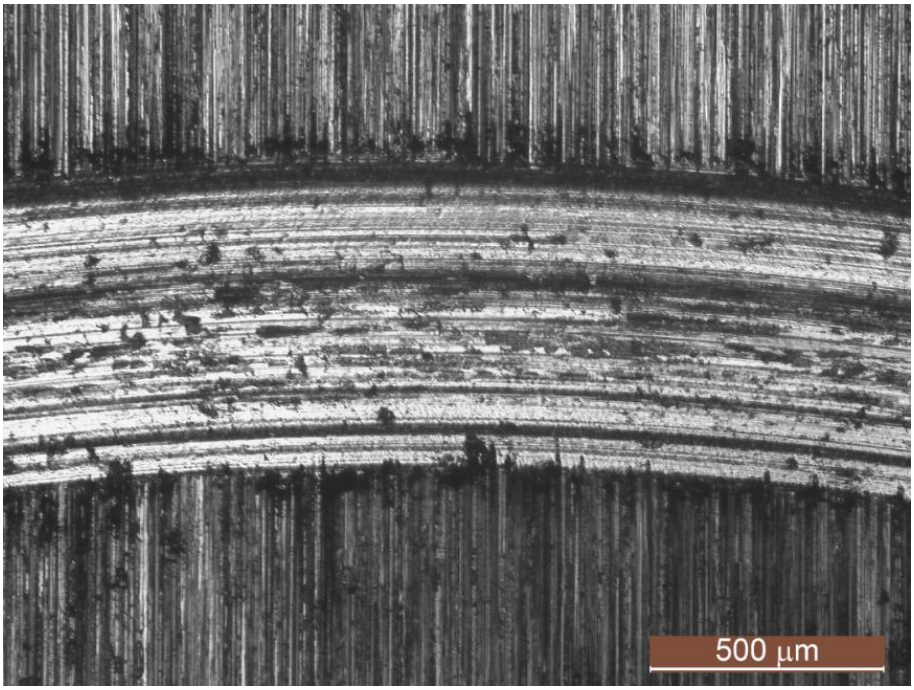

Fig. 5.19: *Micrograph of the wear surface of sample obtained at T = 970 °C, p = 4 MPa and v = 300 mm/s*

In Fig. 5.20(a) and (b) it is reported what seems to be tribo-film consisting of highly-strained oxidized material [156]. This phenomenon can be explained taking into account the increased presence of pores and cracks along the thickness of the coating. Presence of nano-grains is typical after tribological tests for CoCr alloys [157], and typically leads to a type of fatigue wear known as *"nano-grain wear"* [158], consisting of pulled-out grains which form small flattened oxidized particles on the wear surface. With regard to the coating that was sprayed using $T = 1050\,°C$, $p = 5\,MPa$ and $v = 30\,mm/s$, abrasive wear is the main mechanism observed for both values of the radius chosen.

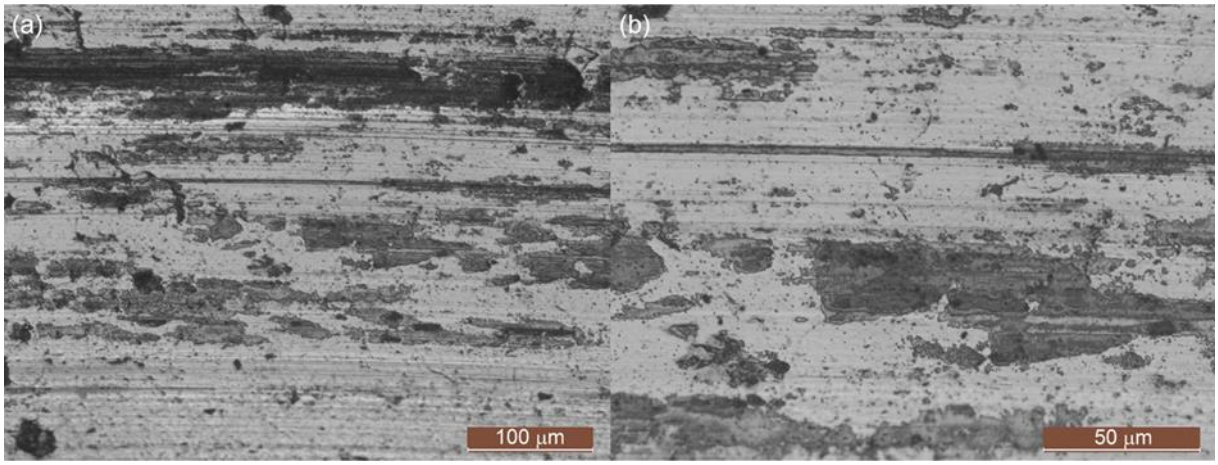

Fig. 5.20: *Micrographs at different magnification of the wear surface of sample obtained at T = 970 °C, p = 4 MPa and v = 300 mm/s: (a) 20×, (b) 50×*

In particular, for $r = 8\,mm$, the presence of deep grooves can be observed along all width of the wear track how shown in Fig. 5.21(a); it can be assumed that ploughing is the main reason of their formation because the edges of the grooves seem to be rounded and forming a ridge volume. Nevertheless, is not so clear if ploughing is the only mechanism involved, so this latter can be considered as a main wear mechanism, even if it is not possible to exclude that cutting concurred to the formation of the grooves. Moreover, it should be noted that pull-out phenomena did not occur during the test and no material remained at the edge of the wear track; as a consequence, wear coefficient shows very low dispersion. On the contrary, on the wear surface related to tests carried out at $r = 20\,mm$, reported in Fig. 5.21(b), there are less deep grooves so wear surface appears smoother but more affected by pull-out phenomena which can be considered the main reason for the greater dispersion of the obtained results. Moreover, the presence of a lot of debris in the wear track during the test has contributed to make smooth the surface, further eroding the surface and leading to a bigger value of the mean value of the wear coefficient. However, if compared with other kind of deposits, CGDS exhibits good tribological properties, in terms of wear coefficient. In some works, focused on the wear behavior of thermal sprayed Stellite-6 coatings, similar values are found when our results are compared with laser clad Stellite-6 coating proposed by Houdková et al. [159].

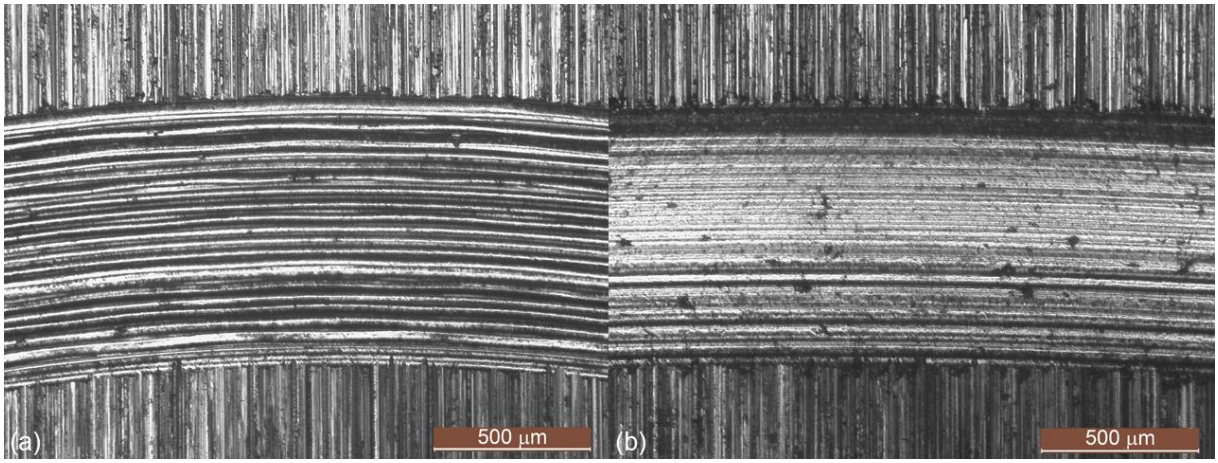

Fig. 5.21: *Micrographs for different track radius of the wear surface of sample obtained at $T = 1050\ °C$, $p = 5\ MPa$ and $v = 30\ mm/s$: (a) $r = 8\ mm$, (b) $r = 20\ mm$*

However, slight differences can be noticed if wear coefficient of cold sprayed Stellite-6 is compared with HVOF Stellite-6 coatings as described in other works [159], [160] in which lower values of measured wear coefficient are reported. The reason for this may be found considering some inter-particle boundaries as weak points in the coating. Pull-out of splats contribute to increase the mass loss at the end of the test while debris tend to increase the severity of abrasion mechanism.

5.3 Tribological behavior of cold sprayed Stellite-6 during reciprocated dry sliding

5.3.1 Microstructure characterization

Cross section of Stellite-6 coatings, optimized following the spraying parameters used in previous studies [161], [162], has been reported in Fig. 5.22. High compactness can be observed and it is also noticeable that oxidation phenomena are not involved during the formation of the coating, due to the lower temperature and higher kinetic energy of CGDS, that tends to prevent this phenomenon. In Fig. 5.22(b) are revealed the particle boundaries that maintain their round shape; This result can be related to the resistance to deformation of the Stellite-6 powder. In fact, compared to other face centered cubic (FCC) metals, such as nickel and aluminum, Stellite-6 has a similar density if compared to nickel ($8.46\ g/cm^3$ and $8.89\ g/cm^3$ respectively), a slightly higher melting temperature ($1558 - 1658\ °C$ and $1453\ °C$ respectively), while their heat capacity values are very close to each other ($421\ J/kgK$ for pure

cobalt and $456\,J/kgK$ for nickel). The main difference has to be sought in the temperature-dependent flow stress, that is strongly related to the ultimate strength. Considering that ultimate strength of cobalt based alloys is much higher if compared to other FCC metals, according to equation proposed by Assadi [2], stellite leads to expected higher critical velocities.

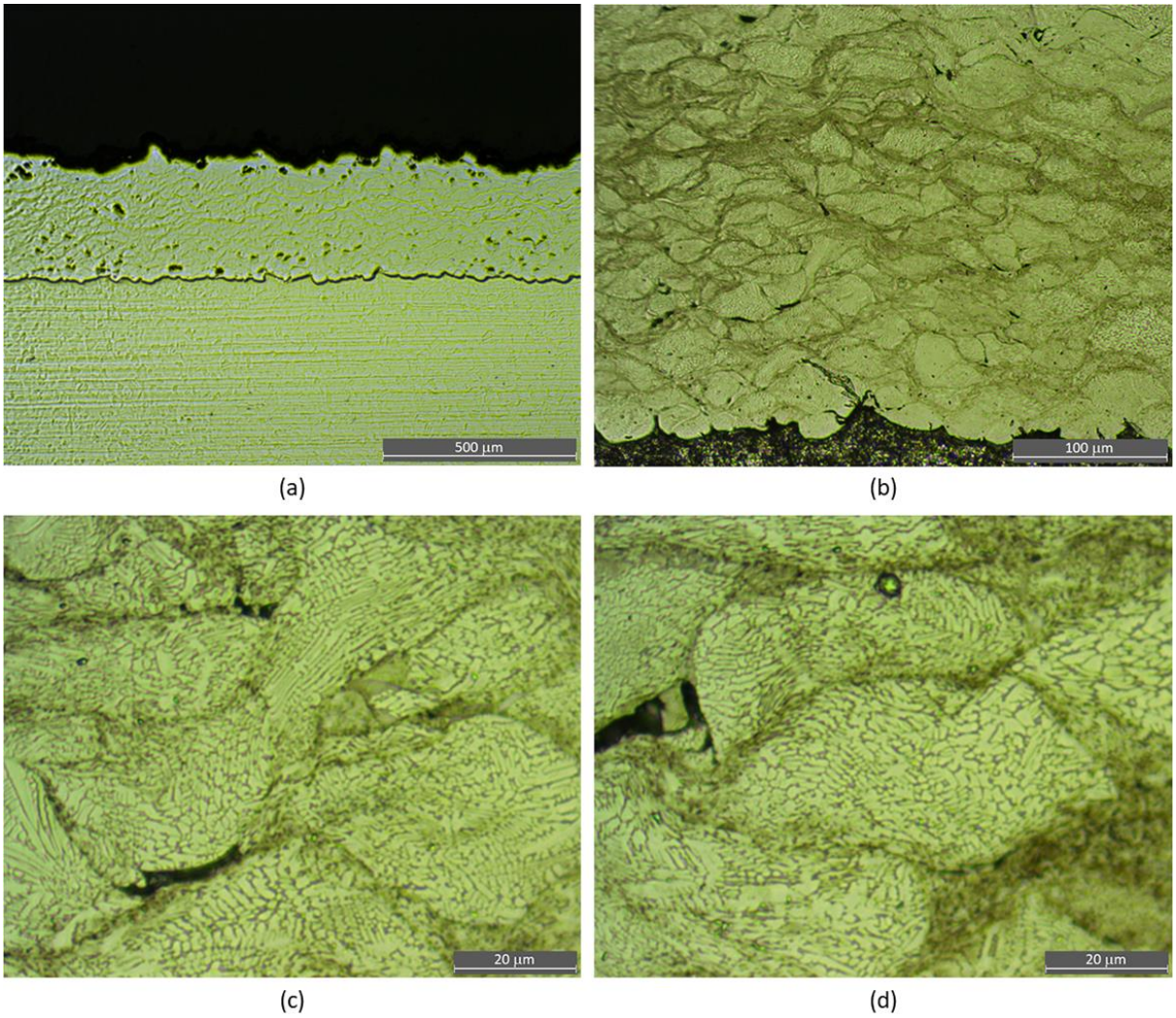

Fig. 5.22: *Optical cross section of the coating at different magnifications: (a) 5×, (b) 20×, (c) & (d) detailed features of the dendrite deformation in the particle at 100× magnification*

Fig. 5.22(b) shows some details of the deformation at the particle boundaries. It can be observed how the deposition mechanisms involve mechanical deformation of both sprayed particles and substrate at the impact interface. In fact, it is possible to observe that, despite the substrate has been just grounded before spraying, substrate-coating interface is not smooth and clearly shows the rounded profile of the impacted particles due to the higher Stellite-6 hardness compared to the steel substrate. Moreover, in Fig. 5.22(c) e (d) are reported some detailed features of the dendrite deformation in the particle, typical of the Co-Cr systems.

5.3.2 Wear tests

The frictional data were collected for all experiments and reported in Fig. 5.23, where can be observed a different trend in the dynamic coefficient of friction comparing the results obtained at low sliding speed and ones obtained at high sliding speed. The mean value of coefficient of friction tends to decrease with the contact pressure when sliding speed was set equal to $0.1\ m/s$, varying in the range $0.4 - 0.65$, whereas tends to decrease in the other case ($v = 0.5\ m/s$), varying from $0.35\ to\ 0.45$. To explain these phenomena, the morphologies of the wear tracks have been analyzed in order to understand the wear mechanisms involved and with the purpose to capture possible local effects like pull-out phenomena, cracks propagation and oxidation of wear surface.

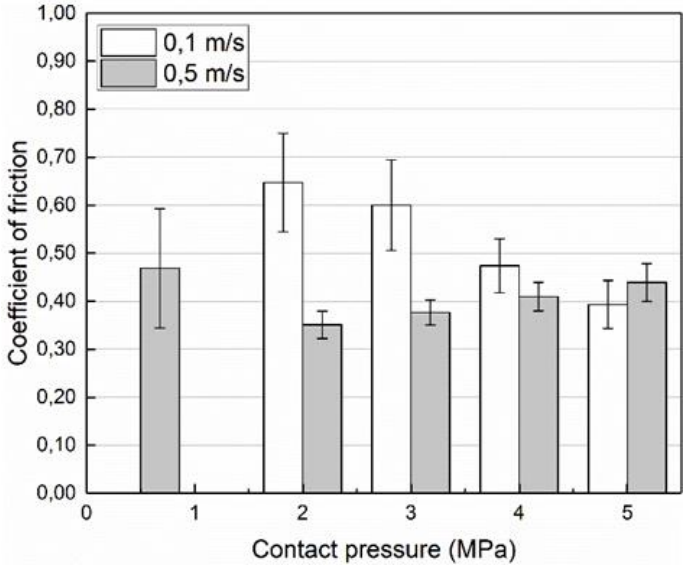

Fig. 5.23: *Evolution of dynamic coefficient of friction as a function of contact pressure for both values of sliding speed tested*

The cross-sections of worn samples shown in Fig. 5.24(d), (e) and (f) show clear evidence of subsurface cracks forming, parallel to the wear surface during tests developed using $0.5\ m/s$ as sliding speed. On the contrary samples tested when sliding speed was set equal to $0.1\ m/s$ do not show the presence of subsuperficial cracks along the thickness of the coating, as highlighted in Fig. 5.24(a), (b) and (c). This information suggest that wear mechanisms change when sliding speed is modified; it can be concluded, for initial analysis, that pull-out phenomena characterize the worn surface of those samples tested in low speed conditions, unlike sample tested at high speed. Nevertheless, wear mechanism involved will be better

addressed in the following sections, where also optical micrographs of the wear surface will be reported and discussed.

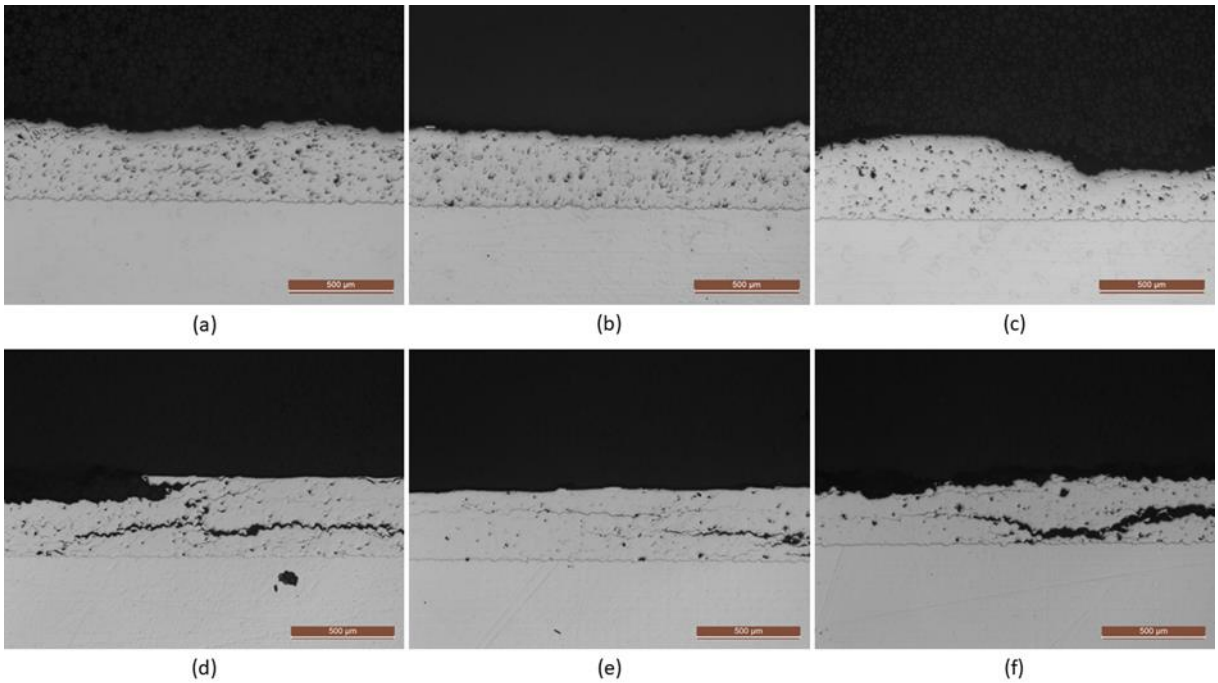

Fig. 5.24: *Optical micrographs of the sample cross-section for different levels of contact pressure and different speed tests: (a) 2 MPa - 0.1 m/s, (b) 3 MPa - 0.1 m/s, (c) 4 MPa - 0.1 m/s, (d) 2 MPa - 0.5 m/s, (e) 3 MPa - 0.5 m/s, (f) 4 MPa - 0.5 m/s*

5.3.2.1 Low speed test

Fig. 5.25 through Fig. 5.28 show the post-wear optical micrographs for the worn surface of samples tested from 2 MPa to 5 MPa.

In Fig. 5.25 is shown the worn track surface of samples tested under a contact pressure equal to 2 MPa; wear mechanism seems to be mainly abrasive throughout all experiments as localized pull-out phenomena characterize the morphology of the wear surface; this assumption can be confirmed by the micrographic observations of the cross section of the samples. In fact, the cross section of all samples that have been tested at 0.1 m/s of sliding speed does not show subsuperficial cracks parallel to the worn surface, as shown in Fig. 5.24(a), (b) and (c), that confirms the formation of pulled-out debris while running tests.

It is also remarkable that at high magnification (Fig. 5.25(b)) the splat boundaries are not evident and the regions where pull-out phenomena are visible are also distant from each other. The worn surface appears to be not oxidized and characterized by visible sharp edge. These observations can be used to explain the results related to the coefficient of friction, that appears to be the highest in the whole experimental campaign. Moreover, as shown in Fig. 5.29, the

amount of volume loss and the wear coefficient are very low if compared with the results obtained increasing both the value of the contact pressure and sliding speed, suggesting that, in spite of the coefficient of friction is high, compared with the other cases, the mechanism involved is the least dangerous.

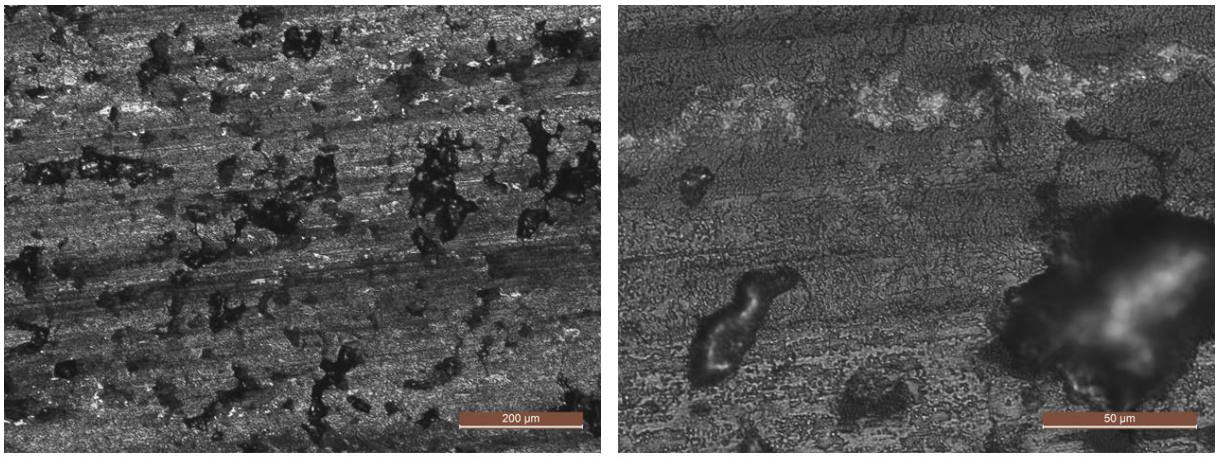

(a) (b)

Fig. 5.25: *Optical micrograph of the wear surface of sample tested under 2 MPa and 0.1 m/s*

In Fig. 5.26 is reported the wear surface of plates tasted under 3 MPa of contact pressure. The presence of zones where pull-out phenomena are evident tend to increase as compared to the sample tested under 2 MPa and, also in case, the presence of carbide can be observed. Due to this the wear coefficient results to be higher if compared to the previous case. Nevertheless, the presence of oxidized material, highlighted by the presence of white zones on the wear track reported in Fig. 5.26(a), can be considered the reason why, in this case, the friction coefficient is lower.

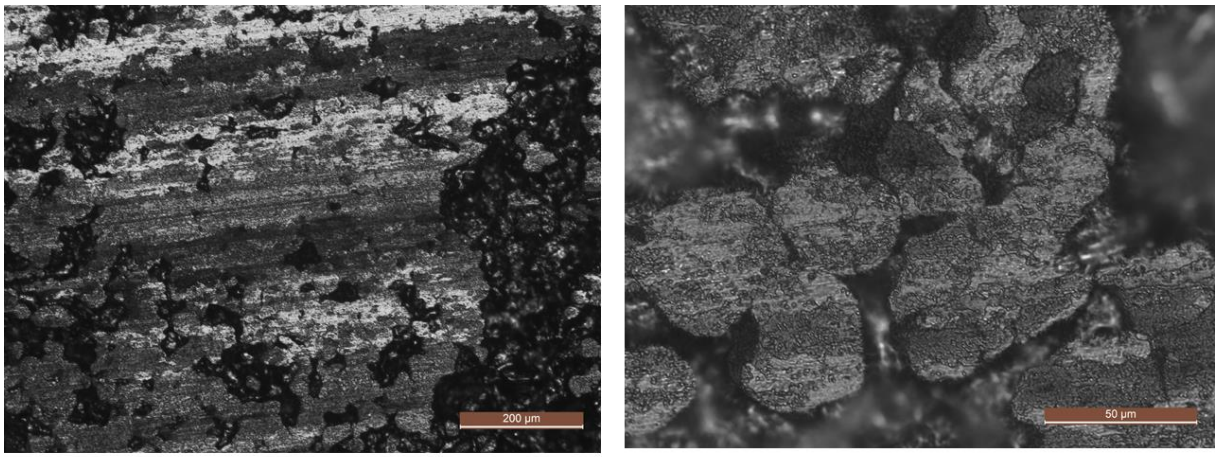

(a) (b)

Fig. 5.26: *Optical micrograph of the wear surface of sample tested under 3 MPa and 0.1 m/s*

The wear surface of the samples tested under 4 MPa of contact pressure is shown in Fig. 5.27. Pull-out phenomena are still observable, but it is interesting to note that regions not subjected to this damage mechanism are characterized by a compact and adherent layer of oxide, formed as a consequence of the higher temperature reached in the contact zone during the sliding; cracks along the splat boundaries are not visible, also at high magnification, as reported in Fig. 5.27(b). Moreover, in Fig. 5.27(b) is also evident the presence oxidized regions on the worn surface of the sample [156].

The presence of nano-grains is typical after tribological tests for CoCr alloys [157], and typically leads to a type of fatigue wear known as *"nano-grain wear"* [158], consisting of pulled-out grains which form small flattened oxidized particles on the wear surface. Due to this phenomenon, dynamic coefficient of friction shows a marked reduction in its value if compared to the results related to the tests carried out under lower load, as reported in Fig. 5.23. On the other hand, Fig. 5.29 shows that both volume loss and wear coefficient tend to be higher, as a consequence of greater presence of zones affected by pull-out phenomena, as confirmed by the microscopic observation.

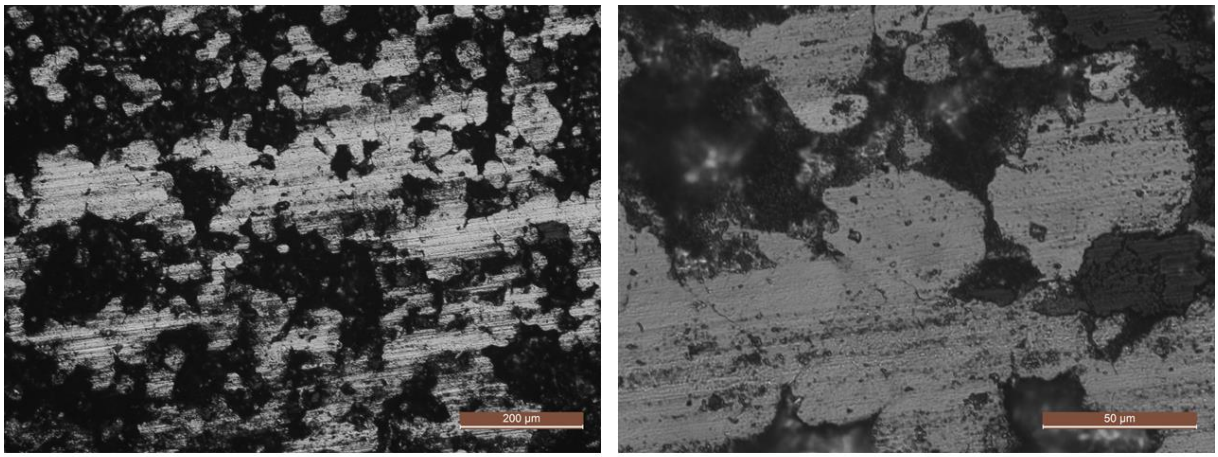

Fig. 5.27: *Optical micrograph of the wear surface of sample tested under 4 MPa and 0.1 m/s*

Likewise, in Fig. 5.28 is reported how appears the surface of the stellite coating after a wear test conducted under 5 MPa of contact pressure. The damage mechanisms that can be observed are still ones that have characterized the wear surface obtained under 4 MPa of contact pressure, that is pull-out, oxidation and *"nano-grain wear"*. It is noticeable that the zones affected by pull-out phenomena are bigger and less localized, leading to a greater volume of material that can be highly strained and displaced across the wear surface. Moreover, due to the high temperature reached during the sliding, these particles appear to be also oxidized.

Interestingly, what appears to be a platelet is peeling from the surface as seen in Fig. 5.28(a) for the 0.1 m/s and 5 MPa test. Importantly, this platelet is of the same order as the particle diameter of the stellite powder used for the realization of the coating, suggesting that these nano-grains leads, also in this case, to a fatigue wear [158]. Fig. 5.29 shows how these loading conditions lead to the greatest value in both trend of volume loss and wear coefficient; this result can be explained considering that the wear surface appears more affected by pull-out phenomena and *"nano-grain wear"*.

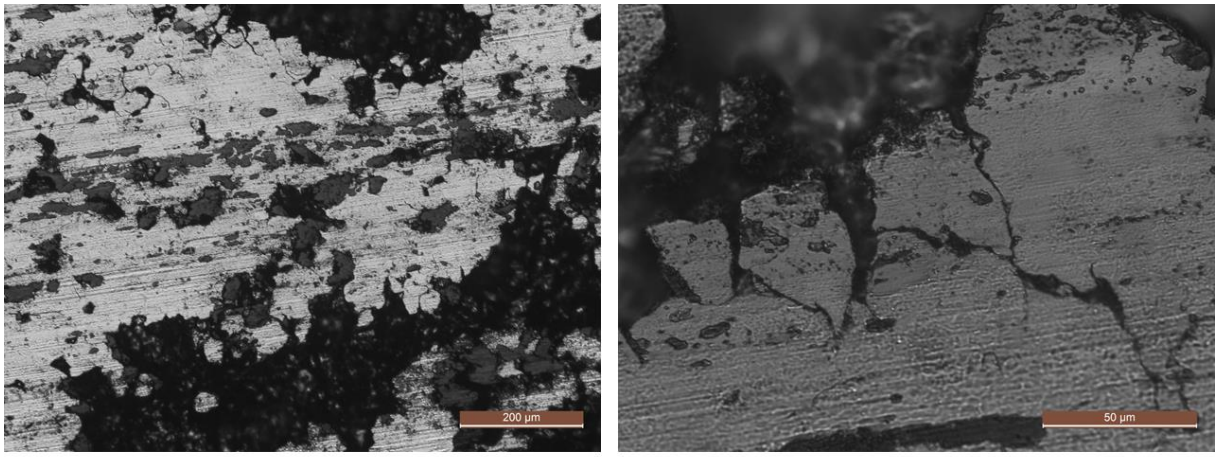

Fig. 5.28: *Optical micrograph of the wear surface of sample tested under 5 MPa and 0.1 m/s*

It is also interesting to note, that the oxidized layer, formed on the surface of the wear track, is characterized by the presence of crack, as shown in Fig. 5.28(b).

Moreover, in Fig. 5.23, is shown that these load conditions imply a very low value of the dynamic coefficient of friction, mainly due to the oxide layer, adherent to the surface and to the presence of oxidized pulled-out particle that act as solid lubricant.

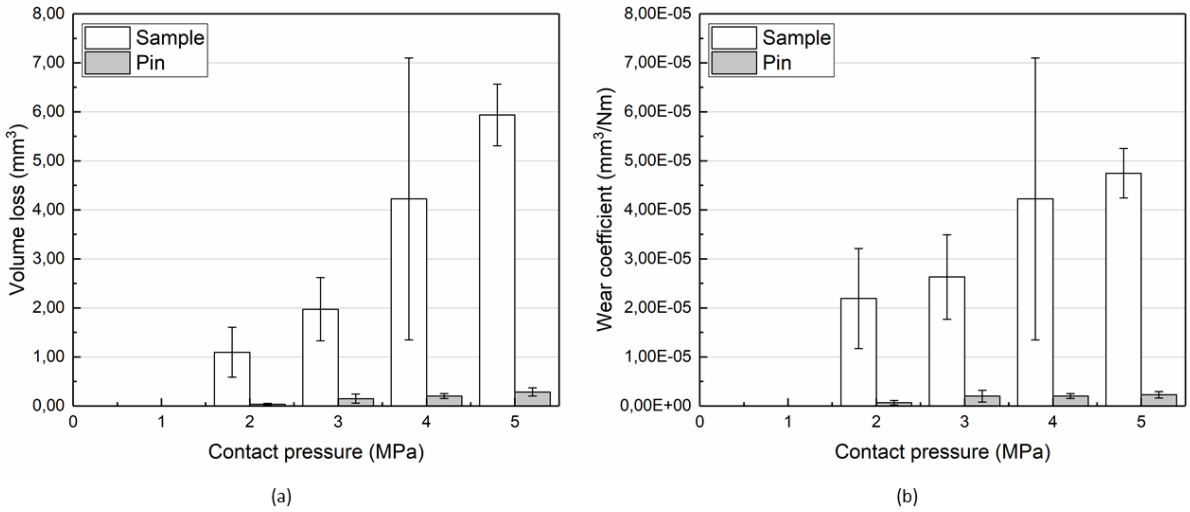

Fig. 5.29: *Volume loss and wear coefficient vs contact pressure plots for 0.1 m/s*

5.3.2.2 High speed test

Fig. 5.30 and Fig. 5.31 show the post-wear micrographs for sample wear surfaces obtained when 2 and 3 MPa are imposed as contact pressure and 0.5 m/s as sliding speed. These surfaces show primarily adhesive wear that can be seen throughout all experiments.

It is noticeable that cross section of the coatings are characterized by the presence of long subsuperficial cracks, as highlighted in Fig. 5.24(d), (e) (f), that allows to exclude the presence of pull-out phenomena and suggest that the primary wear mechanism is the adhesive one.

Likewise, material appears to have been pressed and displaced across the surface as evident in Fig. 5.30(b) and Fig. 5.31(b). Interestingly, what appears to be a platelet, is peeling from the surface as seen in Fig. 5.30(b); in fact, a large platelike piece of material appears to have adhered and been pushed along in the tests carried out at the lowest contact pressure value, i.e. 2 MPa, as can been shown in Fig. 5.30(b). Importantly, this platelet is of the same order as the particle diameters.

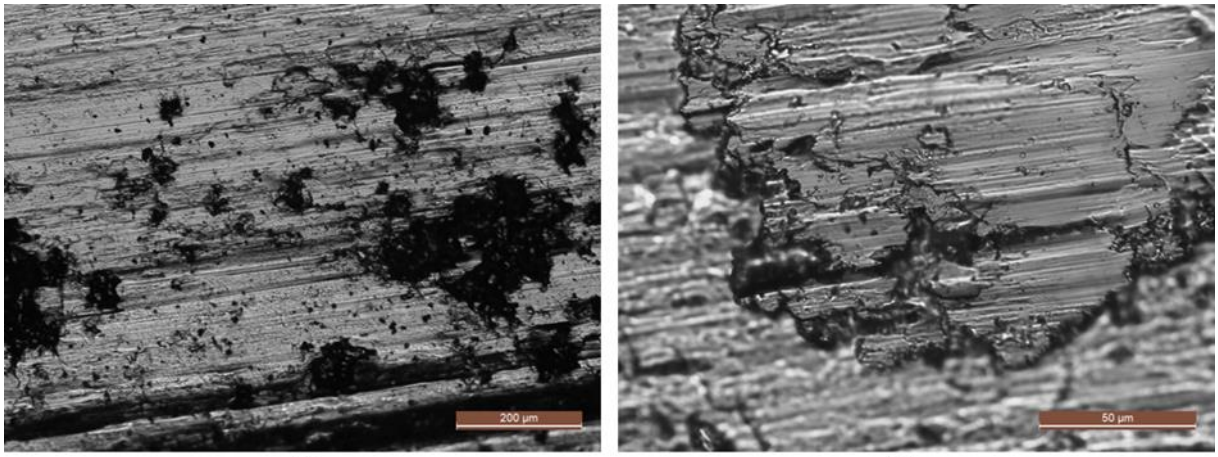

Fig. 5.30: *Optical micrograph of the wear surface of sample tested under 2 MPa and 0.5 m/s*

These observations suggest that pull-out phenomena occur also during high speed test, particularly in tests carried out at low contact pressure levels; in fact, the presence of pull-out is still observable in Fig. 5.30(a) while the areas around seems to be completely oxidized. Moreover, in Fig. 5.23 it can be observed how the dynamic friction coefficient is the lowest when compared with the results obtained in all the other high speed tests.

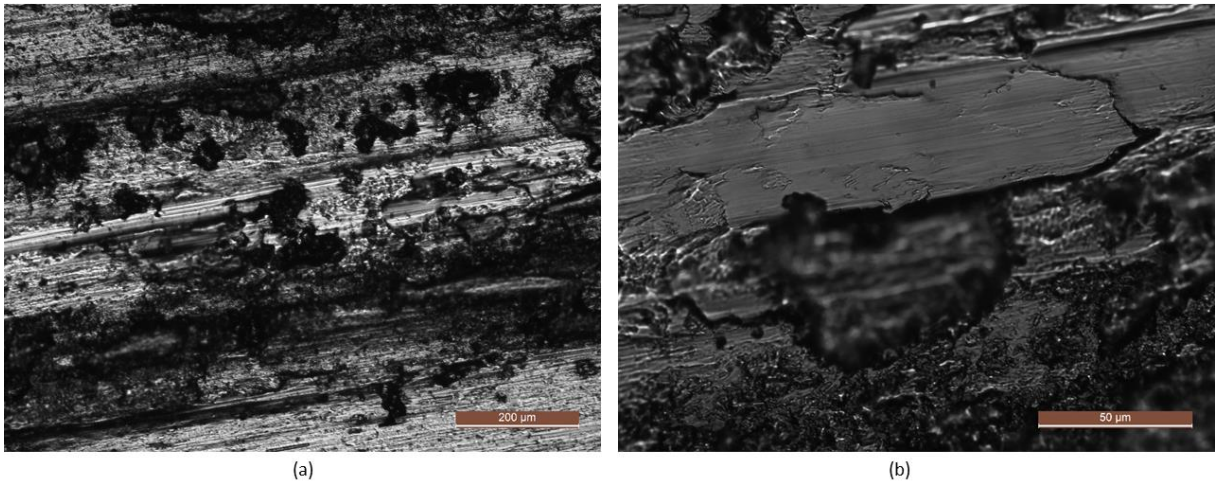

Fig. 5.31: *Optical micrograph of the wear surface of sample tested under 3 MPa and 0.5 m/s*

This latter result can be explained considering a double effect: on the one hand the presence of oxidized material on the wear track tends to form a tribo-film consisting of highly-strained oxidized material [156] which tends to reduce the friction coefficient during the test; on the other hand, due to the higher temperatures reached, as a consequence of the higher value of the sliding speed, the wear transition of metallic materials occurs, leading in this case to a reduction in the measured friction coefficient.

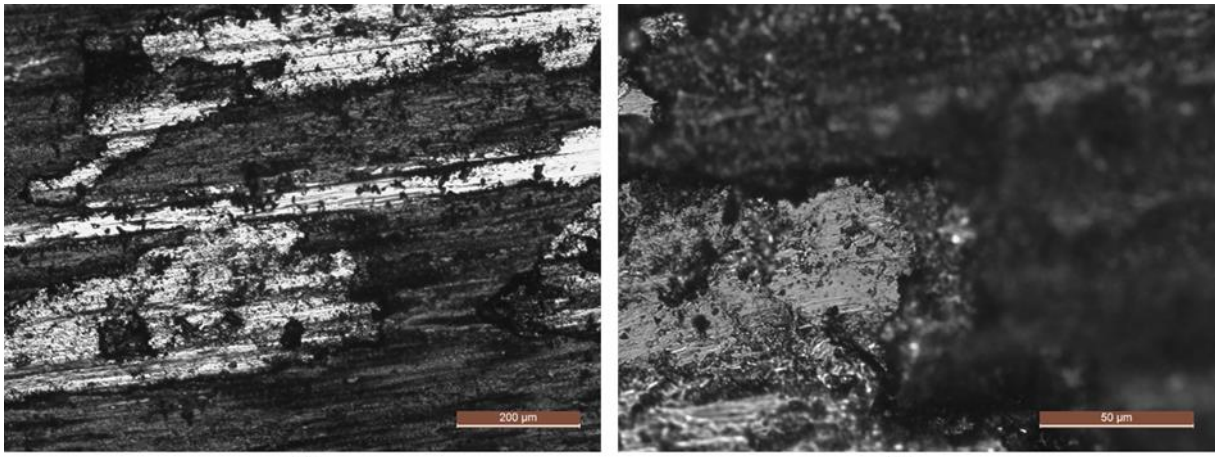

Fig. 5.32: *Optical micrograph of the wear surface of sample tested under 4 MPa and 0.5 m/s*

This latter is a common phenomenon as the parameters of wear test increase [163]–[165], in fact it can be observed a sensitive modification of the wear mechanisms in the high speed test increasing contact pressure since these latter represent the more severe testing conditions. Nevertheless, it was observed that Stellite-6 coating exhibited an almost constant wear rate at high speed tests, as can be seen in Fig. 5.34(b) and Stellite-6 alloy underwent a severe-to-mild wear transition as the sliding velocity increased, especially under higher loads, as confirmed by the linear trend of the volume loss reported in Fig. 5.34(a).

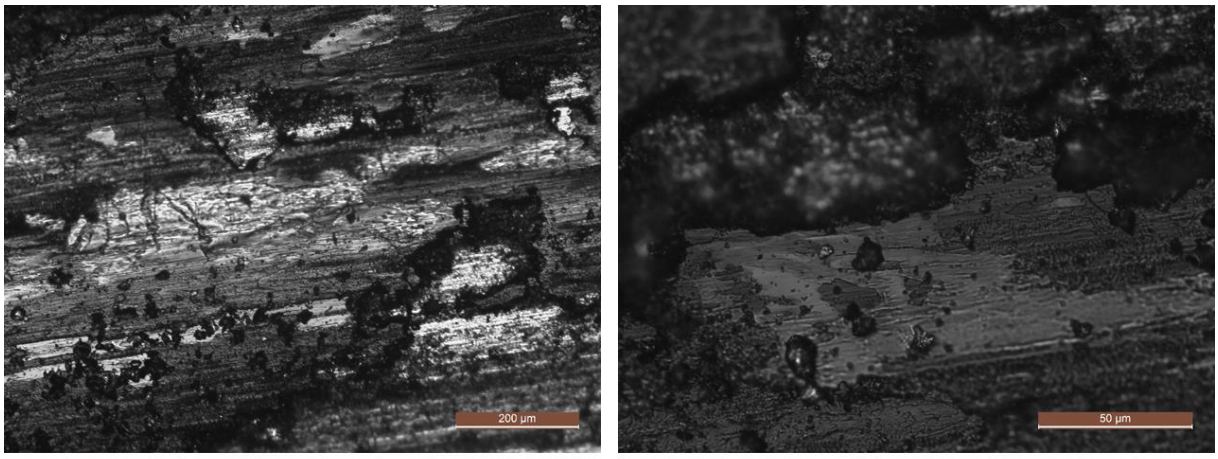

Fig. 5.33: *Optical micrograph of the wear surface of sample tested under 5 MPa and 0.5 m/s*

The wear transition can be also observed comparing the wear track micrographs of worn surface obtained at low contact pressure, i.e. 2 and 3 MPa, (see Fig. 5.30 and Fig. 5.31) with ones obtained under 4 and 5 MPa, reported in Fig. 5.32 and Fig. 5.33 respectively. In fact, increasing contact pressure, the worn surface appears to be less affected by pull-out phenomena while, due

to increased average temperature and the flash temperature of pin, the adhesion is more likely to occur and adhesive wear gradually dominate the wear mechanism.

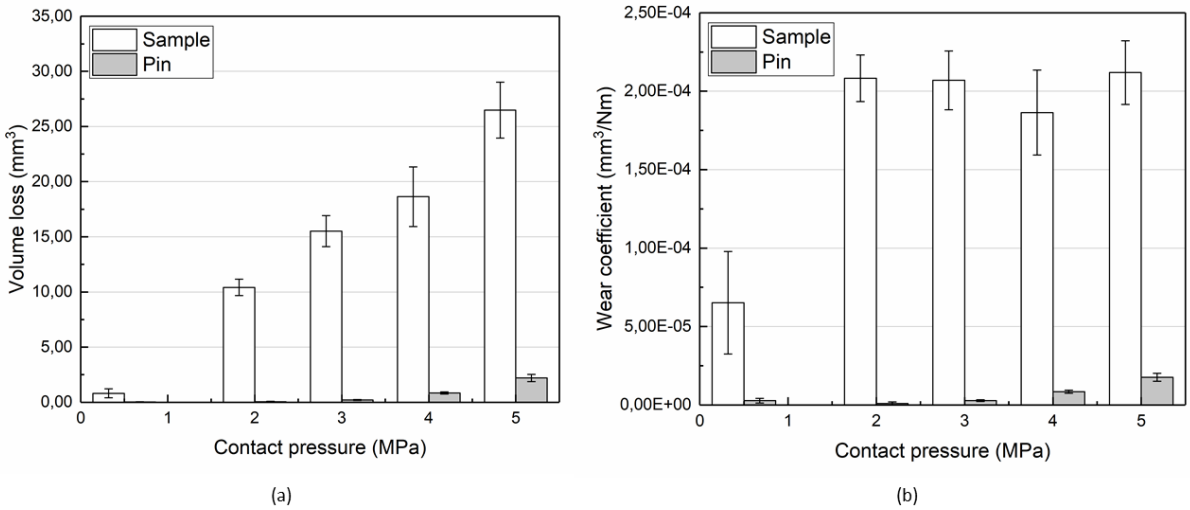

Fig. 5.34: *Volume loss and wear coefficient vs contact pressure plots for 0.5 m/s*

The increasing trend of friction coefficient with the contact pressure, that is reported in Fig. 5.23, further suggests an increase of adhesion between pin and sample.

5.3.3 Nano-indentation tests

The evolution of mechanical properties at the nano scale was also analyzed with the purpose to catch any possible changes in stiffness and hardness response of the coating along the thickness in the region under the worn surface. In this regard an experimental campaign was carried out by a 10 by 10 indentation map was with 30 μm spacing between each indents, while a normal load equal to 50 mN was imposed.

5.3.3.1 Low speed test

The nano-indentation measurements, carried out on the cross section of samples tested in low speed condition ($v = 0{,}1\ m/s$), are reported in Fig. 5.35. It can be observed an almost flat trend in both elastic and hardness response. It is interesting to note that, regarding the evolution of reduced Young's modulus shown in Fig. 5.35(a), its mean value (218 GPa) appears to be lower in the tests carried out at 2 and 3 MPa of contact pressure if compared with that obtained at 4 and 5 MPa (238 GPa).

In the same way, hardness response, highlighted in Fig. 5.35(b), seems to show a similar trend and, also in this case a slight increase in the value of the hardness, increasing the value of the

contact pressure, can be observed. The trends in the hardness and stiffness data may relate to the grain size evolution of the microstructure after wear. In fact, it has been demonstrated experimentally and by numerical simulations [166], [167] that stiffness of materials tends to decrease with grain refinement. This is said to be due to the increased concentration of grain boundaries and thus the presence of intergranular cracks through the nano-grain structure.

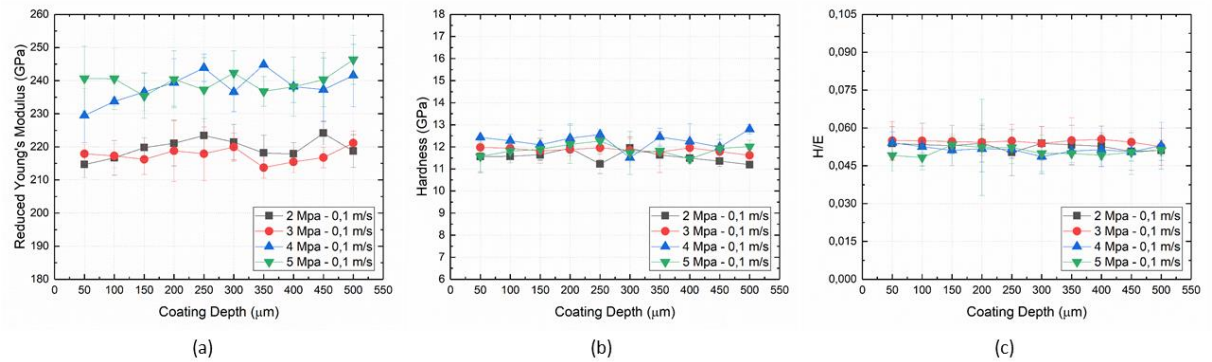

Fig. 5.35: *Plot of the nano-indentation results for reduced elastic modulus, hardness, strain-to-failure ratio vs depth for low speed tests*

As a consequence, it can be assumed that, regarding those tests carried out at low speed and high contact pressure (4 and 5 MPa), the coating is subjected to grain growth phenomena and, at the same time, the higher value of the contact pressure tends to close any possible subsuperficial defects below the worn surface. In the previous section, in fact, it possible to observe how the cross section of coatings tested at low speed are not characterized by the presence of subsuperficial cracks unlike those ones tested at high speed, as can be observed in Fig. 5.24.

The presence of nano-grains are typical after tribological tests for CoCr alloys [157], and typically leads to a type of fatigue wear known as *"nano-grain wear"* [158], consisting of pulled-out grains which form small globular particles on the wear surface – these typically cluster around grooves and oxide boundaries. This type of wear can be observed in all wear tests in varying degrees.

For several materials wear behavior can be related to elastic strain-to-failure ratio, which can be expressed in terms of the ratio between the hardness (H) and the elastic modulus (E) [168], reported in Fig. 5.35(c). In fact, this ratio appears widely quoted as a valuable measure in determining the limit of elastic behavior in a surface contact, which is clearly important for the avoidance of wear [153]. In this case the increase in both stiffness and hardness implies the H/E value tends to be almost constant for all tests carried out at low speed, while the trend of

the wear coefficient of the coatings as a function of the contact pressure is roughly linear, as shown in Fig. 5.29(b).

Therefore, it can be concluded that tribological behavior of cold spray Stellite-6 in *"area-on-flat"* sliding conditions at low speed, it can be concluded that, its wear performance cannot be related to the evolution of strain-to-failure ratio (*H/E*), but it is mainly depending on pull-out phenomena and debonding mechanisms that occur.

Importantly, the changes in the material properties during sliding must be accounted for in a model of wear; variations in material properties naturally affects the stress field under the point of contact which will affect the wear response of the alloy.

5.3.3.2 High speed test

The nano-indentation measurements pointed out in Fig. 5.36 show a reduction in the stiffness (Fig. 5.36(a)) and a similar trend in the hardness response (Fig. 5.36(b)), as a function of the contact pressure. The trends in the hardness can be considered a direct consequence of the high temperature reached during the tests developed at high sliding speed ($v = 0{,}5\ m/s$); high temperature, in fact, often implies noticeable modifications in the coating microstructure so, this behavior may relate to the grain size evolution of the microstructure after wear. In fact, as due to the Hall-Petch effect [166], [167], the hardness of materials tends to increase with grain refinement as a consequence of enhanced dislocation pile-up at grain boundaries. It can be concluded that the decreasing trend observed in the nano-hardness response could be considered as a consequence of grain growth phenomena. Moreover, the observed reduction in the hardness values along the thickness can be also related to the increased presence of cracks inside the coating, clearly observable in Fig. 5.24(d), (f) and (f).

In the same way the relationship between grain size and stiffness has also been demonstrated experimentally and in numerical simulations [169] but, in this case, this marked reduction of the reduced Young's modulus can be explained taking into account the presence of cracks and detachment of material below the surface developed during the sliding, that tend to increase by increasing the contact pressure between pin and sample. In fact, since the elastic response comes from a bigger volume of material, the presence of subsuperficial cracks plays a very important role. This phenomenon is mainly due to the allowed rigid motions of particles debonded from the coatings during the indentation.

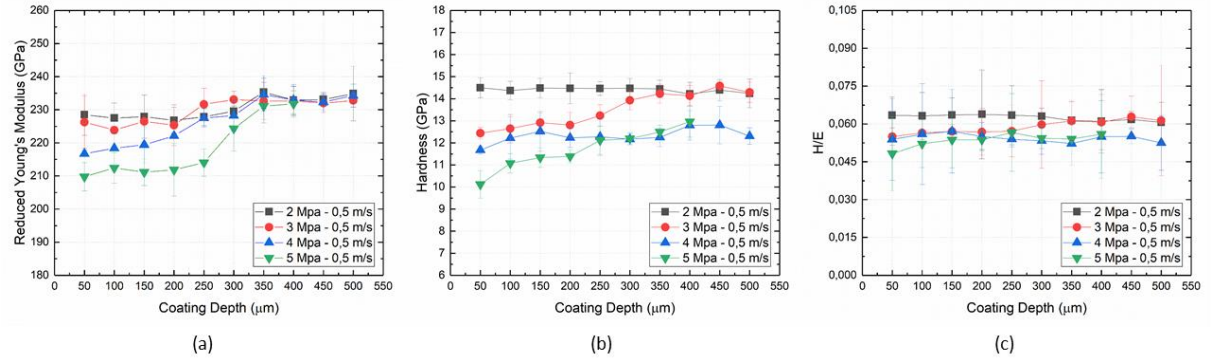

Fig. 5.36: *Plot of the nano-indentation results for reduced elastic modulus, hardness, strain-to-failure ratio vs depth for high speed tests*

In this case, hardness and stiffness evolution at the wear surface results in an almost flat trend of the H/E ratio, as shown in Fig. 5.36(c), as a function of the coating depth.

Moreover, the strain-to-failure ratio response as a function of the contact pressure tends to decrease increasing the value of contact pressure. Nevertheless, these differences are slight and can be considered negligible. This result may be used also to explain how, in the high speed tests, the calculated wear coefficient seems to be unaffected by the level of contact pressure chosen, as shown in Fig. 5.34(b), even though the mechanical properties are directly affected by the load imposed during the tests. As a consequence, it can be concluded that the wear resistance of the coating surface does not noticeable vary with the applied load. In fact, in this latter case, pull-out phenomena do not appear on the worn surface of the samples and wear mechanism are mainly due to adhesive wear mechanism, that is seen to be operative for the Steel-CoCr system.

5.4 Mechanical and vacuum properties of cold sprayed Ti coatings for ultra-high vacuum applications

5.4.1 Influence of the CGDS process parameters

Fig. 5.37 illustrate relevant light micrographs of cross sections of coatings obtained from the selected deposition parameters reported in Table 4.6. Typical coatings obtained at low values of temperature and pressure are shown in Fig. 5.37(a) (T= $350° C$ and $p = 4.0\ MPa$) and in Fig. 5.37(b) ($T = 400\ °C$ and $p = 3.4\ MPa$). Both figures show a marked porosity along the coating thickness coupled with low adhesion to the substrate, as also illustrated in the higher magnification images. Fig. 5.37(c) reports the cross sections of a coating obtained at $T =$

970 °C and $p = 4.0\ MPa$ whereas Fig. 5.37(d) is relative to $T = 1050$ °C and $p = 5.0\ MPa$. Both figures seem to indicate a negligible porosity and an apparent good adhesion with the steel substrates at the scale of the micrographs. Marked local deformations at the interface are also visible in the last two micrographs.

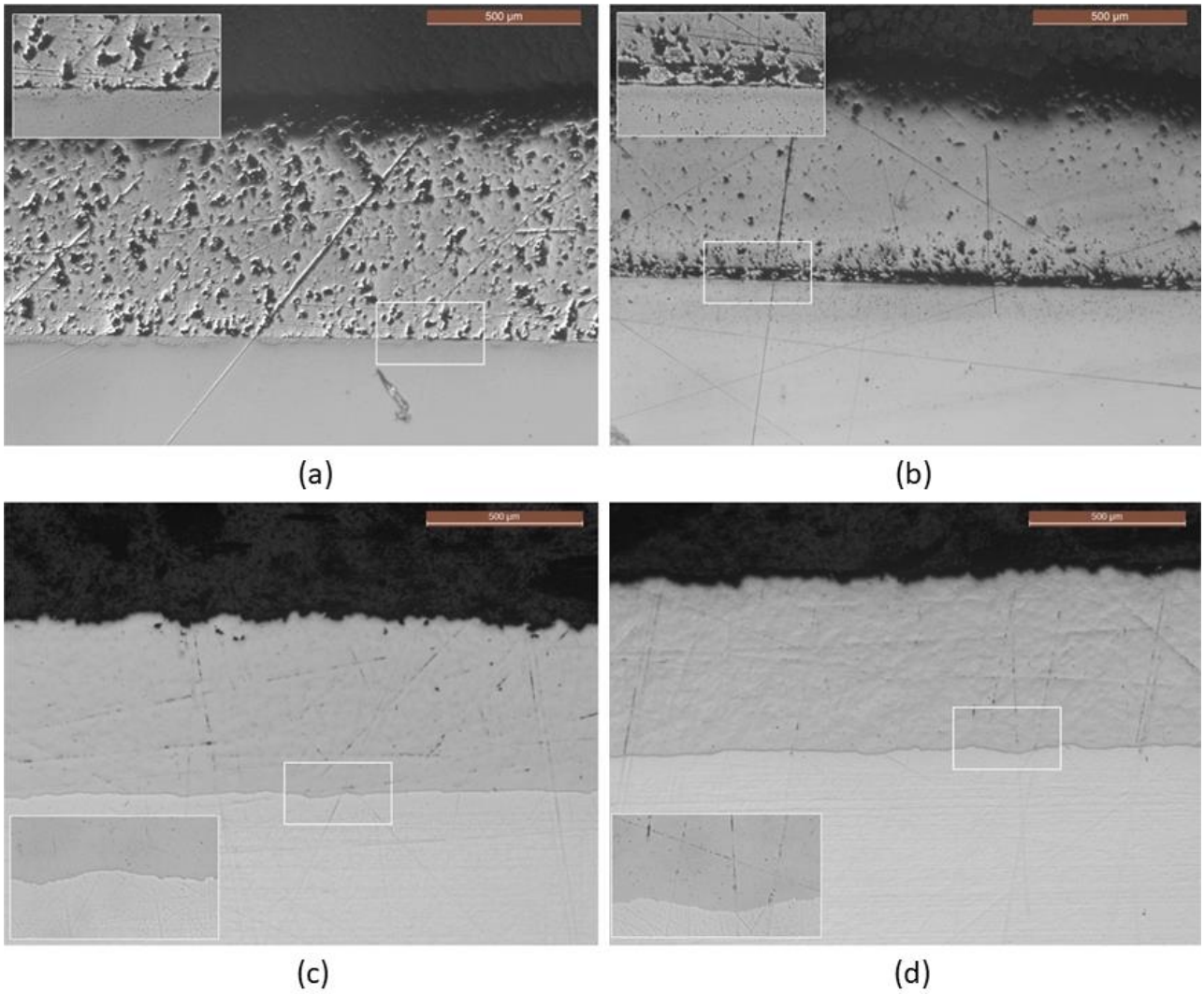

Fig. 5.37: *Optical micrographs of cross sections of coatings obtained from low and high energy deposition parameters: (a) T=350 °C and p=4.0 MPa; (b) T=400 °C and p=3.4 MPa; (c) T=970 °C and p=4.0 MPa; (d) T=1050 °C and p=5.0 MPa*

5.4.2 Micro and nano mechanical properties

Deeper analyses of the coatings obtained with the two high energy deposition conditions ($T = 970\ °C - p = 4.0\ MPa$ and $T = 1050\ °C - p = 5.0\ MPa$) were made by nano indentation tests. Figure 6.a shows the hardness and Young's modulus profiles along the thickness, from the steel-Ti interface to the outer surface, for the coating obtained at $T = 970\ °C$ and $p = 4.0\ MPa$. Each point in the figure represents the average value obtained from 10 different

indents, leading to a matrix of 10×13 indentation points. The standard deviations for each point are also highlighted by the scatter bars.

Similar results were obtained for the other deposition condition ($T = 1050\,°C$ and $p = 5.0\,MPa$), that is data are within the same dispersion bands. This result confirms the outcome of micrographic observations and, therefore, subsequent mechanical and functional tests were limited only to the lower energy condition ($T = 970\,°C$ and $p = 4.0\,MPa$). Furthermore, the figure shows that hardness data appear to be more dispersed than Young's modulus, with coefficient of variations ($c = \sigma/\mu$) equal to 0.10 and 0.05, respectively. This can be attributed to localized effects caused by particle impact, dealing to a non-homogeneous material hardening within the Ti splats as also described in refs. [138], [140], [170]. In fact, both spacing ($40\,\mu m$) and size of the indents ($< 2\,\mu m$) are smaller than typical splat size ($> 50\,\mu m$) and local inhomogeneities caused by particle impacts are captured due to the small process volume of the nano indentation test. During the impact, in fact, local grain refinement occurs at the extremities of the splats, where deformation and plastic flow are more severe if compared with the central zone of the particle. Considering the Hall-Petch effect [166], [167], it is expected that, when the indentation was carried out at the extremity of a single splat, the measured value of nano-hardness is higher if compare with the nano-hardness response of an indentation performed in the middle of the particle. As a consequence, it stands to reason that the highest values of the nano-hardness are obtained when the indentations were carried out at the extremities of the splats. In addition, Fig. 5.38(a) also shows that both hardness and stiffness are almost constant along the coating thickness; that is an additional evidence for good quality coatings.

Nano-indentation results of CGDS coatings were compared with data obtained from bulk Ti Grade 1 cut from a $2mm$ thick sheet. It was found that Young's modulus of the two materials is almost the same while hardness appears to be slightly higher for the coatings. This result further demonstrates the good compactness of the coating, as porosity play a detrimental role on the Young's modulus. The slightly higher hardness is attributed to the marked material hardening caused by cold spray deposition.

Vickers micro-hardness measurements, carried out on the top surface of the coating, revealed a similar dispersion of the data that is attributed to local non-homogeneities. The measured value of $HV_{0.05}$ is 370 ± 36, as highlighted in Fig. 5.38(b).

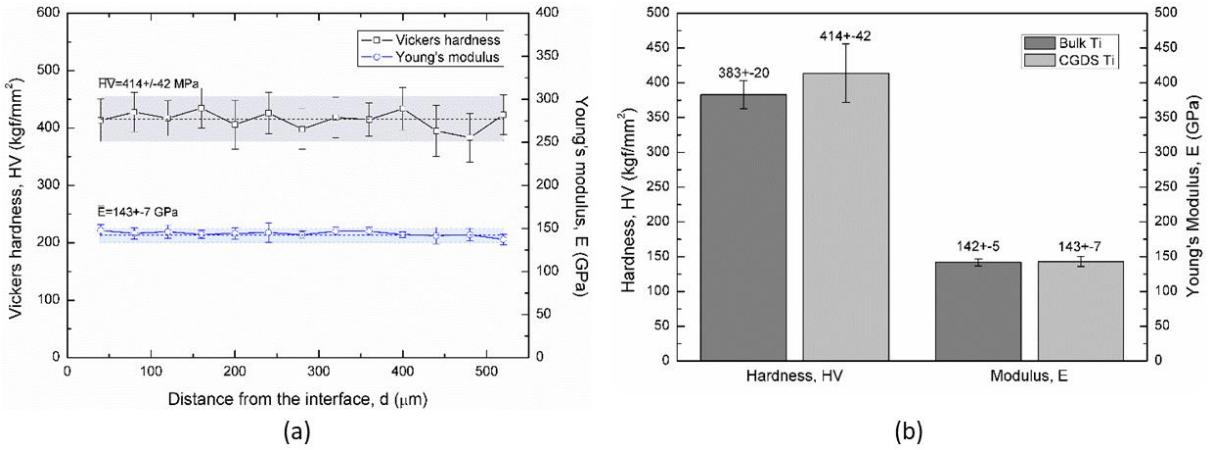

Fig. 5.38: *Hardness and Young's modulus estimated from indentation tests: (a) measurement along the coating thickness; (b) comparison between CGDS Ti coating and bulk Ti*

A deeper analysis of coating obtained at $T = 970\ °C$ and $p = 4.0\ MPa$ was carried out by local measurements at higher indentation load ($100\ mN$). This allows to capture possible inter-splat interaction mechanisms, thanks to the larger stresses and to a process zone comparable with the splat size ($\sim 50\ \mu m$). The splat morphology was highlighted by chemical etching ($92\ ml\ H_2 0, 6\ ml\ HNO_3, 2\ ml\ HF$), as illustrated in Fig. 5.39(a). Fig. 5.39(b), (c) (d) show indents obtained at different locations, that is within the splat (Fig. 5.39(b)) and at the splat boundaries (Fig. 5.39(c) and Fig. 5.39(d)). Fig. 5.39(c) and (d) illustrate two different mechanical responses at the interface. Fig. 5.39(c) shows a typical indent obtained in the case of good interparticle adhesion, similar in terms of both shape and size to the response within the splat shown in Fig. 5.39(b). On the contrary, Fig. 5.39(d) shows a typical indent obtained in the case of weak interface strength. A larger and irregular indent is observed due to a lower local hardness caused by particle debonding.

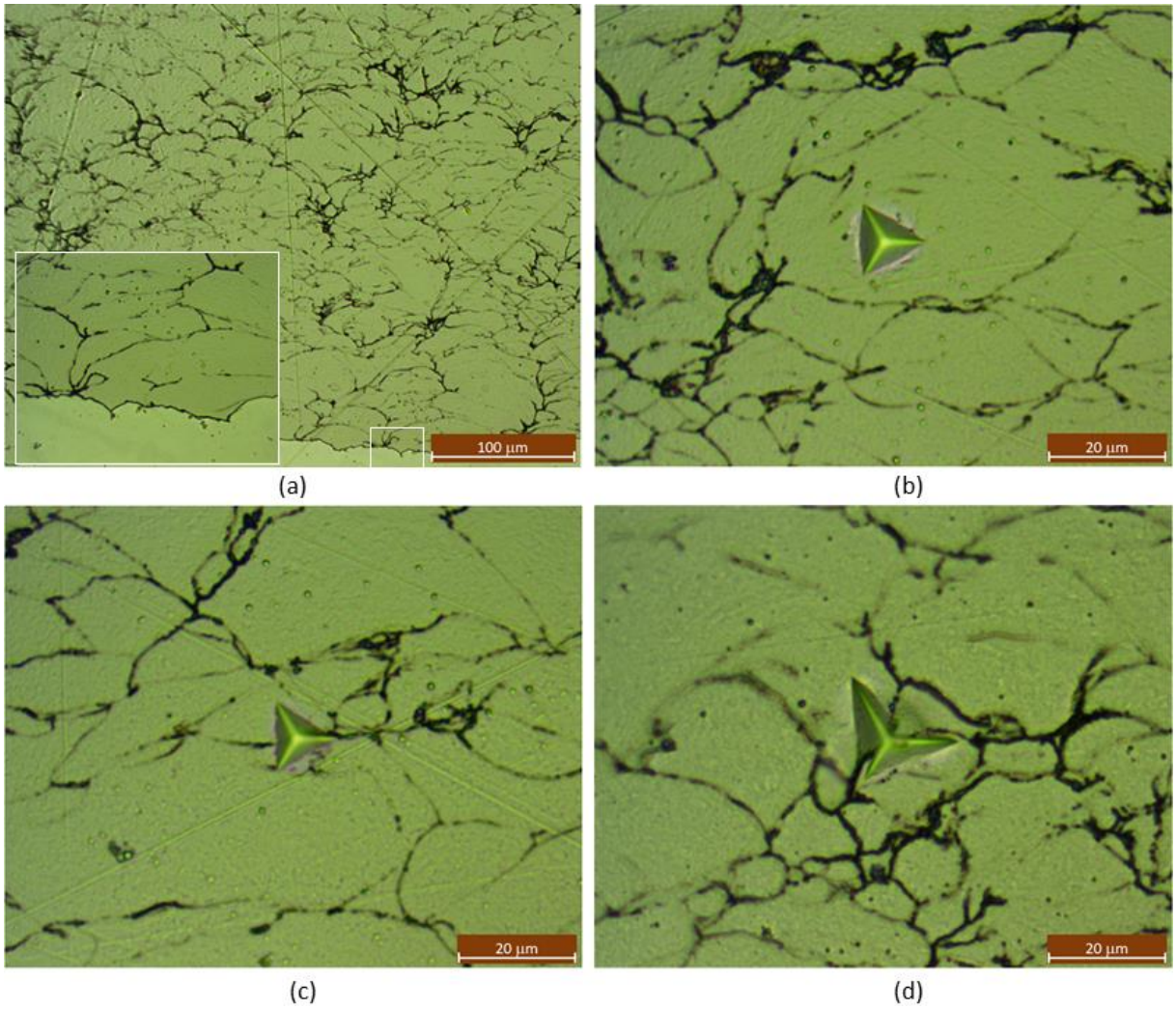

Fig. 5.39: *Light micrographs of a coated sample (T=970° C and p=4.0 MPa): (a) Cross section with highlight of the splat morphology; (b) indentation within the splat; (c) indentation on a splat boundary with good interfacial strength; (d) indentation on a splat boundary with poor interfacial strength*

The mechanisms in Fig. 5.39 are also clearly evident from the force-displacement curves in Fig. 5.40, that reports direct comparisons between the three indentation responses. The curve obtained in the case of poor interface strength (Fig. 5.39(d)) shows a much lower slope of the loading path, resulting in a larger indentation depth. This is a direct consequence of local damage phenomena occurring in the loading stage, mainly due to particle debonding. These local damages can be also captured from inflection points in the curve, as highlighted in Fig. 5.40, that represent the initial development of inter-particle debonding during indentation [138]. This latter mechanism seems to be confirmed by the unchanged unloading stiffness for the three analyzed cases.

Fig. 5.40 also reports the values of elastic and plastic works (W_{el} and W_{pl}) and the corresponding ratio (W_{el}/W_{pl}). It is again shown a similar behavior between intra-splat and inter-splat response in the case of good interfacial strength and a much larger development of plastic work in the case of poor interfacial adhesion.

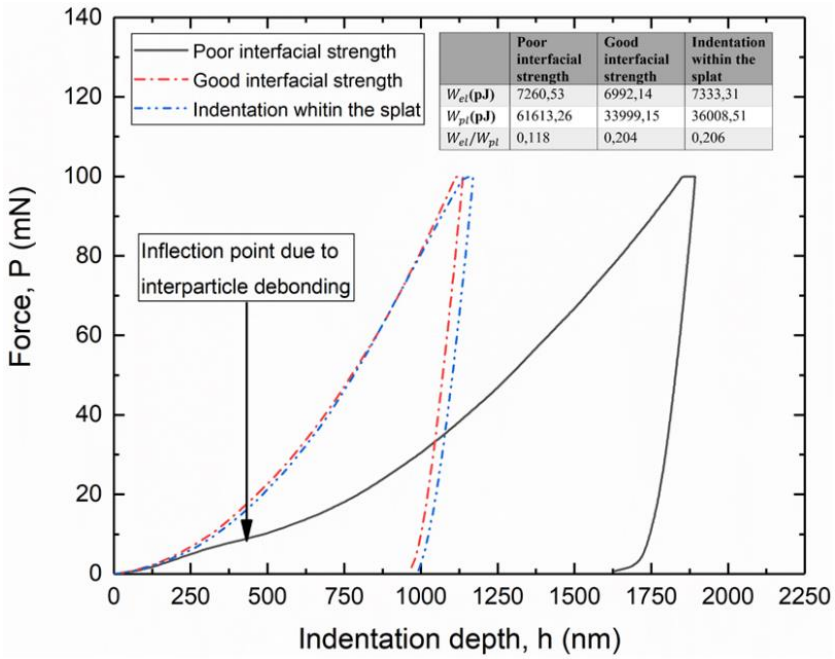

	Poor interfacial strength	Good interfacial strength	Indentation within the splat
W_{el}(pJ)	7260,53	6992,14	7333,31
W_{pl}(pJ)	61613,26	33999,15	36008,51
W_{el}/W_{pl}	0,118	0,204	0,206

Fig. 5.40: *Comparison of the force-displacement curves for local indentations carried out in three different regions (within the splat, splat boundary with good and poor interfacial strength)*

Systematic studies should be carried out with the aim of better analyzing the quality of the deposits, mainly in terms of interface density, as a function of the process parameters. Weak density points could result in possible detrimental effects when dealing with UHV applications, as they represent preferential sites for the formation of tiny leak paths or location of gas trapping leading to inleakage.

A rough estimation of the fraction of weak interfaces was made; a value around 5% was found on about 200 indents.

5.4.3 Adhesion properties

Fig. 5.41 shows the force displacement curves obtained from adhesion tests. Two different behaviors were observed from six nominally identical samples. Large differences in the adhesion strength were recorded among two groups of samples. In particular, three samples (group #2 in. Fig. 5.41) experienced early failures at a nominal stress of $6.4 \pm 1.2\ MPa$ whereas the other three (group #1 in. Fig. 5.41) showed a significantly higher strength equal to $17.8 \pm$

2.2 MPa. Micrographic observations of the fracture surface were carried out for a deeper analysis of the failure mode, as shown in the figure. Complete interfacial fracture occurred in group #1 samples; the coating is completely detached from the coated surface due to the limited adhesion to the steel substrate. This result is in agreement with a previous literature study [138], [140], [171] where even lower strength values were found, in the range $8 - 16\ MPa$, for titanium deposits on stainless-steel substrates with gas (N_2) pressures between 1 and 3 MPa. This result confirms that particle adhesion is a major problem when dealing with hard particles and metal substrates.

As illustrated in Fig. 5.41, adhesion failures were also observed in group #2 samples but the morphology of the fracture surfaces shows mixed mode failure mechanisms; cracks initiate from the external surface of the samples and then propagate by fast fracture phenomena. The cracks are probably due to the formation of external defects/cracks during sample preparation and, therefore, they do not represent the real adhesion strength of the coating. In such cases, highly localized stresses are generated near the crack tip [172] that are much higher than the nominal applied ones.

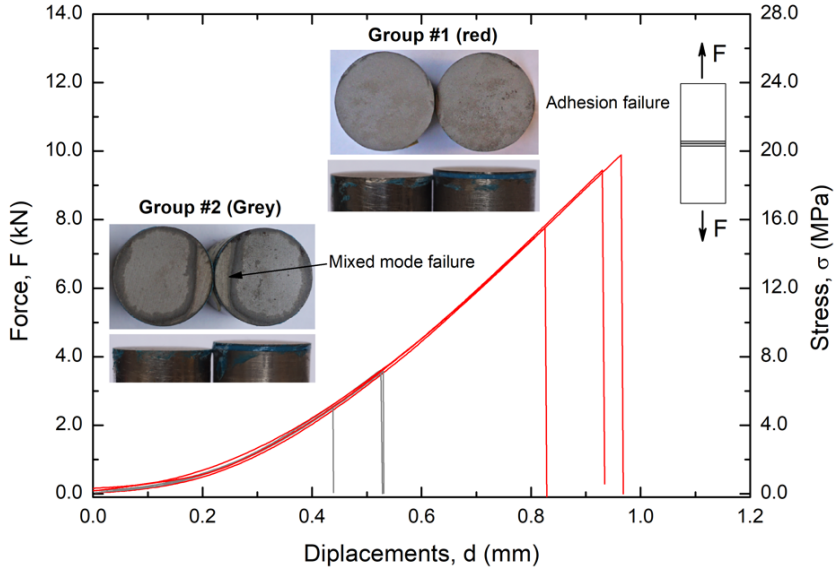

Fig. 5.41: *Force vs displacement curves obtained from adhesion tests with the evidence of two different failure mechanisms.*

5.4.4 Vacuum properties

A typical result obtained by the accumulation-expansion method is shown in Fig. 5.42(a). The signals of the RGA during the opening of the VLV are plotted for 300 μm thick Ti coatings, after 72 hours of accumulation time. As expected, a significant release of H_2 was observed

($mass\ 2\ amu$). However, the leading gas species is N_2 (mass 14 and 28 amu). CH_4 is also clearly identified ($mass\ 12$, 15 and 16 amu). The peak of the Ar signal is about a factor of 100 lower than the one of N_2. The system is enough sensitive to detect an increase of the He ($mass\ 4\ amu$) and CO_2 signals ($mass\ 44\ amu$), but is unable to give any result about CO because the typical peaks of this gas are covered by those of N_2 and CH_4. The RGA did not detect relevant increase of $mass$ 32, 39 and 41 amu. The former is attributed to O_2; the other two signals indicate the presence of C_3H_8, i.e. a sign of hydrocarbon contamination. The same trend was observed for the 500 μm thick coating.

In Fig. 5.42(b), the $mass\ 28\ amu$ curves for the two thicknesses and the background (accumulation vessel without samples) are directly compared for the same accumulation time (72 h). The background signal is around 300 times lower than the ones with the samples. This result rules out the presence of external leaks in the accumulation vessel. The samples are the source of N_2.

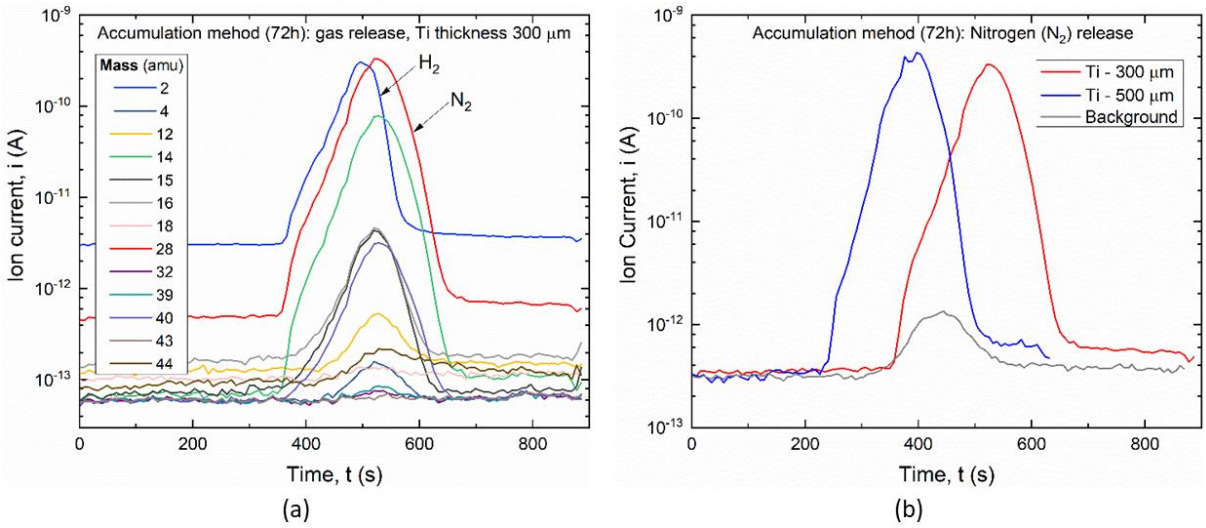

Fig. 5.42: *Gas release of titanium coated samples after 72h of accumulation: (a) release curves for coating thickness of 300 µm and (b) comparison of the N_2 release curves for two coating thickness (300 µm, 500 µm)*

The presence of N_2 can be attributed to three reasons. Firstly, the cold spray process uses nitrogen as propellant gas. Then, N_2 is used in the gas atomization process to produce the Ti powder. Finally, air can be trapped in the coating porosity. The latter hypothesis might be supported by the release of Ar in the ratio expected for the components of air, i.e. of the order of 1%; the absence of O_2 is certainly due to the high sticking probability of baked stainless steel surfaces for this gas. The origin of N_2 release cannot be better identified at this stage of the

research; future studies should be carried out, such as using He as a propellant gas or analyzing the outgassing properties of the powder.

The evolutions of the accumulated H_2 and N_2 quantities, as a function of the accumulation time, are reported in Fig. 5.43. The results obtained from coated samples ($300\ \mu m$, $500\ \mu m$) are compared with the background and bulk titanium. All samples, including Ti Grade 1, have the same total surface area ($4 \times 10^2\ cm^2$).

The Ti samples and the background show a linear increase of the accumulated H_2 quantity. The background outgassing rate per unit surface is about $2 \times 10^{-13}\ mbar\ l\ s^{-1}\ cm^{-2}$. The H_2 outgassing rate of bulk Ti samples is obtained once the background is subtracted. The estimated value is around $2 \times 10^{-14}\ mbar\ l\ s^{-1}\ cm^{-2}$. The trend of H_2 outgassing for the coated samples does not follow the expected linear behavior. The accumulated H_2 quantity tends to stabilize. The H_2 quantity reaches a plateau, which is lower than the background value. These results seem to indicate a H_2 pumping effect of the titanium CGDS coatings. The order of magnitude of the pumping speed is given by the ratio of the outgassing rate to the ultimate pressure reached in the accumulation vessel. For the first value, the one of the bakeout is selected, roughly $10^{-10}\ mbar\ l\ s^{-1}$, since for low accumulation time all measurements are close. The second value is obtained from the ratio of the accumulated gas quantity and the volume of the accumulation vessel ($8 \times 10^4\ mm^3$), i.e. in the order of $10^{-4}\ mbar$. Therefore, the order of magnitude of the pumping speed is $10^{-6}\ l\ s^{-1}$ which gives very low H_2 sticking probability in the order of 10^{-8}.

As expected the accumulated N_2 quantity is negligible for both background and Ti Grade 1 samples. On the contrary, a nearly linear increase with the accumulation time was observed in coated samples, with similar values for the two thickness after $72\ h$. Total accumulated N_2 quantity are lower than H_2 but they are not affected by the background resulting in an higher N_2 outgassing rate of about $6.5 \times 10^{-14}\ mbar\ l\ s^{-1}\ cm^{-2}$.

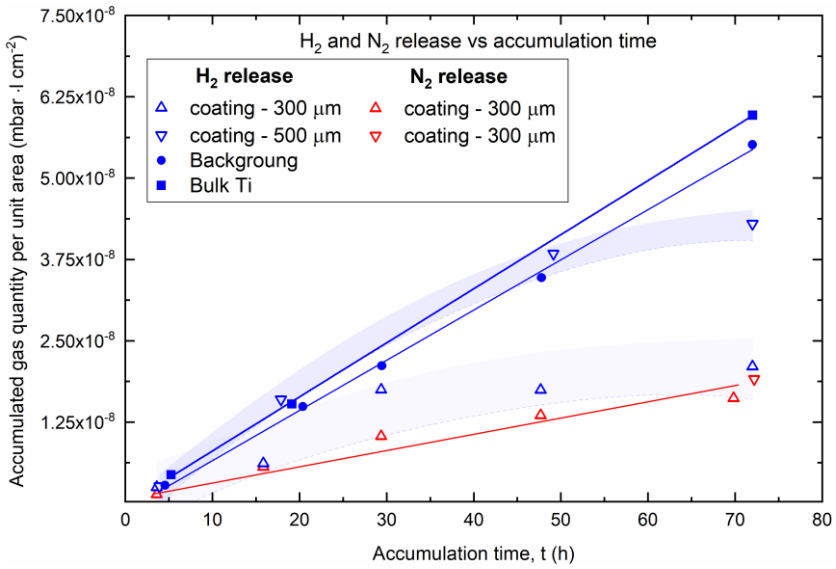

Fig. 5.43: *Accumulated hydrogen quantities as a function of the accumulation time: comparison among coated samples with two thicknesses (300 µm and 500 µm), bulk Ti Grade 1 and the system background. All samples have the same total surface area (4×104 mm²)*

Fig. 5.44 reports the desorption spectra measured by TPD (outgassing rate vs heating temperature) in the temperature range $20\,°C$ to $950\,°C$ (heating rate of $5\,K\,min^{-1}$) for the coated samples with two thicknesses ($300\,\mu m$ and $500\,\mu m$) and bulk Ti Grade 1. Analyzed species are: H_2, N_2, H_2O, CH_4, CO, CO_2, O_2 and Ar.

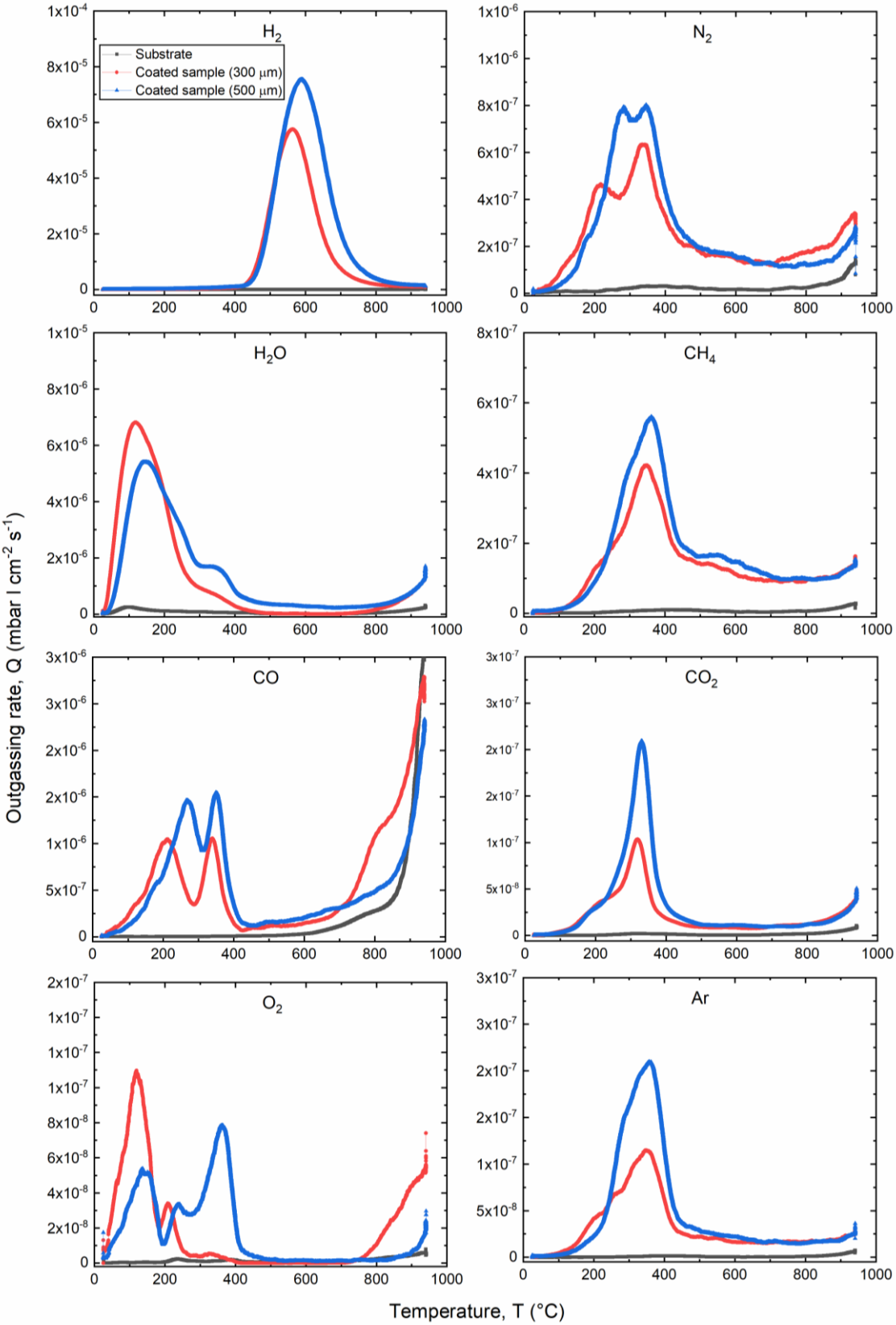

Fig. 5.44: *Thermal desorption spectra (heating rate of 5 K min^{-1}): comparison among coated samples with two thicknesses (300 μm and 500 μm) and bulk Ti Grade 1*

It can be supposed that the increase of N_2 outgassing around $850\ °C$ depends on the system background-substrate and similar considerations apply to other species (e.g. CO); moreover, it seems that outgassing rate are higher in the thicker coatings ($500\ \mu m$) for all species.

Spectra of O_2 seems to be different for the two thicknesses (different peak temperatures), however the values are very low (three order of magnitude lower than H_2). It can be supposed that this trend depends on the smoothing process of the raw data.

Fig. 5.45 reports the calculated H_2 and N_2 gas concentration in the Ti coatings ($ppma$) obtained from samples with two coating thicknesses ($300\ \mu m$ and $500\ \mu m$). For comparison, the same data measured for bulk Ti (Grade 1) are shown.

Coated samples with the two thicknesses show large H_2 concentrations with values of $753\ ppma$ and $441\ ppma$ for the $500\ \mu m$ and $300\ \mu m$ thick coatings, respectively. These concentrations are much higher than bulk Ti, that that is about $83\ ppma$. The figure shows that N_2 concentrations are much lower, with values around $17\ ppma$ and $12\ ppma$ for $500\ \mu m$ and $300\ \mu m$ thick coatings, respectively. As expected bulk Ti does not exhibit measurable values of N_2.

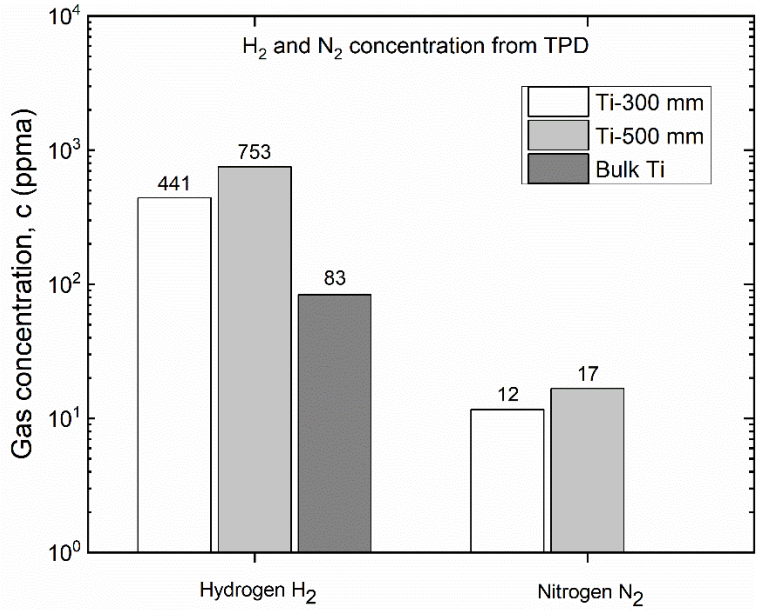

Fig. 5.45: *Hydrogen and nitrogen (H_2 and N_2) gas concentrations (ppma) obtained from thermal programmed desorption for CGDS coated samples (300 µm and 500 µm) and bulk Ti*

The higher H_2 concentration in coated samples can be attributed to the surface roughness of coatings. In fact, surface morphology may increase the total surface involved in the process, leading to a higher outgassing. Hydrogen intake during particle production and the cold spray process might also be the cause of the higher concentration.

5.4.5 Leak tightness

Table 5.1 shows the results of the leak tightness tests. Six different samples, obtained by using optimal deposition parameters ($T = 970\ °C$ and $p = 4.0\ MPa$) with two different thicknesses ($500\ \mu m$ and $800\ \mu m$), were analyzed and two types of tests were carried out (test type #1 and #2), as described in the materials and methods section. Despite the results of micrographic investigations and indentation tests reported in the previous sections that reveled good adhesion to the substrate and no evidence of internal porosity, all the samples in test type #1 experienced relevant leak rates, in the range $1.0 \times 10^{-6} - 6.8 \times 10^{-5}\ mbar\ l\ s^{-1}$, much higher than standard requirements for UHV applications.

In test type #2, leak rates in the range $1.0 \times 10^{-10} - 1.0 \times 10^{-9}\ mbar\ l\ s^{-1}$ were recorded for three samples (1, 4 and 5) over six. This implies that, for these samples, the main leak paths detected in test #1 are located at the coating/substrate interface. This is in agreement with the results of adhesion tests, i.e. interface leak paths have formed due to the low adhesion strength and they may have been triggered by possible local interface damage caused by stresses and/or vibrations during machining operations carried out to remove the steel substrate.

The other three samples, two with thickness of $500\ \mu m$ (2, 3) and one of $800\ \mu m$ (6) exhibited He leak rates between 1.0×10^{-7} and $5.0 \times 10^{-6}\ mbar\ l\ s^{-1}$. The cause is probably through-thickness tiny paths between the splats, possibly triggered by machining operations, that are not easily visible from the micrographic observations. This is in agreement with the weak interfacial strength at some splat boundaries, as confirmed by local indentation measurements (see Fig. 5.39(d)). Results indicate that great care should be devoted for a fine control of the coating process in order to obtain leak tight deposits.

Table 5.1: Results of He leak tightness tests

Sample #	Thickness (μm)	He leak rate (mbar l s^{-1})	
		Test #1	Test #2
1	500	$1.0\ 10^{-6}$	$<1.0\ 10^{-10}$
2	500	$4.0\ 10^{-5}$	$1.0\ 10^{-7}$
3	500	$6.8\ 10^{-5}$	$1.0\ 10^{-6}$
4	800	$3.0\ 10^{-6}$	$6.0\ 10^{-10}$
5	800	$2.0\ 10^{-5}$	$1.0\ 10^{-9}$
6	800	$1.2\ 10^{-5}$	$5.0\ 10^{-6}$

Conclusions and future works

Systematic experimental tests have been carried out in this thesis to assess the mechanical and tribological performance of Stellite-6 coatings and the adhesion and vacuum properties of pure Titanium coatings obtained by Cold Gas Dynamic Spray (CGDS).

Different combinations of process have been analyzed. Mechanical properties have been evaluated on the macro-scale by adhesion test while micro- and nano-indentation tests, under different load, have been used in order to characterize both Stellite-6 and Ti coatings on the micro- and nano scale. Some conclusions can be drawn and have been reported below.

Porosity and oxidation on the splats boundaries are common issues in most of the coating methods whereas CGDS technique, as a solid-state process, could lead to pore- and oxide-free coatings, allowing to eliminate the dilution existing in welding processes commonly used for stellite deposition. Even from the preliminary experiments Cold Gas Dynamic Spray technique has been demonstrated to be successful to produce stellite coatings. In fact, in spite of the difficulty to reach the critical velocity, coatings characterized by low porosity, around 2 %, were obtained. Moreover, high values of surface micro-hardness have been obtained, with a mean value of $700\,HV_{0.1}$, that is higher than the one of Stellite-6 bulk material (around $400\,HV_{0.1}$), thanks to the large plastic deformation and hardening occurring during particle impact. Hardness results show significant variability with coefficient of variation (σ/μ) around 0.2. It is attributed to local mechanisms related to non-homogeneous mechanical properties of the coatings at the micro-scale. This is confirmed by the observed debonding mechanism occurring during indentation near the splat boundary. As a consequence, splat boundaries represent weak point of the coating.

Regarding the tribological properties in the condition imposed by Pin-on-disk experiment, the study revealed that the coefficient of friction is not affected by the applied load, in the range $5-10\,N$, and its low value, around 0.51, suggest that CGDS can be used in anti-wear applications. While the variation of wear rate with the applied load is attributed to local

mechanisms, such as evident the pull-out phenomena observed when the applied load is equal to $5N$.

In the second experimental campaign, together with gas temperature and pressure, the influence of torch scan speed on the mechanical and tribological properties of Stellite-6 coatings was analyzed.

Torch scan speed directly affects the temperature evolution of the substrate during deposition, and this latter value can be considered as a significant indirect process parameter.

The High Pressure CGDS equipment was used and different combinations of high energy deposition parameters while the temperature evolution of the substrate during deposition was also estimated, by infrared thermography. The substrate temperature in the impact zone significantly affects the deformation mechanisms of the particles and, consequently, the quality of the coating. This latter was analyzed by local mechanical measurements, carried out by instrumented micro- and nano-indentations as well as by wear tests.

Results revealed that both direct and indirect process parameters play very important roles on the mechanical and tribological properties of the coatings and optimal conditions were identified.

In particular, high energy parameters ($T \geq 970\ °C$ and $p \geq 4\ MPa$) are required for Stellite-6 alloy, due to its high yield strength and melting point, and, for a given set of T and p, the lower the scan speed (v) the better the mechanical properties of the coatings in terms of compactness, micro- and nano-hardness and reduced Young's modulus.

The effect of the traverse scan speed on compactness and mechanical properties is extremely evident when lowest values of gas temperature and pressure are imposed, whereas for the highest ones less differences are noticeable in the obtained results of micro- and nano-indentation test.

Systematic analysis of IR data revealed that the scanning speed significantly affects the substrate temperature in the impact zone, that it actually considered as a significant driving force for particle deformation. Work hardening introduced during deposition process is affected by scanning speed; for depositions carried out at $300\ mm/s$, in which the substrate temperature is lower, the effect of gas temperature and pressure can be observed. The higher velocity of the particle leads to higher work hardening in the coating obtained at $T = 1050\ °C$ and $p = 5\ MPa$. For the scanning speed equal to $30\ mm$ coatings show very slight difference in the value W_{pl}/W_{tot} ratio, due to the higher temperature reached by the surface.

Regarding tribological properties in pin-on-disk condition, the measured wear coefficient seem to be lower, for both sets of T and p, when the highest value of scan speed is selected. In particular, coatings obtained using T= $970\ °C$, $p = 4\ MPa$ and $v = 300\ mm/s$ showed the presence of tribo-film consisting of highly-strained oxidized material, as a consequence of the presence of several defects along the thickness of the coating; in fact, it was observed that, decreasing scanning speed elastic modulus increases more quickly if compared with trend of the hardness response. In fact, tribological properties are better when the strain-to-failure ratio (H/E) increases. Moreover, the presence of a lot of debris in the wear track during the test has contributed to further erode the surface, leading to a bigger value of the wear coefficient. However, in some works, focused on the wear behavior of thermal sprayed Stellite-6 coatings, similar values are found comparing our results with those ones related to laser clad Stellite-6 coating proposed by Houdková et al. [159].

With regard to the tribological behavior during reciprocated dry sliding, the systematic in-depth study on tribological performance of the wear of Stellite-6 coatings revealed that detachment and pull-out phenomena mainly affect the worn surface of coatings tested in low speed conditions. On the contrary adhesive wear mechanism is operative for high speed test in accordance with the theory of wear for the Steel-CoCr system [156]. These conclusions are supported by the following consideration:

- Plastic deformation mechanisms cause the initiation and propagation of ductile cracks in the subsurface; typically at splat boundaries or pores.
- Material is at first displaced towards the coating surface whereupon detachment of the material due to elastic fracture forms a wear-particle.
- Debris are thin and plate-like with debris size being as large as powder diameter in some cases.
- The trends in wear volume data results to be linear in high speed test and according to Archard equation (Eq. 1.30) unlike volume data related to low speed test.

For all experiments the observed coefficients of friction were in the range of $0.35–0.65$ which is similar to those observed in the literature. Likewise, the volume loss experienced under the given loading conditions was in the same range as those from the literature, typically corresponding to specific wear rates of the order of $6.5 \times 10^{-7} \div 2.5 \times 10^{-6}\ mm^3/Nm$ and $2 \times 10^{-5} \div 5 \times 10^{-5}\ mm^3/Nm$ for the pin and plate respectively in low speed condition ($v =$

$0.1\ m/s$), and of the order of $2.75 \times 10^{-6} \div 2 \times 10^{-5}\ mm^3/Nm$ and $6.5 \times 10^{-5} \div 2.5 \times 10^{-4}\ mm^3/Nm$ for tests carried out at high speed ($v = 0.5\ m/s$) [55], [156], [173].

Differences in the wear coefficient due to speed may be explained considering that, at low speed, wear particles can be reintroduced into the wear track, as a consequence of pull-out phenomena, and heating at the wear interface causes the formation of oxidized zones.

The reduction of dynamic coefficient of friction with the contact pressure has been attributed to the increase of strained oxidized pulled-out particle that act as solid lubricant.

Regarding samples tested at high speed, dynamic coefficient of friction appears to be on average lower compared to low speed experiments, as a consequence of the higher temperature reached during the high speed tests. The increasing trend of coefficient of friction whit the applied load can be attributed to the presence of sharp edge observed on the wear surface.

Cross-sectional material analysis of the worn sample has been carried out using nano-indentation techniques. The experiments revealed a different response in the samples tested in low speed condition compared to those ones tested at high speed. In fact, when the sliding speed was set equal to $0.1\ m/s$ an increase in stiffness with the applied load was observed, due to grain growth phenomena [166], [167] and to the closure of subsuperficial defects below the worn surface but further study is needed to clarify this hypothesis. With regard to high speed tests a reduction in the stiffness and in the hardness response as a function of the contact pressure was observed, due to the increased presence of cracks inside the coating.

Feasibility studies have been undertaken to assess the possible use of cold gas dynamic spray (CGDS) techniques for future developments of the accelerator technologies. In fact, CGDS would provide significant advantages for manufacturing of several multi-materials layered components especially for complex shaped components to be used in ultra-high vacuum (UHV) environments. Material candidates for CGDS coatings at CERN are copper, aluminum and titanium. However, some technical difficulties arise when dealing with titanium coatings on stainless steel substrates due to the high yielding points of both materials.

Both mechanical and vacuum properties of pure titanium coatings on $AISI\ 316L$ steel substrates, obtained by high pressure CGDS equipment, were analyzed. In this regard it can be concluded that high compactness and homogeneity were obtained, when using high energy deposition parameters ($p{\sim}4\ MPa$, T$\sim$1000 $°C$), whereas a limited adhesion strength with steel substrate was measured ($\sim$18 MPa). In fact, interface actually represents the weakest point of this bi-material system.

An abnormal nitrogen release was observed that is attributed to the gas entrapped during deposition (N_2 is the propellent gas used in the CGDS process) or long stay in atmospheric air. The quantity of accumulated hydrogen does not follow a liner rise. Such an intriguing behavior points to the existence of a small (sticking probability in the order of 10^{-8}) but measureable H_2 pumping speed after bakeout at $150\ °C$ for 24 hours.

Unacceptable helium leak rates were detected; they are attributed to interface leak paths. On the contrary, the leak rates through the coating thickness are much lower; complete tightness can be achieved.

Further studies will be carried out in order to better understand the tribological performances of Stellite-6 coatings in a wider range of contact pressure. Different sliding geometry should be evaluated and different environmental conditions, i.e. wet or corrosive, will be analyzed. Moreover, keeping in mind that the temperature reached in the contact zone could imply a noticeable modification in the microstructure of the coating, IR investigation should be carried out in order to better understand the role of the surface temperature on the wear mechanism that occur during the sliding. At the same, a mechanistic material model, that capture the influence of temperature, could be able to clarify this point.

Finally, further studies will aim to improve the interface strength of pure titanium coatings by a better tuning of the process parameters, dedicated surface modifications and optimized robot deposition kinematics. In fact, high adhesion to the substrate is required to avoid the risk to have possible leak paths at the coating-substrate interface.

References

[1] H. Assadi, H. Kreye, F. Gärtner, and T. Klassen, “Cold spraying – A materials perspective,” *Acta Mater.*, vol. 116, pp. 382–407, 2016, doi: 10.1016/j.actamat.2016.06.034.

[2] T. Schmidt *et al.*, “From particle acceleration to impact and bonding in cold spraying,” *J. Therm. Spray Technol.*, vol. 18, no. 5–6, pp. 794–808, 2009, doi: 10.1007/s11666-009-9357-7.

[3] T. Stoltenhoff, H. Kreye, and H. J. Richter, “An analysis of the cold spray process and its coatings,” *J. Therm. Spray Technol.*, vol. 11, no. 4, pp. 542–550, 2002, doi: 10.1361/105996302770348682.

[4] H. Assadi, F. Gärtner, T. Stoltenhoff, and H. Kreye, “Bonding mechanism in cold gas spraying,” *Acta Mater.*, vol. 51, no. 15, pp. 4379–4394, 2003, doi: 10.1016/S1359-6454(03)00274-X.

[5] A. Moridi, S. M. Hassani-Gangaraj, M. Guagliano, and M. Dao, “Cold spray coating: Review of material systems and future perspectives,” *Surf. Eng.*, vol. 30, no. 6, pp. 369–395, 2014, doi: 10.1179/1743294414Y.0000000270.

[6] A. Sova, I. Smurov, M. Doubenskaia, and P. Petrovskiy, “Deposition of aluminum powder by cold spray micronozzle,” *Int. J. Adv. Manuf. Technol.*, vol. 95, no. 9–12, pp. 3745–3752, 2018, doi: 10.1007/s00170-017-1443-2.

[7] S. L. Fu *et al.*, “Novel Method of Aluminum to Copper Bonding by Cold Spray,” *J. Therm. Spray Technol.*, vol. 27, no. 4, pp. 624–640, 2018, doi: 10.1007/s11666-018-0707-1.

[8] P. Sirvent, M. A. Garrido, C. J. Múnez, P. Poza, and S. Vezzù, “Effect of higher deposition temperatures on the microstructure and mechanical properties of Al 2024 cold sprayed coatings,” *Surf. Coatings Technol.*, vol. 337, no. October 2017, pp. 461–470, 2018, doi: 10.1016/j.surfcoat.2018.01.055.

[9] A. Alkhimov, A. Papyrin, and V. Kosarev, “Gas-dynamic spraying method for applying a coating,” *US Pat. 5,302,414*, no. 19, p. 13, 1994, [Online]. Available: https://patentimages.storage.googleapis.com/92/16/7f/93e032d9041894/US5302414.pdf.

[10] “Impact Innovations - Your partner for cold spray and engineering.” https://www.impact-innovations.com/en/coldgas/impactspraysystem511_en.html.

[11] R. N. Raoelison, C. Verdy, and H. Liao, “Cold gas dynamic spray additive manufacturing today: Deposit possibilities, technological solutions and viable applications,” *Mater. Des.*, vol. 133, pp. 266–287, 2017, doi: 10.1016/j.matdes.2017.07.067.

[12] R. C. Dykhuizen, M. F. Smith, D. L. Gilmore, R. A. Neiser, X. Jiang, and S. Sampath, “Impact of high velocity cold spray particles,” *J. Therm. Spray Technol.*, vol. 8, no. 4, pp. 559–564, 1999, doi: 10.1361/105996399770350250.

[13] C. M. Kay and J. Karthikeyan, *High Pressure Cold Spray: Principles and Applications*. ASM International, 2016.

[14] R. C. Dykhuizen and M. F. Smith, “Gas Dynamic Principles of Cold Spray,” *J. Therm. Spray Technol.*, vol. 7, no. 2, pp. 205–212, 1998, doi: 10.1361/105996398770350945.

[15] J. Ghajar Afshin, “The Engineering Handbook,” Oklahoma State University, 2016.

[16] M. Grujicic, C. L. Zhao, C. Tong, W. S. DeRosset, and D. Helfritch, “Analysis of the impact velocity of powder particles in the cold-gas dynamic-spray process,” *Mater. Sci. Eng. A*, vol. 368, no. 1–2, pp. 222–230, 2004, doi: 10.1016/j.msea.2003.10.312.

[17] H. Marsh, “Modern compressible flow,” *International Journal of Heat and Fluid Flow*, vol. 4, no. 1. pp. 59–60, 1983, doi: 10.1016/0142-727x(83)90029-2.

[18] V. K. Champagne, “The Cold Spray Materials Deposition Process. Fundamentals and Applications.” 2007.

[19] R. A. Neiser, J. E. Brockmann, and T. J. O’hern, “Wire melting and droplet atomization in a high velocity oxy-fuel jet,” *Therm. Spray Sci. Technol. C.C. Berndt S. Sampath, Ed., ASM Int.*, pp. 99–104, 1995.

[20] J. Voyer, T. Stoltenhoff, and H. Kreye, “Cold spraying – state of the art and applicability,” in *Proceedings of International Thermal Spray Conference*, 2002.

[21] M. Grujicic, C. L. Zhao, W. . Derosset, and D. Helfritch, “Adiabatic shear instability based mechanism for particle/substrate bonding in the cold-gas dynamic-spray process. Mater Des,” *Mater. Des.*, vol. 25, pp. 681–688, 2004, doi:

10.1016/j.matdes.2004.03.008.

[22] Y. Zou, W. Qin, E. Irissou, J. G. Legoux, S. Yue, and J. A. Szpunar, “Dynamic recrystallization in the particle/particle interfacial region of cold-sprayed nickel coating: Electron backscatter diffraction characterization,” *Scr. Mater.*, vol. 61, no. 9, pp. 899–902, 2009, doi: 10.1016/j.scriptamat.2009.07.020.

[23] M. Vijay, A. Tieu, W. Yan, B. Daniels, and M. Xu, “Enhancing the Adhesion Strength of Cold Gas Dynamic Sprayed Coatings By Preparing the Substrates With the High-Frequency Pulsed Waterjet,” in *2015 WJTA-IMCA Conference and Expo*, 2015.

[24] R. N. Raoelison *et al.*, “Cold gas dynamic spray technology: A comprehensive review of processing conditions for various technological developments till to date,” *Addit. Manuf.*, vol. 19, pp. 134–159, 2018, doi: 10.1016/j.addma.2017.07.001.

[25] R. Kromer, S. Costil, C. Verdy, S. Gojon, and H. Liao, “Laser surface texturing to enhance adhesion bond strength of spray coatings – Cold spraying, wire-arc spraying, and atmospheric plasma spraying,” *Surf. Coatings Technol.*, vol. 352, pp. 642–653, 2018, doi: 10.1016/j.surfcoat.2017.05.007.

[26] M. Grujicic, J. R. Saylor, D. E. Beasley, W. S. DeRosset, and D. Helfritch, “Computational analysis of the interfacial bonding between feed-powder particles and the substrate in the cold-gas dynamic-spray process,” *Appl. Surf. Sci.*, vol. 219, no. 3–4, pp. 211–227, 2003, doi: 10.1016/S0169-4332(03)00643-3.

[27] H. Assadi *et al.*, “On parameter selection in cold spraying,” *J. Therm. Spray Technol.*, vol. 20, no. 6, pp. 1161–1176, 2011, doi: 10.1007/s11666-011-9662-9.

[28] R. G. Maev, E. Strumban, V. Leshchinskiy, and D. Dzhurinskiy, “Repair applications of the LPCS process,” in *CSAT Workshop. Worcester, USA*, 2014.

[29] J. G. Legoux, D. Poirier, and P. Vo, “Development of cold spray coating for nuclear waste storage container application,” in *CSAT Workshop. Worcester, USA*, 2014.

[30] S. Marx and A. Paul, “Cold spray coatings on hard surfaces. other commercial applications,” 2016. https://www.coldsprayteam.com/.

[31] M. Matthews, “COLD SPRAY RESEARCH AND APPLICATIONS IN AUSTRALIAN DEFENCE AND AEROSPACE,” 2012.

[32] C. Widener, B. J. Rob Hrabe, and V. Champagne, “B1 Bomber-FEB Panel Repair by Cold Spray,” in *CSAT Meeting, WPI, Worcester, MA*, 2012.

[33] A. Kashirin, O. Klyuev, T. Buzdygar, and A. Shkodkin, “Modern Applications of the

Low Pressure Cold Spray," *Proc. 2011 Int. Therm. Spray Conf.*, 2011.

[34] R. E. Blose, B. H. Walker, R. M. Walker, and S. H. Froes, "New opportunities to use cold spray process for applying additive features to titanium alloys," *Met. Powder Rep.*, vol. 61, no. 9, pp. 30–37, 2006, doi: 10.1016/S0026-0657(06)70713-5.

[35] "DYMET technology - Application." http://dymet.info/en/app.html.

[36] H. P. Jost, "Tribology — Origin and future," *Wear*, vol. 136, no. 1, pp. 1–17, 1990, doi: https://doi.org/10.1016/0043-1648(90)90068-L.

[37] C. M. Taylor, "Automobile engine tribology—design considerations for efficiency and durability," *Wear*, vol. 221, no. 1, pp. 1–8, 1998, doi: https://doi.org/10.1016/S0043-1648(98)00253-1.

[38] M. B. Peterson and W. O. Winer, *Wear control handbook*. New York, N.Y. (345 East 47th St., New York, N.Y. 10017) : American Society of Mechanical Engineers, ©1980, 1980.

[39] E. Rabinowicz, "Lubrication of Metal Surfaces by Oxide Films," *A S L E Trans.*, vol. 10, no. 4, pp. 400–407, 1967, doi: 10.1080/05698196708972199.

[40] F. P. Bowden and D. Tabor, "The Seizure of Metals," *Proc. Inst. Mech. Eng.*, vol. 160, no. 1, pp. 380–383, 1949, doi: 10.1243/pime_proc_1949_160_036_02.

[41] F. P. Bowden and D. Tabor, "The Friction and Lubrication of Solids," *Am. J. Phys.*, vol. 19, no. 7, pp. 428–429, 1951, doi: 10.1119/1.1933017.

[42] K. C. Antony, "WEAR-RESISTANT COBALT-BASE ALLOYS.," *J. Met.*, vol. 35, no. 2, pp. 52–60, 1983, [Online]. Available: https://www.scopus.com/inward/record.uri?eid=2-s2.0-0020707934&partnerID=40&md5=ad6eda0619c079c2faa5f46e4e41f896.

[43] A. Frenk and W. Kurz, "Microstructural effects on the sliding wear resistance of a cobalt-based alloy," *Wear*, vol. 174, no. 1–2, pp. 81–91, 1994, doi: 10.1016/0043-1648(94)90089-2.

[44] A. Frenk and W. Kurz, "High speed laser cladding: solidification conditions and microstructure of a cobalt-based alloy," *Mater. Sci. Eng. A*, vol. 173, no. 1, pp. 339–342, 1993, doi: https://doi.org/10.1016/0921-5093(93)90240-F.

[45] A. Osma, E. S. Kayali, and M. L. Öveçoğlu, "The effect of elevated temperature and silicon addition on a cobalt-based wear resistant superalloy," *J. Mater. Sci.*, vol. 31, no. 17, pp. 4603–4608, 1996, doi: 10.1007/BF00366358.

[46] I. Radu, D. Y. Li, and R. Llewellyn, “Tribological behavior of Stellite 21 modified with yttrium,” *Wear*, vol. 257, no. 11, pp. 1154–1166, 2004, doi: 10.1016/j.wear.2004.07.013.

[47] J. R. Davis, *Metals Handbook Desk Edition, 2nd Ed.* ASM International, 1998.

[48] A. J. Hickl, “ALTERNATE TO COBALT-BASE HARDFACING ALLOYS.,” *J. Met.*, vol. 32, no. 3, pp. 6–12, 1980, [Online]. Available: https://www.scopus.com/inward/record.uri?eid=2-s2.0-0018996645&partnerID=40&md5=e9fee38ea5a61ca8004ba2c2c9a73a62.

[49] C. J. Heathcock, A. Ball, and B. E. Protheroe, “Cavitation erosion of cobalt-based Stellite® alloys, cemented carbides and surface-treated low alloy steels,” *Wear*, vol. 74, no. 1, pp. 11–26, 1981, doi: https://doi.org/10.1016/0043-1648(81)90191-5.

[50] J. D. WhITTENBERGER, “A Review of: ‘SUPERALLOYS II’ edited by CT. Sims, N.S. Stoloff, and W.C. Hagel A Wiley-Interscience Publication John Wiley & Sons, New York, NY 615 pages, hardcover, 1987,” *Mater. Manuf. Process.*, vol. 7, no. 3, pp. 463–468, 1992, doi: 10.1080/10426919208947432.

[51] K. J. Bhansali and A. E. Miller, “The role of stacking fault energy on galling and wear behavior,” *Wear*, vol. 75, no. 2, pp. 241–252, 1982, doi: https://doi.org/10.1016/0043-1648(82)90151-X.

[52] W. L. Silence, “Effect of Structure on Wear Resistance of Co-, Fe-, and Ni-Base Alloys,” *J. Lubr. Technol.*, vol. 100, no. 3, pp. 428–435, 1978, doi: 10.1115/1.3453203.

[53] J. L. De Mol Van Otterloo and J. T. M. De Hosson, “Microstructure and abrasive wear of cobalt-based laser coatings,” *Scr. Mater.*, vol. 36, no. 2, pp. 239–245, 1997, doi: 10.1016/S1359-6462(96)00346-6.

[54] P. M. DUNCKLEY, T. F. J. QUINN, and J. SALTER, “STUDIES OF THE UNLUBRICATED WEAR OF A COMMERCIAL COBALT-BASE ALLOY AT EMPERATURES UP TO ABOUT 400 C.,” *ASLE TRANS.*, vol. 19, no. 3, p. JULY, 1976, 1976, [Online]. Available: https://www.scopus.com/inward/record.uri?eid=2-s2.0-0016901042&partnerID=40&md5=c5f0bf55e75ff151a791cd4d220c3f0f.

[55] H. So, C. T. Chen, and Y. A. Chen, “Wear behaviours of laser-clad stellite alloy 6,” *Wear*, vol. 192, no. 1–2, pp. 78–84, 1996, doi: 10.1016/0043-1648(95)06769-8.

[56] J. Hasson and L. Otterloo, “Surface engineering with lasers: Application to Co based materials,” *Surf. Eng.*, vol. 13, pp. 471–482, 1997, doi: 10.1179/sur.1997.13.6.471.

[57] C. A. Liu, M. J. Humphries, and D. W. Mason, “Effect of laser-processing parameters

on the formation and properties of a stellite hardfacing coating," *Thin Solid Films*, vol. 107, no. 3, pp. 251–257, 1983, doi: https://doi.org/10.1016/0040-6090(83)90404-2.

[58] A. Frenk, N. Henchoz, and W. Kurz, "Laser cladding of a cobalt-based alloy: Processing parameters and microstructure," *Zeitschrift fuer Met. Res. Adv. Tech.*, vol. 84, no. 12, pp. 886–892, 1993, [Online]. Available: https://www.scopus.com/inward/record.uri?eid=2-s2.0-0027842484&partnerID=40&md5=7f7ae8925930a9b7b390ed04ea71bbcc.

[59] Y. P. Kathuria and A. Tsuboi, "Laser cladding of Stellite #6: a detailed analysis," in *High-Power Lasers: Applications and Emerging Applications*, 1996, vol. 2789, pp. 86–92, doi: 10.1117/12.251166.

[60] A. Frenk, M. Vandyoussefi, J. D. Wagniere, A. Zryd, and W. Kurz, "Analysis of the laser-cladding process for stellite on steel," *Metall. Mater. Trans. B Process Metall. Mater. Process. Sci.*, vol. 28, no. 3, pp. 501–508, 1997, doi: 10.1007/s11663-997-0117-0.

[61] M. L. Capp and J. M. Rigsbee, "Laser processing of plasma-sprayed coatings," *Mater. Sci. Eng.*, vol. 62, no. 1, pp. 49–56, 1984, doi: https://doi.org/10.1016/0025-5416(84)90266-0.

[62] J. Vikström, "Galling resistance of hardfacing alloys replacing Stellite," *Wear*, vol. 179, no. 1, pp. 143–146, 1994, doi: https://doi.org/10.1016/0043-1648(94)90232-1.

[63] J. W. CHRISTIAN, "Kinetics of Martensitic Transformations," in *The Theory of Transformations in Metals and Alloys*, J. W. CHRISTIAN, Ed. Oxford: Pergamon, 2002, pp. 1062–1075.

[64] J. C. Shin, J. M. Doh, J. K. Yoon, D. Y. Lee, and J. S. Kim, "Effect of molybdenum on the microstructure and wear resistance of cobalt-base Stellite hardfacing alloys," *Surf. Coatings Technol.*, vol. 166, no. 2–3, pp. 117–126, 2003, doi: 10.1016/S0257-8972(02)00853-8.

[65] R. Arabi Jeshvaghani, M. Shamanian, and M. Jaberzadeh, "Enhancement of wear resistance of ductile iron surface alloyed by stellite 6," *Mater. Des.*, vol. 32, no. 4, pp. 2028–2033, 2011, doi: 10.1016/j.matdes.2010.11.060.

[66] A. S. C. M. D'Oliveira, R. Vilar, and C. G. Feder, "High temperature behaviour of plasma transferred arc and laser Co-based alloy coatings," *Appl. Surf. Sci.*, vol. 201, no. 1–4, pp. 154–160, 2002, doi: 10.1016/S0169-4332(02)00621-9.

[67] A. Kusmoko, Ȧ, D. Dunne, Ȧ, and H. Li, Ȧ, "A Comparative Study for Wear Resistant

of Stellite 6 Coatings on Nickel Alloy Substrate Produced by Laser Cladding , HVOF and Plasma Spraying Techniques," *Int. J. Curr. Eng. Technol.*, vol. 4, no. 1, pp. 32–36, 2014, [Online]. Available: http://inpressco.com/category/ijcet.

[68] T. S. Sidhu, S. Prakash, and R. D. Agrawal, "Hot corrosion studies of HVOF NiCrBSi and Stellite-6 coatings on a Ni-based superalloy in an actual industrial environment of a coal fired boiler," *Surf. Coatings Technol.*, vol. 201, no. 3–4, pp. 1602–1612, 2006, doi: 10.1016/j.surfcoat.2006.02.047.

[69] H. S. Sidhu, B. S. Sidhu, and S. Prakash, "Solid particle erosion of HVOF sprayed NiCr and Stellite-6 coatings," *Surf. Coatings Technol.*, vol. 202, no. 2, pp. 232–238, 2007, doi: 10.1016/j.surfcoat.2007.05.035.

[70] N. Jegadeeswaran, K. U. Bhat, and M. R. Ramesh, "Oxidation Studies on As-received and HVOF Sprayed Stellite-6 Coating on Turbine Alloys at 800^{o}C," *Int. J. Sci. Eng. Res.*, vol. 4, no. 6, pp. 214–220, 2013, [Online]. Available: http://www.ijser.org.

[71] L. Moskowitz and K. Trelewicz, "HVOF coatings for heavy-wear, high-impact applications," *J. Therm. Spray Technol.*, vol. 6, no. 3, pp. 294–299, 1997, doi: 10.1007/s11666-997-0061-1.

[72] A. Kumar, J. Boy, R. Zatorski, and L. D. Stephenson, "Thermal spray and weld repair alloys for the repair of cavitation damage in turbines and pumps: A technical note," *J. Therm. Spray Technol.*, vol. 14, no. 2, pp. 177–182, 2005, doi: 10.1361/10599630523737.

[73] V. Ocelík, U. de Oliveira, M. de Boer, and J. T. M. de Hosson, "Thick Co-based coating on cast iron by side laser cladding: Analysis of processing conditions and coating properties," *Surf. Coatings Technol.*, vol. 201, no. 12, pp. 5875–5883, 2007, doi: 10.1016/j.surfcoat.2006.10.044.

[74] V. Ocelík, M. Eekma, I. Hemmati, and J. T. M. De Hosson, "Elimination of Start/Stop defects in laser cladding," *Surf. Coatings Technol.*, vol. 206, no. 8–9, pp. 2403–2409, 2012, doi: 10.1016/j.surfcoat.2011.10.040.

[75] A. Kusmoko, D. Dunne, H. Li, and D. Nolan, "Effect of Two Different Energy Inputs for Laser Cladding of Stellite 6 on P91 and P22 Steel Substrates," *Procedia Mater. Sci.*, vol. 6, no. Icmpc, pp. 26–36, 2014, doi: 10.1016/j.mspro.2014.07.005.

[76] A. S. C. M. D'Oliveira, P. S. C. P. Da Silva, and R. M. C. Vilar, "Microstructural features of consecutive layers of Stellite 6 deposited by laser cladding," *Surf. Coatings Technol.*,

vol. 153, no. 2–3, pp. 203–209, 2002, doi: 10.1016/S0257-8972(01)01687-5.

[77] U. de Oliveira, V. Ocelík, and J. T. M. De Hosson, “Residual stress analysis in Co-based laser clad layers by laboratory X-rays and synchrotron diffraction techniques,” *Surf. Coatings Technol.*, vol. 201, no. 3–4, pp. 533–542, 2006, doi: 10.1016/j.surfcoat.2005.12.011.

[78] U. de Oliveira, V. Ocelík, and J. T. M. De Hosson, “Microstresses and microstructure in thick cobalt-based laser deposited coatings,” *Surf. Coatings Technol.*, vol. 201, no. 14, pp. 6363–6371, 2007, doi: 10.1016/j.surfcoat.2006.12.013.

[79] A. Gholipour, M. Shamanian, and F. Ashrafizadeh, “Microstructure and wear behavior of stellite 6 cladding on 17-4 PH stainless steel,” *J. Alloys Compd.*, vol. 509, no. 14, pp. 4905–4909, 2011, doi: 10.1016/j.jallcom.2010.09.216.

[80] R. Singh, D. Kumar, S. K. Mishra, and S. K. Tiwari, “Laser cladding of Stellite 6 on stainless steel to enhance solid particle erosion and cavitation resistance,” *Surf. Coatings Technol.*, vol. 251, pp. 87–97, 2014, doi: 10.1016/j.surfcoat.2014.04.008.

[81] H. Yu, R. Ahmed, H. de V. Lovelock, and S. Davies, “Influence of manufacturing process and alloying element content on the tribomechanical properties of cobalt-based alloys,” *J. Tribol.*, vol. 131, no. 1, pp. 1–12, 2009, doi: 10.1115/1.2991122.

[82] H. So, “The mechanism of oxidational wear,” *Wear*, vol. 184, no. 2, pp. 161–167, 1995, doi: 10.1016/0043-1648(94)06569-1.

[83] J. F. Archard, “Contact and rubbing of flat surfaces,” *J. Appl. Phys.*, vol. 24, no. 8, pp. 981–988, 1953, doi: 10.1063/1.1721448.

[84] V. Hegadekatte, N. Huber, and O. Kraft, “Finite element based simulation of dry sliding wear,” *Model. Simul. Mater. Sci. Eng.*, vol. 13, no. 1, pp. 57–75, 2005, doi: 10.1088/0965-0393/13/1/005.

[85] W. Y. Li *et al.*, “Significant influences of metal reactivity and oxide films at particle surfaces on coating microstructure in cold spraying,” *Appl. Surf. Sci.*, vol. 253, no. 7, pp. 3557–3562, 2007, doi: 10.1016/j.apsusc.2006.07.063.

[86] W. Y. Li, C. Zhang, X. Guo, C. J. Li, H. Liao, and C. Coddet, “Study on impact fusion at particle interfaces and its effect on coating microstructure in cold spraying,” *Appl. Surf. Sci.*, vol. 254, no. 2, pp. 517–526, 2007, doi: 10.1016/j.apsusc.2007.06.026.

[87] T. Schmidt, F. Gärtner, H. Assadi, and H. Kreye, “Development of a generalized parameter window for cold spray deposition,” *Acta Mater.*, vol. 54, no. 3, pp. 729–742,

2006, doi: 10.1016/j.actamat.2005.10.005.

[88] P. Vo, E. Irissou, J. G. Legoux, and S. Yue, “Mechanical and microstructural characterization of cold-sprayed Ti-6Al-4V after heat treatment,” *J. Therm. Spray Technol.*, vol. 22, no. 6, pp. 954–964, 2013, doi: 10.1007/s11666-013-9945-4.

[89] G. Bae *et al.*, “Bonding features and associated mechanisms in kinetic sprayed titanium coatings,” *Acta Mater.*, vol. 57, no. 19, pp. 5654–5666, 2009, doi: https://doi.org/10.1016/j.actamat.2009.07.061.

[90] W. Y. Li *et al.*, “Ti and Ti-6Al-4V coatings by cold spraying and microstructure modification by heat treatment,” *Adv. Eng. Mater.*, vol. 9, no. 5, pp. 418–423, 2007, doi: 10.1002/adem.200700022.

[91] W.-Y. Li, C.-J. Li, and G.-J. Yang, “Effect of impact-induced melting on interface microstructure and bonding of cold-sprayed zinc coating,” *Appl. Surf. Sci.*, vol. 257, no. 5, pp. 1516–1523, 2010, doi: https://doi.org/10.1016/j.apsusc.2010.08.089.

[92] M. M. Sharma, T. J. Eden, and B. T. Golesich, “Effect of Surface Preparation on the Microstructure, Adhesion, and Tensile Properties of Cold-Sprayed Aluminum Coatings on AA2024 Substrates,” *J. Therm. Spray Technol.*, vol. 24, no. 3, pp. 410–422, 2014, doi: 10.1007/s11666-014-0175-1.

[93] K. Yang, W. Li, X. Guo, X. Yang, and Y. Xu, “Characterizations and anisotropy of cold-spraying additive-manufactured copper bulk,” *J. Mater. Sci. Technol.*, vol. 34, no. 9, pp. 1570–1579, 2018, doi: https://doi.org/10.1016/j.jmst.2018.01.002.

[94] H. R. Wang, W. Y. Li, L. Ma, J. Wang, and Q. Wang, “Corrosion behavior of cold sprayed titanium protective coating on 1Cr13 substrate in seawater,” *Surf. Coatings Technol.*, vol. 201, no. 9-11 SPEC. ISS., pp. 5203–5206, 2007, doi: 10.1016/j.surfcoat.2006.07.104.

[95] D. K. Christoulis, S. Guetta, V. Guipont, and M. Jeandin, “The influence of the substrate on the deposition of cold-sprayed titanium: An experimental and numerical study,” *J. Therm. Spray Technol.*, vol. 20, no. 3, pp. 523–533, 2011, doi: 10.1007/s11666-010-9608-7.

[96] K. Binder, J. Gottschalk, M. Kollenda, F. Gärtner, and T. Klassen, “Influence of impact angle and gas temperature on mechanical properties of titanium cold spray deposits,” *J. Therm. Spray Technol.*, vol. 20, no. 1–2, pp. 234–242, 2011, doi: 10.1007/s11666-010-9557-1.

[97] T. Marrocco, D. G. McCartney, P. H. Shipway, and A. J. Sturgeon, “Production of titanium deposits by cold-gas dynamic spray: Numerical modeling and experimental characterization,” *J. Therm. Spray Technol.*, vol. 15, no. 2, pp. 263–272, 2006, doi: 10.1361/105996306X108219.

[98] V. S. Bhattiprolu, K. W. Johnson, O. C. Ozdemir, and G. A. Crawford, “Influence of feedstock powder and cold spray processing parameters on microstructure and mechanical properties of Ti-6Al-4V cold spray depositions,” *Surf. Coatings Technol.*, vol. 335, no. December 2017, pp. 1–12, 2018, doi: 10.1016/j.surfcoat.2017.12.014.

[99] R. Huang, M. Sone, W. Ma, and H. Fukanuma, “The effects of heat treatment on the mechanical properties of cold-sprayed coatings,” *Surf. Coatings Technol.*, vol. 261, pp. 278–288, 2015, doi: 10.1016/j.surfcoat.2014.11.017.

[100] X. T. Luo, Y. K. Wei, Y. Wang, and C. J. Li, “Microstructure and mechanical property of Ti and Ti6Al4V prepared by an in-situ shot peening assisted cold spraying,” *Mater. Des.*, vol. 85, pp. 527–533, 2015, doi: 10.1016/j.matdes.2015.07.015.

[101] C. J. Li and W. Y. Li, “Deposition characteristics of titanium coating in cold spraying,” *Surf. Coatings Technol.*, vol. 167, no. 2–3, pp. 278–283, 2003, doi: 10.1016/S0257-8972(02)00919-2.

[102] W. Li, K. Yang, S. Yin, X. Yang, Y. Xu, and R. Lupoi, “Solid-state additive manufacturing and repairing by cold spraying: A review,” *J. Mater. Sci. Technol.*, vol. 34, no. 3, pp. 440–457, 2018, doi: 10.1016/j.jmst.2017.09.015.

[103] R. Lupoi, “Current design and performance of cold spray nozzles: Experimental and numerical observations on deposition efficiency and particle velocity,” *Surf. Eng.*, vol. 30, no. 5, pp. 316–322, 2014, doi: 10.1179/1743294413Y.0000000214.

[104] W. Y. Li, H. Liao, G. Douchy, and C. Coddet, “Optimal design of a cold spray nozzle by numerical analysis of particle velocity and experimental validation with 316L stainless steel powder,” *Mater. Des.*, vol. 28, no. 7, pp. 2129–2137, 2007, doi: 10.1016/j.matdes.2006.05.016.

[105] S. Yin, M. Meyer, W. Li, H. Liao, and R. Lupoi, “Gas Flow, Particle Acceleration, and Heat Transfer in Cold Spray: A review,” *J. Therm. Spray Technol.*, vol. 25, no. 5, pp. 874–896, 2016, doi: 10.1007/s11666-016-0406-8.

[106] W. Li, C. Cao, and S. Yin, “Solid-state cold spraying of Ti and its alloys: A literature review,” *Prog. Mater. Sci.*, vol. 110, no. December 2019, p. 100633, 2020, doi:

10.1016/j.pmatsci.2019.100633.

[107] S. H. Zahiri, W. Yang, and M. Jahedi, “Characterization of cold spray titanium supersonic jet,” *J. Therm. Spray Technol.*, vol. 18, no. 1, pp. 110–117, 2009, doi: 10.1007/s11666-008-9278-x.

[108] J. Lee, S. Shin, H. J. Kim, and C. Lee, “Effect of gas temperature on critical velocity and deposition characteristics in kinetic spraying,” *Appl. Surf. Sci.*, vol. 253, no. 7, pp. 3512–3520, 2007, doi: 10.1016/j.apsusc.2006.07.061.

[109] T. Hussain, “Cold Spraying of Titanium: A Review of Bonding Mechanisms, Microstructure and Properties,” *Key Eng. Mater.*, vol. 533, pp. 53–90, 2013, doi: 10.4028/www.scientific.net/KEM.533.53.

[110] W. Wong, P. Vo, E. Irissou, A. N. Ryabinin, J. G. Legoux, and S. Yue, “Effect of particle morphology and size distribution on cold-sprayed pure titanium coatings,” *J. Therm. Spray Technol.*, vol. 22, no. 7, pp. 1140–1153, 2013, doi: 10.1007/s11666-013-9951-6.

[111] M. Villa Vidaller, F. Haußler, H. Assadi, F. Gärtner, and T. Klassen, “Influence of substrate on cold sprayed titanium coatings,” in *Proceedings of the International Thermal Spray Conference*, 2015, vol. 2, pp. 1047–1054, [Online]. Available: https://www.scopus.com/inward/record.uri?eid=2-s2.0-84971273188&partnerID=40&md5=0ea4a8c542720e58f54156d78eaa8e51.

[112] Y. Watanabe, C. Yoshida, K. Atsumi, M. Yamada, and M. Fukumoto, “Influence of Substrate Temperature on Adhesion Strength of Cold-Sprayed Coatings,” *J. Therm. Spray Technol.*, vol. 24, 2014, doi: 10.1007/s11666-014-0165-3.

[113] D. Goldbaum *et al.*, “The effect of deposition conditions on adhesion strength of Ti and Ti6Al4V cold spray splats,” *J. Therm. Spray Technol.*, vol. 21, no. 2, pp. 288–303, 2012, doi: 10.1007/s11666-011-9720-3.

[114] T. Hussain, D. G. McCartney, P. H. Shipway, and D. Zhang, “Bonding mechanisms in cold spraying: The contributions of metallurgical and mechanical components,” *J. Therm. Spray Technol.*, vol. 18, no. 3, pp. 364–379, 2009, doi: 10.1007/s11666-009-9298-1.

[115] A. W. Y. Tan *et al.*, “Effects of Traverse Scanning Speed of Spray Nozzle on the Microstructure and Mechanical Properties of Cold-Sprayed Ti6Al4V Coatings,” *J. Therm. Spray Technol.*, vol. 26, no. 7, pp. 1484–1497, 2017, doi: 10.1007/s11666-017-0619-5.

[116] A. M. Vilardell, N. Cinca, A. Concustell, S. Dosta, I. G. Cano, and J. M. Guilemany, “Cold spray as an emerging technology for biocompatible and antibacterial coatings: state of art,” *J. Mater. Sci.*, vol. 50, no. 13, pp. 4441–4462, 2015, doi: 10.1007/s10853-015-9013-1.

[117] J. Pattison, S. Celotto, A. Khan, and W. O’Neill, “Standoff distance and bow shock phenomena in the Cold Spray process,” *Surf. Coatings Technol.*, vol. 202, no. 8, pp. 1443–1454, 2008, doi: 10.1016/j.surfcoat.2007.06.065.

[118] W. Y. Li *et al.*, “Effect of standoff distance on coating deposition characteristics in cold spraying,” *Mater. Des.*, vol. 29, no. 2, pp. 297–304, 2008, doi: 10.1016/j.matdes.2007.02.005.

[119] S. Yin, X. Suo, J. Su, Z. Guo, H. Liao, and X. Wang, “Effects of substrate hardness and spray angle on the deposition behavior of cold-sprayed ti particles,” *J. Therm. Spray Technol.*, vol. 23, no. 1–2, pp. 76–83, 2014, doi: 10.1007/s11666-013-0039-0.

[120] S. Yin, P. He, H. Liao, and X. Wang, “Deposition features of Ti coating using irregular powders in cold spray,” *J. Therm. Spray Technol.*, vol. 23, no. 6, pp. 984–990, 2014, doi: 10.1007/s11666-014-0116-z.

[121] W. Wong, E. Irissou, A. N. Ryabinin, J. G. Legoux, and S. Yue, “Influence of helium and nitrogen gases on the properties of cold gas dynamic sprayed pure titanium coatings,” *J. Therm. Spray Technol.*, vol. 20, no. 1–2, pp. 213–226, 2011, doi: 10.1007/s11666-010-9568-y.

[122] K. Kim, M. Watanabe, K. Mitsuishi, K. Iakoubovskii, and S. Kuroda, “Impact bonding and rebounding between kinetically sprayed titanium particle and steel substrate revealed by high-resolution electron microscopy,” *J. Phys. D. Appl. Phys.*, vol. 42, no. 6, 2009, doi: 10.1088/0022-3727/42/6/065304.

[123] W. Y. Li, H. Liao, C. J. Li, H. S. Bang, and C. Coddet, “Numerical simulation of deformation behavior of Al particles impacting on Al substrate and effect of surface oxide films on interfacial bonding in cold spraying,” *Appl. Surf. Sci.*, vol. 253, no. 11, pp. 5084–5091, 2007, doi: 10.1016/j.apsusc.2006.11.020.

[124] K. Kim and S. Kuroda, “Amorphous oxide film formed by dynamic oxidation during kinetic spraying of titanium at high temperature and its role in subsequent coating formation,” *Scr. Mater.*, vol. 63, no. 2, pp. 215–218, 2010, doi: 10.1016/j.scriptamat.2010.03.061.

[125] K. H. Kim, M. Watanabe, J. Kawakita, and S. Kuroda, “Grain refinement in a single titanium powder particle impacted at high velocity,” *Scr. Mater.*, vol. 59, no. 7, pp. 768–771, 2008, doi: 10.1016/j.scriptamat.2008.06.020.

[126] K. H. Kim, M. Watanabe, and S. Kuroda, “Bonding mechanisms of thermally softened metallic powder particles and substrates impacted at high velocity,” *Surf. Coatings Technol.*, vol. 204, no. 14, pp. 2175–2180, 2010, doi: 10.1016/j.surfcoat.2009.12.001.

[127] A. M. Birt, V. K. Champagne, R. D. Sisson, and D. Apelian, “Microstructural Analysis of Cold-Sprayed Ti-6Al-4V at the Micro- and Nano-Scale,” *J. Therm. Spray Technol.*, vol. 24, no. 7, pp. 1277–1288, 2015, doi: 10.1007/s11666-015-0288-1.

[128] R. R. Chromik *et al.*, “Modified ball bond shear test for determination of adhesion strength of cold spray splats,” *Surf. Coatings Technol.*, vol. 205, no. 5, pp. 1409–1414, 2010, doi: 10.1016/j.surfcoat.2010.07.037.

[129] S. I. Imbriglio *et al.*, “Adhesion strength of titanium particles to alumina substrates: A combined cold spray and LIPIT study,” *Surf. Coatings Technol.*, vol. 361, no. September 2018, pp. 403–412, 2019, doi: 10.1016/j.surfcoat.2019.01.071.

[130] K. Yang, W. Li, X. Yang, and Y. Xu, “Anisotropic response of cold sprayed copper deposits,” *Surf. Coatings Technol.*, vol. 335, no. December 2017, pp. 219–227, 2018, doi: 10.1016/j.surfcoat.2017.12.043.

[131] S. Yin, R. Jenkins, Y. Xingchen, and R. Lupoi, “Microstructure and mechanical anisotropy of additively manufactured cold spray copper deposits,” *Mater. Sci. Eng. A*, vol. 734, 2018, doi: 10.1016/j.msea.2018.07.096.

[132] N. Cinca and J. M. Guilemany, “Structural and properties characterization of stellite coatings obtained by cold gas spraying,” *Surf. Coatings Technol.*, vol. 220, pp. 90–97, 2013, doi: 10.1016/j.surfcoat.2012.11.026.

[133] N. Cinca, E. López, S. Dosta, and J. M. Guilemany, “Study of stellite-6 deposition by cold gas spraying,” *Surf. Coatings Technol.*, vol. 232, pp. 891–898, 2013, doi: 10.1016/j.surfcoat.2013.06.120.

[134] ASTM International, “ASTM G99-05: Standard Test Method for Wear Testing with a Pin-on-Disk Apparatus,” *ASTM Stand.*, vol. 04, no. 02, pp. 1–5, 2007, doi: 10.1520/G0099-05R16.2.

[135] J. W. CHRISTIAN, “Equilibrium and general kinetic theory,” in *The Theory of Transformations in Metals and Alloys*, J. W. CHRISTIAN, Ed. Oxford: Pergamon, 2002,

pp. 1–22.

[136] ASTM International, “ASTM E2109−01: Test Methods of Determining Area Percentage Porosity in Thermal Sprayed Coatings,” *ASTM Stand.*, vol. 03, no. 01, pp. 1–8, 2014, doi: 10.1520/E2109-01R14.2.

[137] X. Qiu *et al.*, “Microstructure, microhardness and tribological behavior of Al2O3 reinforced A380 aluminum alloy composite coatings prepared by cold spray technique,” *Surf. Coatings Technol.*, vol. 350, no. July, pp. 391–400, 2018, doi: 10.1016/j.surfcoat.2018.07.039.

[138] D. Goldbaum *et al.*, “Mechanical behavior of Ti cold spray coatings determined by a multi-scale indentation method,” *Mater. Sci. Eng. A*, vol. 530, no. 1, pp. 253–265, 2011, doi: 10.1016/j.msea.2011.09.083.

[139] G. Bolelli, B. Bonferroni, H. Koivuluoto, L. Lusvarghi, and P. Vuoristo, “Depth-sensing indentation for assessing the mechanical properties of cold-sprayed Ta,” *Surf. Coatings Technol.*, vol. 205, no. 7, pp. 2209–2217, 2010, doi: 10.1016/j.surfcoat.2010.08.146.

[140] M. A. Garrido, P. Sirvent, and P. Poza, “Evaluation of mechanical properties of Ti6Al4V cold sprayed coatings*,” *Surf. Eng.*, vol. 34, no. 5, pp. 399–406, 2018, doi: 10.1080/02670844.2017.1398442.

[141] “ISO 14577-1:2002, Metallic materials — Instrumented indentation test for hardness and materials parameters — Part 1: Test method.”

[142] W. C. Oliver and G. M. Pharr, “An improved technique for determining hardness and elastic modulus using load and displacement sensing indentation experiments,” *J. Mater. Res.*, vol. 7, no. 6, pp. 1564–1583, 1992.

[143] S. Weiller *et al.*, “Cold spray as an innovative process to develop leak tight aluminum coatings for ultrahigh vacuum applications in a large particle high-energy collider,” in *Proceedings of the International Thermal Spray Conference*, 2019, vol. 2019-May, pp. 831–837, [Online]. Available: https://www.scopus.com/inward/record.uri?eid=2-s2.0-85071522115&partnerID=40&md5=6b5c1f189f04bc779b261e0b2f00aa49.

[144] R. Cimino, V. Baglin, and F. Schäfers, “Potential Remedies for the High Synchrotron-Radiation-Induced Heat Load for Future Highest-Energy-Proton Circular Colliders,” *Phys. Rev. Lett.*, vol. 115, no. 26, pp. 1–5, 2015, doi: 10.1103/PhysRevLett.115.264804.

[145] T. Novoselova, P. Fox, R. Morgan, and W. O’Neill, “Experimental study of titanium/aluminium deposits produced by cold gas dynamic spray,” *Surf. Coatings*

Technol., vol. 200, no. 8, pp. 2775–2783, 2006, doi: 10.1016/j.surfcoat.2004.10.133.

[146] S. Gulizia *et al.*, "Characterisation of cold spray titanium coatings," *Mater. Sci. Forum*, vol. 654–656, pp. 898–901, 2010, doi: 10.4028/www.scientific.net/MSF.654-656.898.

[147] ASTM International, "ASTM C633-13: Standard Test Method for Adhesion or Cohesion Strength of Thermal Spray Coatings," *ASTM Standard*, vol. 02, no. 05. pp. 1–7, 2001, doi: 10.1520/C0633-13.Copyright.

[148] G. Cattenoz *et al.*, "Vacuum acceptance tests for the UHV room temperature vacuum system of the LHC during LS1," *IPAC 2014 Proc. 5th Int. Part. Accel. Conf.*, no. June, pp. 2357–2359, 2014.

[149] P. A. Redhead, "Recommended practices for measuring and reporting outgassing data," *J. Vac. Sci. Technol. A Vacuum, Surfaces, Film.*, vol. 20, no. 5, pp. 1667–1675, 2002, doi: 10.1116/1.1496783.

[150] Z. Arabgol, M. Villa Vidaller, H. Assadi, F. Gärtner, and T. Klassen, "Influence of thermal properties and temperature of substrate on the quality of cold-sprayed deposits," *Acta Mater.*, vol. 127, pp. 287–301, 2017, doi: 10.1016/j.actamat.2017.01.040.

[151] C. Chen *et al.*, "Numerical investigation of transient coating build-up and heat transfer in cold spray," *Surf. Coatings Technol.*, vol. 326, pp. 355–365, 2017, doi: 10.1016/j.surfcoat.2017.07.069.

[152] Y. Zou, D. Goldbaum, J. A. Szpunar, and S. Yue, "Microstructure and nanohardness of cold-sprayed coatings: Electron backscattered diffraction and nanoindentation studies," *Scr. Mater.*, vol. 62, no. 6, pp. 395–398, 2010, doi: 10.1016/j.scriptamat.2009.11.034.

[153] T. L. Oberle, "Wear of metals," *Wear*, vol. 1, no. 4, pp. 317–332, 1958, doi: 10.1016/0043-1648(58)90004-8.

[154] J. Halling, "The tribology of surface films," *Thin Solid Films*, vol. 108, no. 2, pp. 103–115, 1983, doi: 10.1016/0040-6090(83)90496-0.

[155] C. Rebholz, A. Leyland, J. M. Schneider, A. A. Voevodin, and A. Matthews, "Structure, hardness and mechanical properties of magnetron-sputtered titanium-aluminium boride films," *Surf. Coatings Technol.*, vol. 120–121, pp. 412–417, 1999, doi: 10.1016/S0257-8972(99)00490-9.

[156] D. H. E. Persson, "On the Mechanisms behind the Tribological Performance of Stellites (PhD dissertation)," Acta Universitatis Upsaliensis, Uppsala, 2005.

[157] R. Namus, P. Zeng, and W. M. Rainforth, "Correlation of the wear transition in CoCrMo

alloys with the formation of a nanocrystalline surface layer and a proteinaceous surface film," *Wear*, vol. 376–377, pp. 223–231, 2017, doi: 10.1016/j.wear.2016.11.046.

[158] R. Büscher, G. Täger, W. Dudzinski, B. Gleising, M. A. Wimmer, and A. Fischer, "Subsurface microstructure of metal-on-metal hip joints and its relationship to wear particle generation," *J. Biomed. Mater. Res. - Part B Appl. Biomater.*, vol. 72, no. 1, pp. 206–214, 2005, doi: 10.1002/jbm.b.30132.

[159] Š. Houdková, Z. Pala, E. Smazalová, M. Vostřák, and Z. Česánek, "Microstructure and sliding wear properties of HVOF sprayed, laser remelted and laser clad Stellite 6 coatings," *Surf. Coatings Technol.*, vol. 318, pp. 129–141, 2017, doi: 10.1016/j.surfcoat.2016.09.012.

[160] A. Renz, B. Prakash, J. Hardell, and O. Lehmann, "High-temperature sliding wear behaviour of Stellite®12 and Tribaloy®T400," *Wear*, vol. 402–403, no. October 2017, pp. 148–159, 2018, doi: 10.1016/j.wear.2018.02.013.

[161] P. Magarò, A. L. Marino, C. Maletta, M. Tului, and A. Di Schino, "Tribological properties of wear-resistant coatings obtained by cold gas dynamic spray," *Procedia Struct. Integr.*, vol. 9, pp. 287–294, 2018, doi: 10.1016/j.prostr.2018.06.030.

[162] P. Magarò *et al.*, "Effect of process parameters on the properties of Stellite-6 coatings deposited by Cold Gas Dynamic Spray," *Surf. Coatings Technol.*, vol. 377, no. August, p. 124934, 2019, doi: 10.1016/j.surfcoat.2019.124934.

[163] S. Q. Wang, L. Wang, Y. T. Zhao, Y. Sun, and Z. R. Yang, "Mild-to-severe wear transition and transition region of oxidative wear in steels," *Wear*, vol. 306, no. 1–2, pp. 311–320, 2012, doi: 10.1016/j.wear.2012.08.017.

[164] M. X. Wei, S. Q. Wang, X. H. Cui, and K. M. Chen, "Characteristics of extrusive wear and transition of wear mechanisms in elevated-temperature wear of a carbon steel," *Tribol. Trans.*, vol. 53, no. 6, pp. 888–896, 2010, doi: 10.1080/10402004.2010.501950.

[165] S. Q. Wang, M. X. Wei, F. Wang, and Y. T. Zhao, "Transition of elevated-temperature wear mechanisms and the oxidative delamination wear in hot-working die steels," *Tribol. Int.*, vol. 43, no. 3, pp. 577–584, 2010, doi: 10.1016/j.triboint.2009.09.006.

[166] H. S. Kim and M. B. Bush, "Effects of grain size and porosity on the elastic modulus of nanocrystalline materials," *Nanostructured Mater.*, vol. 11, no. 3, pp. 361–367, 1999, doi: 10.1016/S0965-9773(99)00052-5.

[167] A. Latapie and D. Farkas, "Effect of grain size on the elastic properties of nanocrystalline

α-iron," *Scr. Mater.*, vol. 48, no. 5, pp. 611–615, 2003, doi: 10.1016/S1359-6462(02)00467-0.

[168] C. Yu, R. Yang, Y. Feng, Y. Huan, G. Peng, and T. Zhang, "Relationships between the work recovery ratio of indentation and plastic parameters for instrumented spherical indentation," *MRS Commun.*, vol. 5, no. 1, pp. 89–94, 2015, doi: 10.1557/mrc.2015.10.

[169] T. Y. Kim, J. E. Dolbow, and E. Fried, "Numerical study of the grain-size dependent Young's modulus and Poisson's ratio of bulk nanocrystalline materials," *Int. J. Solids Struct.*, vol. 49, no. 26, pp. 3942–3952, 2012, doi: 10.1016/j.ijsolstr.2012.08.023.

[170] D. Goldbaum, R. R. Chromik, S. Yue, E. Irissou, and J. G. Legoux, "Mechanical property mapping of cold sprayed Ti splats and coatings," *J. Therm. Spray Technol.*, vol. 20, no. 3, pp. 486–496, 2011, doi: 10.1007/s11666-010-9546-4.

[171] H. Fukanuma and N. Ohno, "A study of adhesive strength of cold spray coatings," *Proc. Int. Therm. Spray Conf.*, pp. 329–334, 2004.

[172] R. I. Stephens, A. Fatemi, R. R. Stephens, and H. O. Fuchs, *Metal Fatigue in Engineering*. 2000.

[173] R. Ahmed, H. L. De Villiers Lovelock, S. Davies, and N. H. Faisal, "Influence of Re-HIPing on the structure-property relationships of cobalt-based alloys," *Tribol. Int.*, vol. 57, pp. 8–21, 2013, doi: 10.1016/j.triboint.2012.06.025.

La borsa di dottorato è stata cofinanziata con risorse del
Programma Operativo Nazionale Ricerca e Innovazione 2014-2020 (CCI 2014IT16M2OP005)
Fondo Sociale Europeo, Azione I.1 “Dottorati Innovativi con caratterizzazione Industriale”

UNIONE EUROPEA
Fondo Sociale Europeo

Ministero dell'Università e della Ricerca